ISBN 978-82-326-5797-1 (printed ver.)
ISBN 978-82-326-6154-1 (electronic ver.)
ISSN 1503-8181 (printed ver.)
ISSN 2703-8084 (electronic ver.)

NTNU
Norwegian University of
Science and Technology

Doctoral theses at NTNU, 2021:216

NTNU

Tor Martin Lystad

Doctoral thesis

Doctoral theses at NTNU, 2021:216

NTNU
Norwegian University of
Science and Technology
Thesis for the degree of
Philosophiae Doctor
Faculty of Engineering
Department of Structural Engineering

Tor Martin Lystad

Long-term extreme buffeting response investigations for long-span bridges considering uncertain turbulence parameters based on field measurements

NTNU
Norwegian University of
Science and Technology

Tor Martin Lystad

Long-term extreme buffeting response investigations for long-span bridges considering uncertain turbulence parameters based on field measurements

Thesis for the degree of Philosophiae Doctor

Trondheim, June 2021

Norwegian University of Science and Technology
Faculty of Engineering
Department of Structural Engineering

NTNU
Norwegian University of
Science and Technology

NTNU
Norwegian University of Science and Technology

Thesis for the degree of Philosophiae Doctor

Faculty of Engineering
Department of Structural Engineering

ISBN 978-82-326-5797-1 (printed ver.)
ISBN 978-82-326-6154-1 (electronic ver.)
ISSN 1503-8181 (printed ver.)
ISSN 2703-8084 (electronic ver.)

Doctoral theses at NTNU, 2021:216

PRINTED IN NORWAY
NO - 1598

NORDIC SWAN ECOLABEL
Printed matter
2041 0731

Printed by Skipnes Kommunikasjon AS

Abstract

When bridges become increasingly longer, the dynamic behavior from wind and waves can dominate the structural load effects. To build better knowledge about the dynamic behavior of long-span bridges subjected to turbulent wind in complex terrain, the Norwegian University of Science and Technology has instrumented the Hardanger Bridge with a full-scale measurement system. The Hardanger Bridge measurement program, along with many full-scale measurement efforts on long-span bridges around the world, has shown a large scatter in the measured buffeting response when plotted against the mean wind velocity. In current long-span bridge design practice, the mean wind velocity is the only wind field parameter that is treated as a random variable when defining the design wind load conditions. The observed scattered buffeting response is a worry concerning the accuracy of the current practice, since it indicates that the uncertainty of other turbulence parameters also considerably affects the buffeting response. In this thesis, the accuracy and limitations of the current design practice for calculation of extreme buffeting load effects in long-span bridges are investigated.

The wind field information defining the basis for design of such bridges, is fundamental to achieve a reliable extreme load definition. The traditional methods for wind field measurements are investigated by comparing the in-situ mast measurements and terrain model wind tunnel tests performed before the design of the Hardanger Bridge with wind measurements along the span of the current bridge.

The full long-term method is recognized as the most accurate way to predict the extreme response of a structure subjected to stochastic dynamic loads. However, in current design practice for buffeting action of long-span bridges this has not yet become the standard way to estimate the extreme responses. In the work presented herein, the long-term extreme buffeting response of the Hardanger Bridge is investigated, considering the turbulence variability effects and the short-term extreme response uncertainty. The turbulence parameters are described as random variables through a probabilistic turbulence model. The findings show that both the turbulence variability and the short-term extreme response uncertainty is very important for the design response of the Hardanger Bridge girder. The buffeting response predicted by the long-term methods are compared with the scattered acceleration responses measured in full-scale at the Hardanger Bridge, showing substantial improvements to the current design methods.

Numerical integration of the full long-term problem often becomes to computationally demanding for practical applications. The accuracy of computationally efficient, reliability-based, approximate long-term methods is investigated for the application to the buffeting load effects of the Hardanger Bridge. Design approaches suitable for practical applications to a full bridge system is suggested by utilizing the established long-term methods. Finally, a new algorithm for structural long-term extreme response calculations is proposed, exhibiting several attractive qualities in terms of accuracy and computational efficiency.

Acknowledgements

The work presented in this thesis has been funded by Norconsult AS and the Research Council of Norway as an industrial PhD project under the project number 263389/O30.

I am truly grateful for the opportunity provided by Norconsult to fulfill my desire to learn and to follow my passion of engineering long-span bridges both in terms of research and as an eager (relatively) young engineer. I am grateful for the brilliant work environment with extremely competent, and friendly colleagues.

A special thank you to Magnar Myhre, Kjetil Ruud, Marianne Bjelland and Asbjørn Gjerding-Smith for believing in me and for making the challenging combination between the role as an engineering consultant and a researcher become manageable. Also, a great thank you to my two industry supervisors, and engineering role models, Alexander Kyte and Jon Solemsli for everything I have learned from you and will continue to learn in the years to come. And of course, a sincere thank you to my dear colleague, friend and fellow PhD-candidate, Henrik Skyvulstad for sharing both frustrations and joys during this rollercoaster of emotions called a PhD education.

I would also like to express my deepest gratitude to my supervisor Professor Ole Øiseth for guiding me through this process. You truly have a brilliant mind, and I am privileged to be able to learn from you.

Also, a special thank you to Aksel Fenerci who practically has been a bonus supervisor throughout this project. You are an excellent researcher and I have learned so much from our discussions and your thorough effort in revising and finalizing the manuscripts presented in this thesis.

Thank you to all past and present members of the structural dynamics group, and especially to the members during the time I stayed with you full time. You know who you are, the list is becoming long, so to avoid the risk of missing someone, I'll leave it at that. Also, thank you to my co-supervisor Professor Anders Rønnquist. You and Professor Øiseth make a great team in managing the structural dynamics group.

Mom and dad (Anne-Lise Lystad and Tor-Morten Lystad), thank you for your limitless love and support in all aspects of my life.

Finally, and most importantly, thank you to my dear girls, Josefine, Mathilde and Caroline. You bring so much joy and happiness to my life, and any frustrating and challenging day can easily be turned around when I get to come home to you.

Preface

This thesis is submitted in partial fulfilment of the requirements for the degree *Philosophiae Doctor (Ph.D.)* at the Norwegian University of Science and Technology (NTNU). The work has been carried out at the Department of Structural Engineering, Faculty of Engineering and funded by Norconsult AS and the Research Council of Norway.

Professor Ole Øiseth, Professor Anders Rønnquist, Alexander Kyte and Jon Solemsli has supervised the work.

The thesis is based on four papers either published or submitted to international peer-reviewed scientific journals and one conference paper published in the conference proceedings.

Tor Martin Lystad
Trondheim, Norway
June 2021

List of appended papers

I. Lystad TM, Fenerci A, Øiseth O. Evaluation of mast measurements and wind tunnel terrain models to describe spatially variable wind field characteristics for long-span bridge design. J Wind Eng Ind Aerodyn 2018;179:558–73. https://doi.org/10.1016/J.JWEIA.2018.06.021.

II. Lystad TM, Fenerci A, Øiseth O. Aerodynamic Effect of Non-uniform Wind Profiles for Long-Span Bridges. Proc. XV Conf. Ital. Assoc. Wind Eng. Vent. 2018. Lect. Notes Civ. Eng., vol. 27, 2019. https://doi.org/10.1007/978-3-030-12815-9_34.

III. Lystad TM, Fenerci A, Øiseth O. Buffeting response of long-span bridges considering uncertain turbulence parameters using the environmental contour method. Eng Struct 2020;213:110575. https://doi.org/10.1016/J.ENGSTRUCT.2020.110575.

IV. Lystad TM, Fenerci A, Øiseth O. Long-term extreme buffeting response of cable-supported bridges with uncertain turbulence parameters. Eng Struct 2021;236:112126. https://doi.org/10.1016/j.engstruct.2021.112126.

V. Lystad TM, Fenerci A, Øiseth O. Full long-term extreme structural response with sequential Gaussian process surrogate modelling. Submitted for journal publication

Other scientific contributions

I. Lystad TM, Fenerci A, Øiseth O. Wind field characteristics at the Hardanger Bridge site: Comparison of wind tunnel terrain model tests with full-scale measurements. 7th Eur. African Conf. Wind Eng. (EACWE 2017), Liege, Belgium, 2017.

II. Lystad TM, Fenerci A, Øiseth O. Turbulence variability effects on the buffeting response of a long-span suspension bridge. The 15th International Conference on Wind Engineering (ICWE 19), Beijing, China, 2019.

III. Lystad TM, Fenerci A, Øiseth O. Long-term extreme buffeting response of long-span bridges considering uncertain turbulence parameters. IABSE Congress Ghent 2021, Submitted.

Contents

1 Introduction

1.1 Background and motivation

1.1.1 Longer and more slender bridges

Long-span bridges have enabled the crossing of increasingly wider obstacles like rivers, fjords, lakes and canyons, over the last century. Suspension bridges have been the bridge technology used to realize the longest unsupported bridge spans. Giant engineering leaps were taken in the United States (U.S.) during the 1930s with the opening of the George Washington Bridge (suspension bridge with a main span of 1067m [1]) in 1931 and the iconic Golden Gate Bridge (main span of 1280m [2]) in 1937. However, the bridge engineering community were given a stark warning about moving too fast forward with new technologies following the collapse of the infamous Tacoma Narrows Bridge in 1940, just months after its opening. After the collapse, wind engineering research skyrocketed for long-span bridge applications, and buffeting actions and aeroelastic phenomena were thoroughly studied.

No significant increase in suspension bridge spans was made after Tacoma Narrows collapse until the Humber Bridge (main span of 1410m [3]) opened in the United Kingdom in 1981. Several long-span suspension bridges were constructed in Europe and Asia during the post-world war two period from 1960. The Akashi Kaikyo Bridge in Japan (main span of 1991m [4]) is still the world record holder, though it will be overtaken by the Çanakkale 1915 Bridge (main span of 2023m), which is under construction at the time of writing. Since the start of the millennium, an incredible amount of long-span suspension bridges has emerged in China following rapid economic growth. The development of long-span suspension bridges is illustrated in Figure 1, where the 100 longest suspension bridges are plotted against the year of completion. Additionally, the longest suspension bridges currently under design and construction are shown.

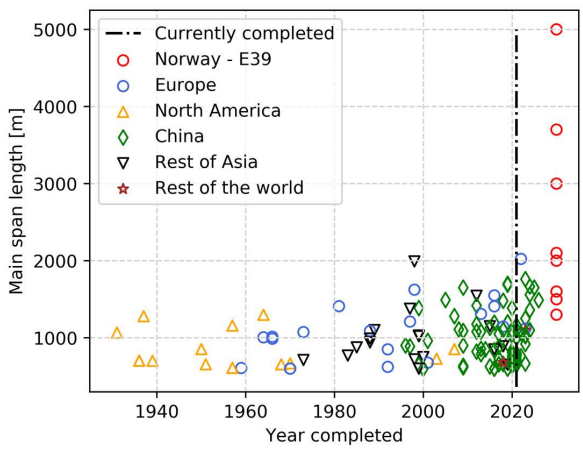

Figure 1: World's longest suspension bridge spans (completed and currently under construction) [5] illustrated together with the planned fjord crossings for the Coastal highway route E39

During the last decades, the cable-stayed bridge concept has seen a rapid increase in bridge spans, from the Alex Fraser Bridge in 1986 with a main span of 465 m to the current record holder, the Russkij Bridge, which opened in Russia in 2012 with a main span of 1104 m [6]. The cable-supported bridge technology has also seen a new application by the impressive hybrid design of the Third Bosphorus Bridge (also known as the Yavuz Sultan Selim Bridge) which opened in Turkey in 2016 with a main span of 1408 m [7].

In addition to cable-supported bridges, floating bridges have been used for long fjord-, lake- and river crossings. The world's longest floating bridge is the Evergreen Point Floating Bridge in Seattle, U.S., with a floating span of 2350 m, continuously tethered to the lake bottom. The world's two only end-anchored floating bridges were constructed in Norway in the early 1990s. The longest end-anchored floating bridge is the Nordhordland Bridge with a floating span of 1246 m which opened in 1994 [8] just north of the city of Bergen. The other end-anchored floating bridge is the Bergsøysundet Bridge with a floating span of 933 m [8], which opened in 1992, some 300 kilometres north, close to the city of Kristiansund.

Both the Nordhordland Bridge and the Bergsøysundet Bridge is part of the current Coastal Highway Route E39 along the west coast of Norway. Large parts of the landscape along this road consists of high mountains and deep fjords, so the current E39 is hampered by tunnels and ferry connections. This part of Norway is an important economic region as the offshore energy and fish farm industries are managed from this area, making efficient infrastructure a key to further economic growth along the country's west coast.

The Norwegian government is currently planning to build a Ferry Free Coastal Highway Route E39 [9], replacing 9 ferries with bridges and tunnels and reducing the travelling time between the two cities Kristiansand and Trondheim from 21 hours to an impressive 11 hours. Extreme bridge concepts are currently being planned to cross the broad and deep fjords along the highway route. The planning is a coordinated effort managed by the Norwegian Public Roads Administration (NPRA), consisting of development projects performed by Norwegian consultant companies and extensive research activities.

The fjords are as wide as up to 5 km and as deep as 1300 m, and bridge concepts such as ultra-long suspension bridges, submerged floating tunnels, floating bridges and suspension bridges with bridge towers supported by tension-leg platforms (TLP) are considered. All these bridge concepts are incredibly slender, and most are highly susceptible to buffeting actions from turbulent wind loads.

The planned fjord crossings are shown in Table 1, indicating the bridge concepts under consideration for each fjord. The considered fjord crossings are also shown in Figure 1, together with the world's longest suspension bridge spans, to illustrate the extreme span lengths and the technological leaps needed to realize the vision of a Ferry Free Coastal Highway Route E39.

Table 1: Fjord crossings along the Coastal Highway Route E39 with indication of bridge concepts under consideration

Fjord crossing	Fjord		Possible bridge concept			
	Width [m]	Depth [m]	Suspensi-on bridge	Submerged floating tunnel	Floating bridge	TLP-suspension bridge
Halsafjorden	2 000	600	X		X	X
Julsundet	1 600	600	X			
Sulafjorden	3 000/3 800	500	X	X		X
Vartdalsfjorden	2 100	600	X	X	X	X
Nordfjorden	1 500	500	X			
Sognefjorden	3 700	1 300	X	X		X
Bjørnafjorden	5 000	450			X	
Langenuen	1 300	500	X			

1.1.2 Design practice for long-span bridges

The response to dynamic wind loads becomes a significant load effect for the structural design as bridges become slender. This is due to the wind spectrum having its highest energy at low frequencies. The span length development raises a need to revisit the buffeting response calculation methodology widely used in the design of long-span bridges, to ensure that the safety and reliability of future long-span bridges are maintained.

For long-span bridges where the response from dynamic wind loading dominates the load effects relevant for design, the quality of the information about the wind field characteristics available for the design calculations governs the achieved structural reliability. In-situ mast measurements [10–14] and wind tunnel tests of terrain models [15–18] have traditionally been the primary approach to build knowledge about the local wind field. Numerical methods such as meteorological mesoscale models and more detailed computational fluid dynamics (CFD) [19–21] are also used to supplement site measurements, and the traditional mast measurements are being assisted by LIDAR technology [22] to measure wind field properties at interesting positions where mast measurements are not possible. There are positives and negatives with all methods mentioned above. Some of the most profound advantages and limitations of each method are indicated in Table 2.

Table 2: Advantages and limitations of each method to build information about the local wind field

Method	Advantages	Limitations
Mast measurements	The most exact measurement technique	Provide data in only one local position
Terrain models	Provide data in several positions	Uncertainties in abilities to model the full-scale effects
Numerical models	Provide data in several positions. Hindcast data can improve the statistical basis.	Uncertainties in abilities to model turbulence appropriately. Computationally demanding.
LIDAR	Provide real measurement data in several positions	Limitations in turbulence registration (unconservative predictions), sampling rate and special resolution.

The characteristic load effect used in structural design calculations is defined by a yearly exceedance probability, p. This probability can be expressed through a statistical return period in years, $p = 1/N_{yr}$. A common simplification in design calculations for linear systems is to assume that the the return period of the load effect is equal to the return period of the load. This approach will, in general, not be correct for a long-span bridge subjected to turbulent wind loading since the load effect is a stochastic process. However, in current bridge engineering practice, this simplification is widely used. The characteristic load effect is often calculated as the expected extreme response from a short-term storm defined by a mean wind velocity with a return period, N_{yr}, and its corresponding deterministic turbulence parameters. This approach introduces two important assumptions: 1) The variability of the turbulence parameters can be neglected or treated in a simplified manner, and 2) the uncertainty of the short-term extreme peak response can be treated deterministically by its expected value.

For the design of offshore structures subjected to stochastic dynamic environmental loads, the extreme design load effects are addressed through long-term response calculation methodology [23,24]. In this way, all important environmental parameters can be treated as random variables, and the uncertainty of the short-term extreme response can be modelled appropriately.

In the design rules for wind energy generation systems [25], probabilistic models for both the mean wind velocity and the along-wind turbulence standard deviation are provided, and long-term methods are encouraged.

However, in the field of long-span bridge design, such methods have not yet been adopted, with the possibility of introducing inaccuracies and uncertainties that affects the structural reliability.

1.1.3 Structural monitoring of long-span bridges

The basic principle of structural engineering is to design structures that fulfil a predefined need in a safe and reliable way. Throughout the design phase, the engineer makes assumptions and choices based on scientific knowledge and experience, but the outcome is always uncertain to some extent until the structure is built. Structural monitoring is essential to verify and calibrate such assumptions by comparing the choices made during the design and the completed structure's measured behaviour. In addition to verifying the design, structural monitoring systems have seen increasing applications for Structural Health Monitoring (SHM) in recent years. The purpose of SHM systems is to assist the operation and maintenance of the structure by detecting damages, structural changes, settlements, etc. and is an active field of research [26–28].

Several full-scale measurement programs for long-span bridges have been performed in recent years [3,29-38]. What has been observed in many studies is that the measured buffeting response is scattered when plotted against the mean wind velocity. This effect has also been seen at the Hardanger Bridge in Norway, where studies have shown that the significant variability in the measured response can be explained by the variability of the turbulence parameters [40,41].

1.2 Objectives and scope

1.2.1 Research objectives

The main objective of this thesis is to investigate the accuracy of the methods currently used to design long-span bridges subjected to dynamic wind loads and propose a methodology suitable for

design purposes to reduce the uncertainties of the design load predictions. To achieve this, the Hardanger Bridge is studied, and the following research objectives are addressed:

Investigate the effectiveness of measurement methods to describe the wind field properties at a bridge site. Before the bridge is built, information about the local wind field properties is needed as a basis for the design. The predicted design load effects of a bridge subjected to wind load greatly depend on reliable wind field information. One way to reduce the uncertainties imposed by the current design methodology is to utilize more information from the measurement data. Therefore, it is highly relevant to evaluate the methods used to acquire this information.

Investigate which wind field parameters that should be described as stochastic variables when defining the design storm conditions for long-span bridges. In the current bridge design methodology, the mean wind velocity is usually the only wind field parameters described stochastically. From full-scale measurements of long-span bridges, this has been seen to be insufficient to describe the variable buffeting response accurately. This thesis investigates which turbulence parameters that should be described stochastically to improve the current practice.

Study and compare simplified methods with the full long-term method to estimate the design buffeting load effect with a target return period, N_{yr}. The full long-term method (FLM) is considered the most accurate method to calculate the long-term extreme load effects due to stochastic dynamic environmental loads [23]. However, numerical integration of the FLM is extremely computationally demanding and, consequently, becomes unviable for many practical purposes. The accuracy and efficiency of simplified methods shall be investigated, such as the short-term environmental contour method [42] and approximate long-term methods based on reliability solution algorithms such as the inverse first-order reliability method (IFORM) [43,44].

Make recommendations of methods suitable for design purposes to effectively and accurately predict the buffeting design load effects for long-span bridges. The thesis aims to recommend which turbulence parameters should be considered, which simplified methods are appropriate, and ways to correct the simplified methods to reduce the current design methodology's uncertainty. Also, the thesis aims to propose more efficient methods that can produce accurate estimates of the long-term extreme buffeting load effects for the design of long-span bridges.

1.2.2 Scope of the thesis

The Hardanger Bridge is used as a case study in the research presented in this thesis. The bridge is situated in complex terrain, and the wind field properties are site-specific. The methods used are generally applicable, but the results obtained cannot be generalized directly.

Only mast measurements and wind tunnel terrain models are investigated in the wind measurements study, and methods such as LIDARs and numerical models are not considered.

The wind field is assumed stationary and Gaussian within each short-term period in the research presented in this thesis. Wind loads are often separated into synoptic and non-synoptic winds [45], and in areas of the world where non-synoptic winds dominate the extreme buffeting load effects, special considerations concerning non-stationarity and probabilistic modelling are needed [46].

In the buffeting response calculations, the aerodynamic admittance is taken as unity, and the spatial correlation of the buffeting loads are considered equal to the correlation of the turbulence. This

choice is due to the lack of experimental data for the Hardanger Bridge girder to model these effects properly. The Hardanger Bridge girder's aerodynamic properties have been investigated in [47] and have not been the focus of this thesis.

The probabilistic turbulence model is based on the work presented by Fenerci and Øiseth [47] from approximately four years of measurement data. The duration of the measurement period is limited, which can affect the accuracy of the extreme event predictions for turbulence parameters and the mean wind velocity.

The Hardanger Bridge site's topography channels the strong winds along the Hardanger Fjord into two distinct wind directions perpendicular to the bridge span. This particular behaviour has simplified the probabilistic modelling of the wind field concerning the wind direction, which may become more complex for other bridge sites.

1.3 Structure of the thesis

In chapter 2, the Hardanger Bridge, the surrounding terrain and the structural monitoring project is presented. The bridge is thoroughly studied throughout this thesis, and results from the monitoring project are used to investigate the properties of the wind field and compare measured and predicted acceleration response. In chapter 3, the theoretical basis for the essence of the work presented in this thesis is introduced. Chapter 4 presents a summary of the main findings, followed by conclusions and suggestions for further work in chapter 5 and 6, respectively. After that, the appended papers, consisting of three published journal papers, one conference paper and one manuscript submitted for journal publication, follows. The papers can be grouped into the following topics:

- Wind field measurements and spatial wind field variations (Papers 1 and 2)
- Long-term buffeting response of long-span bridges considering turbulence variability (Papers 3 and 4)
- Efficient calculation of the long-term extreme response (Paper 5)

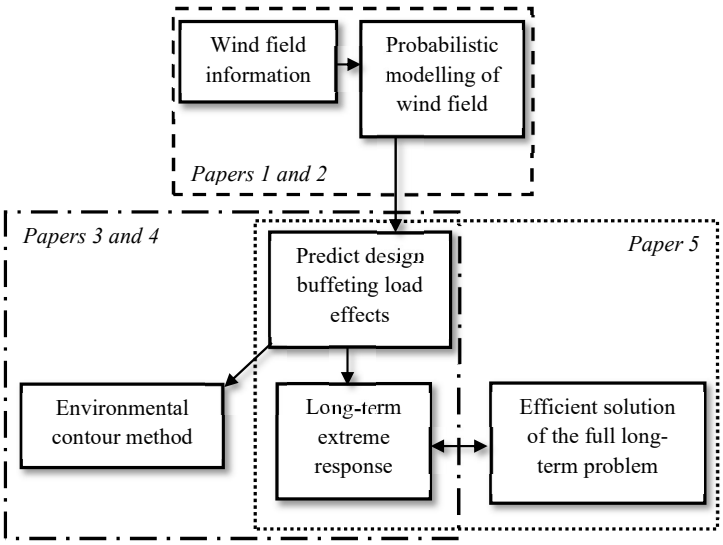

Figure 2: Structure of the thesis and connection between the appended papers

2 The Hardanger Bridge monitoring project

2.1 The Hardanger Bridge and the local topography

The Hardanger Bridge currently has the longest bridge span in Norway, with a suspended main span of 1310 m. The side spans are short, and column supported concrete box girders going straight from the bridge towers and into rock tunnels on both sides of the bridge.

The Hardanger Bridge crosses the Hardanger fjord close to the west coast of Norway. The bridge is beautifully situated between high and steep mountains dropping straight into the deep Hardanger fjord. The terrain is typical for the landscape in this part of Norway, drawing thousands of tourists worldwide every year. Although beautiful, the local topography creates a complex wind field with strong terrain induced effects. The site is located between the stormy coastline to the west and the high, relatively flat, mountain region of Hardangervidda to the east, giving two very different flow characteristics for easterly and westerly winds. The Hardanger Bridge is presented in its dramatic surroundings in Figure 3.

Figure 3: The Hardanger Bridge from the east

The mountains closest to the northern tower are steep and reach as high as up to 1200 m. The southern tower is located on a headland called Buneset. This headland has a plateau at approximately 120 m above mean sea level before the mountains reach up to an elevation of approximately 1200 m. Towards the east, the mountains reach as high as 1600 m, and towards the west, the highest mountain tops in the near vicinity are approximately 1100 m high. The surrounding topography is illustrated in Figure 4.

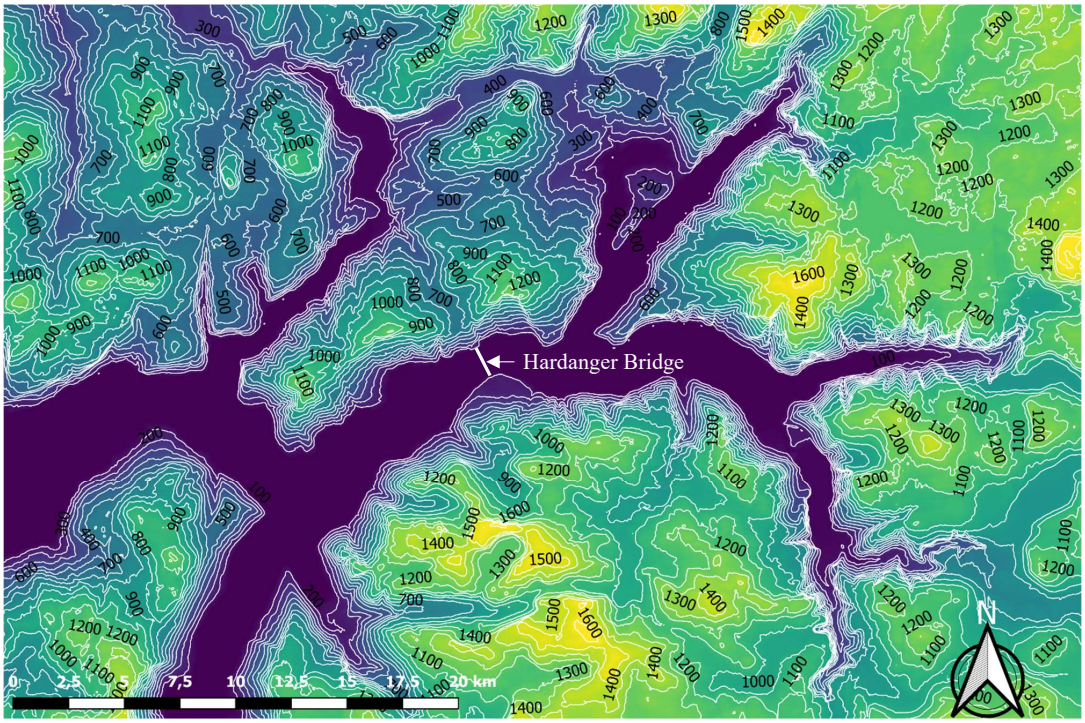

Figure 4: Local topography of the Hardanger Bridge site (100 m elevation contours indicated) (map data from ®Kartverket)

The Hardanger Bridge carries two driving lanes and one pedestrian lane, making the girder only 18.3 m wide and the distance between the cable planes only 14.5 m. The long main span combined with such a narrow girder is unusual, making the bridge extraordinarily slender. The girder height is 3.3 m and has a constant vertical curvature with a radius of 20 000 m.

The girder is a classic aerodynamically shaped stiffened steel box girder. Guide vanes and a vortex spoiler in the middle of the bottom steel plate is appended to the girder to reduce vortex-induced vibrations. An illustration of the bridge girder is shown in Figure 5.

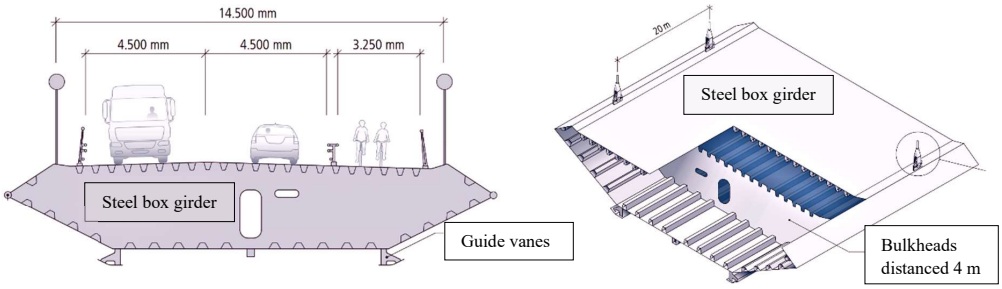

Figure 5: The Hardanger Bridge girder (Illustration courtesy of NPRA)

Figure 6: Aerodynamic details and vertical curvature of the Hardanger Bridge girder

2.2 Structural monitoring system

Shortly after the bridge opening in august 2013, the Norwegian University of Science and Technology instrumented the Hardanger Bridge with a monitoring system. The focus of the research project was to build knowledge about the buffeting behavior of Norway's longest suspension bridge, situated in a complex terrain typical for the Norwegian west coast. The project was connected to the extensive research carried out by the NPRA to develop the technology needed

for a safe realization of the planned extreme fjord crossings along the Ferry-Free Coastal Highway Route E39 [9].

The monitoring system consists of 9 ultrasonic triaxial anemometers, of which 8 are positioned along the bridge span and one in the northern tower top. The anemometers are of the type WindMaster Pro 3D from Gill Instruments, capable of measuring the range 0-65 m/s with a resolution of 0.001 m/s and a sampling frequency of 32 Hz. The 8 anemometers positioned along the span are attached to the hangers (except for the midspan sensor attached to a light pole) approximately 8 m above the bridge deck level. The monitoring system also consists of 20 triaxial accelerometers, of which 16 are positioned along the bridge girder, and two in each tower top. The sensors are of the type CUSP-3D series triaxial strong-motion accelerographs from Canterbury Seismic Instruments, with a measurement range of +/- 4g and a maximum sampling frequency of 200 Hz. The accelerometers are mounted pairwise on the bulkheads inside the steel box girder to measure lateral-, vertical- and torsional motion.

The measurement system is thoroughly described in [40], and the measurement database is published with open access for the benefit of the whole research community [48,49].

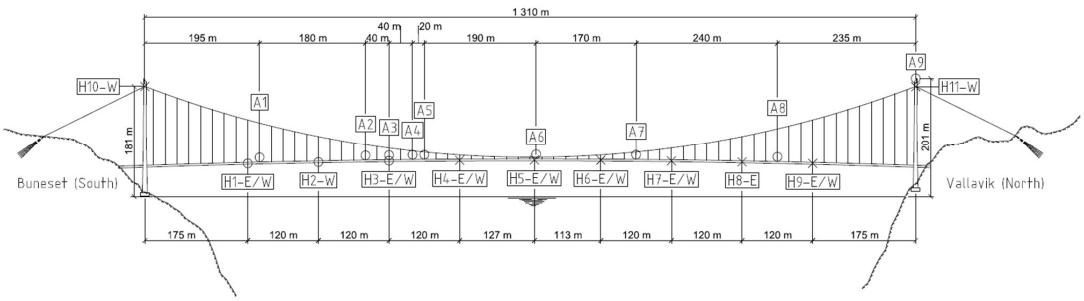

Figure 7: Sensor layout of the Hardanger Bridge monitoring system consisting of 9 ultrasonic anemometers (A1-A9) and 20 triaxial accelerometers (H1-H11, where E indicates the east side of the girder, and W indicate the west side of the girder)

2.3 Probabilistic turbulence model

As a result of the Hardanger Bridge full-scale monitoring research project, Fenerci and Øiseth [47] established a probabilistic turbulence model for the Hardanger Bridge site. The model is based on a Kaimal type auto-spectra [50] and a normalized cross-spectra [51] as defined in Eq. (1):

$$\frac{S_{u,w}f}{\sigma_{u,w}^{\ 2}} = \frac{A_{u,w}f_z}{(1+1.5A_{u,w}f_z)^{5/3}} \ , \ f_z = \frac{fz}{U}$$
$$C_{u,w} = \exp(-K_{u,w}\frac{f\Delta x}{U}) \tag{1}$$

where f is the frequency, z is the height above the ground, U is the mean wind velocity, $\sigma_{u,w}$ are the standard deviations of the along wind- (u) and the vertical (w) turbulence, $A_{u,w}$ are the nondimensional spectral parameters, $K_{u,w}$ are the decay coefficients and Δx is the separation distance along the bridge span. In the probabilistic model, all turbulence parameters defined in Eq.

(1) is described as random variables following log-normal distributions conditional on mean wind velocity and wind direction. The log-normal probability density function can be written as follows:

$$f(x) = \frac{1}{x\sigma\sqrt{2\pi}} \exp\left\{\frac{-(\ln x - \mu)^2}{2\sigma^2}\right\} \; ; \; x > 0 \tag{2}$$

where μ (the mean of the natural logarithm of the random variable) and σ (the standard deviation of the natural logarithm of the random variable) are the distribution parameters, and x is the random variable.

An advantage with log-normal turbulence variables is that the joint distribution can be described by the marginal distribution of each variable and a correlation matrix between the random variables. The marginal log-normal distributions from the probabilistic model in [47] are defined in Table 3, and the correlation matrix between the turbulence parameters are presented in Table 4. The model is based on measurements taken at approximately 68 m above mean sea level, 8 m above the Hardanger Bridge girder.

Table 3: Log-normal distribution parameters from the probabilistic turbulence model, conditional on mean wind velocity and direction [47]. The model is established from measurements at 68 m above mean sea level.

		σ_u	σ_w	A_u	A_w	K_u	K_w
East	μ	0.122+0.039U	-0.657+0.032U	2.67+0.0248U	0.7076	1.9385	1.7932
	σ	0.2566	0.2632	0.4538	0.4466	0.2652	0.3423
West	μ	0.122+0.039U	-0.657+0.032U	2.407+0.048U	1.2075	2.1093	2.1633
	σ	0.3159	0.3021	0.5282	0.4943	0.268	0.3322

Table 4: Correlation coefficient matrix from the probabilistic turbulence model, conditional on the wind direction [47]. The model is established from measurements at 68 m above mean sea level.

		σ_u	σ_w	A_u	A_w	K_u	K_w
East	σ_u	1	0.7608	0.2641	0	0	0
	σ_w	0.7608	1	0	0.2571	0	0
	A_u	0.2641		1	0.1633	0	0
	A_w	0	0.2571	0.1633	1	0	0
	K_u	0	0	0	0	1	0.3261
	K_w	0	0	0	0	0.3261	1
West	σ_u	1	0.8148	0.4087	0	0	0
	σ_w	0.8148	1	0	0.2851	0	0
	A_u	0.4087	0	1	0.3065	0	0
	A_w	0	0.2851	0.3065	1	0	0
	K_u	0	0	0	0	1	0.4725
	K_w	0	0	0	0	0.4725	1

3 Long-term extreme response methodology

3.1 Buffeting of cable-supported bridges

3.1.1 The dynamic system in modal coordinates

Calculation methods for the dynamic bridge response due to stochastic wind loads are still mainly based on the buffeting theory first introduced by Davenport [52] and improved by Scanlan and Tomko [53–55].

The buffeting response of long-span bridges can be calculated in the frequency domain based on the multimodal theory [56–58]. The equation of motion of the dynamic system can be described in the frequency domain as

$$\begin{aligned}&\tilde{\mathbf{M}}_S\mathbf{G}_{\ddot{\eta}}(\omega)+[\tilde{\mathbf{C}}_S-\tilde{\mathbf{C}}_{ae}(U,\omega)]\mathbf{G}_{\dot{\eta}}(\omega)\\&+[\tilde{\mathbf{K}}_S-\tilde{\mathbf{K}}_{ae}(U,\omega)]\mathbf{G}_{\eta}(\omega)=\mathbf{G}_{\tilde{\mathbf{Q}}_{load}}(U,\omega)\end{aligned} \tag{3}$$

where ω is the angular frequency, $\tilde{\mathbf{M}}_S$, $\tilde{\mathbf{C}}_S$ and $\tilde{\mathbf{K}}_S$, are the structural mass-, damping- and stiffness matrices, respectively, in modal coordinates. $\tilde{\mathbf{C}}_{ae}$ and $\tilde{\mathbf{K}}_{ae}$, are the aeroelastic damping and stiffness matrices respectively, representing the motion-induced forces. $\mathbf{G}_{\eta}$, $\mathbf{G}_{\dot{\eta}}$, $\mathbf{G}_{\ddot{\eta}}$ and $\mathbf{G}_{\mathbf{Q}_{load}}$ are the Fourier transforms of the displacement-, velocity-, acceleration response and the load process, respectively.

The system can further be written more compactly as follows:

$$\mathbf{G}_{\eta}(\omega)=\widetilde{\mathbf{H}}(\omega)\mathbf{G}_{\tilde{\mathbf{Q}}_{load}}(\omega) \tag{4}$$

where the frequency response function is defined as

$$\begin{aligned}&\widetilde{\mathbf{H}}(\omega)=\{-\tilde{\mathbf{M}}_S\omega^2+[\tilde{\mathbf{C}}_S-\tilde{\mathbf{C}}_{ae}(U,\omega)]i\omega\\&+[\tilde{\mathbf{K}}_S-\tilde{\mathbf{K}}_{ae}(U,\omega)]\}^{-1}\end{aligned} \tag{5}$$

3.1.2 Aerodynamic motion induced forces

The aerodynamic motion induced forces can be described in modal coordinates as follows:

$$\begin{aligned}\tilde{\mathbf{K}}_{ae}(U,\omega)&=\int_L\mathbf{\Phi}^T(x)\mathbf{k}_{ae}(U,\omega)\mathbf{\Phi}(x)dx\\\tilde{\mathbf{C}}_{ae}(U,\omega)&=\int_L\mathbf{\Phi}^T(x)\mathbf{c}_{ae}(U,\omega)\mathbf{\Phi}(x)dx\end{aligned} \tag{6}$$

where $\mathbf{k}_{ae}(U,\omega)$ and $\mathbf{c}_{ae}(U,\omega)$ are the local aerodynamic stiffness and damping matrices, respectively, which can be described either by the quasi-steady theory or by frequency dependent aerodynamic derivatives.

In the quasi-steady theory, the motion induced forces are based on relative motion considerations and the local matrices become as follows [59]:

$$\mathbf{k}_{ae}(U) = \frac{\rho U^2 B}{2}\begin{bmatrix} 0 & 0 & (D/B)C_D' \\ 0 & 0 & C_L' \\ 0 & 0 & BC_M' \end{bmatrix}$$
$$\mathbf{c}_{ae}(U) = -\frac{\rho U B}{2}\begin{bmatrix} 2(D/B)C_D & ((D/B)C_D' - C_L & 0 \\ 2C_L & (C_L' + (D/B)C_D & 0 \\ 2BC_M & BC_M' & 0 \end{bmatrix} \tag{7}$$

Where ρ is the air density, D is the cross-wind dimension of the structural member, B is the along wind dimension, and C_D, C_L and C_M are the static coefficients for drag, lift and pitching moment respectively, and C_i' are their derivatives with respect to the angle of attack.

The quasi-steady theory has some limitations due to the matrices not being complete. Especially the torsional terms in the damping matrix can be significant. By using aerodynamic derivatives from dynamic wind tunnel tests, it is possible to establish full matrices for both the stiffness and damping as follows:

$$\mathbf{k}_{ae}(U,\omega) = \frac{\rho B^2 \omega^2}{2}\begin{bmatrix} P_4^* & P_6^* & BP_3^* \\ H_6^* & H_4^* & BH_3^* \\ BA_6^* & BA_4^* & B^2 A_3^* \end{bmatrix}$$
$$\mathbf{c}_{ae}(U,\omega) = \frac{\rho B^2 \omega}{2}\begin{bmatrix} P_1^* & P_5^* & BP_2^* \\ H_5^* & H_1^* & BH_2^* \\ BA_5^* & BA_1^* & B^2 A_2^* \end{bmatrix} \tag{8}$$

where the terms inside the matrices are frequency-dependent-, nondimensional aerodynamic derivatives.

For the buffeting calculations performed in this thesis, the aerodynamic properties of the Hardanger Bridge girder is taken from the wind tunnel tests performed by Siedziako et al. [60]. The motion-induced forces on the bridge girder have been described in terms of aerodynamic derivatives.

3.1.3 Stochastic wind load formulation

The wind field can be described as a stationary stochastic process through the cross-spectral density matrix

$$\mathbf{S}_V(\Delta s, U, \omega) = \begin{bmatrix} S_{uu}(\Delta s, U, \omega) & S_{uw}(\Delta s, U, \omega) \\ S_{uw}(\Delta s, U, \omega) & S_{ww}(\Delta s, U, \omega) \end{bmatrix} \tag{9}$$

where S_{nm} are the cross-spectral densities of the n and m components of the turbulence between two points separated in space by the distance Δs.

The cross-spectral density for a single turbulence component can be described through the auto-spectral density function and the normalized cross-spectra defined in Eq. (1):

$$S_{nn}(\Delta s, U, \omega) = S_n(U, I_n, \omega) C_n(\Delta s, U, \omega) \tag{10}$$

where S_n is the auto-spectral density function, and C_n is the normalized cross-spectra and $n=u,w$.

Having established the cross-spectral density matrix for the wind field process, the spectral matrix of the buffeting force on the structure in modal coordinates can be defined as

$$\mathbf{S}_{\tilde{Q}_{load}} = \iint_L \mathbf{\Phi}^T(s_1)\mathbf{B}_q(U,\omega)\mathbf{S}_V(\Delta s,\omega)\mathbf{B}_q^T(U,\omega)\mathbf{\Phi}(s_2)ds_1 ds_2 \tag{11}$$

where $\mathbf{\Phi}(s_i)$ is the mode shape matrix, and $\mathbf{B}_q$ is the load transfer matrix for the buffeting load on the structure. The load spectral density matrix is calculated by considering two points at a time, s_1 and s_2.

The buffeting matrix can be defined as [59]:

$$\mathbf{B}_q(\omega) = \frac{\rho U B}{2}\begin{bmatrix} 2(D/B)C_D A_{yu}(\omega) & ((D/B)C_D' - C_L)A_{yw}(\omega) \\ 2C_L A_{zu}(\omega) & (C_L' + (D/B)C_D)A_{zw}(\omega) \\ 2BC_M A_{\theta u}(\omega) & BC_M' A_{\theta w}(\omega) \end{bmatrix} \tag{12}$$

where $A_{ij}(\omega)$ are the frequency-dependent aerodynamic admittance functions.

3.1.4 Response calculation

When the dynamic system is established in modal coordinates, the modal response spectral density from a stochastic dynamic load can be calculated as:

$$\mathbf{S}_\eta(\omega) = \widetilde{\mathbf{H}}^*(\omega)\mathbf{S}_{\tilde{Q}}(\omega)\widetilde{\mathbf{H}}^T(\omega) \tag{13}$$

where $\mathbf{S}_{\tilde{Q}}$ is the modal load cross-spectral density matrix. Furthermore, the modal response can be transformed back to real coordinates with the following transformation to achieve the response spectral density matrix:

$$\mathbf{S}_R(\omega) = \mathbf{\Phi}(x)\mathbf{S}_\eta(\omega)\mathbf{\Phi}^T(x) = \mathbf{\Phi}(x)\widetilde{\mathbf{H}}^*(\omega)\mathbf{S}_{\tilde{Q}}(\omega)\widetilde{\mathbf{H}}^T(\omega)\mathbf{\Phi}^T(x) \tag{14}$$

where $\mathbf{\Phi}(x)$ contains the mode shapes in real coordinates. Displacement mode shapes are used to obtain displacements, and section force mode shapes are used to get section forces etc.

3.2 Short-term response statistics

If the zero-mean response process of a dynamic system excited by environmental loads can be assumed Gaussian, ergodic and stationary within a short-term period, the short-term extreme value distribution of that process is completely defined by the mean upcrossing rate of a short-term response threshold $\tilde{r}$, and the short-term duration $\tilde{T}$ [23]. The mean $\tilde{r}$-upcrossing rate can be defined as

$$v^+(\tilde{r} \mid \mathbf{w}) = \frac{1}{2\pi}\sqrt{\frac{m_2(\mathbf{w})}{m_0(\mathbf{w})}}\exp\left\{-\frac{\tilde{r}^2}{2m_0(\mathbf{w})}\right\} = v^+(0)\exp\left\{-\frac{\tilde{r}^2}{2m_0(\mathbf{w})}\right\} \tag{15}$$

where **w** is the vector containing the environmental variables, $\nu^{+}(0)$ is the zero-upcrossing rate, and m_i are the ith moment of the response spectrum $\mathbf{S}_{\tilde{R}|\mathbf{W}}(\omega\,|\,\mathbf{w})$:

$$m_i(\mathbf{w}) = \int_0^{\infty} \omega^i \mathbf{S}_{\tilde{R}|\mathbf{W}}(\omega\,|\,\mathbf{w})d\omega \tag{16}$$

and ω is the angular frequency. For a given short-term period $\tilde{T}$, the short-term extreme value cumulative distribution function (CDF) can be defined as

$$F_{\tilde{R}|\mathbf{W}}(\tilde{r}\,|\,\mathbf{w}) = \exp\left\{-\nu^{+}(\tilde{r}\,|\,\mathbf{w})\tilde{T}\right\} = \exp\left\{-\frac{\tilde{T}}{2\pi}\sqrt{\frac{m_2(\mathbf{w})}{m_0(\mathbf{w})}}\exp\left\{-\frac{\tilde{r}^2}{2m_0(\mathbf{w})}\right\}\right\} \tag{17}$$

In a short-term extreme value analysis, the expected value of the short-term extreme response distribution is often used as the design value. The expected value of the short-term extreme response can be estimated as follows, provided that $\ln(\nu^{+}(0)\tilde{T})$ is sufficiently large:

$$E[\tilde{R}] = \left\{\sqrt{2\ln(\nu^{+}(0)\tilde{T})} + \frac{\gamma}{\sqrt{2\ln(\nu^{+}(0)\tilde{T})}}\right\}\sqrt{m_0(\mathbf{w})} = k_p\sqrt{m_0(\mathbf{w})} \tag{18}$$

where $\gamma \approx 0.5772$ is the Euler constant, $E[\cdot]$ is the expectation operator, and k_p is the short-term peak factor.

3.3 The full long-term method

The full long-term method (FLM) is recognized as the most accurate way to estimate the extreme response of a structure subjected to stochastic wind and wave loading [23]. During a long-term period, T, the environmental load conditions is, in principle, a nonstationary process. This is handled by dividing the long-term process into short-term periods $\tilde{T}$ that can be considered stationary and ergodic. The long-term extreme response CDF can then be calculated based on the short-term response statistics weighted by the probability of the occurrence of each short-term load condition.

Different formulations of the full-long-term method can be found in the literature, but under the appropriate assumptions, they are mathematically equivalent [61].

3.3.1 Formulation based on the upcrossing rate of the short-term response

Naess [62] proposed a formulation that calculates the full long-term extreme value CDF based on the $\tilde{r}$-upcrossing rate of each short-term process. Since the response process during a long-term period, T, can no longer be considered a stationary process, Eq. (17) is generalized by replacing the short-term upcrossing rate with its mean value over the long-term period:

$$F_R(r) = \exp\left\{-T\frac{1}{T}\int_0^T \nu^{+}(r,t)dt\right\} \tag{19}$$

By describing the long-term period as a sequence of stationary short-term periods, the following formulation is reached:

$$F_R(r) = \exp\left\{-T\int_{\mathbf{W}} v^+(\tilde{r} \mid \mathbf{w}) f_{\mathbf{W}}(\mathbf{w}) d\mathbf{w}\right\} \tag{20}$$

where $f_{\mathbf{W}}(\mathbf{w})$ is the joint probability density function (PDF) of the environmental parameters defined in the vector $\mathbf{w}$, $T = N_{st}\tilde{T}$ is the long-term period, and N_{st} is the number of short-term conditions. This formulation is the full long-term formulation with the least limiting assumptions [61], relying only on the ergodicity assumption and that the high-level upcrossings follow a Poisson distribution.

3.3.2 Formulations based on all short-term extreme values

Borgman [63] presented an expression for the long-term extreme value CDF based on the short-term extreme values:

$$F_R(r) = \exp\left\{\int_{\mathbf{W}} \ln\left\{F_{\tilde{R}|\mathbf{W}}(\tilde{r} \mid \mathbf{w})\right\} f_{\mathbf{W}}(\mathbf{w}) d\mathbf{w}\right\} \tag{21}$$

This formulation is valid under the assumption of statistically independent short-term extreme values. The formulation proposed by Borgman [63] is based on an ergodic averaging. This is often referred to as the exact formulation of the full long-term extreme value CDF, but it should be noted that it is exact under the appropriate assumtions. An approximate formulation of this problem exists as well, which is based on the population mean and not the ergodic average, hence the approximation. The formulation reads:

$$\overline{F}_R(r) = \int_{\mathbf{W}} F_{\tilde{R}|\mathbf{W}}(\tilde{r} \mid \mathbf{w}) f_{\mathbf{W}}(\mathbf{w}) d\mathbf{w} \tag{22}$$

Eq. (22) is often a good approximation, although it is strictly unconservative, as shown by Jensen's inequality theorem, stating that the expected value of a function is greater than or equal to the expected value of the function after a concave transformation. In Eq. (21), the natural logarithm is a concave function, and the following applies [64]:

$$F_R(r) \le \overline{F}_R(r) \tag{23}$$

and in effect, the N_{yr} return period response quantity estimated by the approximate formulation is less than or equal to the exact formulation.

3.3.3 Formulation based on all short-term peak values

The full long-term method formulation based on all short-term peak values was first presented by Battjes [65]. For a process that is narrow banded, Gaussian, stationary and ergodic, the CDF of all the peaks in a short-term process follows a Rayleigh distribution:

$$F_{\tilde{R}_p|\mathbf{W}}(\tilde{r} \mid \mathbf{w}) = 1 - \exp\left\{-\frac{\tilde{r}^2}{2m_0(\mathbf{w})}\right\} \tag{24}$$

Battjes showed that, under the assumption of statistically independent short-term peaks, the long-term extreme value CDF could be described as follows

$$F_R(r) = \frac{1}{\overline{v}^+(0)}\int_{\mathbf{W}} v^+(0 \mid \mathbf{w}) F_{\tilde{R}|\mathbf{W}}(r \mid \mathbf{w}) f_{\mathbf{W}}(\mathbf{w}) d\mathbf{w} \tag{25}$$

where

$$\overline{v}^{+}(0) = \int_{\mathbf{W}} v^{+}(0 \mid \mathbf{w}) f_{\mathbf{W}}(\mathbf{w}) d\mathbf{w} \tag{26}$$

3.4 Reliability methods

3.4.1 Formulating the full long-term method as a reliability problem

The approximate formulation for the full long-term extreme value CDF shown in Eq. (22) can be reformulated as a reliability problem. An interesting effect of this reformulation is that it can be efficiently solved in an approximate manner using known structural reliability solution algorithms such as the first-order reliability method (FORM).

The general reliability problem can be written as [66]:

$$p_f = \int_{G(\mathbf{x}) \le 0} f_{\mathbf{X}}(\mathbf{x}) d\mathbf{x} \tag{27}$$

where p_f is the failure probability, $\mathbf{X}$ is a vector of random variables described by the joint PDF $f_{\mathbf{X}}(\mathbf{x})$, and $G(\mathbf{x})$ is the limit state function in the real space. In the general reliability problem, $\mathbf{X}$ contains random variables describing the uncertain load and the uncertain capacity, and then $G(\mathbf{x}) \le 0$ defines failure.

The approximate formulation of the long-term extreme value problem can be rewritten to a similar format:

$$\overline{F}_R(r) = \int_{\mathbf{W}} F_{\tilde{R}|\mathbf{W}}(\tilde{r} \mid \mathbf{w}) f_{\mathbf{W}}(\mathbf{w}) d\mathbf{w} = \int_{\mathbf{W}} \int_{\tilde{r} \le r} f_{\tilde{R}|\mathbf{W}}(\tilde{r} \mid \mathbf{w}) d\tilde{r} f_{\mathbf{W}}(\mathbf{w}) d\mathbf{w} \tag{28}$$

If a vector $\mathbf{X} = \left[\mathbf{W}, \tilde{R}\right]$ is defined, a joint PDF of the environmental variables and the short-term extreme response can be constructed as:

$$f_{\mathbf{X}}(\mathbf{x}) = f_{\tilde{R}|\mathbf{W}}(\tilde{r} \mid \mathbf{w}) f_{\mathbf{W}}(\mathbf{w}) \tag{29}$$

and then Eq. (28) is rewritten to the same format as Eq. (27):

$$\overline{F}_R(r) = \int_{\tilde{r} \le r} f_{\mathbf{X}}(\mathbf{x}) d\mathbf{x} = 1 - \int_{G(\mathbf{x}) \le 0} f_{\mathbf{X}}(\mathbf{x}) d\mathbf{x} = 1 - p_f \tag{30}$$

where $G(\mathbf{x}) = r - \tilde{r}$.

Giske et al. [64] proposed a method to formulate the exact full long-term method shown in Eq. (21) as a reliability problem and avoid the strictly unconservative simplification that the formulation in Eq. (22) introduces. Since $\ln\left\{F_{\tilde{R}|\mathbf{W}}(\tilde{r} \mid \mathbf{w})\right\}$ is not a CDF, they rewrote the expression:

$$F_R(r) = \exp\left\{\int_{\mathbf{W}} \left(1 + \ln\left\{F_{\tilde{R}|\mathbf{W}}(\tilde{r} \mid \mathbf{w})\right\}\right) f_{\mathbf{W}}(\mathbf{w}) d\mathbf{w} - 1\right\} \tag{31}$$

and then introduced a new random variable, Y, so a CDF-like function could be defined as:

$$F_{Y|\mathbf{W}}(y\,|\,\mathbf{w}) = \max\left(1+\ln\left\{F_{\tilde{R}|\mathbf{W}}(\tilde{r}\,|\,\mathbf{w})\right\},0\right) \tag{32}$$

Thus, the formulation reads:

$$F_R(r) \approx \exp\left\{\int_{\mathbf{W}} F_{Y|\mathbf{W}}(y\,|\,\mathbf{w}) f_{\mathbf{W}}(\mathbf{w}) d\mathbf{w} - 1\right\} \tag{33}$$

Similar to the definition in Eq. (30), the reliability problem becomes:

$$F_R(r) \approx \exp\left\{-\int_{G(\mathbf{x})\le 0} f_{\mathbf{X}}(\mathbf{x}) d\mathbf{x}\right\} = \exp\left\{-p_f\right\} \tag{34}$$

where

$$f_{\mathbf{X}}(\mathbf{x}) = F_{Y|\mathbf{W}}(y\,|\,\mathbf{w}) f_{\mathbf{W}}(\mathbf{w}) \tag{35}$$

3.4.2 Solving the long-term extreme value problem using reliability methods

The FORM procedure can be used to calculate the probability of exceedance, p_f, by transforming the random variables in **X** into the standard normal space, **U**, and minimizing the distance to the limit state function:

$$\beta = \arg\min|\mathbf{u}|;\ \text{constrained to } g(\mathbf{u}) = 0 \tag{36}$$

where $g(\mathbf{u}) = r - \tilde{r}(\mathbf{u}) = 0$ is the limit-state function in the standard normal space. The reliability index β is related to the return period as follows:

$$\beta = -\Phi^{-1}(1/[\frac{N_{yr} \times 365.25 \times 24 \times 60}{\tilde{T}}]) \tag{37}$$

where $\Phi(.)$ is the standard normal CDF, N_{yr} is the statistical return period in years and $\tilde{T}$ short-term duration in minutes.

In the FORM, the limit-state function is approximated by a first-order Taylor expansion through the design point identified in the standard normal space [66]. The approximation is illustrated in Figure 8.

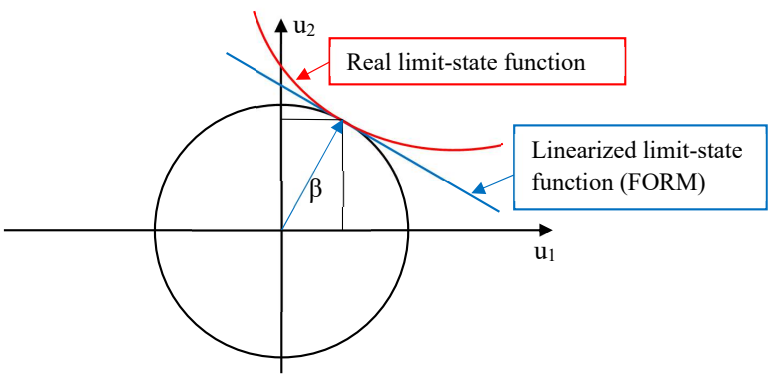

Figure 8: Visualization of the FORM procedure

The failure probability is related to the reliability index by the relationship:

$$p_f = \int_{g(\mathbf{u})\leq 0} f_{\mathbf{U}}(\mathbf{u})d\mathbf{u} = \Phi(-\beta) \tag{38}$$

However, in the inverse FORM procedure, the reliability index is indirectly known through the given return period, and the response, r, is sought. Thus, the solution to the long-term extreme value problem in Eq. (30) is found by maximizing the response under the following constraint:

$$r = \arg\max \tilde{r}(\mathbf{u});\ \text{constrained to } |\mathbf{u}| = \beta \tag{39}$$

When the long-term response is assessed by this approach, **X** from Eq. (29) contains the environmental variables, **W** and the short-term extreme response $\tilde{R}$.

The environmental contour method (ECM) [42] is an efficient approach to estimate the long-term extreme response by a short-term extreme value analysis. This method decouples the variability in the environmental parameters and the variability in the extreme response [67], and only the variability in the load parameters are considered directly. The effect of the extreme value uncertainty is often simplified by choosing a higher percentile of the short-term extreme response probability distribution as the design value [68]. The environmental contour method is also based on the IFORM algorithm, but in this method the random vector is reduced to $\mathbf{X} = [\mathbf{W}]$.

3.4.3 Transformation of random variables

When using the FORM, the random variables need to be transformed between the real space and the standard normal space. Given the standard normal variables, u_1, u_2, … , u_n and the related real stochastic variables, v_1, v_2, … , v_n, the following transformation into the real space is needed:

$$\Phi(u_1, u_2, ..., u_n) \rightarrow F_{V_1V_2....V_n}(v_1, v_2, ..., v_n) \tag{40}$$

where $F_{V_1V_2....V_n}(v_1, v_2, ..., v_n)$ is the joint CDF of the real stochastic variables. An example of such a transformation is shown in Figure 9. If the real variables are uncorrelated, each variable can be transformed independently as follows:

$$F_{V_n}(v_n) = \Phi(u_n) \Leftrightarrow v_n = F_{V_n}^{-1}[\Phi(u_n)] \tag{41}$$

However, if the variables are correlated, the transformation becomes more complicated, and for the general problem, a transformation procedure such as the Rosenblatt or Nataf transformation needs to be applied [66].

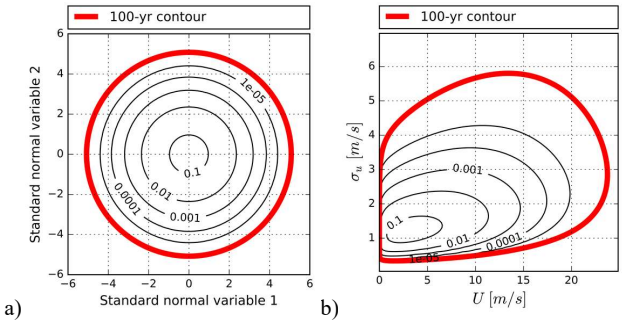

Figure 9: Joint PDF illustration of the transformation of variables between a) the standard normal space and b) the real space, considering the mean wind velocity and the along-wind turbulence standard deviation as the random variables.

The Rosenblatt procedure [69] is a widely used transformation because it is general and quite simple to use. The transformation procedure is based on the relationship where the joint CDF can be established from the product of conditional marginal CDFs, as shown in Eq. (42):

$$F_{V_1,V_2,\ldots,V_{n-1}}(v_1,v_2,\ldots,v_{n-1}) = F_{V_1}(v_1)F_{V_2|V_1}(v_2 \mid v_1)\ldots F_{V_n|V_1,V_2,\ldots,V_{n-1}}(v_n \mid v_1,v_2,\ldots,v_{n-1}) \tag{42}$$

The Rosenblatt procedure is a stepwise transformation using conditional CDFs as follows:

$$\begin{aligned}
F_{V_1}(v_1) = \Phi(u_1) \quad &\Leftrightarrow \quad v_1 = F_{V_1}^{-1}\left[\Phi(u_1)\right] \\
F_{V_2|V_1}(v_2|v_1) = \Phi(u_2) \quad &\Leftrightarrow \quad v_2|v_1 = F_{V_2|V_1}^{-1}\left[\Phi(u_2)\right] \\
F_{V_3|V_1,V_2}(v_3|v_1,v_2) = \Phi(u_3) \quad &\Leftrightarrow \quad v_3|v_1,v_2 = F_{V_3|V_1,V_2}^{-1}\left[\Phi(u_3)\right] \\
&\ldots \\
F_{V_n|V_1,V_2,\ldots,V_{n-1}}(v_n|v_1,v_2,\ldots,v_{n-1}) = \Phi(u_n) \quad &\Leftrightarrow \quad v_n|v_1,v_2,\ldots,v_{n-1} = F_{V_n|V_1,V_2,\ldots,V_{n-1}}^{-1}\left[\Phi(u_n)\right]
\end{aligned} \tag{43}$$

In the special case where the stochastic variables are normally distributed in the real space, the transformation from the uncorrelated standard normal space to the correlated real space is linear. It can be shown that if **X** is a vector containing the real variables v_i and **Y** is a vector containing the standard normal uncorrelated variables u_i, then the transformation can be described as follows:

$$\mathbf{Y} = \mathbf{A}(\mathbf{X} - \mathbf{M}_X) \quad \Leftrightarrow \quad \mathbf{X} = \mathbf{A}^{-1}\mathbf{Y} + \mathbf{M}_X \tag{44}$$

where $\mathbf{M}_X = \begin{bmatrix} \mu_{V_1} & \mu_{V_2} & \ldots & \mu_{V_n} \end{bmatrix}^T$ is a vector containing the mean values of the normally distributed variables v_i, and **A** is a transformation matrix. For normally distributed variables, **A** can be calculated based on the covariance matrix $\mathbf{C}_{XX}$ as follows:

$$\mathbf{C}_{XX} = \begin{bmatrix} \sigma_{V_1}^{\ 2} & \rho_{12}\sigma_{V_1}\sigma_{V_2} & \ldots & \rho_{1n}\sigma_{V_1}\sigma_{V_n} \\ \rho_{21}\sigma_{V_2}\sigma_{V_1} & \sigma_{V_2}^{\ 2} & \ldots & \rho_{2n}\sigma_{V_2}\sigma_{V_n} \\ \ldots & \ldots & \ldots & \ldots \\ \rho_{n1}\sigma_{V_n}\sigma_{V_1} & \rho_{n2}\sigma_{V_n}\sigma_{V_2} & \ldots & \sigma_{V_n}^{\ 2} \end{bmatrix} \tag{45}$$

$$\begin{aligned} &\mathbf{A} = \mathbf{D}^T \mathbf{S}^T \\ &\mathbf{D} = diag[1/\sqrt{\lambda_j}] \quad , \quad j = 1,2,...,n \\ &\mathbf{S} = \begin{bmatrix} \mathbf{S}_1 & \mathbf{S}_2 & ... & \mathbf{S}_n \end{bmatrix} \end{aligned} \tag{46}$$

where σ_{Vj} is the standard deviation, ρ_{jk} is the correlation coefficient between the normally distributed variables, λ_j is the eigenvalues, and $\mathbf{S}_j$ is the eigenvector of the correlation matrix $\mathbf{C}_{XX}$. This transformation procedure is often referred to as the Singular Value Decomposition (SVD), but the transformation matrix **A** can also be found by Cholesky decomposition of $\mathbf{C}_{XX}$, which is Hermitian and positive definite:

$$\mathbf{C}_{XX} = \mathbf{A}^{-1}\mathbf{A}^{-T} \tag{47}$$

If the stochastic variables are log-normally distributed in the real space, the same transformation applies to find the associated normal distribution. Thus, the log-normally distributed variables can be found as:

$$\mathbf{X} = \exp(\mathbf{A}^{-1}\mathbf{Y} + \mathbf{M}_X) \tag{48}$$

3.4.4 Finding the design point by the ECM and the IFORM

The critical storm condition on the environmental contour for a considered response quantity can be found by manual iterations and engineering judgment, but it can also be found by numerical optimization. The ECM is similar to the IFORM, but the number of random variables included is reduced in the ECM since the variability of the short-term response itself is excluded. The difference in the dimensionality of the problems is illustrated in Figure 10.

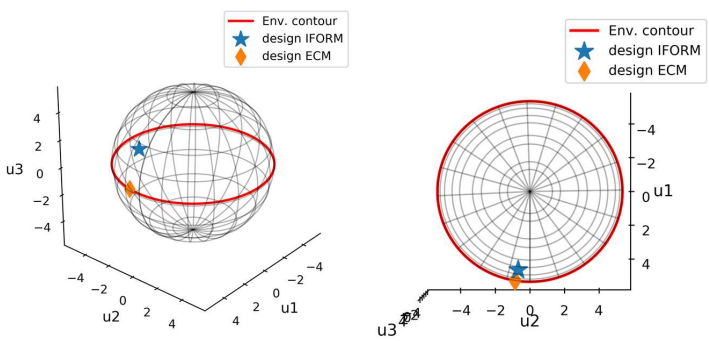

Figure 10: Illustration of the difference between ECM and IFORM and the effect of the added dimension due to the inclusion of the short-term extreme response uncertainty shown in the standard normal space

In the IFORM, the short-term extreme value $\tilde{r}(\mathbf{u})$ is found directly by transformation of the **u**-vector, but in the ECM, $\tilde{r}(\mathbf{u})$ can be treated as a deterministic value given the environmental variables defined by the **u**-vector and calculated as the short-term expected extreme value defined in Eq. (18).

The iteration algorithm to solve the IFORM problem shown in Eq. (30) and Eq. (34), as proposed by Li and Foschi [43] reads:

$$\mathbf{u}^{k+1} = \beta \frac{\nabla \tilde{r}_{n+1}(\mathbf{u}^k)}{\left|\nabla \tilde{r}_{n+1}(\mathbf{u}^k)\right|} \tag{49}$$

where n is the number of environmental variables and k indicates the iteration. Since the short-term extreme value uncertainty is not included as a variable in the ECM, the expression above reduces to:

$$\mathbf{u}^{k+1} = \beta \frac{\nabla \tilde{r}_{n}(\mathbf{u}^k)}{\left|\nabla \tilde{r}_{n}(\mathbf{u}^k)\right|} \tag{50}$$

3.5 Gaussian process regression

A Gaussian process can be defined as a sequence of random variables which can be described by a joint Gaussian distribution. Hence, the Gaussian process can be defined entirely by its mean- and covariance function. Gaussian process regression has become a popular method in machine learning [70] due to its simple form and since it can be described by closed form expressions. As a result, Gaussian process regression can be used in a Bayesian updating approach to create a surrogate model of a real function by introducing sequentially sampled observed data from the function. The method has also been used in long-term response related problems in recent years [71–75].

An input vector $\mathbf{x}$ with its corresponding output function value $y = f(\mathbf{x})$ is defined. The input vector $\mathbf{x}$ is drawn from the vector $\mathbf{X}$, which contains all $\mathbf{x}_i$, and $\mathbf{y}$ is the vector of function outputs containing all y_i. The real function value can now be approximated by a Gaussian process:

$$f(\mathbf{x}) \approx \mathrm{GP}(m(\mathbf{x}), k(\mathbf{x}_i, \mathbf{x}_j)) \tag{51}$$

where the GP*(.)* operator indicates a Gaussian process, and the mean function and the covariance function of the Gaussian Process can be defined as:

$$\begin{aligned} m(\mathbf{x}) &= E[f(\mathbf{x})] \\ k(\mathbf{x}_i, \mathbf{x}_j) &= E[(f(\mathbf{x}_i) - m(\mathbf{x}_i))(f(\mathbf{x}_j) - m(\mathbf{x}_j))] \end{aligned} \tag{52}$$

The covariance function, $k(\mathbf{x}_i, \mathbf{x}_j)$ is often referred to as the *kernel* or the *kernel function*. The kernel function describes the covariance between the random variables in the function-space defined by $\mathbf{X}$. There are several covariance function models commonly used in Gaussian process regression [70]. Some of the most popular formulations are presented in Table 5. The covariance functions are defined so that the Gaussian process is a smooth function over the function-space.

Perhaps the most used kernel function model is a special case of the γ-exponential kernel, known as the squared exponential covariance function:

$$k(\mathbf{x}_i, \mathbf{x}_j) = \sigma_f^{\,2} \exp\left(-\frac{\left|\mathbf{x}_i - \mathbf{x}_j\right|^2}{2l^2} \right) \tag{53}$$

where σ_f^2 is the variance of the kernel and l is the length scale parameter. The length scale parameter is a so-called hyperparameter of the Gaussian process, and a large length scale defines a

high correlation between points far away from each other in the function space and thus a slowly varying Gaussian process. A small length scale defines a Gaussian process with quick variations.

Table 5: Commonly used kernel functions

Kernel	Formulation
γ-exponential	$\sigma_f^2 \exp\left[-\left(\frac{\lvert \mathbf{x}_i - \mathbf{x}_j \rvert}{l}\right)^{\gamma}\right]$
Matérn 3/2	$\sigma_f^2 \left(1+\sqrt{3}\lvert \mathbf{x}_i - \mathbf{x}_j \rvert\right)\exp\left(-\sqrt{3}\lvert \mathbf{x}_i - \mathbf{x}_j \rvert\right)$
Matérn 5/2	$\sigma_f^2 \left(1+\sqrt{5}\lvert \mathbf{x}_i - \mathbf{x}_j \rvert+\frac{5}{3}\lvert \mathbf{x}_i - \mathbf{x}_j \rvert^2\right)\exp\left(-\sqrt{5}\lvert \mathbf{x}_i - \mathbf{x}_j \rvert\right)$
Rational quadratic	$\sigma_f^2 \left(1+\frac{\lvert \mathbf{x}_i - \mathbf{x}_j \rvert^2}{2\alpha l^2}\right)^{-\alpha}$

If the function-space is considered as a discretized space defined by the input points, $\mathbf{X}_d$, the Gaussian Process can be defined as:

$$f_d = f(\mathbf{X}_d) \approx N\left(\mathbf{M}_{X_d}, \mathbf{K}(\mathbf{X}_d, \mathbf{X}_d)\right) \tag{54}$$

Where the *N(.)* operator indicates a normal distribution, $\mathbf{M}_{X_d}$ is a vector containing the mean function at the input points defined by $\mathbf{X}_d$, and $\mathbf{K}(\mathbf{X}_d, \mathbf{X}_d)$ is the covariance matrix.

The definition in Eq. (54) is referred to as the prior definition since no information about the real function is introduced. Now, a set of input/output observations from the real function can be added, $y_t = f(\mathbf{x}_t)$, and the Gaussian Process of the unknown discretized points f_d can be defined conditional on the known observations y_t. Eq. (55) is referred to as the posterior definition since it is formulated conditional on the observed training data.

$$\begin{bmatrix} y_t \\ f_d \end{bmatrix} = N\left(\begin{bmatrix} \mathbf{M}_{X_t} \\ \mathbf{M}_{X_d} \end{bmatrix}, \begin{bmatrix} \mathbf{K}(\mathbf{X}_t, \mathbf{X}_t) & \mathbf{K}(\mathbf{X}_t, \mathbf{X}_d) \\ \mathbf{K}(\mathbf{X}_d, \mathbf{X}_t) & \mathbf{K}(\mathbf{X}_d, \mathbf{X}_d) \end{bmatrix}\right) \tag{55}$$

This expression can be further generalized by introducing noise to possible uncertain observations:

$$\begin{bmatrix} y_t \\ f_d \end{bmatrix} = N\left(\begin{bmatrix} \mathbf{M}_{X_t} \\ \mathbf{M}_{X_d} \end{bmatrix}, \begin{bmatrix} \mathbf{K}(\mathbf{X}_t, \mathbf{X}_t) + \sigma_n^2 \mathbf{I} & \mathbf{K}(\mathbf{X}_t, \mathbf{X}_d) \\ \mathbf{K}(\mathbf{X}_d, \mathbf{X}_t) & \mathbf{K}(\mathbf{X}_d, \mathbf{X}_d) \end{bmatrix}\right) \tag{56}$$

where σ_n^2 is the variance of a Gaussian noise connected to the training data. This noise level is also defined as a hyperparameter and can represent uncertainty in the observations. This uncertainty definition is often suitable where the observations come from experiments.

Further, it can be shown that the predictive mean and covariance of the Gaussian process can be found as follows [70]:

$$\begin{aligned}\mu_{f_d|\mathbf{X}_t,\mathbf{y}_t,\mathbf{X}_d} &= \overline{f}_d = E\left[f_d \mid \mathbf{X}_t,\mathbf{y},\mathbf{X}_d\right] = \mathbf{M}_{X_d} + \mathbf{K}(\mathbf{X}_d,\mathbf{X}_t)\left[\mathbf{K}(\mathbf{X}_t,\mathbf{X}_t)+\sigma_n^2\mathbf{I}\right]^{-1}(\mathbf{y}_t - \mathbf{M}_{X_t}) \\ \Sigma_{f_d|\mathbf{X}_t,\mathbf{X}_d} &= \mathrm{cov}(f_d) = \mathbf{K}(\mathbf{X}_d,\mathbf{X}_d) - \mathbf{K}(\mathbf{X}_d,\mathbf{X}_t)\left[\mathbf{K}(\mathbf{X}_t,\mathbf{X}_t)+\sigma_n^2\mathbf{I}\right]^{-1}\mathbf{K}(\mathbf{X}_t,\mathbf{X}_d)^T\end{aligned} \tag{57}$$

Note that the covariance of the Gaussian process $\Sigma_{f_d|\mathbf{X}_t,\mathbf{X}_d}$, is independent of the function value of the observations and only rely in the position of the observations.

In a Bayesian updating approach, observations can be introduced sequentially, and the introduction of new observations can be based on the points where the uncertainty of the Gaussian process is large, for instance, indicated by a large variance according to Eq. (57). The function used to identify where a new observation should be introduced is referred to as the learning function.

A standard Gaussian process learning function when the best model description is sought in the whole function space is defined in Eq. (58). This function suggests introducing observations where the standard deviation of the posterior Gaussian process is large.

$$\mathbf{x}_{t,next} = \arg\max\left[\left|\Sigma_{f_d|\mathbf{X}_t,\mathbf{X}_d}(\mathbf{x})\right|^{1/2}\right] \tag{58}$$

4 Summary of appended papers

4.1 Declaration of authorship

The idea behind the main direction of the research presented in this thesis is credited to Professor Ole Øiseth. The work builds on the findings in the doctoral thesis of Aksel Fenerci [76], and the probabilistic turbulence model established during that study was used in the work presented herein. Professor Ole Øiseth planned and led the installation of the Hardanger Bridge monitoring system, and Aksel Fenerci, Knut Andreas Kvåle and Øyvind Wiig Petersen structured the data from the measurements.

The PhD candidate Tor Martin Lystad is the first author of all the appended papers.

In paper 1, Tor Martin Lystad and Professor Ole Øiseth planned the study, and Tor Martin Lystad implemented the numerical tools and performed the statistical analyses. Tor Martin Lystad wrote the manuscript in frequent discussions with both Professor Ole Øiseth and Aksel Fenerci. Both co-authors, Professor Ole Øiseth and Aksel Fenerci contributed with proof-reading of the manuscript.

In paper 2, Tor Martin Lystad planned the study in frequent discussion with both Professor Ole Øiseth and Aksel Fenerci. Tor Martin Lystad implemented the methods for buffeting response calculations in his preferred programming language, Python [77], based on the Matlab [78] implementation written by Professor Ole Øiseth. Lystad further extended the implementations to include the possibility of inhomogeneous wind conditions. Lystad also developed other numerical tools used in the paper and wrote the manuscript. Professor Ole Øiseth and Aksel Fenerci contributed further with proof-reading of the manuscript.

In papers 3, 4 and 5, Tor Martin Lystad planned the study in frequent discussion with Professor Ole Øiseth and Aksel Fenerci. Lystad implemented all necessary numerical tools and performed all analyses. Lystad wrote the manuscripts in close communication with Aksel Fenerci and Professor Ole Øiseth, who also contributed to the manuscripts' proof-reading.

4.2 Paper 1 [79]

Lystad TM, Fenerci A, Øiseth O. “Evaluation of mast measurements and wind tunnel terrain models to describe spatially variable wind field characteristics for long-span bridge design”, Journal of Wind Engineering and Industrial Aerodynamics 2018;179:558–73.

The first paper compares in-situ mast measurements and wind tunnel terrain model tests performed before the design of the Hardanger Bridge with the wind field measurements along the span from the Hardanger Bridge full-scale measurement program. The aim is to investigate the performance of mast measurements and wind tunnel terrain model tests for predicting the wind field characteristics for long-span bridges in complex terrains. The spatial variations of the wind field characteristics, in terms of statistical distributions for turbulence intensity and extreme mean wind velocity, is investigated. The findings indicate relatively large spatial variations in both turbulence intensity and extreme mean wind velocities. The results also indicate local terrain speed-up effects in the mast measurements due to the mast's location on top of an elevated headland. Large nonuniformity is

also identified in simultaneously measured wind profiles for mean wind velocity and the turbulence intensity along the Hardanger Bridge span. The wind tunnel terrain model tests could not adequately predict the spanwise wind profiles measured in full-scale, indicating the importance of large enough models and investigations of different incoming wind directions.

4.3 Paper 2 [80]

Lystad TM, Fenerci A, Øiseth O. "Aerodynamic Effect of Non-uniform Wind Profiles for Long-Span Bridges", Proceedings of the XV Conference of the Italian Association for Wind Engineering. IN VENTO 2018. Lecture Notes in Civil Engineering vol. 27. 2019.

The effect of the large nonuniformity of the measured wind profiles found in paper 1 was investigated for the buffeting response of the Hardanger bridge in paper 2. A probabilistic model for the nonuniformity of the mean wind velocity and the turbulence intensity was established, and some extreme profiles were identified by Monte Carlo simulation from the model. Since the mean wind velocity and turbulence intensity are highly correlated, the effect of the two variables' nonuniformity will, to some extent, cancel each other. However, the effect of the corresponding extreme nonuniform profiles was investigated for the Hardanger Bridge buffeting response, showing possible unfavourable response estimates compared with an equivalent uniform wind field.

4.4 Paper 3 [81]

Lystad TM, Fenerci A, Øiseth O. "Buffeting response of long-span bridges considering uncertain turbulence parameters using the environmental contour method", Engineering Structures 2020;213:110575.

In the third paper, the Hardanger Bridge's buffeting response, considering uncertain turbulence parameters, was investigated. The study investigates the effect of the widely used design approach where the extreme short-term storm condition is based on stochastic modelling of the mean wind velocity and a deterministic description of the turbulence parameters. The Environmental Contour Method (ECM) is used to investigate the 100-year return period storm condition critical for the root-mean-square (RMS) girder section moments of the Hardanger Bridge. All six turbulence parameters defined by the probabilistic model described in chapter 2.3 is described as random variables in addition to the mean wind velocity. The results show that turbulence-induced variability has a significant impact on the predicted bridge girder section moments.

Interestingly, the critical combination of environmental parameters does not necessarily involve the maximum mean wind velocity. Further, the response predictions based on the ECM is compared with the scattered acceleration RMS responses measured in full-scale at the Hardanger Bridge. The results show that the 100-year return period response predicted by the ECM eclipse the scattered data indicating significant improvements compared with the traditional design methodology.

4.5 Paper 4 [82]

Lystad TM, Fenerci A, Øiseth O. "Long-term extreme buffeting response of cable-supported bridges with uncertain turbulence parameters", Engineering Structures 2021;236:112126.

The findings in paper 3 showed the importance of describing the uncertainty of the turbulence parameters when predicting the largest RMS responses of the Hardanger Bridge girder. Another

simplification widely used in current design methodology is to use the expected value of the short-term extreme response to an identified extreme storm condition as the design value. The effect of this simplification is addressed in paper 4, where the turbulence uncertainty and the short-term extreme response uncertainty is included by calculating the 100-year return period extreme design stresses in the Hardanger Bridge girder with the full long-term method (FLM). The variability of the turbulence parameters and the uncertainty in the extreme short-term response are important when estimating the design stresses. The FLM is considered the most accurate way to predict long-term extreme responses. However, the method is very computationally demanding. For practical applications, more computationally efficient approximate methods are often used to estimate the long-term extreme responses. In paper 4, the extreme stresses predicted by the FLM is compared with the Inverse First Order Reliability Method (IFORM) and the ECM. Simple methods suitable to correct the short-term response predicted by the ECM is proposed to obtain an approximation of the long-term response. An approach suitable for practical applications of predicting the long-term extreme buffeting response of conventional cable-supported bridges is suggested based on the established long-term response calculation methods.

4.6 Paper 5

Lystad TM, Fenerci A, Øiseth O. "Full long-term extreme structural response with sequential Gaussian process surrogate modelling" Submitted for journal publication.

In paper 4, approximate methods known from the offshore industry was used to calculate the long-term extreme buffeting response of the Hardanger Bridge girder. Methods such as the IFORM or the ECM are efficient methods, but several approximations in the formulations impose uncertainties to the extreme response estimates. In the last paper of this thesis, a new algorithm based on sequential updating of Gaussian Process surrogate models is proposed to calculate the long-term extreme response based on the FLM formulations. The proposed algorithm is applied to the long-term stresses of the Hardanger Bridge girder described in paper 4. The method shows a computational efficiency comparable to the popular IFORM. However, it has the advantage that by increasing the model's refinement, the result will converge towards the correct solution of the FLM, in contrast to the reliability methods that converges towards an approximate solution. The results show a high performance of the algorithm in the application to the long-term response of the Hardanger Bridge girder, both in terms of computational efficiency and in terms on accuracy of the predicted 100-year return period extreme buffeting stresses.

5 Conclusions

The design methodology for buffeting actions of long-span bridges has been thoroughly investigated through a case study of the Hardanger Bridge. The most profound contribution of this thesis is the results showing the potentially large underestimations of the 100-year return period extreme load effects identified by the methods widely used in the design of such bridges today. When bridges become longer, the buffeting load effects become an increasingly important part of the total design stresses, so uncertainties and underestimations of these load effects can significantly affect the achieved structural reliability. The wind-resistant design process of long-span bridges, from wind field measurements to estimations of the design load effects, are addressed in this thesis, and the following conclusions are reached:

Wind field measurements

- The wind field displayed spanwise nonuniform behaviour for both the mean wind velocity and the turbulence intensity along the Hardanger Bridge girder. The along-wind turbulence intensities varied up to 100%, and the mean wind velocities varied up to 50% along the span for some wind conditions.
- The mean wind velocities measured in the mast used to define the basis for the design of the Hardanger Bridge overpredicted the along span wind field due to terrain speed-up effects.
- The terrain model wind tunnel experiments performed to define the basis for the Hardanger Bridge design were unable to predict the spanwise wind profile adequately. The findings indicated the importance of modelling an appropriately large terrain area and investigating different incoming wind directions.
- A probabilistic model for the nonuniformity of the mean wind velocity and the along-wind turbulence intensity was established based on spanwise wind profiles measured in full-scale along the span of the Hardanger Bridge. Due to extreme nonuniform wind profile realizations from the probabilistic model, the buffeting response showed potential unfavourable effects compared with an equivalent uniform wind field.

Turbulence variability effects on the design buffeting response

- The turbulence uncertainty has large effects on the design buffeting responses of the Hardanger Bridge. Using the ECM, the largest response predicted on the 100-year return period environmental contour exceeded the response on the contour corresponding to the largest mean wind velocity by up to ~60% for the section moments and up to ~45% for the girder stresses.
- The turbulence standard deviations, σ_n, were the most important turbulence parameters to model as stochastic variables when predicting the Hardanger Bridge girder's design load effects. The nondimensional spectral parameters, A_n, did not significantly influence the response of the Hardanger Bridge. However, for even more slender bridges, the variability of this turbulence parameter may be more important.
- To find the 100-year return period long-term extreme response, the expected value of the short-term extreme response predicted by the ECM needed to be multiplied by a factor in

the range 1.11-1.28, depending on the wind direction and the number of turbulence parameters described as random variables. The percentile in the short-term extreme response distribution corresponding to the 100-year return period long-term extreme response was found to be in the range 83%-97%. This observation indicates that the turbulence variability and the extreme short-term response's uncertainty should be accounted for when predicting the design buffeting load effects in long-span bridges.

- By describing the turbulence parameters as random variables, the IFORM and the ECM were able to predict the variability in the scattered extreme peak acceleration response measured in full-scale at the Hardanger Bridge, displaying significant improvement compared with the methodology used for the design of the bridge.

The computational efficiency of the long-term response calculation methods

- The extreme response based on the FLM was too computationally demanding to calculate when the number of turbulence variables became high.
- The reliability-based methods, IFORM and the ECM are computationally efficient and significantly improve the accuracy of the predicted 100-year return period buffeting load effects compared to the current design methodology.
- The suggested Gaussian Process surrogate modelling-based approach showed a computational efficiency similar to the popular IFORM for the long-term buffeting response considering one-, two-, and three probabilistic environmental variables. However, the method outperformed the IFORM in terms of accuracy.
- The reliability-based methods are based on a unique iteration when predicting the N-year return period extreme response of a certain response quantity in a specific position in the structure. When the long-term responses in a full structure is required, the computational advantage of the IFORM will be significantly reduced.
- When calculating the extreme responses based on numerical integration of the FLM, the response quantities in the whole structure can be acquired from each response calculation. So, even though many response analyses are needed to predict the full long-term response, the calculation only needs to be performed once.
- The Gaussian Process surrogate modelling-based approach is computationally efficient and can utilise results from all response quantities in the full structure from each response analyses. Thus, the proposed methodology can significantly outperform other long-term extreme response calculation alternatives in terms of computationally efficiency.

6 Suggestions for further work

Compare numerical methods such as CFD with mast and along span wind measurements. It would be interesting to investigate the modern CFD methods ability to reproduce the turbulence characteristics and the spatial variations of the wind field measured in full-scale at the Hardanger Bridge site.

Fatigue assessment, including uncertain turbulence parameters. The variability of the turbulence parameters generally become larger at lower mean wind velocities. For fatigue assessment due to buffeting loads, the low to moderate mean wind velocity range often dominates fatigue damage. Buffeting loads are not considered critical for the fatigue life of conventional cable-supported bridges. However, when the bridges become longer and the buffeting load effects become more dominant for the total stress, it will also become increasingly important for the bridge's fatigue life.

Refined modelling of the wind direction in the probabilistic model and inclusion of skew winds. The probabilistic turbulence model used in this thesis was established conditional on the wind direction being either from the east or the west. The Hardanger Bridge site's local topography channels the strong winds along the Hardanger Fjord, so this is a reasonable model for this bridge, but the wind direction might need to be handled in another way for other bridges. The wind direction can be considered a random variable and included in the probabilistic model [83,84]. When the wind direction deviates considerably from being perpendicular to the bridge span, the inclusion of skew wind buffeting calculation methods [85] should be considered.

Including the nonuniformity of the wind field in the probabilistic model for long-term response calculations. The nonuniformity was described in terms of a probabilistic model in paper 2 of this thesis, and it could, in principle, be included in the long-term extreme response considerations.

Application of the methods to other bridges and bridge types. The turbulence variability and long-term extreme response of the Hardanger Bridge have been thoroughly studied in this thesis, but applying the methods presented herein to other bridges and bridge types could be interesting. Bridge concepts under consideration for the fjord crossings along the Coastal Highway Route E39, such as ultra-long suspension bridge, long floating bridges and suspension bridges with bridge towers supported by tension leg platforms, can have different response characteristics. This can affect the influence of the different turbulence parameters on the buffeting response, and the effect of the uncertainty of the short-term extreme response distribution might be different from the Hardanger Bridge.

Application of the methods based on probabilistic turbulence models from other bridge sites. The Hardanger Bridge is situated in complex terrain, and similar investigations as the ones performed in this thesis should also be performed on probabilistic turbulence models based on measurements from different bridge sites. This would be a step towards more general conclusions and recommendations for improved design methods for buffeting response of long-span bridges.

7 References

[1] Ammann OH. George Washington Bridge: General Conception and Development of Design. Trans Am Soc Civ Eng 1933;97. https://doi.org/10.1061/TACEAT.0004396.

[2] Golden Gate Bridge H and TD. goldengate.org 2021. https://www.goldengate.org/bridge/history-research/.

[3] Brownjohn JMW, Bocciolone M, Curami A, Falco M, Zasso A. Humber bridge full-scale measurement campaigns 1990–1991. J Wind Eng Ind Aerodyn 1994;52:185–218. https://doi.org/10.1016/0167-6105(94)90047-7.

[4] Kitagawa M. Technology of the Akashi Kaikyo Bridge. Struct Control Heal Monit 2004;11:75–90. https://doi.org/10.1002/stc.31.

[5] Wikipedia - List of longest suspension bridge spans 2021. https://en.wikipedia.org/wiki/List_of_longest_suspension_bridge_spans (accessed February 19, 2021).

[6] Pipinato A. Case study: The Russky bridge. Innov. Bridg. Des. Handb. Constr. Rehabil. Maint., Elsevier Inc.; 2016, p. 671–80. https://doi.org/10.1016/B978-0-12-800058-8.00025-6.

[7] Guesdon M, Erdogan JE, Zivanovic I. The Third Bosphorus Bridge: A Milestone in Long-span Cable Technology Development and Hybrid Bridges. Struct Eng Int 2020:1–8. https://doi.org/10.1080/10168664.2020.1775536.

[8] Eidem ME. Overview of Floating Bridge Projects in Norway. Proc. ASME 2017 36th Int. Conf. Ocean. Offshore Arct. Eng. OMAE2017, 2017, p. 1–6.

[9] Dunham KK. Coastal Highway Route E39 – Extreme Crossings. Transp Res Procedia 2016;14:494–8. https://doi.org/10.1016/J.TRPRO.2016.05.102.

[10] Cao S, Tamura Y, Kikuchi N, Saito M, Nakayama I, Matsuzaki Y. Wind characteristics of a strong typhoon. J Wind Eng Ind Aerodyn 2009;97:11–21. https://doi.org/10.1016/J.JWEIA.2008.10.002.

[11] Li L, Kareem A, Xiao Y, Song L, Zhou C. A comparative study of field measurements of the turbulence characteristics of typhoon and hurricane winds. J Wind Eng Ind Aerodyn 2015;140:49–66. https://doi.org/10.1016/J.JWEIA.2014.12.008.

[12] Wang H, Li A, Hu R. Comparison of Ambient Vibration Response of the Runyang Suspension Bridge under Skew Winds with Time-Domain Numerical Predictions. J Bridg Eng 2011;16:513. https://doi.org/10.1061/(ASCE)BE.1943-5592.0000168.

[13] Wang X, Huang P, Yu X-F, Wang X-R, Liu H-M. Wind characteristics near the ground during typhoon Meari. J Zhejiang Univ Sci A 2017;18:33–48. https://doi.org/10.1631/jzus.A1500310.

[14] Harstveit K. Full scale measurements of gust factors and turbulence intensity, and their relations in hilly terrain. J Wind Eng Ind Aerodyn 1996;61:195–205. https://doi.org/10.1016/0167-6105(96)00047-5.

[15] Hui MCH, Larsen A, Xiang HF. Wind turbulence characteristics study at the Stonecutters

Bridge site: Part I-Mean wind and turbulence intensities. J Wind Eng Ind Aerodyn 2009;97:22–36. https://doi.org/10.1016/j.jweia.2008.11.002.

[16] Hui MCH, Larsen A, Xiang HF. Wind turbulence characteristics study at the Stonecutters Bridge site: Part II: Wind power spectra, integral length scales and coherences. J Wind Eng Ind Aerodyn 2009;97:48–59. https://doi.org/10.1016/j.jweia.2008.11.003.

[17] Li CG, Chen ZQ, Zhang ZT, Cheung JCK. Wind tunnel modeling of flow over mountainous valley terrain. Wind Struct An Int J 2010;13:275–92. https://doi.org/10.12989/was.2010.13.3.275.

[18] Li Y, Hu P, Xu X, Qiu J. Wind characteristics at bridge site in a deep-cutting gorge by wind tunnel test. Jnl Wind Eng Ind Aerodyn 2016;160:30–46. https://doi.org/10.1016/j.jweia.2016.11.002.

[19] Cao S, Wang T, Ge Y, Tamura Y. Numerical study on turbulent boundary layers over two-dimensional hills - Effects of surface roughness and slope. J Wind Eng Ind Aerodyn 2012;104–106:342–9. https://doi.org/10.1016/j.jweia.2012.02.022.

[20] Bitsuamlak GT, Stathopoulos T, Bédard C, Stathopoulos T, Bédard C. Numerical Evaluation of Wind Flow over Complex Terrain: Review. J Aerosp Eng 2004;17:135–45. https://doi.org/10.1061/(ASCE)0893-1321(2004)17:4(135).

[21] Hu P, Li Y, Han Y, Cai SCS, Xu X. Numerical simulations of the mean wind speeds and turbulence intensities over simplified gorges using the SST k - ω turbulence model. Eng Appl Comput Fluid Mech 2016;10:359–72. https://doi.org/10.1080/19942060.2016.1169947.

[22] Cheynet E, Jakobsen JB, Snæbjörnsson J, Reuder J, Kumer V, Svardal B. Assessing the potential of a commercial pulsed lidar for wind characterisation at a bridge site. J Wind Eng Ind Aerodyn 2017;161:17–26. https://doi.org/10.1016/j.jweia.2016.12.002.

[23] Naess A, Moan T. Stochastic Dynamics of Marine Structures. Cambridge University Press; 2013. https://doi.org/10.1017/CBO9781139021364.

[24] Norwegian Technology Standards Institution. NORSOK N-003 Actions and Action Effects. Oslo, Norway: 2007.

[25] The International Electrotechnical Commission. IEC 61400-1: Wind energy generation systems-Part1: Design requirements. 2019.

[26] Xu YL. Making good use of structural health monitoring systems of long-span cable-supported bridges. J Civ Struct Heal Monit 2018;8:477–97. https://doi.org/10.1007/s13349-018-0279-2.

[27] Riches O, Baralos P, Hill C. Queensferry Crossing , UK : durability , maintenance , inspection and monitoring. Proc. Inst. Civ. Eng. – Bridg. Eng., vol. 172, 2019, p. 175–88. https://doi.org/10.1680/jbren.18.00020.

[28] Sun L, Shang Z, Xia Y, Bhowmick S, Nagarajaiah S. Review of Bridge Structural Health Monitoring Aided by Big Data and Artificial Intelligence : From Condition Assessment to Damage Detection. Am Soc OfCivil Eng 2020;146. https://doi.org/10.1061/(ASCE)ST.1943-541X.0002535.

[29] Miyata T, Yamada H, Katsuchi H, Kitagawa M. Full-scale measurement of Akashi–Kaikyo Bridge during typhoon. J Wind Eng Ind Aerodyn 2002;90:1517–27. https://doi.org/10.1016/S0167-6105(02)00267-2.

[30] Macdonald JHG. Evaluation of buffeting predictions of a cable-stayed bridge from full-scale measurements. J Wind Eng Ind Aerodyn 2003;91:1465–83. https://doi.org/10.1016/J.JWEIA.2003.09.009.

[31] Wang H, Li A, Guo T, Xie J. Field measurement on wind characteristic and buffeting response of the Runyang Suspension Bridge during typhoon Matsa. Sci China, Ser E Technol Sci 2009;52:1354–62. https://doi.org/10.1007/s11431-008-0238-y.

[32] Wang H, Asce M, Tao T, Asce SM, Gao Y, Xu F. Measurement of Wind Effects on a Kilometer-Level Cable-Stayed Bridge during Typhoon Haikui. J Struct Eng 2018;144:1–23. https://doi.org/10.1061/(ASCE)ST.1943-541X.0002138.

[33] Wang H, Hu R, Xie J, Tong T, Li A. Comparative Study on Buffeting Performance of Sutong Bridge Based on Design and Measured Spectrum. J Bridg Eng 2013;18:587–600. https://doi.org/10.1061/(ASCE)BE.1943-5592.0000394.

[34] Cheynet E, Bogunovic Jakobsen J, Snæbjörnsson J. Buffeting response of a suspension bridge in complex terrain. Eng Struct 2016;128:474–87. https://doi.org/10.1016/J.ENGSTRUCT.2016.09.060.

[35] Meng X, Nguyen DT, Xie Y, Owen JS, Psimoulis P, Ince S, et al. Design and implementation of a new system for large bridge monitoring—geoshm. Sensors 2018;18. https://doi.org/10.3390/s18030775.

[36] Stephen GA, Brownjohn JMW, Taylor CA. Measurements of static and dynamic displacement from visual monitoring of the Humber Bridge. Eng Struct 1993;15:197–208. https://doi.org/10.1016/0141-0296(93)90054-8.

[37] Mao J-X, Wang H, Feng D-M, Tao T-Y, Zheng W-Z. Investigation of dynamic properties of long - span cable - stayed bridges based on one - year monitoring data under normal operating condition. Struct Control Heal Monit 2018;25:1–19. https://doi.org/10.1002/stc.2146.

[38] Cross EJ, Koo KY, Brownjohn JM., Worden K. Long-term monitoring and data analysis of the Tamar Bridge. Mech Syst Signal Process 2013;35:16–34. https://doi.org/10.1016/J.YMSSP.2012.08.026.

[39] Bietry J, Delaunay D, Conti E. Comparison of full-scale measurement and computation of wind effects on a cable-stayed bridge. J Wind Eng Ind Aerodyn 1995;57:225–35. https://doi.org/10.1016/0167-6105(94)00110-Y.

[40] Fenerci A, Øiseth O, Rönnquist A. Long-term monitoring of wind field characteristics and dynamic response of a long-span suspension bridge in complex terrain. Eng Struct 2017;147:269–84. https://doi.org/10.1016/j.engstruct.2017.05.070.

[41] Fenerci A, Øiseth O. Measured buffeting response of a long-span suspension bridge compared with numerical predictions based on design wind spectra. J Struct Eng 2017;143. https://doi.org/10.1061/(ASCE)ST.1943-541X.0001873.

[42] Winterstein SR, Haver S. Environmental Parameters For Extreme Response : Inverse FORM with Omission Factors. Proc 6th Int. Conf Struct. Saf. Reliab., Innsbruck, Austria: 1993.

[43] Li H, Foschi RO. An inverse reliability method and its application. Struct Saf 1998;20:257–70. https://doi.org/10.1016/S0167-4730(98)00010-1.

[44] Der Kiureghian A, Zhang Y, Li C-C. Inverse Reliability Problem. J Eng Mech

1994;120:1154–9.

[45] Vallis MB, Loredo-Souza AM, Ferreira V, Nascimento EL. Journal of Wind Engineering & Industrial Aerodynamics Classification and identification of synoptic and non-synoptic extreme wind events from surface observations in South America. J Wind Eng Ind Aerodyn 2019;193. https://doi.org/10.1016/j.jweia.2019.103963 R.

[46] Ishihara T, Yamaguchi A. Prediction of the extreme wind speed in the mixed climate region by using Monte Carlo simulation and measure-correlate-predict method 2014. https://doi.org/10.1002/we.1693.

[47] Fenerci A, Øiseth O. Site-specific data-driven probabilistic wind field modeling for the wind-induced response prediction of cable-supported bridges. J Wind Eng Ind Aerodyn 2018;181:161–79. https://doi.org/10.1016/J.JWEIA.2018.09.002.

[48] Fenerci A, Kvåle KA, Wiig Petersen Ø, Rønnquist A, Øiseth O. Dataset from long-term wind and acceleration monitoring of the Hardanger Bridge. J Struct Eng 2021;Forthcomin. https://doi.org/10.1061/(ASCE)ST.1943-541X.0002997.

[49] Fenerci A, Kvåle KA, Wiig Petersen Ø, Rønnquist A, Øiseth O. Wind and Acceleration Data from the Hardanger Bridge. Nor Univ Sci Technol 2020. https://doi.org/10.21400/5ng8980s.

[50] Kaimal J., Wyngaard J., Izumi Y, Coté OR. Spectral characteristics of surface-layer turbulence. Q J R Meteorol Soc 1972;98. https://doi.org/https://doi.org/10.1002/qj.49709841707.

[51] Davenport AG. The spectrum of horizontal gustiness near the ground in high winds. Q J R Meteorol Soc 1961;87:194–211. https://doi.org/https://doi.org/10.1002/qj.49708737208.

[52] Davenport AG. Buffeting of a suspension bridge by storm winds. J Struct Div 1962;88:233–70.

[53] Scanlan RH, Tomko JJ. Airfoil and bridge deck flutter derivatives. J Eng Mech Div 1971;97:1717–37.

[54] Scanlan RH. The action of flexible bridges under wind, I: Flutter theory. J Sound Vib 1978;60:187–99. https://doi.org/10.1016/S0022-460X(78)80028-5.

[55] Scanlan RH. The action of flexible bridges under wind, II: Buffeting theory. J Sound Vib 1978;60:201–11. https://doi.org/10.1016/S0022-460X(78)80029-7.

[56] Jain A, Jones NP, Scanlan RH. Coupled aeroelastic and aerodynamic response analysis of long-span bridges. J Wind Eng Ind Aerodyn 1996;60:69–80. https://doi.org/10.1016/0167-6105(96)00024-4.

[57] Jain A, Jones NP, Scanlan RH. Coupled flutter and buffeting analysis. J Struct Eng 1996;122:716–25. https://doi.org/10.1061/(ASCE)0733-9445(1996)122:7(716).

[58] Chen X, Kareem A, Matsumoto M. Multimode coupled flutter and buffeting analysis of long span bridges. J Wind Eng Ind Aerodyn 2001;89:649–64. https://doi.org/10.1016/S0167-6105(01)00064-2.

[59] Strømmen E. Theory of Bridge Aerodynamics. Second edi. Springer; 2010.

[60] Siedziako B, Øiseth O, Rønnquist A. An enhanced forced vibration rig for wind tunnel testing of bridge deck section models in arbitrary motion. J Wind Eng Ind Aerodyn 2017;164:152–63. https://doi.org/10.1016/J.JWEIA.2017.02.011.

[61] Sagrilo LVS, Naess A, Doria AS. On the long-term response of marine structures. Appl Ocean Res 2011;33:208–14. https://doi.org/10.1016/J.APOR.2011.02.005.

[62] Naess A. Technical note: On the long-term statistics of extremes. Appl Ocean Res 1984;6:227–8. https://doi.org/10.1016/0141-1187(84)90061-0.

[63] Borgman LE. Probabilities for heighest wave in hurricane. J Waterw Harb Coast Eng 1973;99:185–207.

[64] Giske F-IG, Leira BJ, Øiseth O. Full long-term extreme response analysis of marine structures using inverse FORM. Probabilistic Eng Mech 2017;50:1–8. https://doi.org/10.1016/J.PROBENGMECH.2017.10.007.

[65] Battjes JA. Long-term wave height distributions at seven stations around the British Isles. Dtsch Hydrogr Zeitschrift 1972;25:179–89. https://doi.org/10.1007/BF02312702.

[66] Madsen HO, Krenk S, Lind NC. Methods of structural safety. New York: Dover Publications; 1986.

[67] Haver S, Kleiven G. Environmental Contour Lines for Design Purposes: Why and When? 23rd Int. Conf. Offshore Mech. Arct. Eng. Vol. 1, Parts A B, 2004, p. 337–45. https://doi.org/10.1115/OMAE2004-51157.

[68] Kleiven G, Haver S. Met-Ocean Contour Lines for Design; Correction for Omitted Variability in the Response Process. Proc. Fourteenth Int. Offshore Polar Eng. Conf., vol. 1, 2004, p. 202–10.

[69] Rosenblatt M. Remarks on a Multivariate Transformation. Ann Math Stat 1952;23:470–2.

[70] Rasmussen CE, Williams CKI. Gaussian Processes for Machine Learning. Cambridge, Massechusetts: The MIT Press; 2006.

[71] Gramstad O, Agrell C, Bitner-gregersen E, Guo B, Ruth E, Vanem E. Sequential sampling method using Gaussian process regression for estimating extreme structural response. Mar Struct 2020;72. https://doi.org/10.1016/j.marstruc.2020.102780.

[72] Kang F, Asce AM, Li J. Displacement Model for Concrete Dam Safety Monitoring via Gaussian Process Regression Considering Extreme Air Temperature 2020;146:1–16. https://doi.org/10.1061/(ASCE)ST.1943-541X.0002467.

[73] Abdallah I, Lataniotis C, Sudret B. Parametric hierarchical kriging for multi-fidelity aero-servo-elastic simulators — Application to extreme loads on wind turbines. Probabilistic Eng Mech 2019;55:67–77. https://doi.org/10.1016/j.probengmech.2018.10.001.

[74] Wang A, Huang S, Barltrop N. Long Term Extreme Analysis of FPSO Mooring Systems Based on Kriging Metamodel. Proc. ASME 2014 33rd Int. Conf. Ocean. Offshore Arct. Eng., San Fransisco, California, USA: 2014, p. 1–10.

[75] Mohamad MA, Sapsis TP. Sequential sampling strategy for extreme event statistics in nonlinear dynamical systems. Proc Natl Acad Sci U S A 2018;115:11138–43. https://doi.org/10.1073/pnas.1813263115.

[76] Fenerci A. Full-scale investigation of the effects of wind turbulence characteristics on dynamic behavior of long-span cable-supported bridges in complex terrain. Norwegian University of Science and Technology, 2018.

[77] Python Software Foundation. Python Language Reference 2019.

[78] The MathWorks Inc. MATLAB 2019.

[79] Lystad TM, Fenerci A, Øiseth O. Evaluation of mast measurements and wind tunnel terrain models to describe spatially variable wind field characteristics for long-span bridge design. J Wind Eng Ind Aerodyn 2018;179:558–73. https://doi.org/10.1016/J.JWEIA.2018.06.021.

[80] Lystad TM, Fenerci A, Øiseth O. Aerodynamic Effect of Non-uniform Wind Profiles for Long-Span Bridges. Proc. XV Conf. Ital. Assoc. Wind Eng. Vent. 2018. Lect. Notes Civ. Eng., vol. 27, 2019. https://doi.org/10.1007/978-3-030-12815-9_34.

[81] Lystad TM, Fenerci A, Øiseth O. Buffeting response of long-span bridges considering uncertain turbulence parameters using the environmental contour method. Eng Struct 2020;213:110575. https://doi.org/10.1016/J.ENGSTRUCT.2020.110575.

[82] Lystad TM, Fenerci A, Øiseth O. Long-term extreme buffeting response of cable-supported bridges with uncertain turbulence parameters. Eng Struct 2021;236:112126. https://doi.org/10.1016/j.engstruct.2021.112126.

[83] Haghayeghi ZS, Ketabdari MJ. A long-term joint probability model for metocean circular and linear characteristics. Appl Ocean Res 2018;75:143–52. https://doi.org/10.1016/j.apor.2018.03.009.

[84] Vanem E, Hafver A, Nalvarte G. Environmental contours for circular-linear variables based on the direct sampling method. Wind Energy 2020;23:563–74. https://doi.org/10.1002/we.2442.

[85] Xu Y-L. Wind effects on cable-supported bridges. Hong Kong: Wiley; 2013.

Paper I

Tor Martin Lystad, Aksel Fenerci and Ole Øiseth

Evaluation of mast measurements and wind tunnel terrain models to describe spatially variable wind field characteristics for long-span bridge design

Journal of Wind Engineering and Industrial Aerodynamics 2018:179, Copyright Elsevier

Journal of Wind Engineering & Industrial Aerodynamics 179 (2018) 558–573

Contents lists available at ScienceDirect

Journal of Wind Engineering & Industrial Aerodynamics

journal homepage: www.elsevier.com/locate/jweia

Evaluation of mast measurements and wind tunnel terrain models to describe spatially variable wind field characteristics for long-span bridge design

Tor M. Lystad [a,b,*], Aksel Fenerci [b], Ole Øiseth [b]

[a] Bridge Department, Norconsult AS, Sandvika, Norway
[b] Department of Structural Engineering, Norwegian University of Science and Technology, Trondheim, Norway

ARTICLE INFO

Keywords:
Long-span bridge
Nonuniform wind field
Field measurements
Terrain model

ABSTRACT

The quality of the information about the wind field characteristics is crucial for accurately predicting the structural response of a long-span bridge subjected to dynamic wind loads. In this paper, in situ mast measurements and terrain model wind tunnel tests are compared with full-scale measurements of the wind field along the Hardanger Bridge girder. The aim is to investigate the performance of mast measurements and wind tunnel terrain model tests in predicting the wind field characteristics for long-span bridges in complex terrains. Wind field spatial variations and statistical distributions for the mean wind velocity and turbulence intensity are investigated. Extreme value statistics have been applied to compare the mean wind velocity recordings from two different measurement periods. Results showing terrain-induced effects on the wind directions, turbulence intensities and mean wind velocities are presented. Simultaneous spanwise wind profiles for the mean wind velocity and along-wind turbulence intensity are compared between the terrain model wind tunnel tests and the full-scale measurements, and large nonuniformities are identified. The extreme profiles of the turbulence intensities vary as much as 100% along the span, and the mean wind velocity profiles vary up to 50% along the span.

1. Introduction

The Norwegian government is planning a new highway along the west coast of Norway to reduce traveling time between four of the largest cities. The Norwegian west coast is dominated by a terrain with deep fjords and tall, steep mountains, and a highway in this complex terrain demands crossing fjords as wide as 5000 m and as deep as 1300 m with fixed bridge connections. Other extreme crossings are also being proposed around the world, such as the Messina Strait and the Strait of Gibraltar, which pose large engineering challenges. The design for dynamic environmental loads is critical for such structures, and some of the methods used for the design of past bridge structures may not account for the challenges of these extreme projects.

For long-span bridges where the response from dynamic wind loading is dominating the load effects relevant for design, the quality of the information about the wind field characteristics available for the design calculations will govern the achieved structural reliability. In complex inhomogeneous terrain, the spatial variability of the statistical distributions for the wind field parameters can be large. In situ mast measurements and wind tunnel terrain model tests are currently the main approaches used to investigate the local wind field characteristics for long-span bridge design purposes. Other methods such as computational fluid dynamics (CFD) and LIDAR technology are also becoming increasingly attractive as computer performance is increasing and further development is progressing, but the traditional methods will also be important in the future. Mast measurements can be used to record the variability of the local wind field at a single point, and wind tunnel terrain model tests can be used to investigate the spatial transfer of the turbulence characteristics from the mast position to the bridge span. There are a few wind tunnel terrain model experiments for bridge design purposes presented in the literature (Hui et al., 2009a, 2009b, Li et al., 2010, 2015), but there is still a need to investigate this method's ability to spatially transfer mast measurements to the bridge span through studies comparing terrain model results with full-scale measurements, especially in complex terrain.

Design calculations of the dynamic bridge response due to stochastic wind loads are still mainly based on the buffeting theory first introduced by (Davenport, 1962) and improved by (Scanlan, 1978a, 1978b; Scanlan

* Corresponding author. Bridge Department, Norconsult AS, Sandvika, Norway.
E-mail address: tor.martin.lystad@norconsult.com (T.M. Lystad).

https://doi.org/10.1016/j.jweia.2018.06.021
Received 11 April 2018; Received in revised form 16 May 2018; Accepted 29 June 2018
Available online 17 July 2018

and Tomko, 1971). Many full-scale bridge measurement campaigns have been performed to verify the performance of the buffeting theory (Bietry et al., 1995; Brownjohn et al., 1994; Cheynet et al., 2016; Cross et al., 2013; Fenerci et al., 2017; Fenerci and Øiseth, 2018, 2017; Macdonald, 2003; Miyata et al., 2002; Wang et al., 2011, 2013; Xu, 2013), with some campaigns finding good agreement and others finding significant discrepancies. In traditional design approaches, based on a short-term stationary and homogeneous wind field assumption, the turbulence characteristics are commonly chosen as deterministic parameters, although a significant variability in the measured wind field characteristics and bridge responses are presented in several of the referred full-scale measurement campaigns (Fenerci et al., 2017). have shown that it is possible to account for most of the measured response scatter if detailed information about the variability in the wind field parameters is available. More advanced methods such as probabilistic design approaches (Ciampoli et al., 2011; Davenport, 1983; Kareem, 1988; Pagnini, 2010; Pagnini and Solari, 2002; Solari, 1997; Spence and Kareem, 2014; Zhang et al., 2008) or long-term extreme response analysis (Xu et al., 2017) are able to account for the variability in the load to a greater extent, but these methods rely on a more complete statistical description of the load than that used in the traditional methods. Without the bridge in place, the statistical distributions for the wind field parameters can be achieved by mast measurements close to the bridge span, but this approach will rely on the ability to spatially transfer the full statistical distributions to the bridge span.

Several studies in the literature have undertaken the long-term monitoring of turbulence characteristics, thus contributing to the understanding of wind field characteristics in different topographies. Most of the measurement campaigns have been located in typhoon- and monsoon-dominated areas, such as the work performed by (Cao et al., 2009; Choi, 1978; Li et al., 2015; Wang et al., 2017), and have consisted of full-scale bridge monitoring campaigns such as (Hu et al., 2013; Hui et al., 2009a, 2009b; Miyata et al., 2002; Wang et al., 2013, 2011, 2009, 2014). Additionally, for European conditions, many wind field characterization studies can be found in the literature (Bietry et al., 1995; Bocciolone et al., 1992; Brownjohn et al., 1994; Cheynet et al., 2016; Cross et al., 2013; Fenerci et al., 2017; Fenerci and Øiseth, 2018, 2017; Harstveit, 1996; Macdonald, 2003). Although all these studies provide valuable insights, most of them have been based on very few wind sensors (some only measured the wind field characteristics at a single point) that are unable to describe spatial variations in the wind field (Burlando et al., 2013). address the problem of spatially transferring measured wind velocities to a target site using CFD, but on a less detailed scale than what is necessary for terrains that exhibit extreme complexity. For long-span bridge design purposes, there is still a need for studies investigating spatial variations of wind velocities and turbulence characteristics, especially in complex terrain where terrain-induced variations can be large.

In the years prior to the construction of the Hardanger Bridge, in situ mast measurements and wind tunnel terrain model tests were performed to investigate the local wind field characteristics at the bridge site. Since the opening of the bridge in 2013, the Norwegian University of Science and Technology (NTNU) has been monitoring the wind field along the bridge girder using 8 ultrasonic anemometers. This paper is an extension of the preliminary results presented at the European-African Conference on Wind Engineering in 2017 (Lystad et al., 2017). In this paper, we study the spatial variations in the statistical distributions for mean wind velocity and along-wind turbulence intensity at the Hardanger Bridge site and the performance of the traditional wind field characterization methods for describing these statistical distributions along the bridge span in complex terrain.

In section 2 the measurement campaigns used in this study are introduced, and in section 3 flow patterns at the bridge site are interpreted using wind directionality effects as basis. Section 4 investigates the spatial transfer of the mean wind velocity extreme value distributions and the probability density function of the along-wind turbulence intensity between the mast and along girder anemometers. In section 5, spanwise simultaneously measured profiles for mean wind velocity and along wind turbulence intensity from the full-scale measurements are compared with spanwise profiles identified in the wind tunnel terrain model test. Finally, in section 6 conclusions and some recommendations for the use of the investigated methods are presented.

2. Wind field measurements

The Hardanger Bridge is a suspension bridge with a main span of 1310 m, making it the longest bridge span in Norway. The bridge crosses the Hardanger fjord, which is located in complex terrain surrounded by high, steep mountains. The surrounding terrain is extreme, but it is typical for the fjord landscape along the coastline of Norway.

2.1. Full-scale monitoring campaign

After the bridge was opened to the public in 2013, it was instrumented with a state-of-the-art monitoring system measuring wind field characteristics and acceleration responses along the bridge girder. The monitoring system consists of 20 triaxial accelerometers and 9 ultrasonic triaxial anemometers, of which 8 are distributed along the span. An overview of the wind monitoring system is shown in Fig. 2, and the system is described in more detail in (Fenerci et al., 2017).

2.2. Mast measurements

During 1988–1992, the Norwegian Meteorological Institute placed a wind measurement mast on the headland Buneset, close to the southern end of the bridge, to measure the local wind field characteristics for the design of the Hardanger Bridge. Buneset is a headland extending into the fjord with an elevation of 110–130 m above mean sea level. As this headland is relatively flat and the surroundings are steep and complex, Buneset was a suitable position for the mast placement. Fig. 1 shows Buneset on the left in the picture (south), and Fig. 3 shows a picture of the bridge taken from the headland. The mast was instrumented with wind sensors at three levels, 10 m, 30 m and 45 m above ground. The results from the mast measurements are reported by (Harstveit, 1994) and discussed further by (Harstveit, 1996). In (Harstveit, 1994), it was concluded that the sensors at the two lowest levels were disturbed by the forest vegetation on the headland, so the results from these sensors were discarded. They noted that some disturbance may also be present for the 45 m sensor, affecting both the recorded turbulence intensity and the mean wind velocity. The results from the 45 m sensor were used for the design of the Hardanger Bridge, and these results are also used in the present study.

The elevation of the highest sensor (approximately 155–175 m above mean sea level) is also a concern for representing the wind field characteristics along the bridge girder (60 m above mean sea level). The effects of relative elevation, wind speed-ups as the wind flows over the headland, and differences in surface roughness are important factors for the spatial transfer of the wind field characteristics from the mast to the bridge girder.

2.3. Terrain model tests

To quantify the wind field differences between the mast position and the bridge girder and to investigate the spanwise effects such as wind field profiles and covariance, a 1:2000 scale terraced terrain model of the Hardanger Bridge surroundings was tested in the boundary layer wind tunnel at NTNU. The tests were performed by the Department of Energy and Process Engineering at NTNU in 1991, and the results were reported by (Sætran and Malvik, 1991). The boundary layer wind tunnel at NTNU is a closed-circuit wind tunnel with a test section that is 11 m long, 2.7 m wide and 1.8 m high with a maximum wind speed of 30 m/s. Hot-wire anemometers were used in the experiments to measure the along-wind

Fig. 1. The Hardanger Bridge (image by the authors).

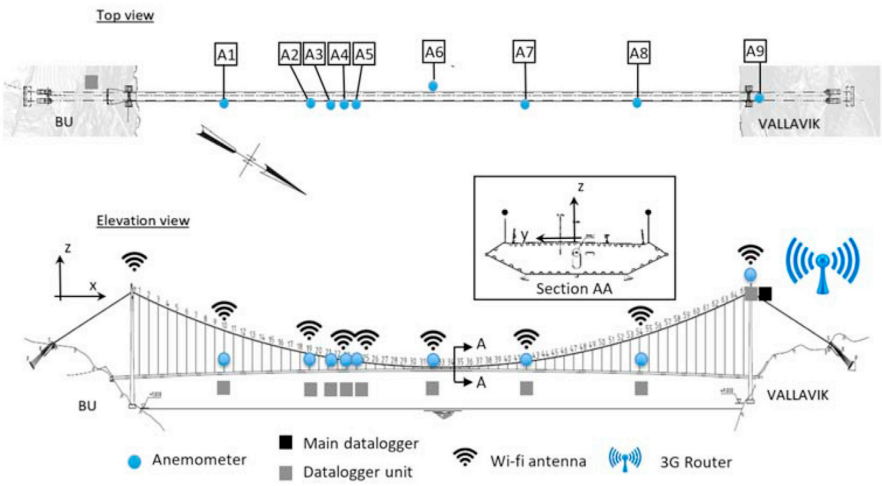

Fig. 2. Full-scale wind field measurement sensor layout.

Fig. 3. Southern tower viewed from the Buneset headland (image by the authors).

component of the fluctuating wind field.

The scale of 1:2000 is larger than the acceptable minimum scale for accurate modeling of the surface flow behavior, suggested by (Bowen, 2003) to be in the range of 1:2500–5000. However (Bowen, 2003), also concluded that for terrain model scales smaller than 1:500, the accuracy of the modeled flow may be significantly reduced. Some studies investigated the surface modeling of such wind tunnel terrain models (Meroney, 1980; Stevenson et al., 1981) and concluded that special attention should be given to the effect of the surface of the model. However, both referenced studies were performed at very small scales, 1:5000 and 1:4000, respectively, which might have affected the surface modeling sensitivity. The terrain model for the Hardanger Bridge was built as a terraced model with 10 mm thick layers and no further surface roughness adjustments.

A terrain model with two main wind directions identified by the mast measurements was tested in the wind tunnel. A map cutout of these two modeled directions is shown in Fig. 4. From the bridge location, the Norwegian coastline is to the west and the inland area is to the east (Meroney, 1980). concluded that the inflow conditions were an important aspect in modeling the local wind flow in complex terrain. For the easterly winds, two different incoming flow cases were tested to investigate the inflow effect on the locally generated wind field. The easterly winds travel over a mountainous region before hitting the bridge site, so the terrain model was subjected to both a smooth incoming flow and a turbulent incoming flow generated with a turbulence grid. However, the westerly winds, coming from the sea, were tested only with smooth inflow conditions, as the local terrain was expected to generate most of the turbulence effects. For all the tests, an incoming wind velocity of 16 m/s was used in the wind tunnel.

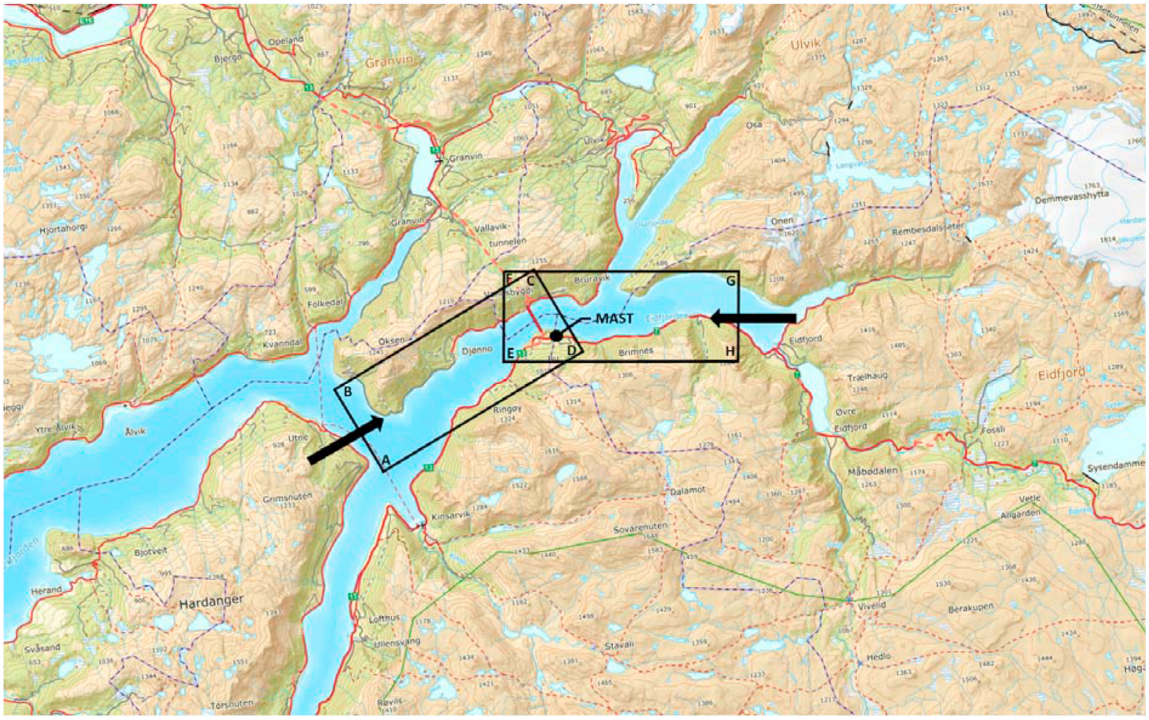

Fig. 4. Terrain model map cutout. ABCD represent westerly winds, and EFGH represent easterly winds (map from Kartverket©; the shown area is approximately 25 × 40 km at full-scale).

3. Effects of wind direction

The directional wind field characteristics measured by the mast are compared with the recorded wind field along the bridge girder from the bridge monitoring campaign in Figs. 5 and 6. The monitoring system anemometers are distributed along the bridge girder, from A1 at the south end to A8 at the north end of the bridge. The mast position is close to the south end of the bridge, so the A1 sensor is the anemometer closest to the mast position.

The strong wind roses shown in Fig. 5 display percentages of the amount of strong wind measurements (>15 m/s) only, and not the total amount of expected wind recordings during the measurement period. It can be observed that the percentage of winds above 18 m/s is larger for the westerly winds than the easterly winds. Considering the westerly winds, the recorded mean wind direction changes slightly towards the midspan coming more directly from the west. Terrain-induced channeling effects become clearer towards each bridge end, where the recorded mean wind is following the southwesterly fjord direction. A possible flow pattern that could explain this behavior is that the dominant incoming wind direction is more directly westerly, but the fjord direction is locally channeling the wind direction at the bridge site. The flow measured at the southern part of the span will then travel a longer distance along the fjord than the wind closer to the midspan, being more strongly affected by the channeling effects. This characteristic flow pattern is illustrated in Fig. 6a (Harstveit, 1994). also indicated a similar flow pattern for the westerly winds, although focusing on the flow over the Buneset headland rather than the along-span behavior. In the northern part of the span, the steep mountainside to the northwest of the bridge is greatly affecting the wind field, and the measured wind directions suggest strong channeling effects at this part of the bridge span.

Towards the east of the bridge, the fjord split into two fjord arms, which causes an interesting spanwise wind field behavior. The dominating winds hitting the southern part of the bridge span, A1-A6, are coming from the southern fjord arm, but towards the northern part of the bridge span, A7-A8, the dominating winds are increasingly coming from the northern fjord arm. Thus, the wind field coming from the east seems to be composed of two different incoming flows channeled by the two fjord arms. The assumed easterly wind flow pattern is illustrated in Fig. 6b.

In Fig. 7, the turbulence intensity wind roses are plotted for the mast measurements and the anemometers distributed along the girder. Only strong winds with mean wind velocities above 10 m/s are presented. For the westerly winds, we observe an increasing turbulence intensity from the southern to the northern part of the span. The very steep mountainside to the northwest of the bridge is increasingly affecting the westerly wind turbulence towards the north. This behavior is also supporting the assumed flow pattern shown in Fig. 6a, where the westerly winds are coming down this steep mountain before hitting the bridge span. For the easterly winds, the turbulence intensity distribution is more uniform. Based on the observation made in the previous section, that the easterly wind field is composed of two different incoming flows, a larger variation in the turbulence characteristics along the span could be expected, but it seems the two fjord arms are generating a similar wind field.

Comparing the turbulence characteristics towards the southern part of the span with the mast measurements, larger percentages of high turbulence intensities are observed for the mast measurements than for the anemometers along the girder. This observation is discussed further in the following sections.

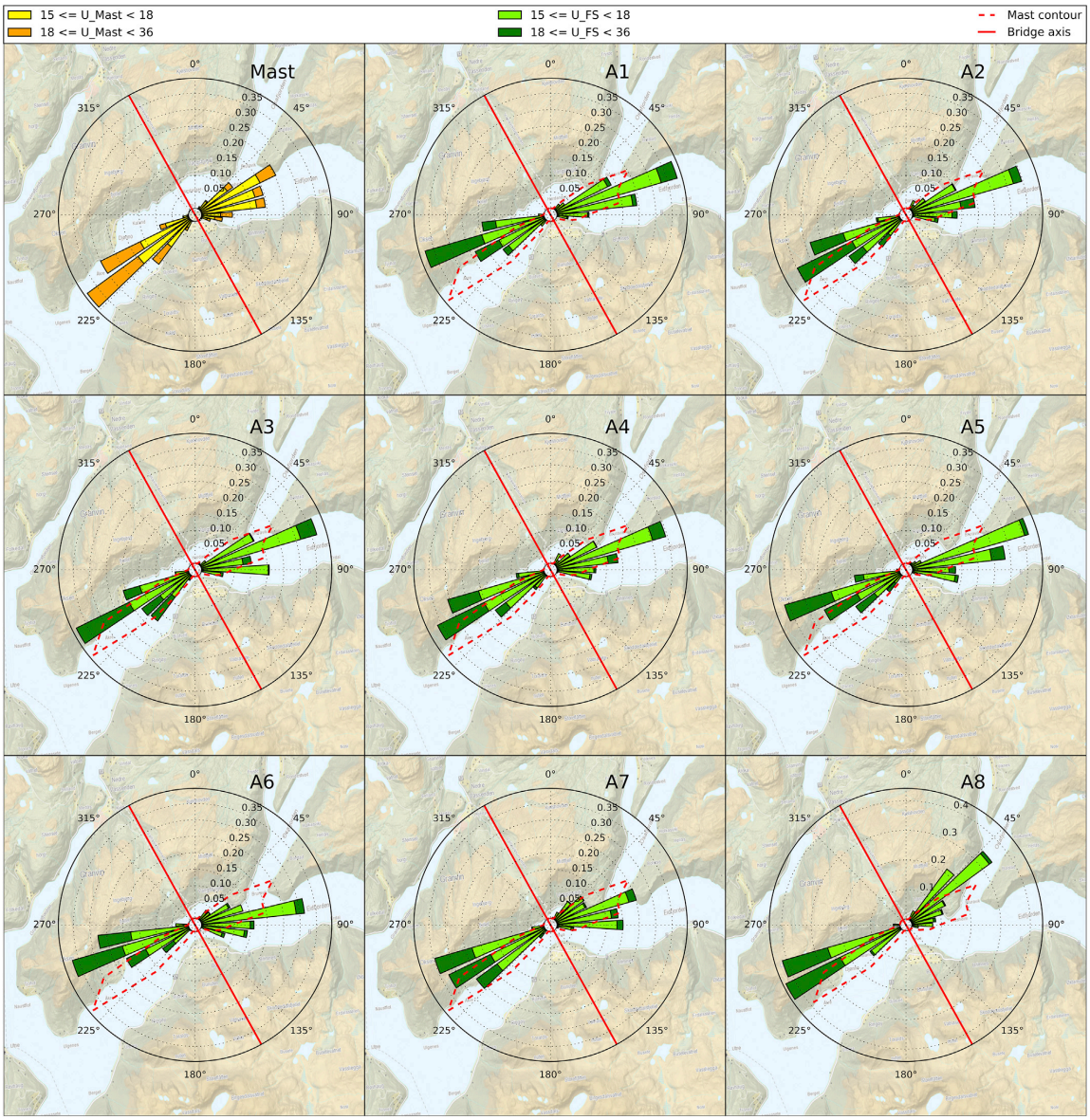

Fig. 5. Mean wind velocity wind roses. The wind roses present percentages of strong winds above 15 m/s only, and are divided into two main wind directions, east and west, with each side adding up to 100% (background from Kartverket©).

It should be noted that the full-scale measurement system is set with an automatic trigger for recordings where one of the anemometers measures a mean wind velocity above 15 m/s. Since a mean wind velocity over the trigger threshold only needs to be measured by one anemometer and due to manually triggered periods, a significant number of measurements between 10 and 15 m/s are still present, although the full distribution is not available in this range. The raw data from the mast measurement results are not available, so the previously binned results presented by (Harstveit, 1994) are used in this study. The available mast turbulence intensities are binned for mean wind velocities above 10 m/s, and not 15 m/s, so for comparison reasons, the same range of mean wind velocities are chosen for the anemometers along the girder.

4. Spatial transfer of wind field characteristics

In situ mast measurements are the most commonly used source of information about the wind field characteristics for the design of long-span bridges. In this section, the performance of the mast measurements in predicting wind field characteristics along the Hardanger Bridge girder is investigated. The results from the four-year mast measurement campaign are compared with the results from four years of along-girder measurements performed by NTNU. Extreme wind speeds and turbulence

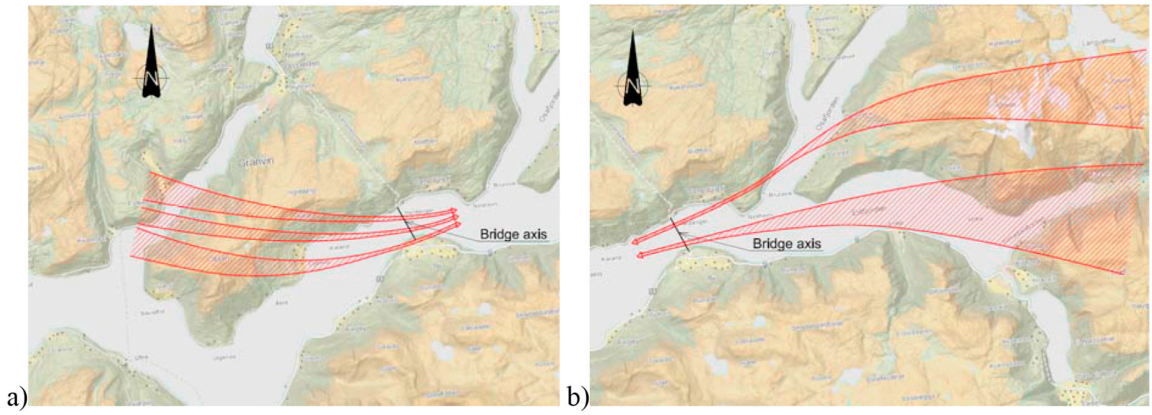

Fig. 6. Characteristic flow pattern; a) westerly winds and b) easterly winds (map from Kartverket©).

intensities are considered, and spatial transfer coefficients between the mast and the positions along the girder are estimated. The spatial transfer coefficients are defined here as the ratio between mast measurements and along span anemometers and will be further discussed in the following sections.

4.1. Extreme value statistics

The mean wind velocity is the most important parameter when predicting the aerodynamic response of a long-span bridge. To create a spatial transfer coefficient for the mean wind velocity between nonsimultaneous recordings from the mast and the along-span anemometers, extreme value distrubutions for the mean wind speed are considered, utilizing the Method of Independent Storms (MIS). The background theory of this method and other recent developments in the field of extreme value statistics are presented in the following paragraphs.

If the parent probability distribution of a stochastic variable is of the exponential type, which is the case for the commonly used Weibull distribution for the mean wind velocity, it can be shown that the asymptotic extreme value distribution will follow a type I generalized extreme value (GEV) distribution form (Gumbel distribution). The general parent cumulative probability distribution form of the exponential type can be written as

$$P_X(x) = 1 - e^{-h(x)} \tag{1}$$

and the type I generalized extreme value cumulative probability distribution can be written as

$$P_Z(z) = 1 - e^{-e^{-y}},\ y = (z-u)/\beta \tag{2}$$

where u and β are the location and scale parameters of the distribution, respectively, and y is the reduced variate. The relationship between the parent distribution, $P_X(x)$, and the asymptotic extreme value distribution, $P_Z(x)$, is expressed below, given that the values of x drawn from the parent distribution are statistically independent and that N is the number of independent storm extreme values drawn from the parent distribution.

$$P_Z(x) = [P_X(x)]^N \tag{3}$$

For the asymptotic limit where N→∞, the extreme value distribution approaches the GEV distribution. The original Gumbel method presented by (Gumbel, 1958) for estimating the extreme value distribution takes advantage of the known shape of the distribution, assuming a type I GEV distribution form. Since the reduced variate y is a linear function for the type I distribution, the Gumbel method estimated the order statistics, u and β, by fitting a straight line to the measurements using linear regression. The reduced variate y can be expressed as follows, using the type I GEV form:

$$y = -\ln[-\ln(P_Z(z))] \tag{4}$$

To obtain realizations of y from the recordings, the extreme value probability $P_Z(z)$ must be calculated for each recording. This can be achieved by ranking the annual extreme value recordings in ascending order giving the lowest recorded annual extreme the rank of $m=1$ and the highest annual extreme the rank of $m=n$, where n is the total number of recorded annual extremes. Then, the non-exceedance extreme value probability of each annual maximum can be calculated from these ranks:

$$P_Z(z) = m/(n+1) \tag{5}$$

The linear regression approach suggested by (Gumbel, 1958) was further investigated by (Lieblein, 1974), who proposed an adjusted method using tabulated coefficients to avoid biased estimates for the order statistics from the fitted curve for the reduced variate. This approach is referred to as the Gumbel-Lieblein BLUE (best linear unbiased estimator) method and was tabulated for up to 16 extreme value recordings by (Lieblein, 1974), and increased to 30 values by (Balakrishnan and Chan, 1992). (Harris, 1996) further generalized the Gumbel-Lieblein BLUE method introducing a new minimum-variance bias free procedure and suggested that the axes in the traditional Gumbel plot should be interchanged (Harris, 1996). also suggested that for extreme wind velocities, a better estimation of the extreme value distribution due to a faster convergence rate was achieved by fitting the square of the mean wind velocity $q=U^2$ to the reduced variate y, an approach also used in the Eurocode (Tamura and Kareem, 2013).

For the general Gumbel-Lieblein BLUE method, only recorded yearly maxima are used to fit the extreme value distribution. This approach demands a very long measurement period to give reliable estimates for the extreme value distribution. However (Cook, 1982), proposed a modified approach taking advantage of more than one extreme recording a year, given that the recorded extreme values are statistically independent, known as the Method of Independent Storms (MIS). By introducing the parameter r for the annual rate of independent storms, the following relationship was proposed:

$$r = n_s/T_s \tag{6}$$

where n_s is the number of independent storm extreme values used in the calculations and T_s is the measurement period in years. Then, the annual extreme value distribution can be expressed as:

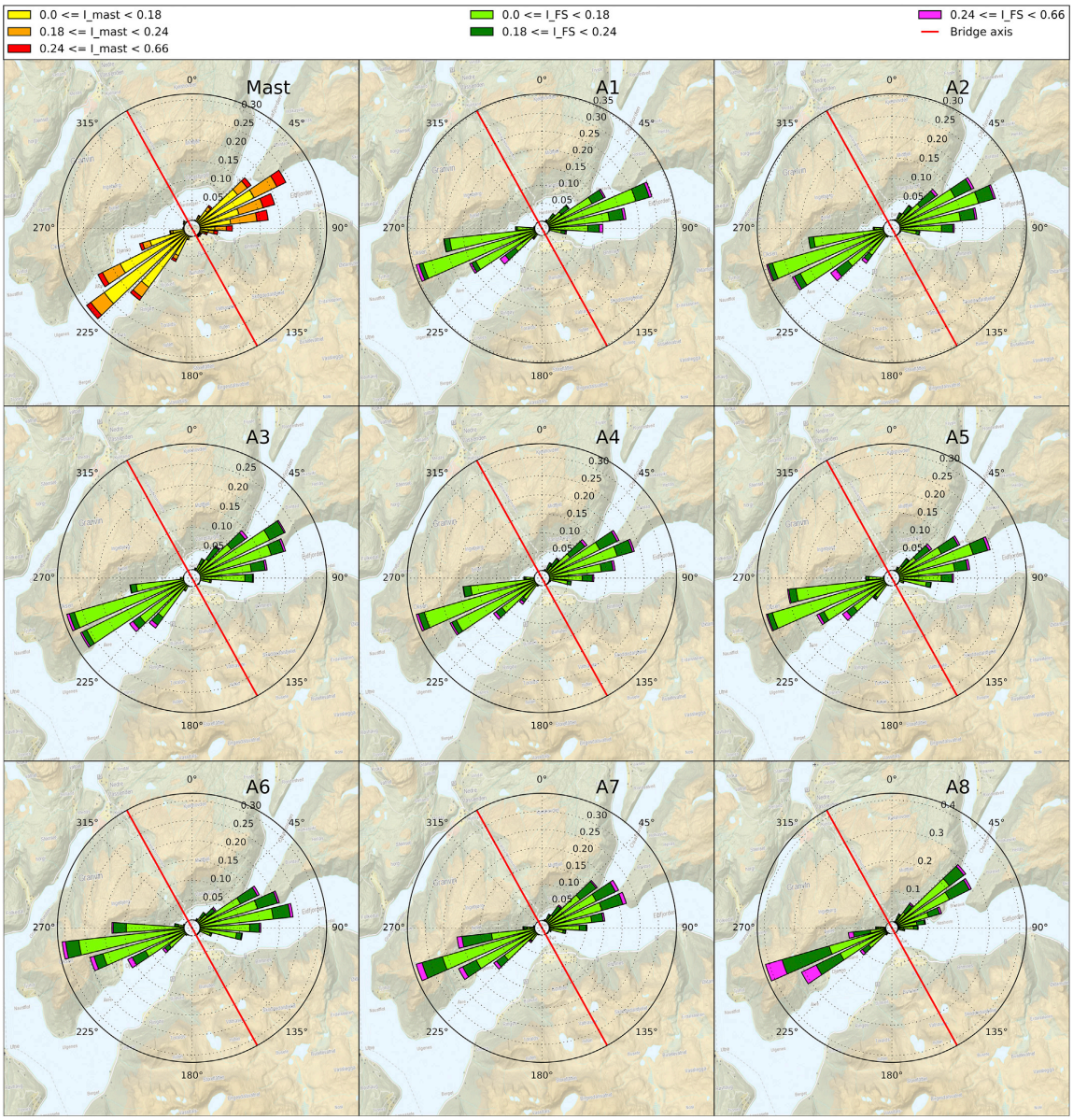

Fig. 7. Turbulence intensity wind roses. The wind roses are divided into two main wind directions, east and west, with each side adding up to 100% (background from Kartverket©).

$$P_Z(z) = [P_{Z-s}(z)]^r = [m_s/(n_s+1)]^r \tag{7}$$

where $P_{Z-s}(z)$ is the individual storms extreme value distribution, m_s is the individual storm rank and $P_Z(z)$ is the annual extreme value distribution. In this way the number of extremes available for practical purposes could be significantly improved. (Cook, 1982) also introduced a method for using the Gumbel-Liebline BLUE approach utilizing more extreme values than the tabulated coefficients from the method would suggest, but a better estimate based on a larger number of extreme values was achieved using Harris' method (Harris, 1999). Recent development in the field of extreme value characterization has shown that using the asymptotic extreme value distribution methods described above may lead to significant discrepancies for the estimation of extreme wind speeds with large return periods (Ian Harris, 2014; Torrielli et al., 2013). Penultimate distribution methods arguing that the number of extremes used, rT_s, is too low to justify an asymptotic assumption where $rT_s \to \infty$ are also presented in the literature (Cook and Harris, 2008, 2004; Harris, 2009) showing better performance for large return periods up to 10 000 years.

In the following investigations, the MIS method based on the Gumbel-Lieblein BLUE approach is used. Other methods may provide better

estimates of the extrapolated large return period extreme wind speeds, but they will rely on a larger number of extremes than that available from the mast measurements in (Harstveit, 1994) to improve the performance compared to the MIS approach. However, for the sake of comparison between nonsimultaneous wind recordings in this study the chosen methodology is deemed satisfactory.

4.2. Mean wind velocity

By applying the individual storms approach and the Gumbel-Lieblein BLUE method, a mean wind velocity extreme value distribution for the mast measurements and the anemometers along the bridge girder was fitted based on the 16 largest statistically independent individual storms during the four-year measuring periods. As noted by Kasperski in (Tamura and Kareem, 2013), the common practice to ensure statistical independence among the recorded individual storm maxima is to require a low mean wind speed over a longer period of 12–24 h, since a single storm may calm down before strengthening again. In the present study, the criterion described by Kasperski was followed, demanding a minimum of 12 h of winds below 15 m/s between the individual storms. However, for the mast measurements, the criterion set to identify statistically independent storms was that the mean wind velocity should fall below 10 m/s between each recorded storm maxima. Although this criterion may principally lead to maxima from the same storm, the time of the measured extreme values are known, and well separated, so the individual storms can also be determined as statistically independent for the mast recordings. The measurements were divided into the two main wind directions, considering westerly and easterly winds separately.

The location of the mast on top of the Buneset headland suggests that wind speed-up effects due to local topography may affect the mean wind velocity, as investigated by (Carpenter and Locke, 1999; Miller and Davenport, 1998). In the European design code for wind actions (Standard Norge, 2009), speed-up effects due to flow over local hill tops can be defined by the terrain shape factor c_o, also referred to as the speed-up ratio in the literature (Miller and Davenport, 1998; Stevenson et al., 1981; Tamura and Kareem, 2013):

$$c_o = v_m / v_{mf} \tag{8}$$

where v_m is the increased wind velocity due to speed-up effects and v_{mf} is the reference velocity.

For the design of the Hardanger Bridge, the terrain model wind tunnel tests were used to estimate the spatial transfer coefficient, or speed-up ratio as defined in Eq. (8), between the mast position and the midspan of the bridge. For the westerly winds, they concluded that the midspan girder wind speed was only 6% lower than the wind speed measured by the mast. For the easterly winds, the measured midspan wind speed was 20% lower than the wind speed in the mast position for the smooth inflow case and 15% lower than that for the turbulent inflow case. Since the strongest winds were measured coming from the west and the wind tunnel tests showed a low difference in the wind velocity between the mast and the girder midspan for this direction, no reduction in the measured mast wind velocities were used in the design.

In Figs. 8 and 9, fitted Gumbel-Lieblein plots are shown for the easterly and westerly winds, respectively, comparing the extreme winds measured by the mast with the along-girder anemometers. The fitted curves are not linear in the plots because the line is fitted to the square of the mean wind velocity and plotted against the linear mean wind velocity axis. In Fig. 10, the fitted extreme value probability distribution is plotted along the bridge span through a contour plot for both easterly and westerly winds. The mean wind velocity, with a statistical return period of 2 and 50 years, is indicated for the along-span variation and the mast extreme wind velocities. In Tables 1 and 2, extreme winds for 2 and 50 year statistical return periods are shown for all sensors, as well as the speed-up ratio for the mast using measurements along the bridge girder as reference wind speeds.

It can be observed that the mast measurements overestimate the wind speed compared with the positions along the girder for both wind directions. Comparing the midspan (A6) speed-up ratios observed from the full-scale measurements with the predicted coefficients from the terrain model wind tunnel test results c, a good estimate for the easterly winds can be observed, but for the westerly winds, the terrain model experiments show a significantly lower speed-up ratio than that observed from the full-scale measurements. This may be explained by observing the difference in wind directions for the westerly winds between the mast measurements and the midspan anemometer, A6, and the assumed flow pattern shown in Fig. 7a. As the westerly direction modelled in the wind tunnel may be slightly inaccurate for the dominating winds, as discussed in the previous sections, important information about the local flow over the Buneset headland may have been lost resulting in an underestimated

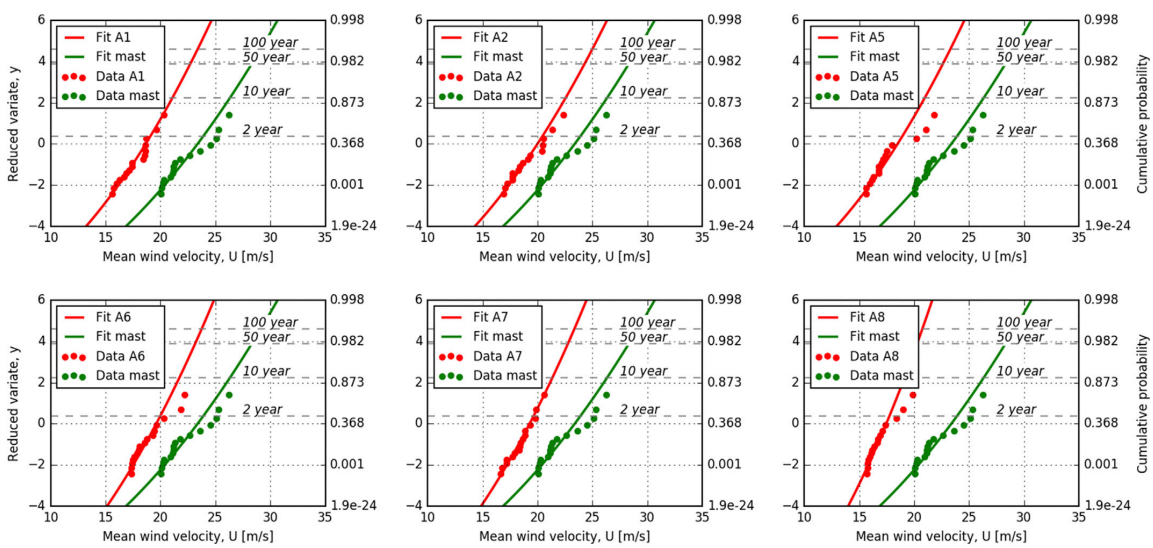

Fig. 8. Gumbel-Lieblein plots for the extreme mean wind velocities of chosen anemometers for easterly winds.

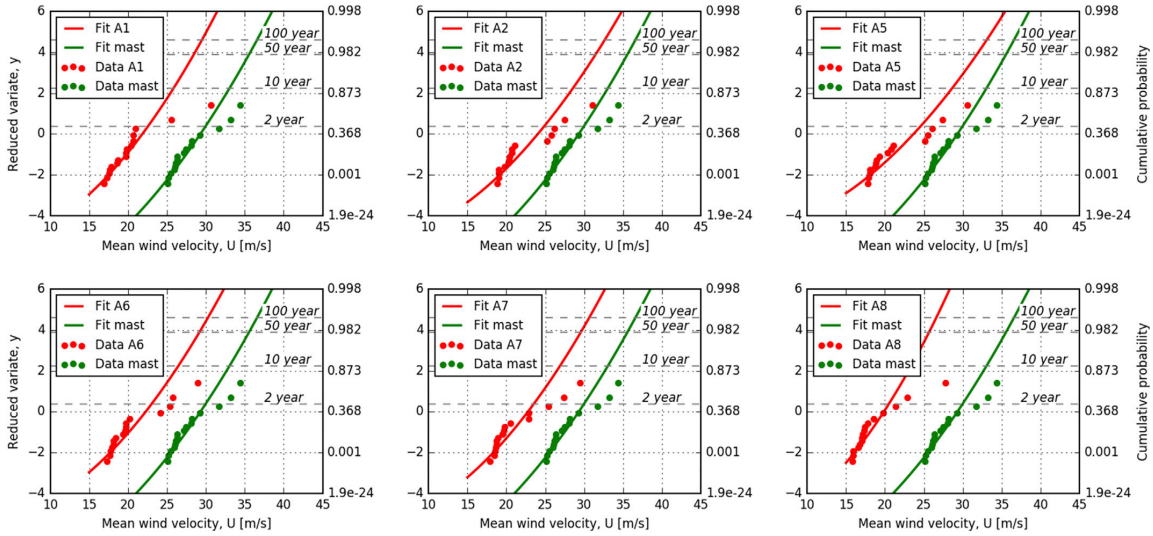

Fig. 9. Gumbel-Lieblein plots for the extreme mean wind velocities of chosen anemometers for westerly winds.

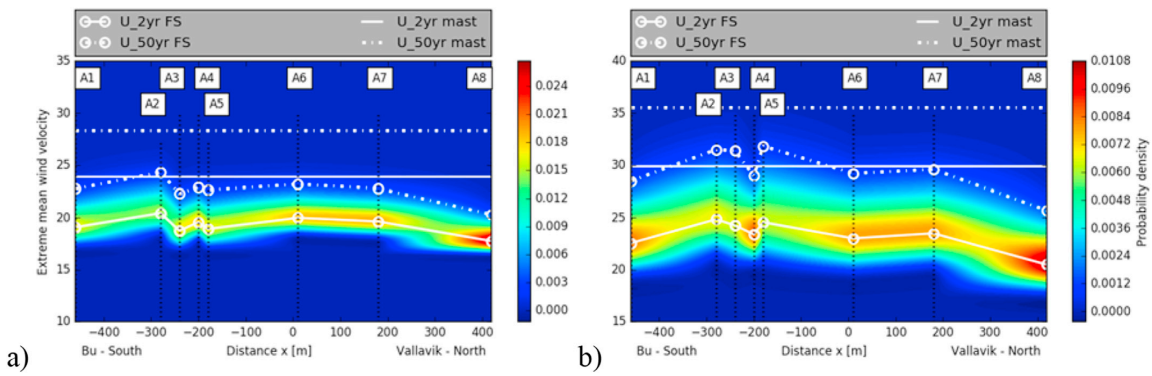

Fig. 10. Extreme value probability density for the mean wind velocity of a) easterly winds and b) westerly winds.

Table 1
Mean wind velocity extreme values and speed-up ratios for the easterly winds.

Sensor	x [m]	U_{2yr}	U_{10yr}	U_{50yr}	U_{100yr}	$c_{o,2yr}$	$c_{o,50yr}$
Mast	~1000	23.9	26.4	28.3	29.1	1	1
A1	460	19.1	21.1	22.7	23.4	1.25	1.25
A2	280	20.4	22.6	24.3	25.0	1.17	1.17
A3	240	18.8	20.7	22.3	22.9	1.27	1.27
A4	200	19.6	21.4	22.9	23.5	1.22	1.24
A5	180	18.9	21.0	22.6	23.3	1.26	1.25
A6	−10	20.0	21.7	23.2	23.8	1.20	1.22
A7	−180	19.6	21.4	22.8	23.4	1.22	1.24
A8	−420	17.7	19.1	20.3	20.7	1.35	1.40
Eurocode	–	–	–	–	–	1.24	
Terrain model	–	–	–	–	–	1.20/1.15	

Table 2
Mean wind velocity extreme values and speed-up ratios for the westerly winds.

Sensor	x [m]	U_{2yr}	U_{10yr}	U_{50yr}	U_{100yr}	$c_{o,2yr}$	$c_{o,50yr}$
Mast	~1000	30.0	33.1	35.6	36.6	1	1
A1	460	22.6	25.9	28.5	29.5	1.33	1.25
A2	280	24.8	28.6	31.5	32.6	1.21	1.13
A3	240	24.3	28.3	31.4	32.6	1.23	1.13
A4	200	23.4	26.5	29.0	29.9	1.28	1.23
A5	180	24.6	28.7	31.8	33.1	1.22	1.12
A6	−10	23.0	26.5	29.2	30.3	1.30	1.22
A7	−180	23.5	26.9	29.6	30.6	1.27	1.20
A8	−420	20.5	23.4	25.7	26.6	1.46	1.38
Eurocode	–	–	–	–	–	1.18	
Terrain model	–	–	–	–	–	1.06	

speed-up ratio.

The European design code for wind actions (Standard Norge, 2009) gives guidelines for calculating local variations in the wind velocity based on the inclination of the upstream hill and the position relative to the hill. The relationship for an inclination ratio of $\Phi = H/L_u > 0.3$ is defined as follows

$$c_o = 1 + 0.6s \tag{9}$$

where s is a factor accounting for the position relative to the hill and the terrain shape. It should be noted that the guidelines given in the Eurocode are not valid for complex terrain such as the Hardanger Bridge site, but it is interesting to see how well the guidelines can perform also under

such conditions. A good performance may indicate isolated effects, less influenced by the surrounding terrain complexity. By applying the calculation procedure for local wind speed-ups over a single hill proposed in the design codes, a speed-up ratio of *1.24* for the easterly winds and *1.18* for the westerly winds can be determined, corresponding very well with the observed speed-up ratios from the full-scale measurements in Tables 1 and 2 In this calculation, $\Phi=0.33$ and $s=0.4$ were used for the easterly winds, and $\Phi=0.5$ and $s=0.3$ were used for the westerly winds, based on the mast distance from the upstream hill and the steepness of the hill.

For the easterly extreme wind velocity distribution plotted in Fig. 10a, a uniform distribution along the span is shown, although slight reductions towards the ends are visible. The same trend can be observed for the westerly wind direction in Fig. 10b, although stronger reductions towards the ends are present. Additionally, a weak linear trend from the A8 sensor in the north to the A5 sensor can be observed for the westerly winds.

In this section, the extreme value statistics have been used to compare recordings from two different measurement periods. Some caution should be used due to possible biased differences between the two periods. There are no long-term wind measurement stations very close to the bridge site that cover both periods, as they are 25 years apart, but a qualitative comparison of the monthly maxima from a measuring station in the same area have been performed without any observed significant differences in the wind velocities. Additionally, the measurement periods of 4 years are relatively long, so a good statistical foundation can be expected, thus adding to the validation of the results.

4.3. Turbulence intensity

The turbulence intensity is another one of the most important wind field characteristics for design of long-span bridges, especially when dealing with buffeting response. Aerodynamic effects such as vortex induced vibrations (VIV) and aeroelastic instability phenomena are also affected by turbulence, however VIV is more critical for lower wind speeds and aeroelastic instability is, or at least should be, critical for higher wind speeds than what is considered in this study. Thus, based on the turbulent wind recordings considered here, the discussion in the following will be related to buffeting effects for long-span bridges. In situ mast measurements are one of the main sources of information about the local turbulence content of the wind field for the design of long-span bridges. In complex terrain, the turbulent wind field can be expected to have large terrain-induced spatial variations, as observed by (Li et al., 2010, 2016). Hence, the positioning of the measurement mast and the physical interpretation of its ability to represent the along-span turbulent wind field characteristics can be very important. In this section, the along-wind turbulence intensity statistical distributions are investigated. The along-wind turbulence intensity is defined as follows:

$$I_u = \sigma_u / U \tag{10}$$

where σ_u is the standard deviation of the fluctuating wind process and U is the mean wind velocity.

The expected value and the variability of the turbulence intensity from the bridge monitoring recordings are compared with the mast measurements. Strong wind recordings with a mean wind velocity above 10 m/s are considered, and again, the wind field is divided into the two dominating directions, easterly and westerly winds, as they display a different behavior. In Figs. 11 and 12, histogram plots of the turbulence intensities along the bridge span are shown together with fitted log-normal probability density functions (PDFs). The fitted PDFs from the mast measurements are indicated in all figures for comparison purposes. The fitted PDF for the strong wind turbulence intensity follows the log-normal distribution very well both for the along-span anemometers and for the mast measurements. In Fig. 13, a contour plot of the PDF for the along-wind turbulence intensity is plotted along the span. The expected value and the 95th percentile of the turbulence intensity are indicated in the same figure. In Tables 3 and 4, the turbulence intensity expected values, standard deviations and 95th percentiles, and the spatial transfer coefficients for these statistical parameters between the mast and the along-span anemometers are presented. The spatial transfer

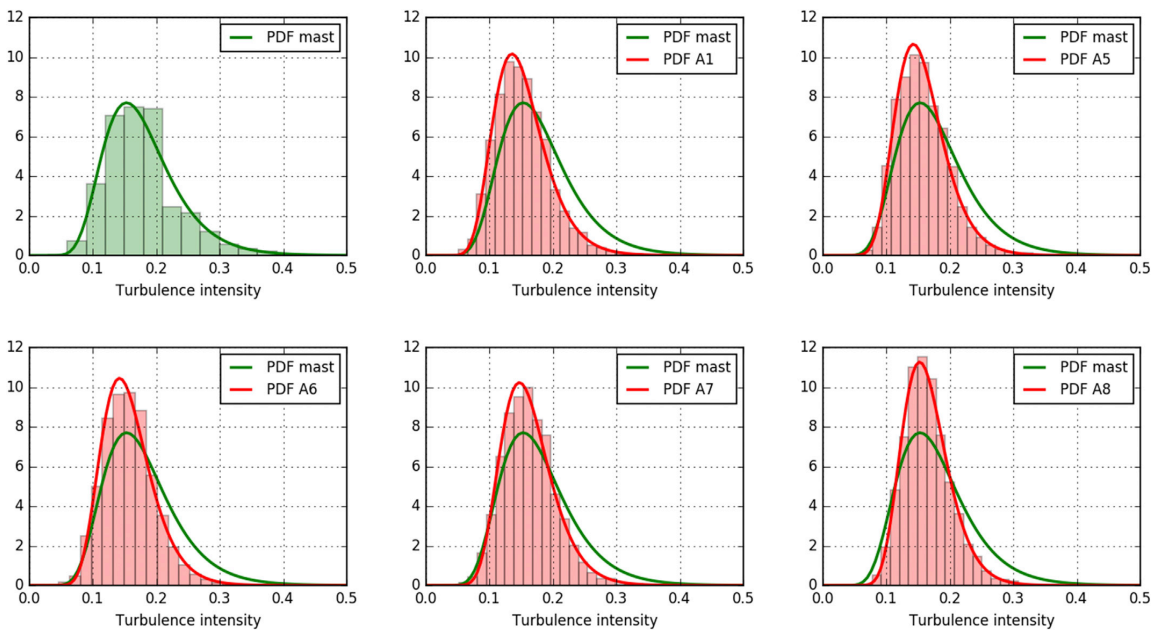

Fig. 11. Fitted probability density functions of chosen anemometers for the easterly along-wind turbulence intensities.

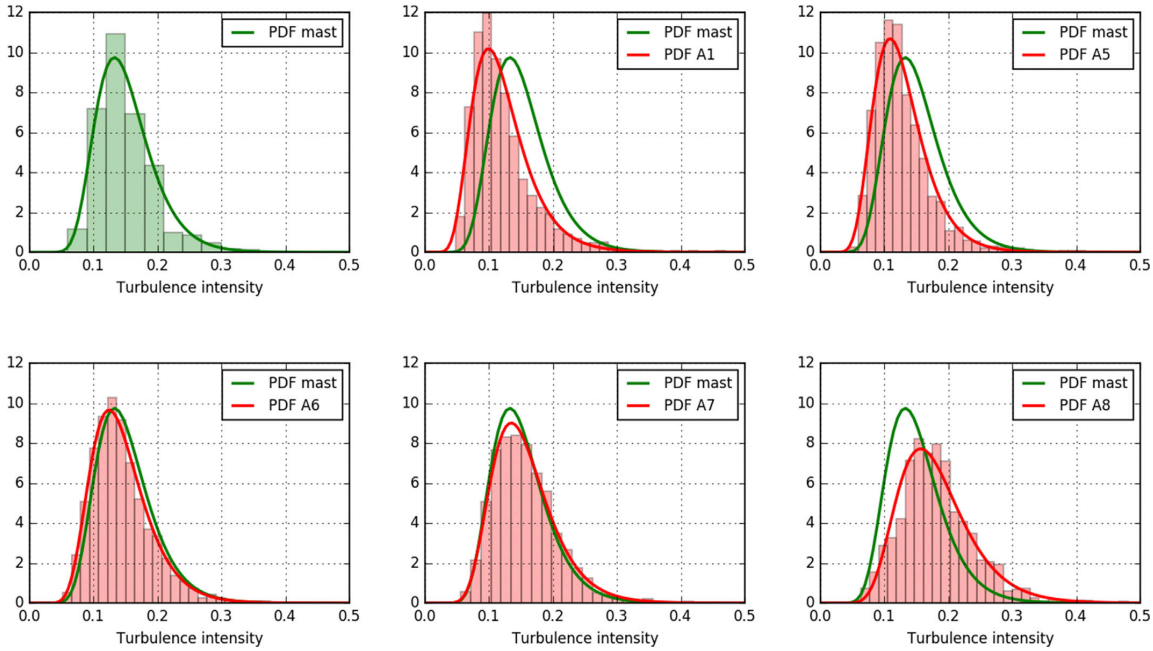

Fig. 12. Fitted probability density functions of chosen anemometers for the westerly along-wind turbulence intensities.

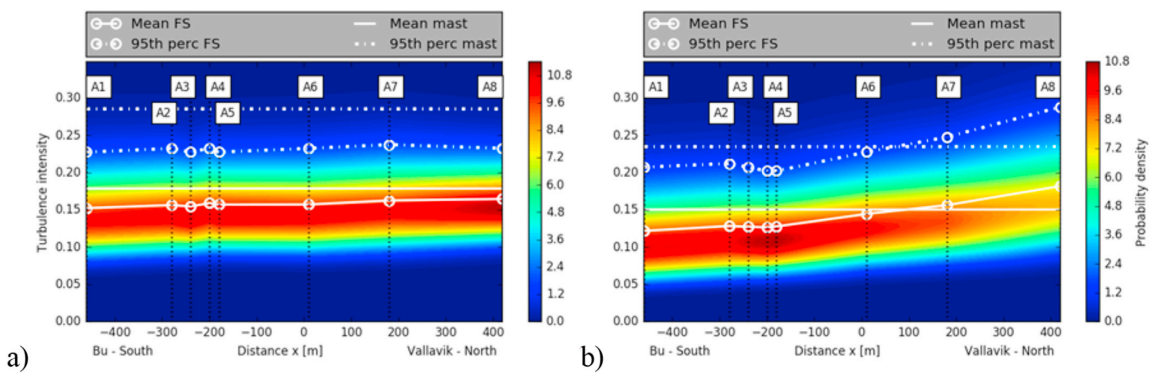

Fig. 13. Probability density distributions for the along-wind turbulence intensity I_u of the a) easterly winds and b) westerly winds.

Table 3
Turbulence intensity statistics and spatial transfer coefficients for the easterly winds.

Sensor	x [m]	Mean	Std	95th	γ_{mean}	γ_{std}	γ_{95th}	μ	σ
ast	~1000	0.179	0.059	0.286	1	1	1	−1.722	0.322
A1	460	0.152	0.043	0.227	1.17	1.36	1.26	−1.883	0.279
A2	280	0.156	0.042	0.232	1.14	1.39	1.23	−1.856	0.266
A3	240	0.155	0.040	0.227	1.16	1.47	1.26	−1.868	0.256
A4	200	0.159	0.042	0.232	1.12	1.40	1.23	−1.840	0.260
A5	180	0.157	0.041	0.227	1.14	1.45	1.26	−1.852	0.254
A6	−10	0.157	0.042	0.232	1.14	1.42	1.23	−1.851	0.260
A7	−180	0.162	0.042	0.237	1.10	1.39	1.20	−1.818	0.256
A8	−420	0.165	0.038	0.232	1.09	1.56	1.23	−1.805	0.226

coefficients are defined as the ratio between the statistical distribution at the mast position (noted *mast*) and the along-span anemometers (noted *anemo*) as

$$\gamma_{stat} = I_{stat,mast} / I_{stat,anemo} \tag{11}$$

where $I_{stat,\ mast}$ and $I_{stat,\ anemo}$ can be any statistical entry such as the mean

Table 4
Turbulence intensity statistics and spatial transfer coefficients for the westerly winds.

Sensor	x [m]	Mean	Std	95th	γ_{mean}	γ_{std}	γ_{95th}	μ	σ
Mast	~1000	0.151	0.046	0.235	1	1	1	−1.889	0.295
A1	460	0.122	0.046	0.207	1.24	0.98	1.14	−2.107	0.369
A2	280	0.128	0.046	0.212	1.18	0.98	1.11	−2.053	0.351
A3	240	0.127	0.044	0.207	1.19	1.04	1.14	−2.062	0.336
A4	200	0.126	0.043	0.202	1.20	1.06	1.16	−2.068	0.331
A5	180	0.128	0.043	0.202	1.19	1.07	1.16	−2.059	0.325
A6	−10	0.144	0.047	0.227	1.05	0.98	1.03	−1.935	0.316
A7	−180	0.156	0.050	0.247	0.97	0.91	0.95	−1.857	0.313
A8	−420	0.182	0.059	0.288	0.83	0.78	0.82	−1.705	0.314

value, standard deviation or 95th percentile of the along-wind turbulence intensity.

Considering the easterly winds, the turbulence intensity is uniformly distributed along the span, both in mean value and variability. Comparing the along-span anemometers with the mast measurements, Table 3 shows that the mast measurements overestimate the mean value by 14% and the 95th percentile by 23% for the midspan sensor A6. Thus, the error made by using the mast measurements directly would, in this case, become larger for a probabilistic design approach than if the design was based on the expected value as a deterministic parameter.

A similar trend can be observed for the westerly winds, where both the mean and variability are larger in the mast measurements than in the along-span anemometers close to the southern bridge end. These observations indicate that the mast measurement turbulence intensities may be affected by the forest vegetation surrounding the mast, as noted and commented upon in the mast report (Harstveit, 1994). European design codes for wind actions (Standard Norge, 2009) state that the standard deviation of the fluctuating wind process should be unchanged by the terrain form creating the speed-up effects discussed in the previous section. Therefore, by increasing the mean wind velocity and keeping the standard deviation of the process unchanged, the turbulence intensity decreases. However (Miller and Davenport, 1998), made observations contradictory to this effect and concluded that the design codes would yield unconservative values for turbulence intensities following these guidelines. Although the surface roughness due to the local forest vegetation on Buneset can explain at least parts of the overestimated turbulence intensities, flow separation effects due to the flow over the headland may also be present, in accordance with the observations made by (Miller and Davenport, 1998). S. Cao also concluded in (Tamura and Kareem, 2013) that flow separation may occur over hilltops when the upstream slope is larger than 17°, which is the case for both wind directions at Buneset.

Another factor that may affect the difference among the turbulence intensity distributions is the incomplete conditional distribution for the wind speeds between 10 and 15 m/s for the bridge monitoring measurements, due to the triggering threshold previously discussed in section 3. However, as shown by (Fenerci and Øiseth, 2017), the conditional turbulence intensity distribution for mean wind velocities in the range of 10–15 m/s is similar to the range of 15–20 m/s for the Hardanger Bridge, and since the error is only connected to the weight of the contributions from this range, this effect is not expected to significantly influence the results.

An interesting behavior can be observed for the westerly winds where the turbulence intensity distributions are changing significantly along the bridge span, showing a very nonuniform behavior in both mean value and variability. The expected value for the turbulence intensity is increasing from south to north by as much as 50%, and the mast measurements change from overestimating the turbulence intensity in the southern part of the span to underestimating it in the northern part. This effect was also indicated in Fig. 7, where high turbulence intensities were observed towards the A8 sensor for westerly winds generated by the mountain to the northwest of the bridge.

It is also noted that the fitted lognormal distributions are following the turbulence intensity histograms very well for all the along-span anemometers. The histograms for the mast measurements are sorted in wider bins due to the available datasets, but a lognormal distribution still follows the distribution well. The lognormal probability density function can be written as

$$f(x) = \frac{1}{x\sigma\sqrt{2\pi}} e^{\left\{\frac{-(\ln x-\mu)^2}{2\sigma^2}\right\}};\ x > 0 \tag{12}$$

where μ (the mean of the natural logarithm of the random variable) and σ (the standard deviation of the natural logarithm of the random variable) are the distribution parameters. The fitted distribution parameters for the turbulence intensities are shown in Tables 3 and 4.

5. Spanwise wind profiles

The wind field characteristics at the Hardanger Bridge site show large spatial variability along the span, especially for the turbulence intensity, as shown in the previous sections. The terrain model wind tunnel tests of the Hardanger Bridge site were used to investigate such terrain-induced spatial variations in the wind field.

In this section, simultaneously measured full-scale wind profiles along the bridge girder are shown for mean wind velocities and along-wind turbulence intensities and compared with the wind profiles measured in the wind tunnel. Only strong winds are considered with a midspan mean wind velocity above 12 m/s.

The full-scale measurement wind profiles are divided into wind direction sectors of 10° and are shown in Figs. 14 and 15 for the easterly and westerly winds, respectively. The measured profiles for the mean wind velocity and turbulence intensity from the wind tunnel tests are indicated in the same figures and are divided into easterly and westerly winds, corresponding to the two terrain models described in the previous sections.

Some spanwise nonuniformity in the wind field can be expected for such a bridge, where the surface roughness is smaller in the middle of the fjord than towards each side. A decrease in mean wind velocity, and corresponding increase in turbulence intensity towards the bridge ends would result from such conditions, however the complexity of the surrounding terrain may distort this behavior. From Fig. 14, a quite uniform wind field is displayed for the first 1-3 sectors of the easterly winds, but for sector 4–7 the surface roughness effect described above is becoming increasingly clear. Though no distinct linear trend is observed from the full-scale measured wind profiles for this wind direction, the profiles measured in the wind tunnel terrain model tests display a clear linear variation both for the mean wind velocity and the turbulence intensity, but with an opposite sign of inclination. The variation is stronger in the test configuration with a turbulent inflow than in the smooth inflow case. The easterly wind direction modeled in the wind tunnel is closest to sectors 4–6 in Fig. 14. Although the linear trend from the wind tunnel tests is not observed at the middle part of the span in the full-scale measurements, a similar trend can be observed for the northern part of the bridge. Here, the mean wind speed is decreasing, and the turbulence

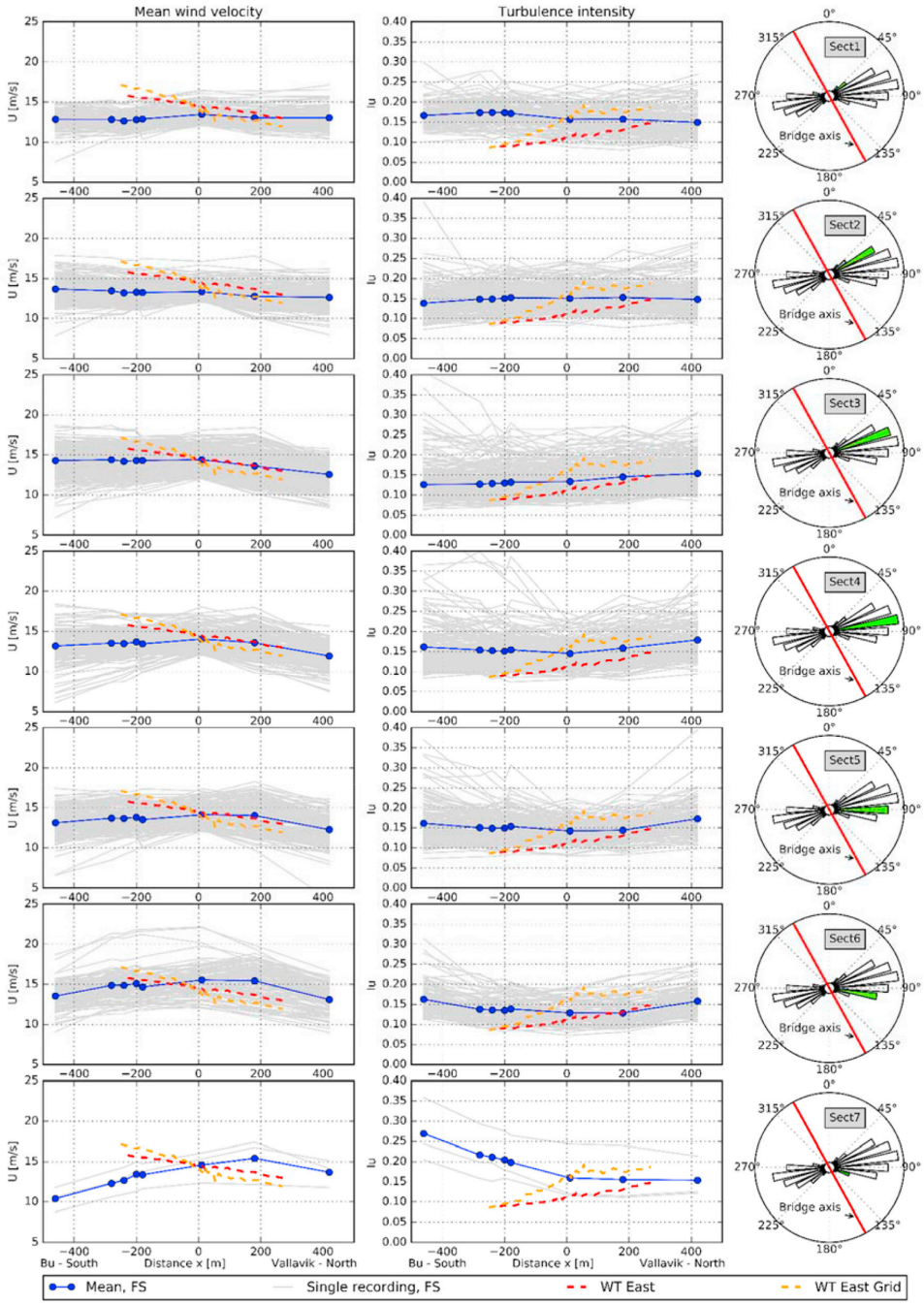

Fig. 14. Along-span simultaneously measured wind field profiles for easterly winds. FS, denotes "Full-scale measurements" and WT denotes "Wind Tunnel tests". On the right side of the figures, midspan (A6) wind rose for the FS profiles are given, highlighting the associated sector for the mean wind direction."

intensity is increasing, in better correspondence with the wind tunnel profiles.

For the westerly winds, it has previously been noted that the modeled terrain direction does not seem to represent the dominant incoming wind direction very well. The modeled direction corresponds best with sectors 8 and 9 for the full-scale measurements shown in Fig. 15. The wind tunnel experiments show a very homogenous behavior for both the mean wind velocity and the turbulence intensity along the span, in strong

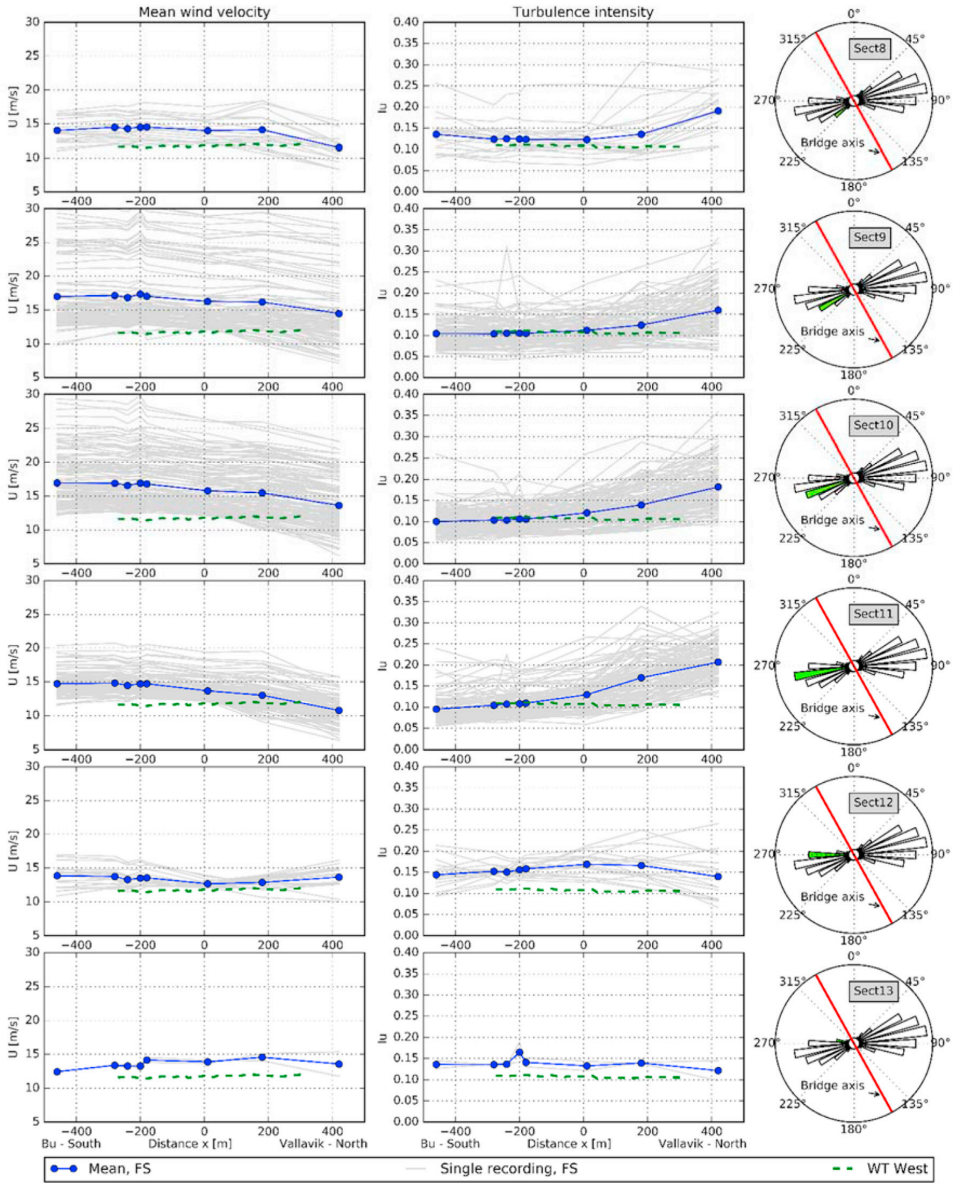

Fig. 15. Along-span simultaneously measured wind field profiles for westerly winds. FS, denotes "Full-scale measurements" and WT denotes "Wind Tunnel tests". On the right side of the figures, midspan (A6) wind rose for the FS profiles are given, highlighting the associated sector for the mean wind direction."

contradiction to what can be observed in Fig. 13. However, for sectors 8 and 9, the homogeneity identified by the terrain model wind tunnel tests seem to correspond quite well to the full-scale measurements for the middle part of the span. The A8 sensor closest to the north end of the bridge shows a different behavior, but this behavior could not be captured by the wind tunnel experiments since only the middle part of the bridge span was investigated. For sectors 10 and 11, a linear trend in both the mean wind velocity and the turbulence intensity profiles is observed. This corresponds to the observation made for the turbulence intensity in Fig. 13, but the trend for the mean wind velocity is clearer in Fig. 15 than in Fig. 10. This trend is an illustration of the strong terrain induced effects on the wind field inhomogeneity at this very complex bridge site.

The full-scale turbulence intensities display a large variability, but the turbulence intensity levels from the wind tunnel tests agree quite well with the measured mean value levels for the corresponding sectors of the westerly winds. This is an indication that most of the turbulence is generated locally for this wind direction. For the easterly winds, the full-scale measurements display levels in the area between the two test configurations, indicating that some influence from the incoming flow affects the local turbulence characteristics as well. These observations agree with the initial assumptions about the inflow conditions and

indicate that the surface model of the terrain model is performing well.

A few studies have investigated the effects of the homogeneity assumption often used in buffeting calculations (Arena et al., 2014; Hu et al., 2017; Zhang, 2007). Fig. 15 shows turbulence profiles that vary as much as 100% over a length of approximately 900 m and mean wind velocities that vary by approximately 50% over the same length. The Hardanger Bridge site is extremely complex; however, it is quite typical for Norwegian terrain. Other areas of the world where long-span bridges are constructed show similar complexities, such as mountain gorge terrains in China, as investigated by (Li et al., 2010, 2016). In such conditions, extreme nonuniform profiles may be important for both the buffeting action and aerodynamic instability effects of long-span bridges.

One of the main approaches to estimate such nonuniformity in the wind field is by using terrain model wind tunnel tests. In this study, some discrepancies in the tested wind field profiles from the wind tunnel were found when compared with the full-scale measurements. However, some promising results were also found, especially for the uniformity in the westerly wind profiles and the turbulence intensity levels predicted by the wind tunnel experiments. Some of the unsatisfactory results from the wind tunnel tests for the Hardanger Bridge site can be explained by the limited size of the terrain model and the limited number of tested incoming wind directions. A larger scale and a larger modeled area would be expected to increase the performance of the wind tunnel test results for the Hardanger Bridge site.

6. Conclusions

The spatial variations in the wind field characteristics at the Hardanger Bridge site have been investigated in this paper. The performance of traditional wind field characterization methods, namely, in situ mast measurements and wind tunnel terrain model experiments, for predicting the wind field along a bridge girder in complex terrain has been studied, and the following conclusions can be drawn:

- The mean wind direction varies along the Hardanger Bridge span indicating terrain-induced effects on the mean wind direction. Caution should be taken when using wind directions measured at a single point as a basis for inflow directions for wind tunnel terrain model tests.
- The easterly wind field was composed of incoming flows from two different fjord arms due to terrain channeling effects.
- Extreme value statistics were used to compare wind speeds between nonsimultaneous measurement campaigns. Local wind speed-up effects measured at the mast location were successfully predicted using the calculation guidelines defined in the European design code for wind actions, despite the limitations of this code regarding complex terrain. The terrain model wind tunnel tests also successfully predicted the speed-up effect for the easterly wind direction but underpredicted the speed-up effect for the westerly winds.
- Turbulence intensity levels measured at the mast were larger than those measured along the bridge span. The larger turbulence intensity measured at the mast can be explained as a combination of flow separation over the hill and local vegetation at the mast location, imposing higher surface roughness. The design guidelines would fail to predict such an effect resulting in an underestimation of the turbulence intensity.
- The probability distribution of the turbulence intensity followed a lognormal probability density function for the mast and for all the along-span anemometers.
- The wind field along the Hardanger Bridge girder displayed spanwise nonuniform behavior for both the mean wind velocity and along-wind turbulence intensity. The turbulence intensities varied up to 100% and the mean wind velocities varied up to 50% along the span.
- The terrain model wind tunnel experiments were unable to adequately predict the spanwise wind profiles for the easterly wind direction, but better agreement was found for the modeled westerly wind directions. This indicates the importance of modeling an appropriately large terrain area and investigating different incoming wind directions.
- In situ mast measurements and terrain model wind tunnel tests as the source of wind field information for design purposes can be a satisfactory method under the following conditions:
  - o Special attention should be given to the position of the mast
  - o The scale and size of the model need to be large enough to allow the testing of several incoming wind directions.
- Single-point mast measurements should be complemented by additional masts, terrain model tests or LIDARs to more accurately capture the spatial transfer.

Funding

The research presented in this paper has been financed by the Norwegian Public Roads Administration (NPRA), the Norwegian Research Council [263389/O30] and Norconsult AS.

Acknowledgments

The authors also thank the NPRA for providing the mast measurement results used in this study.

References

Arena, A., Lacarbonara, W., Valentine, D.T., Marzocca, P., 2014. Aeroelastic behavior of long-span suspension bridges under arbitrary wind profiles. J. Fluid Struct. 50, 105–119. https://doi.org/10.1016/j.jfluidstructs.2014.06.018.

Balakrishnan, N., Chan, P.S., 1992. Order statistics from extreme value distribution, ii: best linear unbiased estimates and some other uses. Commun. Stat. Simulat. Comput. 21, 1219–1246.

Bietry, J., Delaunay, D., Conti, E., 1995. Comparison of full-scale measurement and computation of wind effects on a cable-stayed bridge. J. Wind Eng. Ind. Aerod. 57, 225–235. https://doi.org/10.1016/0167-6105(94)00110-Y.

Bocciolone, M., Cheli, F., Curami, A., Zasso, A., 1992. Wind measurements on the humber bridge and numerical simulations. J. Wind Eng. Ind. Aerod. 42, 1393–1404. https://doi.org/10.1016/0167-6105(92)90147-3.

Bowen, A.J., 2003. Modelling of strong wind flows over complex terrain at small geometric scales. J. Wind Eng. Ind. Aerod. 91, 1859–1871. https://doi.org/10.1016/j.jweia.2003.09.029.

Brownjohn, J.M.W., Bocciolone, M., Curami, A., Falco, M., Zasso, A., 1994. Humber bridge full-scale measurement campaigns 1990–1991. J. Wind Eng. Ind. Aerod. 52, 185–218. https://doi.org/10.1016/0167-6105(94)90047-7.

Burlando, M., De Gaetano, P., Pizzo, M., Repetto, M.P., Solari, G., Tizzi, M., 2013. Wind climate analysis in complex terrains. J. Wind Eng. Ind. Aerod. 123, 349–362. https://doi.org/10.1016/j.jweia.2013.09.016.

Cao, S., Tamura, Y., Kikuchi, N., Saito, M., Nakayama, I., Matsuzaki, Y., 2009. Wind characteristics of a strong typhoon. J. Wind Eng. Ind. Aerod. 97, 11–21. https://doi.org/10.1016/J.JWEIA.2008.10.002.

Carpenter, P., Locke, N., 1999. Investigation of wind speeds over multiple two-dimensional hills. J. Wind Eng. Ind. Aerod. 83, 109–120. https://doi.org/10.1016/S0167-6105(99)00065-3.

Cheynet, E., Bogunovic Jakobsen, J., Snæbjörnsson, J., 2016. Buffeting response of a suspension bridge in complex terrain. Eng. Struct. 128, 474–487. https://doi.org/10.1016/J.ENGSTRUCT.2016.09.060.

Choi, E.C.C., 1978. Characteristics of typhoons over the south China sea. J. Wind Eng. Ind. Aerod. 3, 353–365. https://doi.org/10.1016/0167-6105(78)90038-7.

Ciampoli, M., Petrini, F., Augusti, G., 2011. Performance-based wind engineering: towards a general procedure. Struct. Saf. 33, 367–378. https://doi.org/10.1016/J.STRUSAFE.2011.07.001.

Cook, N.J., 1982. Towards better estimation of extreme winds. J. Wind Eng. Ind. Aerod. 9, 295–323.

Cook, N.J., Harris, R.I., 2008. Postscript to "Exact and general FT1 penultimate distributions of extreme wind speeds drawn from tail-equivalent Weibull parents. Struct. Saf. 30, 1–10. https://doi.org/10.1016/J.STRUSAFE.2006.04.001.

Cook, N.J., Harris, R.I., 2004. Exact and general FT1 penultimate distributions of extreme wind speeds drawn from tail-equivalent Weibull parents. Struct. Saf. 26, 391–420. https://doi.org/10.1016/J.STRUSAFE.2004.01.002.

Cross, E.J., Koo, K.Y., Brownjohn, J.M., Worden, K., 2013. Long-term monitoring and data analysis of the Tamar Bridge. Mech. Syst. Signal Process. 35, 16–34. https://doi.org/10.1016/J.YMSSP.2012.08.026.

Davenport, A.G., 1983. The relationship of reliability to wind loading. J. Wind Eng. Ind. Aerod. 13, 3–27. https://doi.org/10.1016/0167-6105(83)90125-3.

Davenport, A.G., 1962. Buffeting of a suspension bridge by storm winds. J. Struct. Div. 88, 233–270.

Fenerci, A., Øiseth, O., 2018. Strong wind characteristics and dynamic response of a long-span suspension bridge during a storm. J. Wind Eng. Ind. Aerod. 172, 116–138. https://doi.org/10.1016/j.jweia.2017.10.030.

Fenerci, A., Øiseth, O., 2017. Measured buffeting response of a long-span suspension bridge compared with numerical predictions based on design wind spectra. J. Struct. Eng. 143 https://doi.org/10.1061/(ASCE)ST.1943-541X.0001873.

Fenerci, A., Øiseth, O., Rönnquist, A., 2017. Long-term monitoring of wind field characteristics and dynamic response of a long-span suspension bridge in complex terrain. Eng. Struct. 147, 269–284. https://doi.org/10.1016/j.engstruct.2017.05.070.

Gumbel, E.J., 1958. Statistics of Extremes. Columbia University Press, New York.

Harris, R.I., 2009. XIMIS, a penultimate extreme value method suitable for all types of wind climate. J. Wind Eng. Ind. Aerod. 97, 271–286. https://doi.org/10.1016/J.JWEIA.2009.06.011.

Harris, R.I., 1999. Improvements to the `Method of independent storms. J. Wind Eng. Ind. Aerod. 80, 1–30. https://doi.org/10.1016/S0167-6105(98)00123-8.

Harris, R.I., 1996. Gumbel re-visited - a new look at extreme value statistics applied to wind speeds. J. Wind Eng. Ind. Aerod. 59, 1–22. https://doi.org/10.1016/0167-6105(95)00029-1.

Harstveit, K., 1996. Full scale measurements of gust factors and turbulence intensity, and their relations in hilly terrain. J. Wind Eng. Ind. Aerod. 61, 195–205. https://doi.org/10.1016/0167-6105(96)00047-5.

Harstveit, K., 1994. Hardangerbrua - Sluttrapport for Vindmålinger 32/93 KLIMA.

Hu, L., Xu, Y.-L., Huang, W.-F., 2013. Typhoon-induced non-stationary buffeting response of long-span bridges in complex terrain. Eng. Struct. 57, 406–415. https://doi.org/10.1016/J.ENGSTRUCT.2013.09.044.

Hu, L., Xu, Y., Zhu, Q., Guo, A., Kareem, A., 2017. Tropical storm – induced buffeting response of long-span Bridges : enhanced nonstationary buffeting force model. J. Struct. Eng. 143, 4017027. https://doi.org/10.1061/(ASCE)ST.1943-541X.0001745.

Hui, M.C.H., Larsen, A., Xiang, H.F., 2009a. Wind turbulence characteristics study at the Stonecutters Bridge site: Part II: wind power spectra, integral length scales and coherences. J. Wind Eng. Ind. Aerod. 97, 48–59. https://doi.org/10.1016/j.jweia.2008.11.003.

Hui, M.C.H., Larsen, A., Xiang, H.F., 2009b. Wind turbulence characteristics study at the Stonecutters Bridge site: Part I-Mean wind and turbulence intensities. J. Wind Eng. Ind. Aerod. 97, 22–36. https://doi.org/10.1016/j.jweia.2008.11.002.

Ian Harris, R., 2014. A simulation method for the macro-meteorological wind speed and the implications for extreme value analysis. J. Wind Eng. Ind. Aerod. 125, 146–155. https://doi.org/10.1016/J.JWEIA.2013.12.003.

Kareem, A., 1988. Aerodynamic response of structures with parametric uncertainties. Struct. Saf. 5, 205–225. https://doi.org/10.1016/0167-4730(88)90010-0.

Li, C.G., Chen, Z.Q., Zhang, Z.T., Cheung, J.C.K., 2010. Wind tunnel modeling of flow over mountainous valley terrain. Wind Struct. An Int. J. 13, 275–292. https://doi.org/10.12989/was.2010.13.3.275.

Li, L., Kareem, A., Xiao, Y., Song, L., Zhou, C., 2015. A comparative study of field measurements of the turbulence characteristics of typhoon and hurricane winds. J. Wind Eng. Ind. Aerod. 140, 49–66. https://doi.org/10.1016/J.JWEIA.2014.12.008.

Li, Y., Hu, P., Xu, X., Qiu, J., 2016. Wind characteristics at bridge site in a deep-cutting gorge by wind tunnel test. Jnl. Wind Eng. Ind. Aerodyn 160, 30–46. https://doi.org/10.1016/j.jweia.2016.11.002.

Lieblein, J., 1974. Efficient Methods of Extreme-value Methodology. Washington D. C.

Lystad, T.M., Fenerci, A., Sætran, L., Øiseth, O., 2017. Wind field characteristics at the Hardanger Bridge site: comparison of wind tunnel terrain mode tests with full-scale measurements. In: European-african Conference on Wind Engineering.

Macdonald, J.H.G., 2003. Evaluation of buffeting predictions of a cable-stayed bridge from full-scale measurements. J. Wind Eng. Ind. Aerod. 91, 1465–1483. https://doi.org/10.1016/J.JWEIA.2003.09.009.

Meroney, R.N., 1980. Wind-tunnel simulation of the flow over hills and complex terrain. J. Wind Eng. Ind. Aerod. 5, 297–321. https://doi.org/10.1016/0167-6105(80)90039-2.

Miller, C.A., Davenport, A.G., 1998. Guidelines for the calculation of wind speed-ups in complex terrain. J. Wind Eng. Ind. Aerod. 74–76, 189–197. https://doi.org/10.1016/S0167-6105(98)00016-6.

Miyata, T., Yamada, H., Katsuchi, H., Kitagawa, M., 2002. Full-scale measurement of Akashi–Kaikyo bridge during typhoon. J. Wind Eng. Ind. Aerod. 90, 1517–1527. https://doi.org/10.1016/S0167-6105(02)00267-2.

Pagnini, L., 2010. Reliability analysis of wind-excited structures. J. Wind Eng. Ind. Aerod. 98, 1–9. https://doi.org/10.1016/J.JWEIA.2009.08.010.

Pagnini, L.C., Solari, G., 2002. Gust buffeting and turbulence uncertainties. J. Wind Eng. Ind. Aerod. 90, 441–459. https://doi.org/10.1016/S0167-6105(01)00202-1.

Scanlan, R.H., 1978a. The action of flexible bridges under wind, I: flutter theory. J. Sound Vib. 60, 187–199. https://doi.org/10.1016/S0022-460X(78)80028-5.

Scanlan, R.H., 1978b. The action of flexible bridges under wind, II: buffeting theory. J. Sound Vib. 60, 201–211. https://doi.org/10.1016/S0022-460X(78)80029-7.

Scanlan, R.H., Tomko, J.J., 1971. Airfoil and bridge deck flutter derivatives. J. Eng. Mech. Div. 97, 1717–1737.

Solari, G., 1997. Wind-excited response of structures with uncertain parameters. Probabilist. Eng. Mech. 12, 75–87. https://doi.org/10.1016/S0266-8920(96)00027-6.

Spence, S.M.J., Kareem, A., 2014. Performance-based design and optimization of uncertain wind-excited dynamic building systems. Eng. Struct. 78, 133–144. https://doi.org/10.1016/J.ENGSTRUCT.2014.07.026.

Standard Norge, 2009. Eurocode 1: actions on structures - Part 1-4: general actions. Wind Actions.

Stevenson, D.C., Lindley, D., Neal, D., Zealand, N., House, T., Kingdom, U., 1981. A Wind Tunnel Boundary-Layer Simulation of Wind Flow Over Complex Terrain: Effect of Terrain and Model Construction, 21, pp. 271–293.

Sætran, L.R., Malvik, I.M., 1991. Hardangerbrua - Vindteknisk Undersøkelse Av Terrengmodell I Vindtunnel.

Tamura, Y., Kareem, A., 2013. Advanced Structural Wind Engineering. Springer, Japan.

Torrielli, A., Repetto, M.P., Solari, G., 2013. Extreme wind speeds from long-term synthetic records. J. Wind Eng. Ind. Aerod. 115, 22–38. https://doi.org/10.1016/J.JWEIA.2012.12.008.

Wang, H., Hu, R., Xie, J., Tong, T., Li, A., 2013. Comparative study on buffeting performance of Sutong Bridge based on design and measured spectrum. J. Bridge Eng. 18, 587–600. https://doi.org/10.1061/(ASCE)BE.1943-5592.0000394.

Wang, H., Li, A., Guo, T., Xie, J., 2009. Field measurement on wind characteristic and buffeting response of the Runyang Suspension Bridge during typhoon Matsa. Sci. China, Ser. E Technol. Sci. 52, 1354–1362. https://doi.org/10.1007/s11431-008-0238-y.

Wang, H., Li, A., Hu, R., 2011. Comparison of Ambient vibration response of the runyang suspension bridge under skew winds with time-domain numerical predictions. J. Bridge Eng. 16, 513. https://doi.org/10.1061/(ASCE)BE.1943-5592.0000168.

Wang, X., Chen, B., Sun, D., Wu, Y., 2014. Study on typhoon characteristic based on bridge health monitoring system. Sci. World J. 2014 https://doi.org/10.1155/2014/204675.

Wang, X., Huang, P., Yu, X.-F., Wang, X.-R., Liu, H.-M., 2017. Wind characteristics near the ground during typhoon Meari. J. Zhejiang Univ. - Sci. 18, 33–48. https://doi.org/10.1631/jzus.A1500310.

Xu, Y.-L., 2013. Wind Effects on cable-supported Bridges. Wiley, Hong Kong.

Xu, Y., Øiseth, O., Naess, A., Moan, T., 2017. Prediction of long-term extreme load effects due to wind for cable-supported bridges using time-domain simulations. Eng. Struct. 148, 239–253. https://doi.org/10.1016/J.ENGSTRUCT.2017.06.051.

Zhang, L., Li, J., Peng, Y., 2008. Dynamic response and reliability analysis of tall buildings subject to wind loading. J. Wind Eng. Ind. Aerod. 96, 25–40. https://doi.org/10.1016/J.JWEIA.2007.03.001.

Zhang, X., 2007. Influence of some factors on the aerodynamic behavior of long-span suspension bridges. J. Wind Eng. Ind. Aerod. 95, 149–164. https://doi.org/10.1016/J.JWEIA.2006.08.003.

Paper II

Tor Martin Lystad, Aksel Fenerci and Ole Øiseth

Aerodynamic Effect of Non-uniform Wind Profiles for Long-Span Bridges

Proceedings of the XV Conference of the Italian Association for Wind Engineering. IN VENTO 2018. Lecture Notes in Civil Engineering 2019:27

Aerodynamic Effect of Non-uniform Wind Profiles for Long-Span Bridges

T. M. Lystad[1,2](✉), A. Fenerci[2], and O. Øiseth[2]

[1] Bridge Department, Norconsult AS, 1338 Sandvika, Norway
tor.martin.lystad@norconsult.com
[2] Department of Structural Engineering,
Norwegian University of Science and Technology, 7034 Trondheim, Norway

Abstract. Long-span bridges are often designed based on the assumption of wind field homogeneity. At the Hardanger Bridge, the wind field along the bridge span is monitored though 8 triaxial ultrasonic anemometers. Simultaneously recorded profiles for mean wind velocity and turbulence intensity along the span are used to investigate the effect of non-uniform wind profiles on the aerodynamic behaviour of the Hardanger Bridge. Extreme non-uniformity is considered using Monte Carlo simulations to generate extreme, but realistic wind profiles based on the variability of the measured wind field. When the buffeting response of the Hardanger Bridge is considered, significant effects on the behaviour is found.

Keywords: Long-span bridge · Non-uniform wind field · Field measurements · Complex terrain

1 Introduction

Long-span bridges located in complex terrain can be subjected to large wind field variations along the bridge span, as shown in (Lystad et al. 2018). Long-span bridges are often designed under the assumption of wind field homogeneity, however this assumption may not be valid for bridges located in complex terrain, such as the mountainous landscape along the west coast of Norway.

Since 2013, the Norwegian University of Science and Technology has been monitoring the wind field along the Hardanger Bridge girder through 8 triaxial ultrasonic anemometers. The Hardanger Bridge is a suspension bridge with a main span of 1 310 m, located in complex terrain. The measured wind field display large non-uniformity along the bridge span.

The effect of idealized non-uniform mean wind velocity profiles on the buffeting response and the aerodynamic stability of long-span bridges has been studied by (Arena et al. 2014; Zhang 2007), showing possible significant effects on the aerodynamic behavior. A non-uniform mean wind velocity profile measured from terrain model wind tunnel tests of the Stonecutters Bridge surroundings was also investigated in (Hu et al. 2017), without any significant impacts to the bridge behavior. However, to the authors knowledge, investigations of the effect of extreme, but realistic non-uniform wind profiles based on full-scale measurements has not been treated in the literature.

F. Ricciardelli and A. M. Avossa (Eds.): INVENTO 2018, LNCE 27, pp. 427–439, 2019.
https://doi.org/10.1007/978-3-030-12815-9_34

In this paper, non-uniform profiles of mean wind velocity and turbulence intensity measured in full-scale at the Hardanger Bridge site are investigated. A measure of the variability of the recorded non-uniformity is obtained by fitting the measured wind profiles to chosen shape functions using linear regression. Profiles of mean wind velocity and corresponding turbulence intensity are generated through Monte Carlo simulations from the joint probability distribution of the fitted shape function coefficients. Finally, the effect of some simulated extreme non-uniform wind profiles on the buffeting response of the Hardanger Bridge are shown.

2 Full-Scale Measurement Program

The Hardanger Bridge is a suspension bridge with a main span of 1 310 m, located along the west coast of Norway. The bridge is crossing the Hardanger fjord surrounded by tall and steep mountains, forming a very complex topography.

Since the opening of the bridge in 2013, a monitoring system has been recording the wind field along the bridge span as well as in the southern tower top. Also, acceleration response of the girder and towers has been recorded. An overview of the wind measurement system is given in Fig. 1 and the system is described in more detail in (Fenerci et al. 2017).

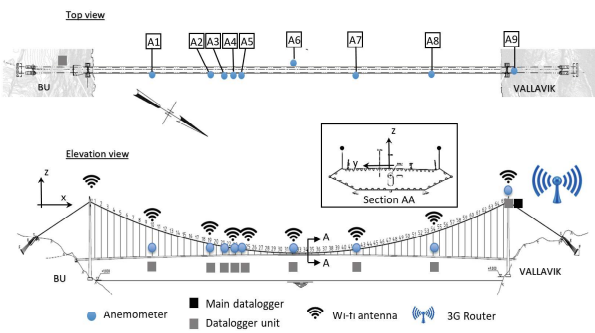

Fig. 1. Overview of the full-scale wind measurement system at the Hardanger Bridge

The Hardanger fjord is creating strong orographic channelling effects on the wind field subjected to the bridge structure, generating two very distinct incoming wind directions from the east and west. This behaviour can be observed in Fig. 2, where the midspan wind rose for strong winds with mean wind velocities above 15 m/s is shown. The wind rose shown in Fig. 2 is plotted on top of a map showing the surrounding topography, and it should be noted that the surrounding mountains reach up to above 1000 m. For a more thorough description of the surrounding topography, the reader is referred to (Fenerci et al. 2017; Fenerci and Øiseth 2017; Lystad et al. 2018).

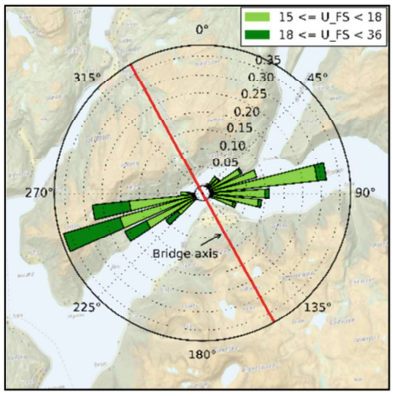

Fig. 2. Mean wind velocity rose for strong winds above 15 m/s, measured in the midspan. The wind rose is divided into two main wind directions, east and west, with each side adding up to 100% (base map with courtesy of Kartverket©)

3 Non-uniform Wind Profiles

3.1 Measurements

Along-span wind profiles for mean wind velocity and along-wind turbulence intensity for strong winds recorded at the Hardanger Bridge are shown in Fig. 3. Only measurements with a midspan 10-min time-averaged mean wind velocity above 15 m/s are considered, and extreme non-uniform measured profiles are highlighted.

By observing the general shape of the measured profiles, it is seen that the profiles may be described quite well by the combination of a linear variation and a cosine function. The following wind profile model is proposed:

$$U(x) = U_0 + a_1 x - a_2[1 - \cos(\frac{\pi}{L}x)] = U_0\{1 + \hat{a}_1 x - \hat{a}_2[1 - \cos(\frac{\pi}{L}x)]\} \quad (1)$$

$$I(x) = I_0 + b_1 x - b_2[1 - \cos(\frac{\pi}{L}x)] = I_0\{1 + \hat{b}_1 x - \hat{b}_2[1 - \cos(\frac{\pi}{L}x)]\} \quad (2)$$

where the a_1 and b_1 coefficients describe the linear variation and the a_2 and b_2 coefficients scale the cosine shape function. Another model for the non-uniformity of the mean wind velocity was shown in (Zhang 2007), but this model is deemed less suitable for the methodology described in the present study.

In the present study, only the non-uniformity in mean wind velocity and turbulence intensity is investigated. However, it should be noted that non-uniformity in other parameters, such as integral length scale, decay coefficients and yaw-angle may also be of importance. In (Lystad et al. 2018) it is shown how the yaw-angle is varying along the bridge span causing different upstream situations for the different parts of the span.

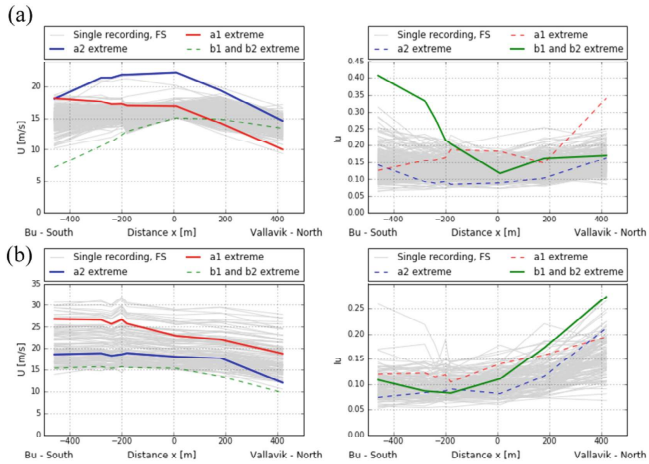

Fig. 3. Measured wind profiles and highlighted extreme non-uniformity, (a) The wind recordings of easterly winds, (b) recordings of westerly winds.

For comparison of the non-uniformity effect it is interesting to consider wind profiles with the same along span mean value. To achieve this the midspan value of the wind profile, U_0 and I_0, and thus the normalized non-uniformity coefficients $\hat{a}_i$ and $\hat{b}_i$ are scaled based on Eqs. (3) and (4), demanding the same along span mean values, U_{eq} and I_{eq} for all profiles.

$$U_{eq} = \frac{1}{L}\int_{-L/2}^{L/2} U(x)dx = U_0[1 - \hat{a}_2 + \frac{2}{\pi}\hat{a}_2] \tag{3}$$

$$I_{eq} = \frac{1}{L}\int_{-L/2}^{L/2} I(x)dx = I_0[1 - \hat{b}_2 + \frac{2}{\pi}\hat{b}_2] \tag{4}$$

Using linear regression, the non-uniform wind profile models described in Eqs. (1)–(4) are fitted to all measured wind profiles shown in Fig. 3. By doing so, the distribution of the normalized fitted coefficients, $\hat{a}_i$ and $\hat{b}_i$, can be obtained and a probability distribution can be adopted. The mean wind velocity profiles and the corresponding along-wind turbulence intensity profiles are used, so the joint probability density function (PDF) of all the normalized coefficients, $\hat{a}_1$, $\hat{a}_2$, $\hat{b}_1$ and $\hat{b}_2$ can be fitted. A normal distribution is assumed in the present study for the simplicity of describing a joint PDF. The marginal fitted PDF's for the normalized coefficients are shown in Fig. 4.õ

It can be observed from Table 1 that the mean value of the linear variation described by $\hat{a}_1$ and $\hat{b}_1$ is larger for the westerly winds than the easterly winds,

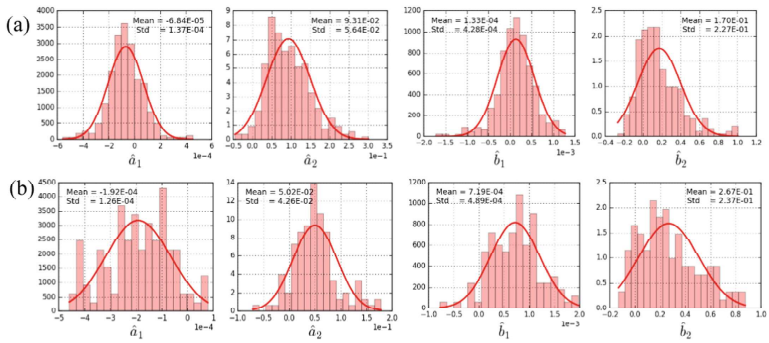

Fig. 4. Marginal PDF's for the normalized coefficients, (a) easterly winds, (b) westerly winds

confirming the qualitative observation made from Fig. 3. However, considering the cosine shape function coefficients $\hat{a}_2$ and $\hat{b}_2$ the easterly winds are displaying the largest mean value for the normalized non-uniformity coefficient for the mean wind velocity profiles, but the westerly winds are showing generally larger non-uniformity in the turbulence intensity profile.

Table 1. Key statistics for the fitted normalized non-uniformity coefficients

	Easterly winds		Westerly winds	
Coeff	Mean	Std	Mean	Std
$\hat{a}_1$	−6.84E−05	1.37E−04	−1.92E−04	1.26E−04
$\hat{a}_2$	9.31E−02	5.64E−02	5.02E−02	4.26E−02
$\hat{b}_1$	1.33E−04	4.28E−04	7.19E−04	4.89E−04
$\hat{b}_2$	−1.70E−01	2.27E−01	−2.67E−01	2.37E−01

Table 2. Correlation coefficients for the normalized non-uniformity coefficients for easterly winds

Coeff	$\hat{a}_1$	$\hat{a}_2$	$\hat{b}_1$	$\hat{b}_2$
$\hat{a}_1$	1.000	0.136	−0.784	−0.151
$\hat{a}_2$	0.136	1.000	−0.208	−0.704
$\hat{b}_1$	−0.784	−0.208	1.000	0.111
$\hat{b}_2$	−0.151	−0.704	0.111	1.000

A high correlation between $\hat{a}_i$ and $\hat{b}_i$ in mean wind velocity and turbulence intensity can be expected, as the turbulence intensity is, by definition, inversely proportional to the mean wind velocity. By studying Table 2 this expected effect is observed as the

Table 3. Correlation coefficients for the normalized non-uniformity coefficients for westerly winds

Coeff	$\hat{a}_1$	$\hat{a}_2$	$\hat{b}_1$	$\hat{b}_2$
$\hat{a}_1$	1.000	−0.390	−0.504	0.215
$\hat{a}_2$	−0.390	1.000	0.465	−0.502
$\hat{b}_1$	−0.504	0.465	1.000	−0.657
$\hat{b}_2$	0.215	−0.502	−0.657	1.000

correlation between $\hat{a}_1$ and $\hat{b}_1$, and $\hat{a}_2$ and $\hat{b}_2$ is in the range of 70–80%. However, by studying the westerly winds in Fig. 4(b) and Table 3 a larger randomness is observed in the normalized non-uniformity coefficients as well as in the correlation between them.

3.2 Simulations

Based on the fitted joint PDF of the normalized non-uniformity coefficients, Monte Carlo simulations can be applied to generate a large number of non-uniform wind profiles. The simulations are based on a chosen equivalent mean wind velocity of 40 m/s and an equivalent along-wind turbulence intensity of 15%. The fitted coefficients are generally based on lower measured wind speeds than the chosen equivalent mean wind velocity, but utilizing the normalized format of the non-uniformity coefficients it is interesting to investigate the effects of the observed non-uniformity at design wind speed levels. Extreme, but realistic, simulated profiles may be picked based on a chosen criterion. In this study the simulations are sorted in ascending order based on the absolute value of the normalized non-uniformity profiles, $\hat{a}_i$ and $\hat{b}_i$. To obtain an extreme non-uniform situation from the simulated profiles the nearest-rank method may be applied to the sorted lists of simulations for each normalized non-uniformity coefficient. Let, N, be the number of simulations and, n, be the simulation number in the sorted list, the simulated profile with a chosen percentile may be calculated as

$$n = \left\lceil \frac{P}{100} N \right\rceil \tag{5}$$

In Fig. 5, $N = 1000$ simulated profiles for each main wind direction, westerly and easterly winds, are shown. Extreme profiles picked according to the criterion described above are indicated as highlighted solid lines. The simulated wind profile of the other variable corresponding to the ranked variable extreme profile are dotted in the same colour in the figure. The normalized non-uniformity coefficients for the picked extreme profiles are shown in Table 4. Significant non-uniformity in the extreme simulated wind profiles both for mean wind velocity and along-wind turbulence intensity can be observed.

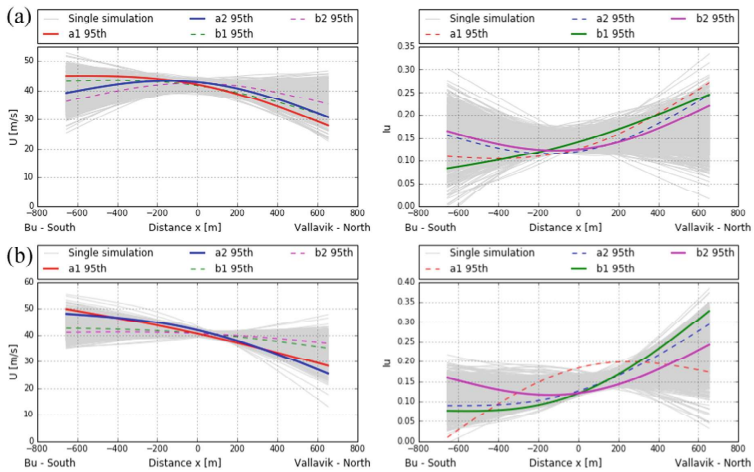

Fig. 5. Monte Carlo simulated wind profiles for, (a) easterly winds and, (b) westerly winds. Extreme simulations are highlighted along with the simulation of the corresponding variable (dotted).

Table 4. Model coefficients for the highlighted extreme non-uniformity profiles

Wind dir	Extreme type	U_O	$\hat{a}_1$	$\hat{a}_2$	I_O	$\hat{b}_1$	$\hat{b}_2$
East	$\hat{a}_{1,95th}$	42.02	−3.10E−04	1.32E−01	0.13	9.72E−04	−4.94E−01
	$\boldsymbol{\hat{a}_{2,95th}}$	**42.87**	**−1.50E−04**	**1.84E−01**	**0.12**	**5.48E−04**	**−6.51E−01**
	$\hat{b}_{1,95th}$	41.69	−2.28E−04	1.12E−01	0.14	8.75E−04	−1.58E−01
	$\hat{b}_{2,95th}$	42.49	−1.64E−05	1.61E−01	0.13	3.35E−04	−5.31E−01
West	$\hat{a}_{1,95th}$	40.53	−4.04E−04	3.61E−02	0.18	6.82E−04	5.01E−01
	$\hat{a}_{2,95th}$	41.85	−4.12E−04	1.22E−01	0.13	1.23E−03	−5.18E−01
	$\boldsymbol{\hat{b}_{1,95th}}$	**40.69**	**−1.41E−04**	**4.69E−02**	**0.12**	**1.59E−03**	**−6.83E−01**
	$\hat{b}_{2,95th}$	40.60	−7.74E−05	4.04E−02	0.12	5.25E−04	−6.61E−01

It should be noted that the described criterion is not a statistically complete procedure to identify a situation corresponding to an extreme load event, but it can provide valuable information for illustration purposes.

4 Case Study: The Hardanger Bridge

4.1 Theoretical Background

The effect of the simulated extreme non-uniform wind profiles on the dynamic response of The Hardanger Bridge is investigated. The Hardanger Bridge is a symmetrical suspension bridge with a main span of 1 310 m and no side spans.

The response calculations are performed in the frequency domain using the multimode theory described in (Chen et al. 2001; Jain et al. 1996a, b). The equation of motion of the dynamic system can be described in the frequency domain as

$$\begin{aligned}&\tilde{\mathbf{M}}_S\mathbf{G}_{\ddot{\eta}}(\omega)+[\tilde{\mathbf{C}}_S-\tilde{\mathbf{C}}_{ae}(U,\omega)]\mathbf{G}_{\dot{\eta}}(\omega)\\&+[\tilde{\mathbf{K}}_S-\tilde{\mathbf{K}}_{ae}(U,\omega)]\mathbf{G}_{\eta}(\omega)=\mathbf{G}_{\hat{\mathbf{Q}}_{load}}(U,\omega)\end{aligned} \tag{6}$$

where ω is the angular frequency, $\tilde{\mathbf{M}}_S$, $\tilde{\mathbf{C}}_S$ and $\tilde{\mathbf{K}}_S$, are the structural mass-, damping - and stiffness matrices, respectively, in modal coordinates. $\tilde{\mathbf{C}}_{ae}$ and $\tilde{\mathbf{K}}_{ae}$, are the aeroelastic damping and stiffness matrices respectively, representing the motion induced forces. $\mathbf{G}_{\eta}$, $\mathbf{G}_{\dot{\eta}}$, $\mathbf{G}_{\ddot{\eta}}$ and $\mathbf{G}_{\mathbf{Q}_{load}}$ are the Fourier transforms of the displacement-, velocity-, acceleration response and the load process, respectively. In practice, the structural part of the equation has been calculated based on the finite element method, with ABAQUS (Dassault Systèmes, Waltham n.d.), and the aeroelastic motion induced forces are described based on wind tunnel experiments (Siedziako et al. 2017).

The wind field is described as a stationary stochastic process through the cross-spectral density matrix

$$\mathbf{S}_V(\Delta x,U,\omega)=\begin{bmatrix}S_{uu}(\Delta x,U,\omega) & S_{uw}(\Delta x,U,\omega)\\ S_{uw}(\Delta x,U,\omega) & S_{ww}(\Delta x,U,\omega)\end{bmatrix} \tag{7}$$

where S_{nm} are the cross spectral densities for the n and m components of the turbulence between two points separated in space by the distance Δx. In the current study, the off-diagonal terms of the cross-spectral density matrix are assumed to be negligible. The cross-spectral density for a single turbulence component can be described through the auto-spectral density function and the normalized co-spectra:

$$S_{nn}(\Delta x,U,\omega)=S_n(U,I_n,\omega)C_n(\Delta x,U,\omega) \tag{8}$$

$$C_n(\Delta x,\omega)=\exp(-K_n\frac{\omega\Delta x}{2\pi U}) \tag{9}$$

where S_n is the auto-spectral density function, C_n is the normalized co-spectra, and K_n is the decay coefficient. Having established the cross-spectral density matrix for the wind field process, the spectral matrix of the buffeting force on the structure in modal coordinates can be defined as

$$\mathbf{S}_{\tilde{\mathbf{Q}}_{load}} = \iint_L \Phi^T(x_1)\mathbf{B}_q(U,\omega)\mathbf{S}_V(\Delta x,\omega)\mathbf{B}_q^H(U,\omega)\Phi(x_2)dx_1dx_2 \tag{10}$$

where $\Phi(x_i)$ is the mode shape matrix and $\mathbf{B}_q$ is the load transfer matrix for the buffeting load on the structure. The load spectral density matrix is calculated by considering two points at a time, x_1 and x_2. Having a non-uniform wind field, the mean wind velocity and turbulence intensity will differ at the two points considered, so an adjustment to the original buffeting theory first described by (Davenport 1962; Scanlan and Tomko 1971) has to be made. In the present study, a simple adjustment is done by defining the cross-spectral density for the considered turbulence component as the product of the square root of the auto-spectral density in each point and a normalized co-spectra based on the average of the mean wind velocity from the two points considered. Hence, the following adjustment can be made to Eq. (8):

$$\begin{aligned} &S_{nn}[\Delta x, U(x_1), U(x_2), \omega] = \\ &\sqrt{S_n[U(x_1), I_n(x_1), \omega]}\sqrt{S_n[U(x_2), I_n(x_2), \omega]}C_n(\Delta x, U_{avrg}, \omega) \end{aligned} \tag{11}$$

where $U_{avrg} = [U(x_1) + U(x_2)]/2$.

The buffeting load transfer matrix is also a function of the mean wind velocity, and to account for the non-uniformity of the buffeting matrix corresponding to each of the points considered in Eq. (10), it is adjusted using the actual mean wind velocity in that point. Thus, the cross-spectral density matrix for the buffeting force on the structure can be redefined as

$$\mathbf{S}_{\tilde{\mathbf{Q}}_{load}} = \iint_L \begin{aligned} &\{\Phi^T(x_1)\mathbf{B}_q[U(x_1),\omega]\mathbf{S}_V[\Delta x, U(x_1), U(x_2), \omega] \\ &\mathbf{B}_q^H[U(x_2),\omega]\Phi(x_2)\}dx_1dx_2 \end{aligned} \tag{12}$$

The motion induced forces are integrated using the full non-uniform mean wind velocity profile as follows:

$$\tilde{\mathbf{K}}_{ae}(U(x),\omega) = \int_L \Phi^T(x)\mathbf{K}_{ae}(U(x),\omega)\Phi(x)dx \tag{13}$$

$$\tilde{\mathbf{C}}_{ae}(U(x),\omega) = \int_L \Phi^T(x)\mathbf{C}_{ae}(U(x),\omega)\Phi(x)dx \tag{14}$$

where $\mathbf{K}_{ae}$, and $\mathbf{C}_{ae}$ are described by the dimensionless aerodynamic derivatives.

4.2 Modal Analysis

Contributions from the 90 first still air modes was included in the modal analysis, resulting in a cut off frequency of 1.6 Hz. In Fig. 6 the two first lateral, vertical and torsional vibration mode shapes are shown, and in Table 5 the first 15 modes are summarized.

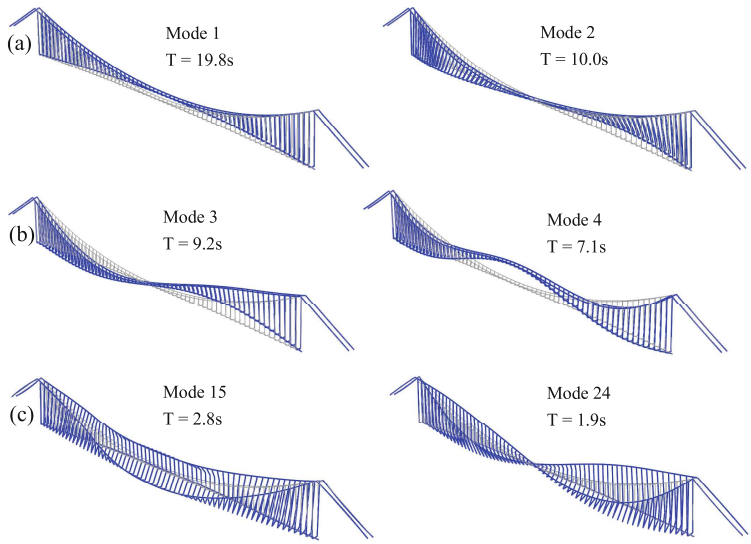

Fig. 6. Mode shapes of the Hardanger Bridge, (a) Two first lateral vibrations modes, (b) Two first vertical vibration modes, (c) Two first torsional vibration modes

Table 5. The frequency, period and shape of the first 15 modes of the Hardanger Bridge

Mode	Frequency	Period	Shape description
1	0.051	19.77	Lateral sym.
2	0.100	10.00	Lateral asym.
3	0.109	9.18	Vertical asym.
4	0.141	7.08	Vertical sym.
5	0.174	5.75	Lateral sym.
6	0.200	4.99	Vertical sym.
7	0.211	4.74	Vertical asym.
8	0.222	4.51	Cabel vibration
9	0.230	4.34	Cabel vibration
10	0.235	4.26	Cabel vibration
11	0.245	4.08	Cabel vibration
12	0.273	3.66	Vertical sym.
13	0.302	3.31	Lateral asym.
14	0.329	3.04	Vertical asym.
15	0.356	2.81	Torsional sym.

4.3 Buffeting Response

Using the methodology described above, the buffeting short-term extreme value for the horizontal, vertical and torsional displacement responses as well as the bending - and torsional cross-sectional moments has been calculated for the Hardanger Bridge girder. The tested extreme non-uniformity profiles are the cosine shaped extreme for the mean wind velocity from the easterly direction and the linearly varying extreme along-wind turbulence intensity profile for the westerly winds, highlighted in Table 4 and shown again in Fig. 7. Only the along-wind turbulence intensity is based on the full-scale measurements in this study, and the vertical component is assumed to be 50% of the along-wind component, adopting the same along span profile shape.

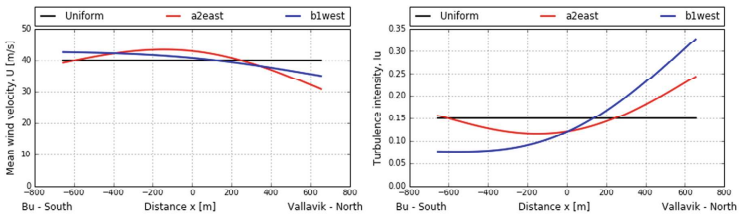

Fig. 7. Extreme non-uniform wind profiles used in buffeting calculations

Significant effects on the response can be observed in Fig. 8, for all response quantities considered. For the *a2east* profile all buffeting response quantities are lower than for the uniform situation. The reason for this is the opposite trends of the mean wind velocity and the turbulence intensity, cancelling each other out when considering buffeting action. A combination like this is natural, since the turbulence intensity is inverse proportional to the mean wind velocity. This observed effect highlights the limitations of the simple sorting criterion used in the present study where only extreme non-uniformity for each variable, either mean wind velocity or turbulence intensity, is sorted, and the corresponding profile has no influence on the sorting criterion. Adopting such an approach would not be suitable to identify the combined extreme non-uniformity situation for the considered bridge response, but merely to identify extreme profiles for the purpose of illustration. Also, different sorting criterions would be appropriate for the consideration of different response processes. For instance, an unfavorable combination of mean wind velocity and turbulence intensity would be critical for the buffeting response, but considering flutter instability the mean wind velocity is the driving process and an extreme mean wind velocity profile should be chosen with less emphasis on the combination with turbulence intensity. Possible sorting criterions for the simulated non-uniformity profiles are not investigated in the present study and could be subject for further work on this topic.

Although a cancelling out effect is observed for the considered *a2east* profiles, the *b1west* simulation show unfavorable conditions for the buffeting response of the Hardanger Bridge. The very high turbulence intensity towards the north end of the bridge is

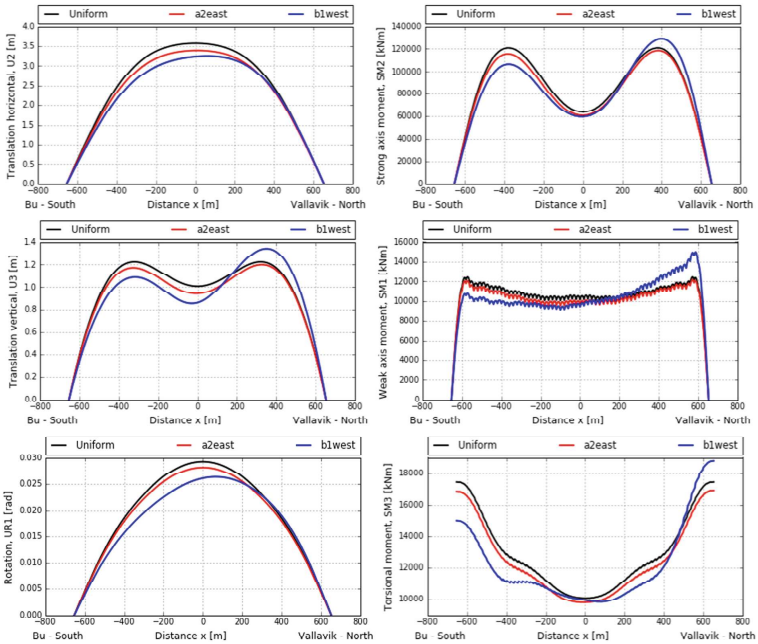

Fig. 8. Along span buffeting response of the Hardanger Bridge subjected to different wind profiles

generating large responses for all sectional moments shown in Fig. 8. Especially the weak axis moment, *SM1*, shows an underestimation of about 25% using the uniformity assumption compared with the simulated extreme non-uniformity profile.

5 Conclusions

A proposed method for investigating extreme non-uniformity effects for long-span bridges has been presented in this study. Measured full-scale wind profiles from the complex terrain of the Hardanger Bridge site are used as basis for simulation of extreme, but realistic non-uniform profiles of mean wind velocity and along-wind turbulence intensity and the following conclusions are drawn:

- The measured wind field profiles for westerly winds show a linearly varying trend. The easterly winds display a more typical effect where mean wind velocity is larger in the midspan than towards the bridge ends, and the opposite is the case for the turbulence intensity, due to terrain roughness changes along the span.

- A larger randomness in the fitted normalized non-uniformity coefficients was observed for the westerly winds than the easterly winds, indicating a dependence between the observed non-uniformity and the upstream terrain complexity.
- In complex terrain, extreme non-uniformity in the wind field can be expected, to the extent that should not be neglected in design of long-span bridges.
- The inverse nature of the mean wind velocity and the corresponding turbulence intensity will to some extent cancel out the non-uniformity effects on the buffeting response. So, to investigate extreme effects due to non-uniformity, an unfavourable combination of mean wind speed and turbulence intensity should be considered.

Acknowledgements. The research presented in this study has been financed by the Norwegian Public Roads Administration (NPRA), the Norwegian Research Council and Norconsult AS. The authors appreciate all these contributions.

References

Arena A, Lacarbonara W, Valentine DT, Marzocca P (2014) Aeroelastic behavior of long-span suspension bridges under arbitrary wind profiles. J Fluids Struct 50:105–119. https://doi.org/10.1016/j.jfluidstructs.2014.06.018

Chen X, Kareem A, Matsumoto M (2001) Multimode coupled flutter and buffeting analysis of long span bridges. J Wind Eng Ind Aerodyn 89:649–664. https://doi.org/10.1016/S0167-6105(01)00064-2

Dassault Systèmes, Waltham (n.d.) ABAQUS

Davenport AG (1962) Buffeting of a suspension bridge by storm winds. J Struct Div 88:233–270

Fenerci A, Øiseth O (2017) Measured buffeting response of a long-span suspension bridge compared with numerical predictions based on design wind spectra. J Struct Eng 143. https://doi.org/10.1061/(ASCE)ST.1943-541X.0001873

Fenerci A, Øiseth O, Rönnquist A (2017) Long-term monitoring of wind field characteristics and dynamic response of a long-span suspension bridge in complex terrain. Eng Struct 147:269–284. https://doi.org/10.1016/j.engstruct.2017.05.070

Hu L, Xu Y, Zhu Q, Guo A, Kareem A (2017) Tropical storm – induced buffeting response of long-span bridges: enhanced nonstationary buffeting force model. J Struct Eng 143:04017027. https://doi.org/10.1061/(ASCE)ST.1943-541X.0001745

Jain A, Jones NP, Scanlan RH (1996a) Coupled aeroelastic and aerodynamic response analysis of long-span bridges. J Wind Eng Ind Aerodyn 60:69–80. https://doi.org/10.1016/0167-6105(96)00024-4

Jain A, Jones NP, Scanlan RH (1996b) Coupled flutter and buffeting analysis. J Struct Eng 122:716–725

Lystad TM, Fenerci A, Øiseth O (2018) Evaluation of mast measurements and wind tunnel terrain models to describe spatially variable wind field characteristics for long-span bridge design. J Wind Eng Ind Aerodyn 179:558–573. https://doi.org/10.1016/J.JWEIA.2018.06.021

Scanlan RH, Tomko JJ (1971) Airfoil and bridge deck flutter derivatives. J Eng Mech Div 97:1717–1737

Siedziako B, Øiseth O, Rønnquist A (2017) An enhanced forced vibration rig for wind tunnel testing of bridge deck section models in arbitrary motion. J Wind Eng Ind Aerodyn 164:152–163. https://doi.org/10.1016/J.JWEIA.2017.02.011

Zhang X (2007) Influence of some factors on the aerodynamic behavior of long-span suspension bridges. J Wind Eng Ind Aerodyn 95:149–164. https://doi.org/10.1016/J.JWEIA.2006.08.003

Paper III

Tor Martin Lystad, Aksel Fenerci and Ole Øiseth

Buffeting response of long-span bridges considering uncertain turbulence parameters using the environmental contour method

Engineering structures 2020:213, Copyright Elsevier

Engineering Structures 213 (2020) 110575

Contents lists available at ScienceDirect

Engineering Structures

journal homepage: www.elsevier.com/locate/engstruct

Buffeting response of long-span bridges considering uncertain turbulence parameters using the environmental contour method

Tor M. Lystad[a,b,*], Aksel Fenerci[b], Ole Øiseth[b]

[a] Bridge Department, Norconsult AS, Sandvika, Norway
[b] Department of Structural Engineering, Norwegian University of Science and Technology, Trondheim, Norway

ARTICLE INFO

Keywords:
Long-span bridge
Environmental contour method
Turbulence variability
Probabilistic design

ABSTRACT

Full-scale monitoring of the Hardanger Bridge has revealed significant turbulence-induced variability in the measured acceleration response. In this paper, a probabilistic model is used to describe the uncertain turbulence parameters, and the environmental contour method is used to investigate the long-term root-mean-square (RMS) response of the Hardanger Bridge. The results show that turbulence-induced variability has a significant impact on the bridge girder section moments. It is also interesting that the critical combination of environmental parameters does not necessarily involve the maximum mean wind velocity. By using the environmental contour method to account for turbulence uncertainty, the scattered acceleration RMS response measurements from the Hardanger Bridge are successfully eclipsed by 100-year return period response estimates, showing vast improvements compared with the traditional design methodology. The investigations presented in this paper show that the environmental contour method can be used to improve the accuracy and reduce the uncertainty in buffeting response calculations for long-span bridge design.

1. Introduction

The trend in international bridge engineering is that increasingly longer passages are crossed with long-span bridges. As experience and development progress, more audacious bridge crossings are considered, such as the Messina Strait and the Strait of Gibraltar. In Norway, the government is planning to build a continuous highway along the west coast of the country [1]. Such a highway would have to cross several fjords with extreme long-span bridges, replacing the current ferry connections. Many of the bridge concepts under consideration are extremely slender, such as floating bridges spanning up to 5500 m and suspension bridges with main spans over 3000 m. Buffeting response from turbulent wind loading governs the design stresses for these types of structures, so uncertainties connected to the description of the turbulent wind field must be properly handled as it significantly affects the overall structural reliability.

Since 2013, the Norwegian University of Science and Technology has performed full-scale measurements of the wind field characteristics and acceleration responses of the Hardanger Bridge, the longest suspension bridge in Norway. The results from the measurement campaign have been presented in a series of papers [2–7], showing significant turbulence-induced variability in the measured dynamic response. Several full-scale measurement studies have been performed on long-span bridges around the world, showing similar variability in the measured response [8–17]. In the traditional design methodology for long-span bridges, only the mean wind velocity is treated as a stochastic variable because it is considered a very dominating load parameter. The corresponding turbulence parameters are then chosen deterministically based on design codes or site measurements. The results from the previously referenced studies indicate that this methodology is too simplified and may introduce significant uncertainty to the response estimates.

Long-term extreme response calculations have long been the standard for the design of offshore structures subjected to wave loading [18]. In such calculations, the load parameters and the short-term extreme response can be treated as stochastic variables. The environmental contour method [19] is an efficient approach to estimate the long-term extreme response by a short-term extreme value analysis. This method decouples the variability in the environmental parameters and the variability in the extreme response itself [20], and only the variability in the load parameters are considered directly. The effect of the extreme value uncertainty is often simplified by choosing a higher percentile of the short-term extreme response probability distribution as the design value. Environmental contours can be established using several methods, such as the inverse first order reliability method (FORM), inverse second order reliability method (SORM), the highest

* Corresponding author at:Bridge Department, Norconsult AS, Sandvika, Norway.
E-mail address: tor.m.lystad@ntnu.no (T.M. Lystad).

https://doi.org/10.1016/j.engstruct.2020.110575
Received 14 November 2019; Received in revised form 20 March 2020; Accepted 24 March 2020

density contour method (HDC) or Monte Carlo simulation [21–23]. The inverse FORM is the most common and is the methodology applied in this work.

The environmental contour method can also be used to estimate the long-term response of structures subjected to wind loading with uncertain turbulence parameters [24–27]. Some studies using long-term response analyses for bridges, including the mean wind velocity distribution, have been performed [28,29], but long-term methods, including uncertain turbulence parameters, have not been studied in depth in the field of bridge engineering. Other probabilistic frameworks for buffeting response have also been suggested in the literature [30–37], but in long-term analyses, the probabilistic considerations are isolated to the dynamic extreme response, making it very interesting for practical design purposes. Probabilistic approaches, such as the environmental contour method, rely on a solid statistical description of the environmental variables, and some probabilistic models for uncertain turbulence parameters can be found in the literature [5,38].

The environmental load situations critical for design purposes are often the high return period cases. This means that the joint probability density functions (PDFs) for the environmental parameters need to describe the tail region properly or significant uncertainty can be expected [39]. Many efforts have been made to improve the environmental contour estimates for high return periods [40–45], but most studies focus on wave loading and not turbulent wind. In bridge engineering, the mean wind velocities with long return periods are often estimated from the extreme value distribution directly. In this paper, the tail of the mean wind velocity parent PDF is estimated from extreme wind measurements using asymptotic extreme value theory [46]. Instead of extrapolating the interesting tail region by fitting the PDF to the full mean wind velocity dataset, the less important low wind speed range is extrapolated based on the extreme values in the tail.

In Section 3 of this paper, environmental contours are established based on the probabilistic turbulence model for the Hardanger Bridge site developed by Fenerci and Øiseth [5]. In Section 4, the turbulence variability effect on the design response of the Hardanger Bridge girder has been investigated using constrained numerical optimization to identify the environmental situation most critical for the bridge girder section moments. The findings show that the design storm does not correspond to the event of the maximum mean wind velocity, but indeed, the turbulence parameters should be treated as stochastic variables. In Section 5, vast improvements are achieved by using this method to compare the calculated acceleration root-mean-square (RMS) response with the scattered response from the full-scale measurements of the Hardanger Bridge. The traditional approach is not able to describe the variability in the measured response, whereas the environmental contour method can be used to find an upper and lower bound for the response as a function of the mean wind velocity, corresponding well with the scattered response observed from the full-scale measurements.

The environmental contour method is suitable for design purposes, and the investigations presented in this paper show that it can be used for turbulent wind loads to improve the accuracy and reduce the uncertainty in buffeting response calculations for long-span bridges.

2. The environmental contour method

The environmental contour method can be used to identify design storms corresponding to a target statistical return period. Then, the critical combination of the environmental parameters on the contour for an interesting structural response can be identified. The environmental contours are based on the joint PDFs of two or more random variables. The inverse FORM technique requires taking combinations of stochastic variables in the standard normal space and transforming the variables into real space using linear-, Rosenblatt- or Nataf transformations [47]. As an example, a two-dimensional transformation is shown in Fig. 1, including the mean wind velocity and the along-wind turbulence standard deviation for the easterly winds.

In the standard normal space, the statistical return period for a short-term process is related to the reliability index, β, as follows:

$$\beta = -\Phi^{-1}(1/[\frac{R_{yr} \times 365.25 \times 24 \times 60}{T_s}]) \tag{1}$$

where Φ is the standard normal cumulative density function (CDF), R_{yr} is the statistical return period in years, and T_s is the short-term duration in minutes. Given the standard normal variables, $u_1, u_2, \ldots, u_n$ and the related real stochastic variables, $v_1, v_2, \ldots, v_n$, the following transformation into the real space is needed:

$$\Phi(u_1, u_2, \ldots, u_n) \rightarrow F_{V_1 V_2 \ldots V_n}(v_1, v_2, \ldots, v_n) \tag{2}$$

where $F_{V_1 V_2 \ldots V_n}(v_1, v_2, \ldots, v_n)$ is the cumulative joint distribution of the real stochastic variables. If the real variables are uncorrelated, the variables can be transformed independently as follows:

$$F_{V_n}(v_n) = \Phi(u_n) \Leftrightarrow v_n = F_{V_n}^{-1}[\Phi(u_n)] \tag{3}$$

However, if the variables are correlated, the transformation becomes more complicated, and generally, a transformation procedure such as the Rosenblatt or Nataf transformation needs to be applied.

The Rosenblatt procedure [48] is a widely used transformation because it is general and quite simple to use. The transformation procedure is based on the relationship where the joint CDF can be established from the product of conditional marginal CDFs, as shown in Eq. (4):

$$\begin{aligned} &F_{V_1, V_2, \ldots, V_{n-1}}(v_1, v_2, \ldots, v_{n-1}) \\ &\quad = F_{V_1}(v_1) F_{V_2|V_1}(v_2|v_1) \ldots F_{V_n|V_1, V_2, \ldots, V_{n-1}}(v_n|v_1, v_2, \ldots, v_{n-1}) \end{aligned} \tag{4}$$

The Rosenblatt procedure is a stepwise transformation using conditional CDFs as follows:

$$\begin{aligned} &F_{V_1}(v_1) = \Phi(u_1) \;\Leftrightarrow\; v_1 = F_{V_1}^{-1}[\Phi(u_1)] \\ &F_{V_2|V_1}(v_2|\, v_1) = \Phi(u_2) \;\Leftrightarrow\; v_2|\, v_1 = F_{V_2|V_1}^{-1}[\Phi(u_2)] \\ &F_{V_3|V_1, V_2}(v_3|\, v_1, v_2) = \Phi(u_3) \;\Leftrightarrow\; v_3|\, v_1, v_2 = F_{V_3|V_1, V_2}^{-1}[\Phi(u_3)] \\ &\qquad \cdots \\ &F_{V_n|V_1, V_2, \ldots, V_{n-1}}(v_n|\, v_1, v_2, \ldots, v_{n-1}) = \Phi(u_n) \;\Leftrightarrow\; v_n|\, v_1, v_2, \ldots, v_{n-1} \\ &\qquad\qquad = F_{V_n|V_1, V_2, \ldots, V_{n-1}}^{-1}[\Phi(u_n)] \end{aligned} \tag{5}$$

In the special case where the stochastic variables are normally distributed in the real space, the transformation from the uncorrelated standard normal space to the correlated real space is linear. It can be shown that if $\mathbf{X}$ is a vector containing the real variables v_i and $\mathbf{Y}$ is a vector containing the standard normal uncorrelated variables u_i, then the transformation can be described as follows:

$$\boldsymbol{Y} = \boldsymbol{A}(\boldsymbol{X} - \boldsymbol{M}_X) \;\Leftrightarrow\; \boldsymbol{X} = \boldsymbol{A}^{-1}\boldsymbol{Y} + \boldsymbol{M}_X \tag{6}$$

where $\boldsymbol{M}_X = [\mu_{V_1} \;\; \mu_{V_2} \;\; \cdots \;\; \mu_{V_n}]^T$ is a vector containing the mean values of the normally distributed variables v_i, and $\mathbf{A}$ is a transformation matrix. For normally distributed variables, $\mathbf{A}$ can be calculated based on the covariance matrix $\mathbf{C}_{XX}$ as follows:

$$\boldsymbol{C}_{XX} = \begin{bmatrix} \sigma_{V_1}^2 & \rho_{12}\sigma_{V_1}\sigma_{V_2} & \cdots & \rho_{1n}\sigma_{V_1}\sigma_{V_n} \\ \rho_{21}\sigma_{V_2}\sigma_{V_1} & \sigma_{V_2}^2 & \cdots & \rho_{2n}\sigma_{V_2}\sigma_{V_n} \\ \cdots & \cdots & \cdots & \cdots \\ \rho_{n1}\sigma_{V_n}\sigma_{V_1} & \rho_{n2}\sigma_{V_n}\sigma_{V_2} & \cdots & \sigma_{V_n}^2 \end{bmatrix} \tag{7}$$

$$\begin{aligned} \boldsymbol{A} &= \boldsymbol{D}^T \boldsymbol{S}^T \\ \boldsymbol{D} &= diag\,[1/\sqrt{\lambda_j}\,],\; j = 1, 2, \ldots, n \\ \boldsymbol{S} &= [\boldsymbol{S}_1 \;\; \boldsymbol{S}_2 \;\; \ldots \;\; \boldsymbol{S}_n] \end{aligned} \tag{8}$$

where σ_{Vj} is the standard deviation, ρ_{jk} is the correlation coefficient between the normally distributed variables, λ_j is the eigenvalues and $\mathbf{S}_j$ is the eigenvector of the correlation matrix $\mathbf{C}_{XX}$. This transformation procedure is often referred to as the Singular Value Decomposition (SVD), but the transformation matrix $\mathbf{A}$ could also be found by Cholesky decomposition of $\mathbf{C}_{XX}$, which is Hermitian and positive definite:

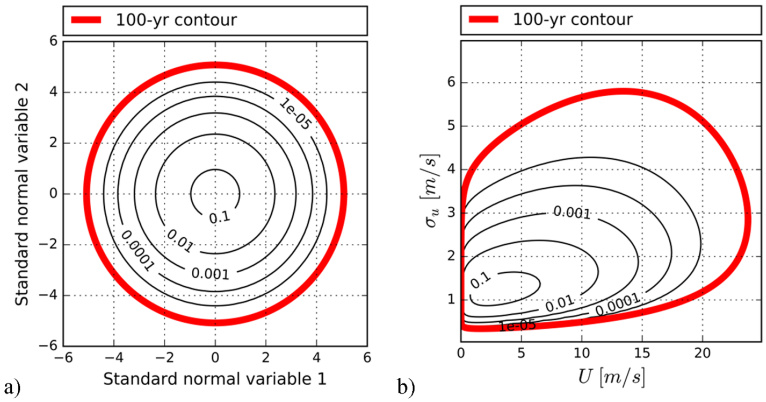

Fig. 1. Isoprobabilistic contours and the 100-year return period contour from the joint PDF of the mean wind velocity and the along-wind turbulence standard deviation for the easterly winds shown in a) the standard normal space, and b) the real space.

$$\boldsymbol{C}_{XX} = \boldsymbol{A}^{-1}\boldsymbol{A}^{-T} \tag{9}$$

If the stochastic variables are lognormally distributed in real space, the same transformation applies to find the associated normal distribution, and the lognormally distributed variables can be found as follows:

$$\boldsymbol{X} = \exp(\boldsymbol{A}^{-1}\boldsymbol{Y} + \boldsymbol{M}_X) \tag{10}$$

3. Wind field environmental contours for the Hardanger Bridge site

3.1. Probabilistic turbulence field

A probabilistic turbulence model using lognormal random turbulence parameters was established by Fenerci and Øiseth [5] for the Hardanger Bridge site in Norway (see Fig. 2), based on information from the full-scale measurement program thoroughly described in [2]. The turbulence spectra were assumed to be properly modeled using a Kaimal-type auto-spectra [49] and a normalized cross-spectra [50] as defined by Eq. (11). The cross-spectral densities between turbulence components, u and w are not described by the probabilistic model, and has been neglected in this study.

$$\frac{S_{u,w}f}{\sigma_{u,w}^2} = \frac{A_{u,w}f_z}{(1+1.5A_{u,w}f_z)^{5/3}}, f_z = \frac{fz}{U}$$
$$C_{u,w} = \exp(-K_{u,w}\frac{f\Delta x}{U}) \tag{11}$$

where f is the frequency, z is the height above the ground, U is the mean wind velocity, $\sigma_{u,w}$ are the standard deviations of the turbulent process, $A_{u,w}$ are the nondimensional spectral parameters, and $K_{u,w}$ are the decay coefficients. The probabilistic model only considers along-span turbulence correlation, so the decay coefficients noted $K_{u,w}$ will refer to the along-span correlation throughout this paper. Using the definition in Eq. (11), the along-span turbulence cross-spectral density can be completely defined through six turbulence parameters for a given mean wind velocity and wind direction. Only two distinct wind directions, namely, the east and the west, were considered due to the channeled flow in the fjord, bounded by mountains on the sides (see Fig. 3). When the turbulence parameters are described with lognormal distributions, the full probabilistic model can be described by the distribution parameters and the correlation matrix given in Tables 1 and 2. The lognormal probability density function can be written as follows:

$$f(x) = \frac{1}{x\sigma\sqrt{2\pi}}\exp\left\{\frac{-(\ln x-\mu)^2}{2\sigma^2}\right\};\ x > 0 \tag{12}$$

where μ (the mean of the natural logarithm of the random variable) and σ (the standard deviation of the natural logarithm of the random variable) are the distribution parameters, and x is the random variable.

For comparison, the turbulence parameters used in the design of the bridge are presented in Table 3. It should also be noted that all turbulence parameters shown in Tables 1–3 refer to the characteristics at the girder height, $z \approx 68$ m. Therefore, in all calculations presented in this paper, a constant vertical profile for both the turbulence and the mean wind velocity is assumed. This introduces a slight underestimation of the main cable load, however, the most influential contribution from the wind on the main cables is due to loading toward the midspan where the error from this simplification becomes small. Consequently, this simplification is not expected to affect the results or conclusions from this work.

3.2. PDF of the mean wind velocity

Since the probabilistic turbulence model described in the previous section is established conditional on the mean wind velocity, the PDF of the mean wind speed is also needed in estimating the environmental contours. However, the Hardanger Bridge full-scale measurement

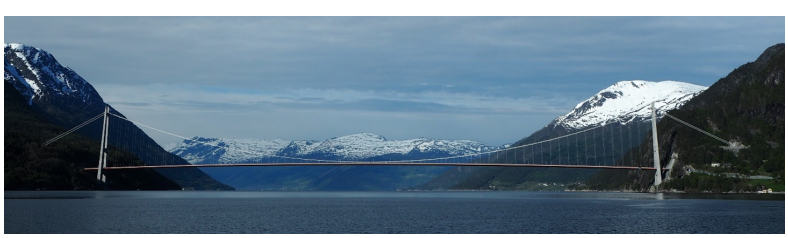

Fig. 2. The Hardanger Bridge seen from the east (Picture by the authors).

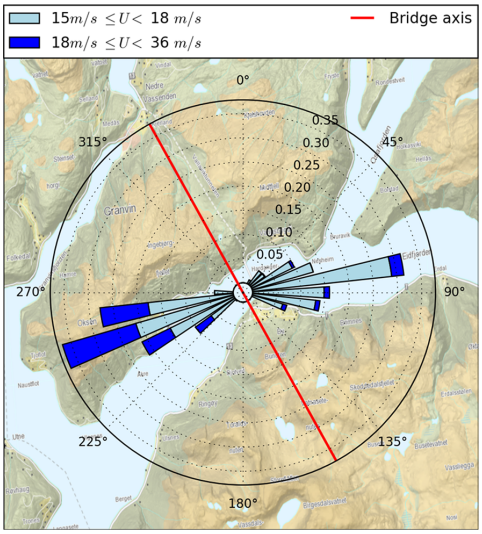

Fig. 3. Mean wind velocity wind rose at the Hardanger Bridge midspan. Only strong winds above 15 m/s are shown, and the rose shows wind speed percentages normalized for each wind direction summarizing to 100% for both easterly and westerly winds.

system was set up with a triggering setting that records only strong wind events. If a 1-minute mean wind velocity above 15 m/s is measured at any position along the bridge girder, the next 30 min is stored, including the first triggering minute. A histogram of all recorded 10-minute mean wind velocities is shown in Fig. 4. Because of the triggering system, the statistical basis is only complete for the high mean wind velocities. However, some data are available for lower wind speeds also, due to manually triggered periods of continuous measurements.

It is expected that the critical environmental parameter combinations for the buffeting response of the Hardanger Bridge are in the tail region of the mean wind velocity marginal PDF since this is the most influential parameter for this response [2]. Benefiting from this limited range of interest, the environmental contour in this region can be established directly based on the mean wind velocity extreme value distribution.

Lystad et al. [6] established the extreme value distributions for the measured mean wind velocity in 8 positions along the Hardanger Bridge span. The tail of the parent CDF can be transformed from an estimated extreme value distribution using asymptotic extreme value theory [46] as follows:

$$F_Z(x) = [F_X(x)]^N \Leftrightarrow F_X(x) = [F_Z(x)]^{1/N} \tag{13}$$

where $F_Z(x)$ is the annual extreme value CDF, $F_X(x)$ is the parent CDF and N is the number of annual 10-minute short-term periods. By using this relationship, the tail region of the mean wind velocity parent CDF can be described directly by the extreme value distribution.

The full dataset of the mean wind velocity is expected to follow a Weibull distribution, and the extremes will consequently follow a Gumbel distribution. In Fig. 5, the tail of the mean wind velocity parent CDF is shown for both the easterly and the westerly winds. The extreme value distribution was established using the method of independent storms (MIS) and the Gumbel-Lieblein BLUE method [52–54] based on the measured 16 strongest statistically independent storms (blue dots), from 4-years of continuous measurements. Details on the selection of independent storms and the extreme value distribution estimates can be found in [6]. As shown in Fig. 5, the transformed extreme value distribution (red line) is only able to describe the tail region of the parent distribution. To describe the full CDF for the mean wind velocity, the tail of the CDF is fitted to the transformed extreme value distribution using the least-squares technique. In this way, the body of the parent

Table 2
Correlation coefficient matrix from the probabilistic turbulence model, conditional on the wind direction [5].

		σ_u	σ_w	A_u	A_w	K_u	K_w
East	σ_u	1	0.7608	0.2641	0	0	0
	σ_w	0.7608	1	0	0.2571	0	0
	A_u	0.2641		1	0.1633	0	0
	A_w	0	0.2571	0.1633	1	0	0
	K_u	0	0	0	0	1	0.3261
	K_w	0	0	0	0	0.3261	1
West	σ_u	1	0.8148	0.4087	0	0	0
	σ_w	0.8148	1	0	0.2851	0	0
	A_u	0.4087	0	1	0.3065	0	0
	A_w	0	0.2851	0.3065	1	0	0
	K_u	0	0	0	0	1	0.4725
	K_w	0	0	0	0	0.4725	1

Table 3
Design basis turbulence characteristics in the girder height for the Hardanger Bridge [51].

	I_u	I_w	A_u	A_w	K_u	K_w
Design Basis	0.136	0.068	40.8	3.3	8.8	6.3

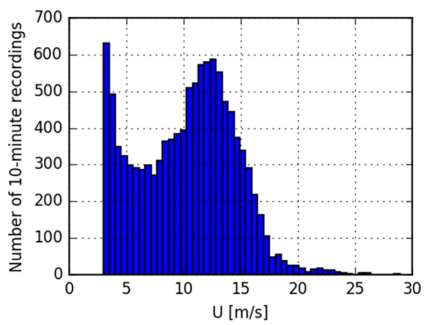

Fig. 4. Histogram of 10-minute midspan mean wind velocity recordings with 1 m/s sample bins.

Table 1
Lognormal distribution parameters from the probabilistic turbulence model, conditional on the mean wind velocity and wind direction [5].

		σ_u	σ_w	A_u	A_w	K_u	K_w
East	μ	$0.122 + 0.039U$	$-0.657 + 0.032U$	$2.67 + 0.0248U$	0.7076	1.9385	1.7932
	σ	0.2566	0.2632	0.4538	0.4466	0.2652	0.3423
West	μ	$0.122 + 0.039U$	$-0.657 + 0.032U$	$2.407 + 0.048U$	1.2075	2.1093	2.1633
	σ	0.3159	0.3021	0.5282	0.4943	0.268	0.3322

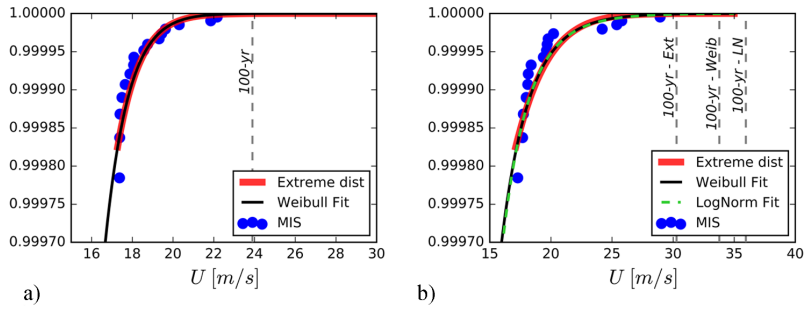

Fig. 5. Upper tail of the mean wind velocity parent CDF showing measured storms, the transformed extreme value distribution, and the fitted Weibull and lognormal distribution for (a) easterly winds and (b) westerly winds.

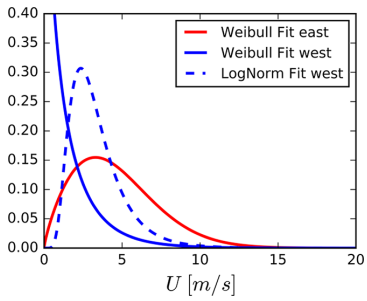

Fig. 6. Fitted parent PDFs for the mean wind velocity.

distribution is extrapolated from the important tail region instead of the other way around.

In Fig. 6, the fitted Weibull PDFs are shown in the full mean wind velocity range for both wind directions. The Weibull probability density function can be written as follows:

$$f(x) = \frac{k}{\lambda}\left(\frac{x}{\lambda}\right)^{(k-1)} \exp\left\{-\left(\frac{x}{\lambda}\right)^{k}\right\}; x > 0 \tag{14}$$

where k and λ are the distribution parameters, and x is the random variable. The fitted Weibull distribution displays a classical shape for the easterly winds but not for the westerly winds. A lognormal distribution will also have Gumbel distributed extremes, so a lognormal CDF was also fitted to the data, displaying a more physical shape.

For the easterly winds, the fitted parent distribution follows the transformed extreme value distribution very well, estimating almost exactly the same 100-year return period mean wind velocity. However, for the westerly winds, both fitted parent distribution models differ slightly from the transformed extreme value distribution, resulting in relatively large deviations in the 100-year return period estimates (see Table 5). The fitted distribution parameters are shown together with the R-squared values in Table 4. The R-squared values are quite close to 1 for all the models, but still the deviation in high return period estimates becomes large, illustrating the sensitivity of these estimates.

It should be noted that Eq. (13) assumes independence between the drawn values form the random variable, X. When predicting the extreme value distribution $F_Z(x)$ from continuously recorded 10-minute mean wind velocities, this assumption will not hold and uncertainties will be introduced, since adjacent recordings will likely be correlated. However, in this study the parent distribution is estimated from the extreme value distribution. The estimated extreme value distribution is uncertain, due to a low number of data, but this data is chosen as statistically independent values, so the assumption of statistical independence in Eq. (13) should hold for this approach. Estimating 100-year return periods, based on short measurement time-series, will introduce uncertainty. This is likely the main reason for the observed deviations seen in Table 5 for the westerly winds.

Table 4
Fitted probability distribution parameters and R-squared values for the mean wind velocity.

	Weibull distribution			Lognormal distribution		
	λ	k	R^2	σ	μ	R^2
East	5.1941	1.7946	0.99999	N/A	N/A	N/A
West	1.4063	0.8616	0.99872	0.4894	1.0967	0.99757

3.3. Environmental contours

The probabilistic turbulence model is established as lognormally distributed variables conditional on the mean wind velocity and wind direction. However, the mean wind velocity is usually described by a Weibull distribution and not a lognormal distribution. To establish the environmental contours for combinations of the lognormally distributed turbulence parameters and the Weibull distributed mean wind velocity using the inverse FORM technique, a combination of the Rosenblatt transformation and the linear transformation can be applied.

The mean wind velocity can be transformed first as if it was the first step of a Rosenblatt transform:

$$F_U(U) = \Phi(u_1) \;\Leftrightarrow\; U = F_U^{-1}[\Phi(u_1)] \tag{15}$$

Then, instead of taking one variable at a time using conditional CDFs as shown in Eq. (5), all the remaining lognormally distributed turbulence variables can be transformed in the same operation using the linear transformation described in Section 2, given the already transformed mean wind velocity:

$$F_{\sigma_u,\sigma_w,A_u,A_w,K_u,K_w|U}(\sigma_u, \sigma_w, A_u, A_w, K_u, K_w|\, U) \rightarrow \Phi(u_2, u_3, u_4, u_5, u_6) \tag{16}$$

In Figs. 7 and 8, the environmental contour lines for combinations of the mean wind velocity and the six turbulence parameters are shown for both easterly and westerly winds. Contour lines based directly on the transformed extreme value distribution (asymptotic) of the mean wind velocity are shown together with the contours based on the fitted parent PDFs shown in Fig. 6 (Weibull and lognormal). As Figs. 7 and 8

Table 5
Estimated 100-year return period mean wind velocities from the extreme value distribution and the fitted parent distributions.

	Extreme	Weibull	Lognormal
East	23.759	23.900	N/A
West	30.281	33.787	35.950

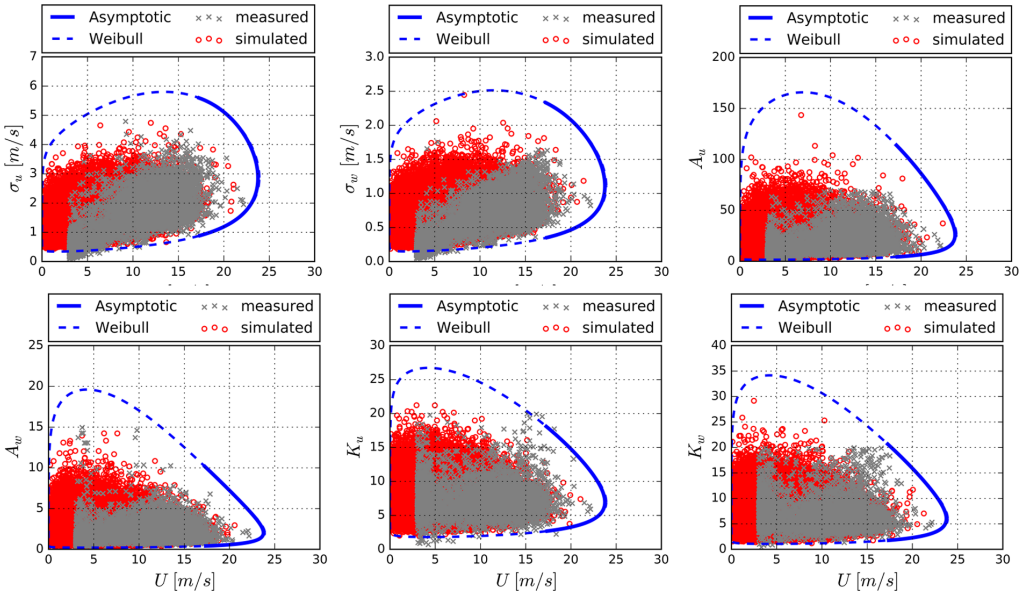

Fig. 7. Environmental contours of turbulence components and mean wind velocity for easterly winds.

show, the transformed extreme value distribution overlaps almost perfectly with the fitted parent distribution for the easterly winds, but relatively large deviations between the methods can be seen in the tail region for the westerly winds.

Figs. 7 and 8 also show the full-scale measurement data used as the basis for the probabilistic turbulence model. To illustrate the missing data in the lower mean wind velocity range due to the triggering in the measurement system, Monte Carlo simulated points from the probabilistic model are shown in the backgrounds of the plots. The number of simulated points correspond to the number of 10-minute time windows in a 4-year period ($N = 4 \times 365.25 \times 24 \times 6 = 210\,384$).

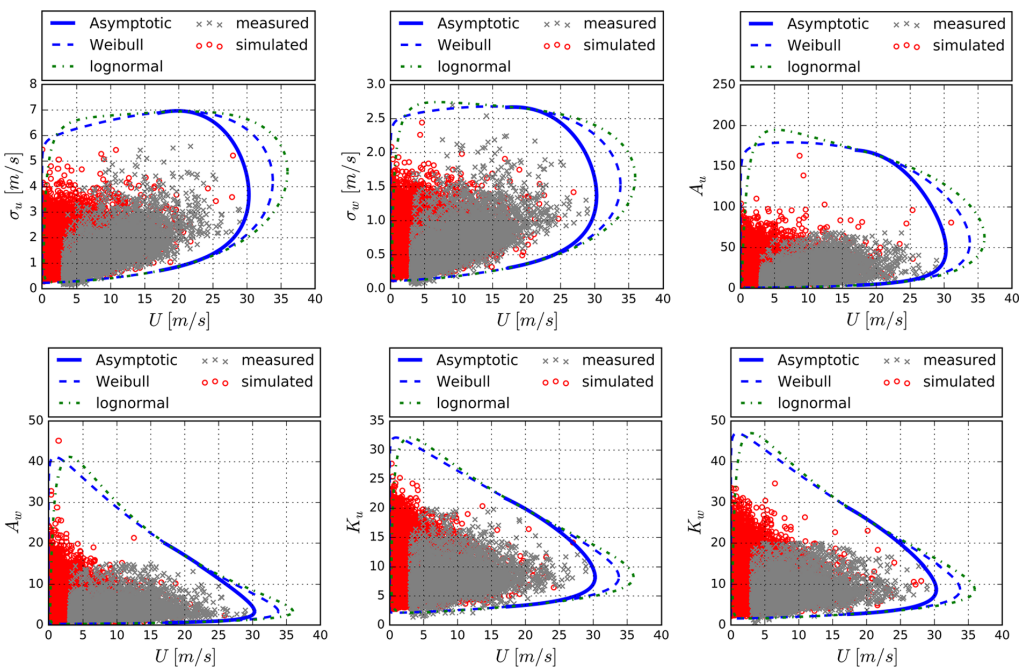

Fig. 8. Environmental contours of turbulence components and mean wind velocity for westerly winds.

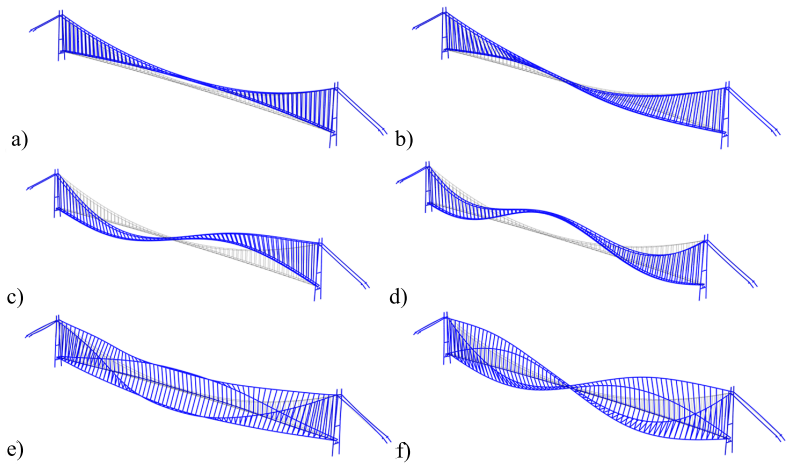

Fig. 9. Mode shapes of the Hardanger Bridge: (a) First lateral mode (19.8 s), (b) Second lateral mode (10.0 s), (c) First vertical mode (9.2 s), (d) Second vertical mode (7.1 s), (e) First torsional mode (2.8 s) and (f) Second torsional mode (1.9 s).

4. Long-term RMS buffeting response by the environmental contour method

4.1. Buffeting analysis

Buffeting response calculations of the Hardanger Bridge are performed in the frequency domain using the multimode theory, described in detail in [55–59], and implemented in the python programming language [60]. The response is calculated in normalized modal coordinates, and the response spectral density in real coordinates are achieved by the following transformation:

$$\boldsymbol{S}_r(\omega) = \boldsymbol{\Phi}(x)\boldsymbol{S}_\eta(\omega)\boldsymbol{\Phi}^T(x) \tag{17}$$

where $\boldsymbol{S}_r(\omega)$is the response spectral density matrix in real coordinates, $\boldsymbol{S}_\eta(\omega)$is the modal response spectrum, and $\boldsymbol{\Phi}(x)$is a vector containing the natural mode shapes. The structural properties of the system are based on a 3D finite element model in Abaqus [61]. From the Abaqus model it is possible to extract the section forces corresponding to a normalized deformation mode shape. By using these section force mode shapes in the transformation described by Eq. (17), the response spectral density matrix for the section forces is achieved directly. The aeroelastic self-excited forces are described based on wind tunnel experiments [62], and the structural damping ratio is chosen as 0.5% of the critical damping for all modes.

Table 6
The frequency, period and shape of the first 15 natural modes of the Hardanger Bridge.

Mode	Frequency [Hz]	Period [s]	Shape description
1	0.051	19.77	Lateral sym.
2	0.100	10.00	Lateral asym.
3	0.109	9.18	Vertical asym.
4	0.141	7.08	Vertical sym.
5	0.174	5.75	Lateral sym.
6	0.200	4.99	Vertical sym.
7	0.211	4.74	Vertical asym.
8	0.222	4.51	Cabel vibration
9	0.230	4.34	Cabel vibration
10	0.235	4.26	Cabel vibration
11	0.245	4.08	Cabel vibration
12	0.273	3.66	Vertical sym.
13	0.302	3.31	Lateral asym.
14	0.329	3.04	Vertical asym.
15	0.356	2.81	Torsional sym.

The modes affecting the considered response has been identified by convergence calculations. Considering the section forces, the first 6 lateral, the first 14 vertical, and the first 6 torsional modes are included in the calculations. For acceleration responses, all contributing modes below a cut-off frequency of 1 Hz are included in the calculations. This means that some high frequency contribution to the buffeting accelerations will be excluded, but for comparison reasons the cut-off frequency is chosen consistent with the filtering of the full-scale measurement data presented in Section 5. In Fig. 9, the first two eigenmodes in the main degrees of freedom are shown, and the natural periods of the first 15 modes are presented in Table 6, along with a description of the mode shape.

The wind field is described as a stationary stochastic process through the cross-spectral density matrix as follows:

$$\boldsymbol{S}_V(\Delta s, \omega) = \begin{bmatrix} S_{uu}(\Delta s, \omega) & S_{uw}(\Delta s, \omega) \\ S_{uw}(\Delta s, \omega) & S_{ww}(\Delta s, \omega) \end{bmatrix} \tag{18}$$

where S_{nm} represents the cross-spectral densities for the n and m components of the turbulence between two points separated in space by the distance Δs. In the current study, the off-diagonal terms of the cross-spectral density matrix are assumed to be negligible. The cross-spectral density for a single turbulence component can be described through the auto-spectral density function and the normalized cross-spectra as follows:

$$S_{nn}(\Delta s, \omega) = S_n(\omega)C_n(\Delta s, \omega) \tag{19}$$

$$C_n(\Delta s, \omega) = \exp\left(-\sqrt{\left(K_{nx}\frac{\omega\Delta x}{2\pi U}\right)^2 + \left(K_{nz}\frac{\omega\Delta z}{2\pi U}\right)^2}\right) \tag{20}$$

where S_n is the auto-spectral density function, C_n is the normalized cross-spectra, and K_{nx} and K_{nz} are the decay coefficients in the along-span- and vertical directions, respectively. The vertical decay coefficients will be assumed to be constant ($K_{uz} = 10, K_{wz} = 3$) because these are not included in the probabilistic model.

The steady-state static coefficients used in the calculations are shown in Table 7 [62]. Effects from aerodynamic admittance are neglected by setting the admittance functions to unity. From the investigations performed by [63] it was observed that by neglecting the three-dimensional admittance, consisting of the two-dimensional strip theory admittance function and the effect where the load correlation on the girder may be larger than the turbulence correlation, a slightly

Table 7
Steady-state static coefficients used in the buffeting analyses (0-degree angle of attack).

Bridge member	*Width* [m]	*Depth* [m]	C_D	C_L	C_L'	C_M	C_M'
Girder	18.3	3.33	1.050	−0.363	2.220	0.017	0.786
Main cables	0.6	0.6	1.0/0.7	0	0	0	0

conservative estimate of the aerodynamic buffeting forces could be expected. The cable drag loads have been estimated based on [64] for a painted circular cable based on a Reynolds number of approximately 1.5e6. The estimated cable drag coefficient is 1.0, but to account for some shielding effects, the drag coefficient for the downstream main cable is reduced to 0.7. Wind loads on other bridge members, such as hangers and towers, are neglected in these calculations because they are expected to have very little effect on the dynamic response of the bridge girder.

4.2. Self-excited forces

When using long-term calculation procedures such as the environmental contour method, behavior at lower mean wind velocities than what is usually considered can become interesting. A challenge arises for the self-excited forces since information about the aerodynamic derivatives (ADs) for low reduced velocities is desirable. This means that the extrapolation of the ADs outside the range where test data are available need to be handled carefully.

The self-excited forces can be written in the frequency domain as follows [65]:

$$
\begin{aligned}
q_y &= \tfrac{1}{2}\rho U^2 B\left(KP_1^*\tfrac{\dot{r}_y}{U} + KP_2^*\tfrac{B\dot{r}_\theta}{U} + K^2P_3^* r_\theta + K^2P_4^*\tfrac{r_y}{B} + KP_5^*\tfrac{\dot{r}_z}{U} + K^2P_6^*\tfrac{r_z}{B}\right)\\
q_z &= \tfrac{1}{2}\rho U^2 B\left(KH_1^*\tfrac{\dot{r}_z}{U} + KH_2^*\tfrac{B\dot{r}_\theta}{U} + K^2H_3^* r_\theta + K^2H_4^*\tfrac{r_z}{B} + KH_5^*\tfrac{\dot{r}_y}{U} + K^2H_6^*\tfrac{r_y}{B}\right)\\
q_\theta &= \tfrac{1}{2}\rho U^2 B^2\left(KA_1^*\tfrac{\dot{r}_z}{U} + KA_2^*\tfrac{B\dot{r}_\theta}{U} + K^2A_3^* r_\theta + K^2A_4^*\tfrac{r_z}{B} + KA_5^*\tfrac{\dot{r}_y}{U} + K^2A_6^*\tfrac{r_y}{B}\right)
\end{aligned}
\tag{21}
$$

where $K=(\omega B)/U$ is the reduced frequency, and r_n is the displacement motions. Zasso [66] proposed a convention where the ADs were fitted to the test data using the force components (aerodynamic derivative multiplied with the K or K^2 for the damping and stiffness ADs, respectively) going directly into Eq. (21), as shown in Figs. 10a and 11a. This would re-scale the amplitude of the AD's making them more similar throughout the reduced frequency range, compared with the Scanlan convention [65]. Extrapolations outside the reduced velocity range where test data are available is a challenge since no physical model is available. In this work, this extrapolation was performed by keeping the force component constant outside the test range. This choice is made by a lack of good alternatives, but in this way, the extrapolations are controlled, and the extrapolated ADs display a physical behavior toward the low reduced-velocity range for the important ADs. It should be noted that the convention used here only differs from the Scanlan convention in the domain where the AD model is fitted to the test data, and the mathematical modelling of the forces will be equivalent.

In Figs. 10 and 11, the aerodynamic derivatives from the wind tunnel tests performed by [62] are plotted together with fitted 2nd order polynomial functions. The polynomials are fitted to the format of force components going directly into Eq. (21), as shown in Figs. 10a and 11a. The resulting ADs plotted in the classical format are shown in Figs. 10b and 11b.

4.3. Section-moment buffeting response on the contours

In this section, the section-moment standard deviations from the buffeting action of the Hardanger Bridge girder are investigated as functions of the mean wind velocity and turbulence parameters. In Fig. 12, the response spectral densities of the section moments are shown for all positions along the bridge girder.

To find the critical environmental load situation for a considered response quantity, combinations of environmental variables on the contour can be picked based on engineering judgment and manual iterations, or it can be found automatically using numerical optimization. For environmental contour lines based on only two stochastic variables, it can be relatively simple to find the critical combination using only a few manual iterations, but for contour surfaces with 3 variables or contour manifolds with more than 3 variables, it becomes increasingly challenging to identify the critical combinations manually.

A challenge with numerical optimization is separating local from global maxima on the optimized function. For the cases investigated in this work, local maxima on the response function are not expected, and simple optimization algorithms should be sufficient. However, the

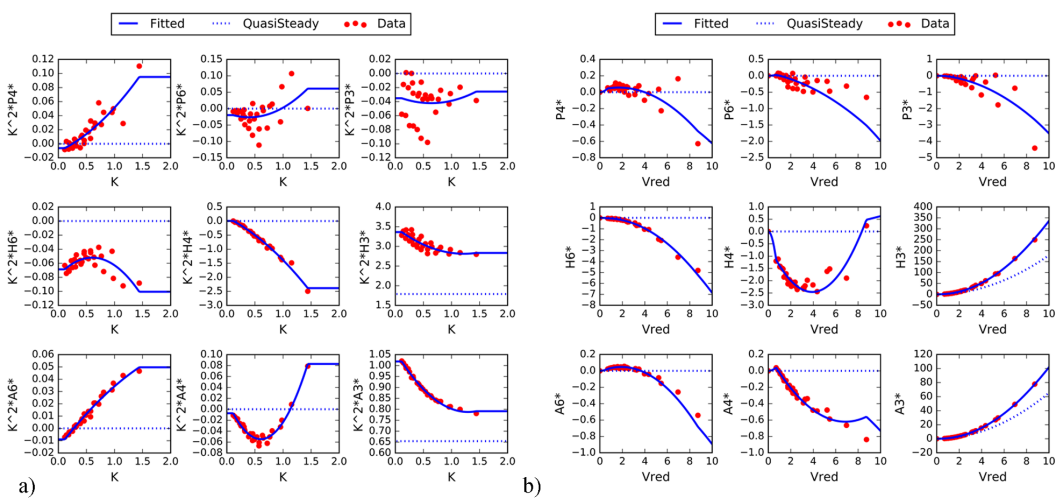

Fig. 10. Fitted polynomial functions for the stiffness-related aerodynamic derivatives: (a) force component format ($K=(\omega B)/U$) and (b) classical format ($Vred = U/\omega B$).

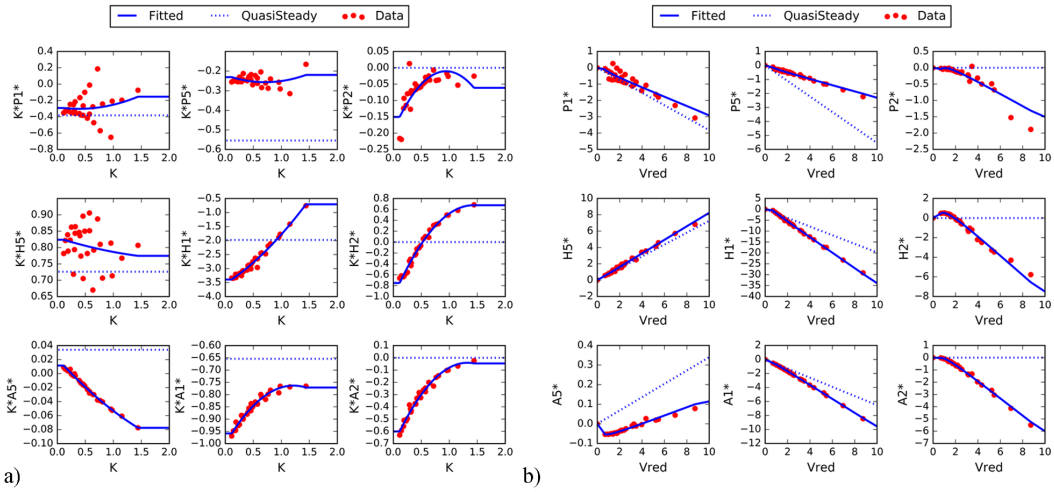

Fig. 11. Fitted polynomial functions for the damping-related aerodynamic derivatives: a) force component format ($K = (\omega B)/U$) and b) classical format ($Vred = U/\omega B$).

optimization algorithms need to be constrained to only find solutions on the environmental contour. The optimization algorithm used in this study is the sequential least-squares programming method (SLSQP) [67]. This algorithm can be used with boundary constraints as well as user-defined constraint functions.

Objective function:

The function to be optimized is the short-term response calculation as a function of the environmental variables:

$$response = f(\boldsymbol{X}) \tag{22}$$

where $\mathbf{X} = [v_1, v_2, v_3, \ldots, v_n]$ and v_i are the environmental variables.

Constraint function:

The constraint demands that all accepted combinations of $\mathbf{X}$ should be on the environmental contour-line, surface, or manifold, depending on the number of variables included, for a given statistical return period. The constraint function needs to transform the variables into the standard normal space and check if they refer to points with the target distance to the origin, namely the reliability index, β, as follows:

$$|\boldsymbol{Y}| - \beta = 0 \tag{23}$$

where $\mathbf{Y} = [u_1, u_2, u_3, \ldots, u_n]$ and u_i are the standard normal uncorrelated variables.

The quarter-span RMS weak- and strong-axis moments (σ_{sm1} and σ_{sm2}, respectively), as well as the torsional moment (σ_{sm3}) in the girder, is calculated along the contour lines for combinations of the mean wind velocity and the different turbulence parameters. The variation in RMS response along the contour lines based on direct transformation from the extreme value distribution is shown in Figs. 13 and 14. In these plots, the mean wind velocity together with one turbulence parameter is described with the environmental contour method, while the other turbulence parameters are chosen to correspond to the tips of the contours, the case of maximum mean wind velocity. The position on the contour line with the highest buffeting response is indicated with a star in the plots. The RMS response and the environmental variables corresponding to this position are shown in Tables 8 and 9. In the backgrounds of Figs. 13 and 14, isoresponse lines corresponding to constant response as a function of the mean wind velocity and the turbulence parameter under consideration are shown. If the isoresponse lines are straight and vertical, the investigated buffeting response is not sensitive to variation in the turbulence parameter under consideration, but if the lines are inclined, the turbulence parameter is important.

The turbulence standard deviations are the most influential parameters on the investigated buffeting response. The along-wind turbulence standard deviation (σ_u) has a significant effect on the weak- and strong-axis moments in the girder quarter spans but little effect on the torsional moment response. The vertical turbulence standard deviation (σ_w) has a large effect on the weak-axis moment and the torsional moment but less effect on the strong-axis moment.

From Figs. 13 and 14, it can be seen from the isoresponse lines that the response is sensitive to the decay coefficients ($K_{u,w}$), but since the contour lines become narrow toward the high wind speeds, the effect on the design response is less significant. The section-moment buffeting

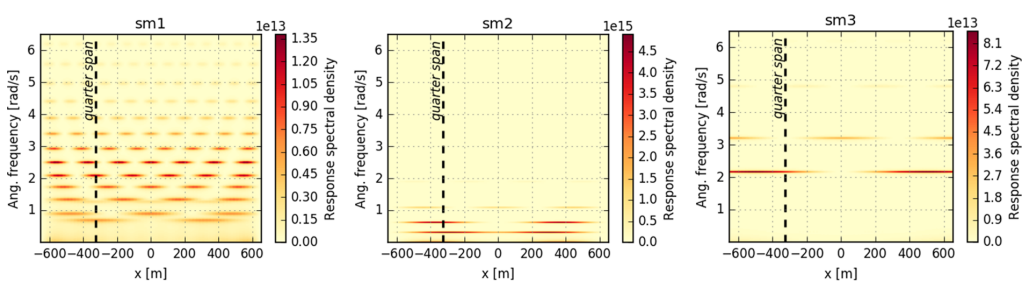

Fig. 12. Response spectral density of the weak axis (sm1), strong axis (sm2) and torsional moment (sm3) for a 30 m/s mean wind velocity case with design basis turbulence definition.

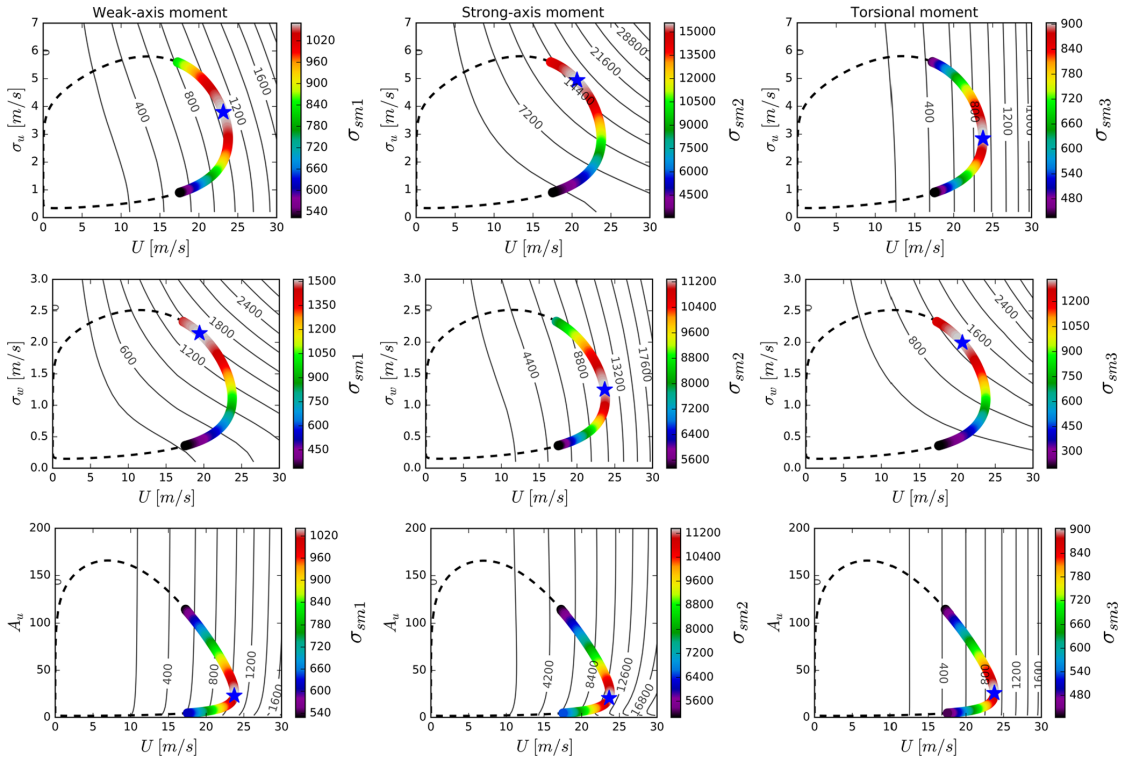

Fig. 13. Buffeting RMS response of weak-axis (sm1), strong-axis (sm2) and torsional moments (sm3) [kNm] along contours for the turbulence components and mean wind velocity for easterly wind, where the larges response is indicated with a blue star marker, and isoresponse lines are shown in the background.

responses of the Hardanger Bridge are not very sensitive to variation in the nondimensional spectral parameters ($A_{u,w}$), but it should be noted that bridges with even lower eigenfrequencies may be more sensitive to variations in these parameters.

In Figs. 15 and 16, the two turbulence parameters most influential to the section moment RMS responses are combined with the mean wind velocity in three-dimensional contour surfaces. The most critical turbulence parameters for the section moments are identified from the two-dimensional contours in Tables 8 and 9 as follows:

- Weak-axis moment, *sm1*; the along-wind and vertical turbulence standard deviations ($\sigma_{u,w}$),
- Strong-axis moment, *sm2*; the along-wind turbulence standard deviation (σ_u) and the along-wind turbulence decay coefficient (K_u),
- Torsional moment, *sm3*; the vertical turbulence standard deviation (σ_w) and the vertical turbulence decay coefficient (K_w).

The maximum response standard deviations and the three-dimensional contour surfaces and seven-dimensional contour manifolds, including all the turbulence parameters, are predicted using constrained numerical optimization and summarized in Tables 10 and 11. The results show significant effects from the turbulence variability on the design environmental conditions for the Hardanger Bridge, with an increased response of up to ~60% when comparing the critical point on the environmental contour surface with the point of the maximum mean wind velocity.

5. Comparison with full-scale response measurements

In Fig. 17, the 10-minute average measured midspan lateral-, vertical- and torsional acceleration RMS responses are shown for the westerly and easterly wind directions for the Hardanger Bridge. The high frequency contribution to the acceleration measurements was removed from the data by low-pass filtering the recorded response with a cut-off frequency of 1 Hz. The traffic density on the Hardanger Bridge is relatively low, and by filtering out the high frequency content, negligible effects from traffic loading are expected for the strong wind acceleration responses. For more information about the processing of the acceleration measurements, the reader is referred to [2].

The measured scatter points are colored based on data density multiplied by the mean wind velocity squared. A second-order polynomial function is fitted to the measurements, as shown in Fig. 17. Using the deterministically chosen design basis turbulence parameters from Table 3, the acceleration responses are calculated and plotted in Fig. 17. Comparing these lines obtained from the design basis values with the measured response shows the limitations of the traditional design methodology, which is unable to describe the scattered response observed from the measurements.

An upper and lower bound for the acceleration response was calculated as a function of the mean wind velocity using the environmental contour method to investigate how the measured midspan acceleration response corresponds with the response predictions. These estimates were calculated by finding the maximum and minimum responses on a 100-year return period environmental contour surface constrained to a given mean wind velocity. Thus, for each considered mean wind velocity, a point for the upper and lower bound lines was identified. The environmental contour bounds were based on contour surfaces from the mean wind velocity together with the following turbulence parameters:

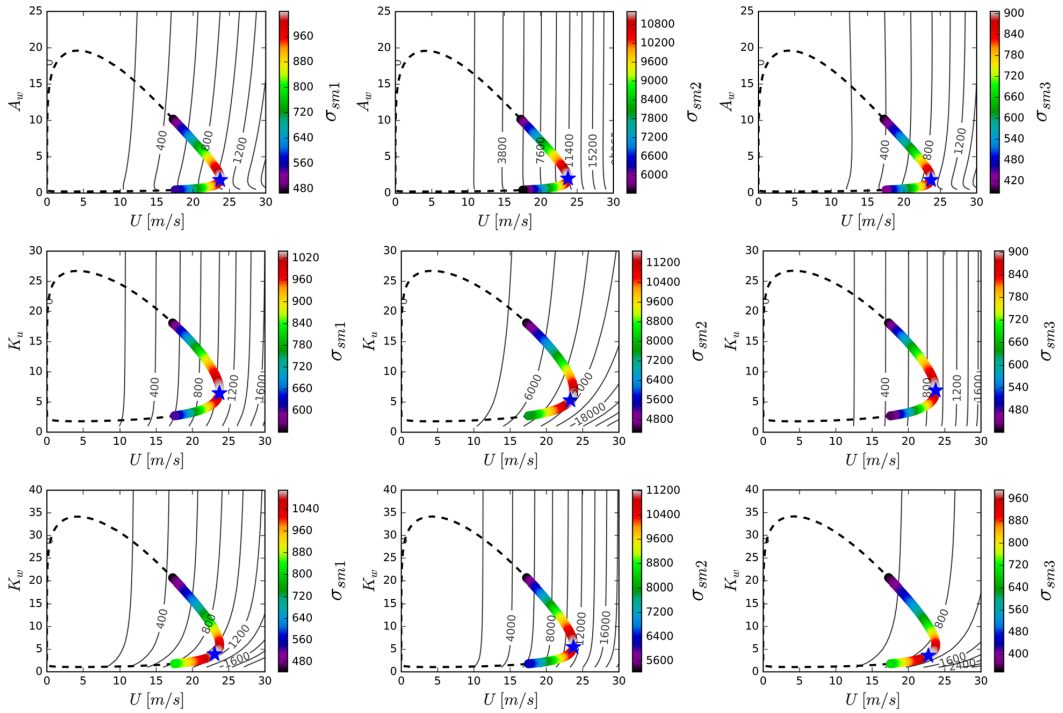

Fig. 13. (*continued*)

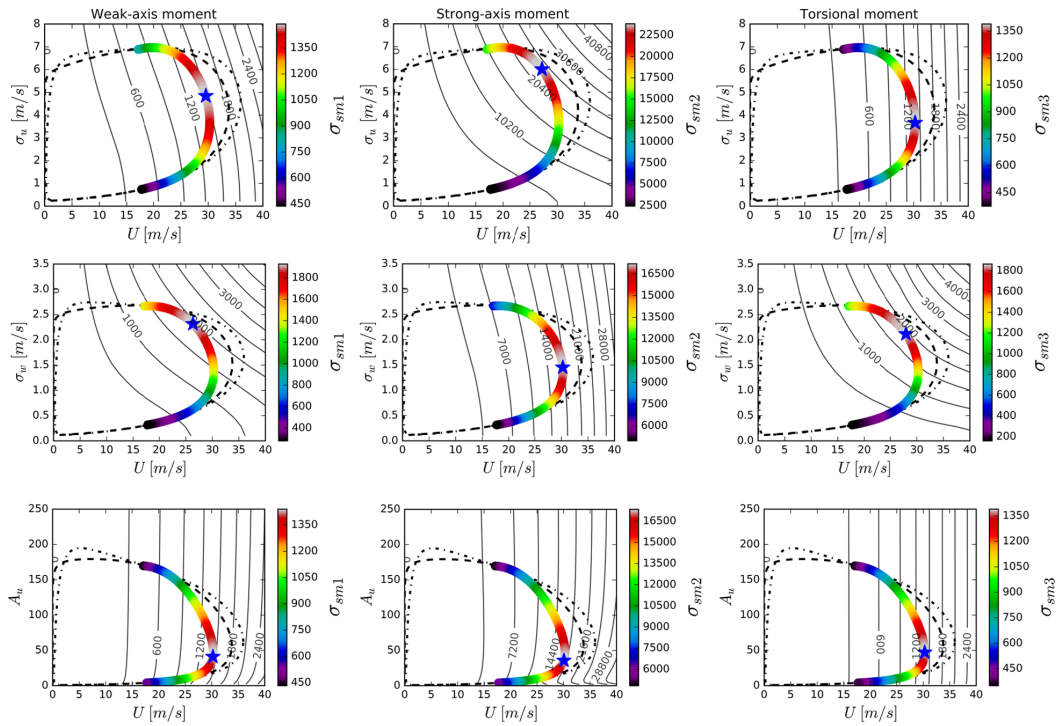

Fig. 14. Buffeting RMS response of weak-axis (sm1), strong-axis (sm2) and torsional moments (sm3) [kN m] along contours for the turbulence components and mean wind velocity for westerly winds, where the larges response is indicated with a blue star marker, and isoresponse lines are shown in the background.

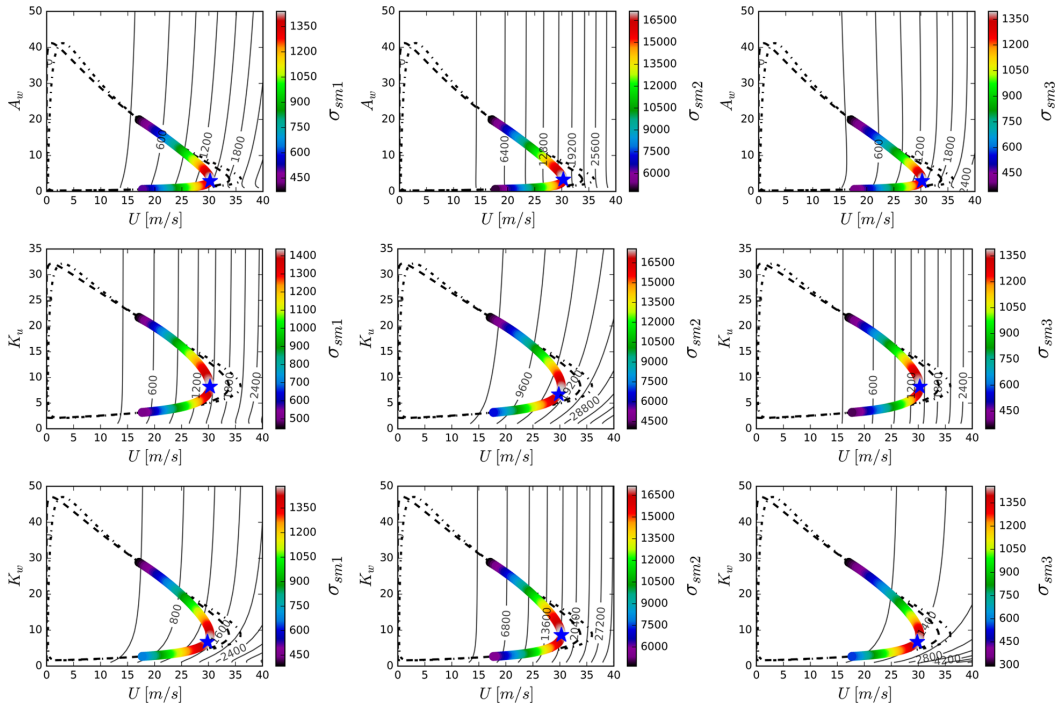

Fig. 14. (*continued*)

- Horizontal acceleration, *a2*; the along-wind turbulence standard deviation (σ_u) and the along-wind turbulence decay coefficient (K_u),
- Vertical acceleration, *a3*; the along-wind and vertical turbulence standard deviations ($\sigma_{u,w}$),
- Torsional acceleration, *ar1*; the vertical turbulence standard deviation (σ_w) and the vertical turbulence decay coefficient (K_w).

As shown in Fig. 17, the acceleration response bounds predicted by the environmental contour method eclipse most of the measured scatter for all response quantities and both wind directions. These bounds are based on the 100-year return period environmental contours and compared with approximately 4 years of measurement data. Theoretically, all measurement data should lie within these bounds, but uncertainties in the probabilistic turbulence model, the buffeting calculations and the simplification where only the two most important turbulence parameters are included in the environmental contours may affect these results.

When considering the horizontal acceleration, the trend in the scatter is followed very well for both wind directions, but especially for the easterly winds, the bounds are too narrow to be able to eclipse the full scatter of the measurement data. Limitations in the probabilistic turbulence model, such as omitting the angle of attack, may affect the predicted response. Additionally, other assumptions made in the buffeting calculations, such as the assumption of stationarity, may affect the results.

The vertical acceleration response bounds cover the measured scatter data very well for both wind directions. In addition to uncertainties regarding the probabilistic turbulence model and simplifications in the buffeting calculations, some uncertainty from the self-excited forces is introduced for the vertical acceleration response. The midspan acceleration response spectral densities normalized with the maximum response spectrum amplitude for each mean wind velocity are shown in Fig. 18. The reduced velocity range where aerodynamic derivative test data are available is indicated in the plots. For the vertical acceleration response, many contributions come from the reduced velocity range extrapolated from the AD test range. This introduces some uncertainty into the vertical acceleration response estimates.

When considering the torsional response, the predicted torsional

Table 8
Maximum RMS section moments in the girder quarter span from contour lines based on the mean wind velocity and one turbulence parameter for easterly winds. The percentage of increased response compared with the event of the maximum mean wind speed ($U = 23.76$ m/s, $\sigma_u = 2.84$ m/s, $\sigma_w = 1.10$ m/s, $A_u = 25.8$, $A_w = 2.01$, $K_u = 6.92$, $K_w = 5.98$) is indicated.

Contour variables	U m/s	Turb Var	σ_{sm1} kN m	%	U m/s	Turb Var	σ_{sm2} kN m	%	U m/s	Turb Var	σ_{sm3} kN m	%
U	23.76	–	1039	0	23.76	–	11,206	0	23.76	–	903	0
U, σ_u	23.13	3.80 m/s	1070	3	20.64	4.94 m/s	15,580	39	23.76	2.84 m/s	903	0
U, σ_w	19.43	2.15 m/s	1513	46	23.67	1.25 m/s	11,284	1	20.64	2.00 m/s	1333	48
U, A_u	23.73	23.0	1041	0	23.64	20.5	11,358	1	23.76	25.8	903	0
U, A_w	23.73	1.80	1039	0	23.76	2.02	11,206	0	23.73	1.80	906	0
U, K_u	23.73	6.47	1039	0	23.31	5.30	11,688	4	23.76	6.92	903	0
U, K_w	23.06	3.89	1110	7	23.73	5.48	11,221	0	22.76	3.58	992	10

Table 9
Maximum RMS section moments in the girder quarter span from contour lines based on the mean wind velocity and one turbulence parameter for westerly winds. The percentage of increased response compared with the event of the maximum mean wind speed (U = 30.30 m/s, σ_u = 3.66 m/s, σ_w = 1.36 m/s, A_u = 47.1, A_w = 3.32, K_u = 8.21, K_w = 8.65) is indicated.

Contour variables	U m/s	Turb Var	σ_{sm1} kN m	%	U m/s	Turb Var	σ_{sm2} kN m	%	U m/s	Turb Var	σ_{sm3} kN m	%
U	30.28	–	1437	0	30.28	–	17,131	0	30.28	–	1390	0
U, σ_u	29.55	4.84 m/s	1488	4	27.20	6.01 m/s	23,821	39	30.28	3.66 m/s	1390	0
U, σ_w	26.36	2.32 m/s	1928	34	30.25	1.45 m/s	17,198	0	27.94	2.11 m/s	1865	34
U, A_u	30.22	41.1	1440	0	30.07	35.7	17,337	1	30.28	47.1	1390	0
U, A_w	30.22	2.93	1440	0	30.28	3.32	17,131	0	30.22	2.93	1396	0
U, K_u	30.28	8.21	1437	0	29.81	6.70	17,555	2	30.28	8.21	1390	0
U, K_w	29.81	6.73	1483	3	30.28	8.65	17,131	0	29.81	6.73	1458	5

accelerations seem to be strongly overpredicted for both wind directions. Almost all the contributions to the response are based on self-excited forces outside the reduced velocity AD test range, except for the very high mean wind velocities. Along with sensitivity to the static coefficients, this will introduce significant uncertainty to these predictions.

6. Conclusions

Turbulence uncertainty effects on the buffeting response of the Hardanger Bridge girder have been investigated using the environmental contour method. The results show large effects on the predicted response and potential for substantial improvements to the current

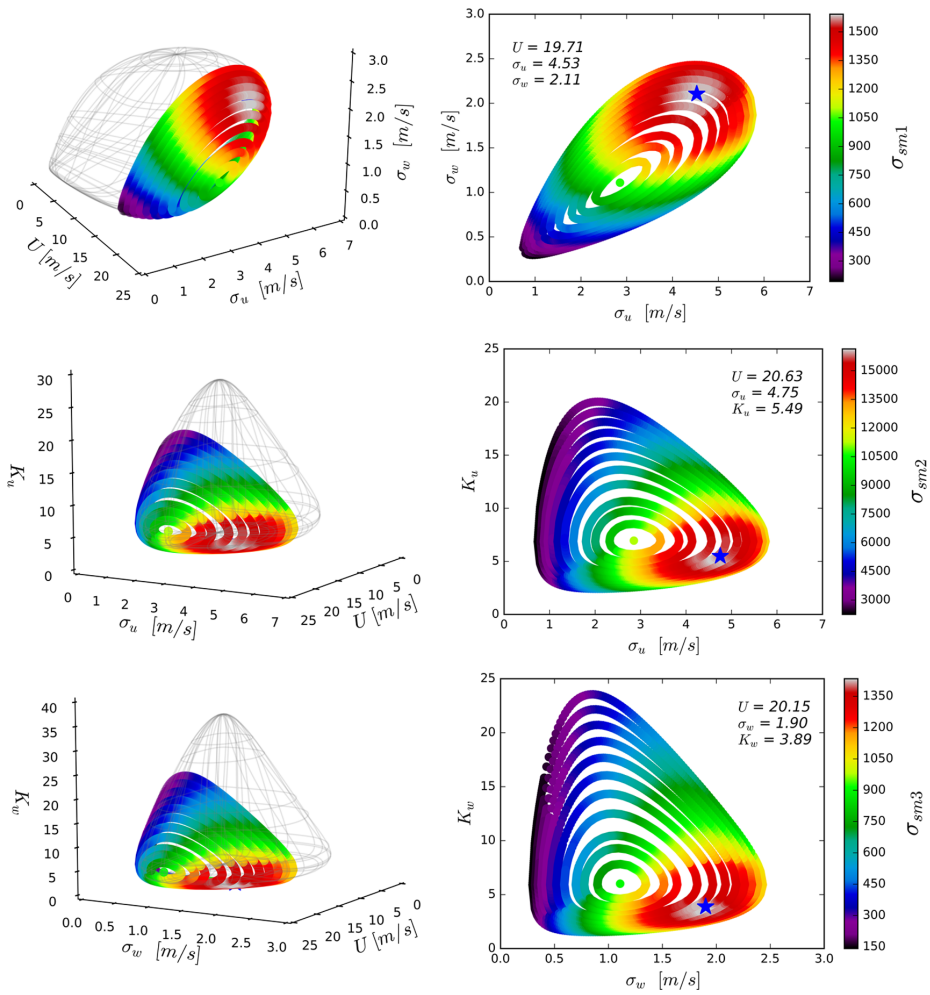

Fig. 15. Buffeting RMS response of weak-axis (sm1), strong-axis (sm2) and torsional moments (sm3) [kN m] on contour surfaces for the turbulence components and mean wind velocity for easterly wind, where the larges response is indicated with a blue star marker.

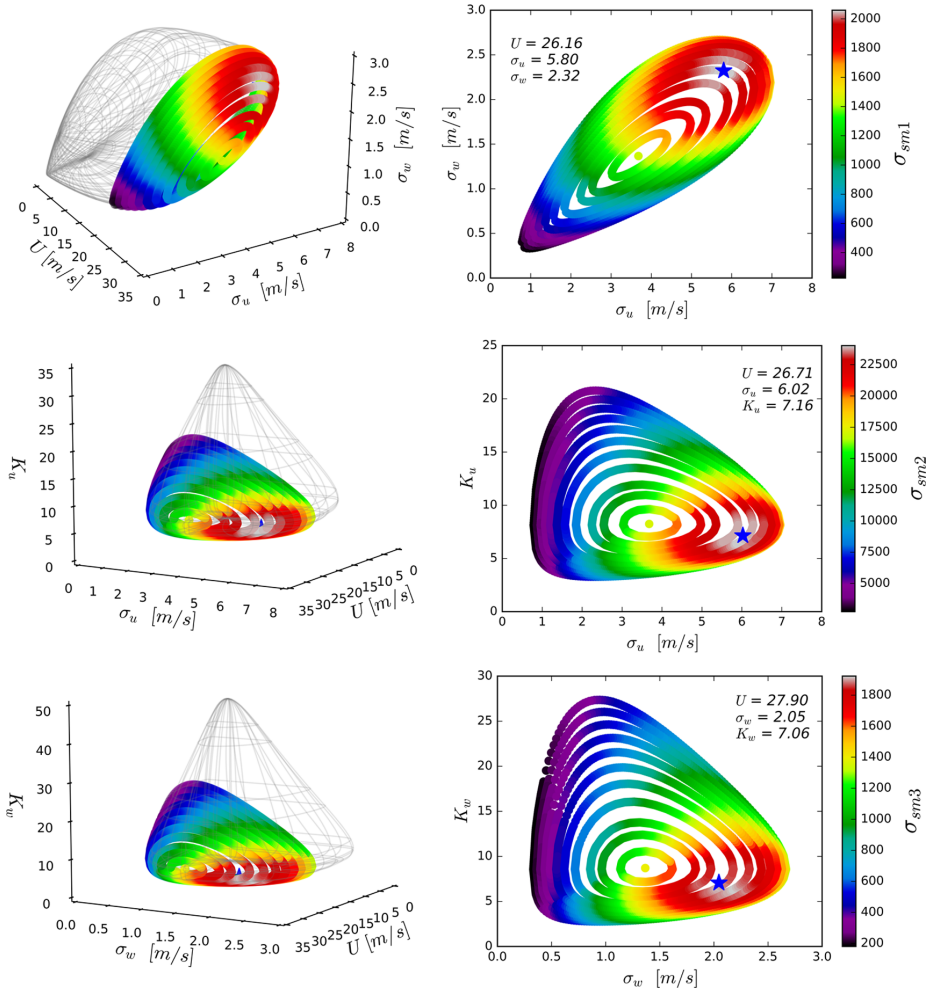

Fig. 16. Buffeting RMS response of weak-axis (sm1), strong-axis (sm2) and torsional moments (sm3) [kN m] on contour surfaces for the turbulence components and mean wind velocity for westerly winds, where the larges response is indicated with a blue star marker.

design methodology. The following conclusions can be drawn:

- By describing the turbulence parameters with lognormal distributions, the transformation between the standard normal space and the real space is practically achievable for multiple variables even with a limited amount of measurement data.
- Numerical optimization algorithms constrained to find solutions on the environmental contour were successfully used in the investigations presented in this paper. The method is especially suitable when the number of environmental variables exceeds two.
- The knowledge that the critical environmental situations will be in the tail of the mean wind velocity marginal distribution can be used

Table 10
Easterly winds maximum RMS section moments in the girder quarter span identified from numerical optimization on the environmental contours considering interesting turbulence parameter combinations. The percentage of increased response compared with the event of the maximum mean wind speed is indicated.

Contour variables	U m/s	σ_u m/s	σ_w m/s	A_u –	A_w –	K_u –	K_w –	σ_{sm1} kN m	%	σ_{sm2} kN m	%	σ_{sm3} kN m	%
U	23.76	2.84	1.10	25.8	2.01	6.92	5.98	1039	0	11,206	0	903	0
U, σ_u, σ_w	19.71	4.53	2.11	25.8	2.01	6.92	5.98	1599	54	–	–	–	–
U, σ_u, K_u	20.63	4.75	0.96	25.8	2.01	5.49	5.98	–	–	16,232	45	–	–
U, σ_w, K_w	20.15	2.41	1.90	25.8	2.01	6.92	3.89	–	–	–	–	1438	59
All	19.26	4.33	2.00	22.4	2.32	6.11	3.93	1683	62	–	–	–	–
All	20.51	4.70	1.74	25.8	2.09	5.47	5.14	–	–	16,716	49	–	–
All	20.27	4.08	1.87	23.3	2.29	6.22	3.90	–	–	–	–	1418	57

Table 11
Westerly winds maximum RMS section moments in the girder quarter span identified from numerical optimization on the environmental contours considering interesting turbulence parameter combinations. The percentage of increased response compared with the event of the maximum mean wind speed is indicated.

Contour variables	U m/s	σ_u m/s	σ_w m/s	A_u –	A_w –	K_u –	K_w –	σ_{sm1} kNm	%	σ_{sm2} kNm	%	σ_{sm3} kNm	%
U	30.3	3.66	1.36	47.1	3.32	8.21	8.65	1437	0	17,131	0	1390	0
U, σ_u, σ_w	26.2	5.80	2.32	47.1	3.32	8.21	8.65	2070	44	–	–	–	–
U, σ_u, K_u	26.7	6.02	1.20	47.1	3.32	7.16	8.65	–	–	24,431	43	–	–
U, σ_w, K_w	27.9	3.37	2.05	47.1	3.32	8.21	7.06	–	–	–	–	1929	39
All	25.9	5.64	2.26	37.7	3.69	7.46	6.96	2112	47	–	–	–	–
All	26.4	5.94	2.12	47.3	3.24	7.07	7.73	–	–	24,830	45	–	–
All	27.9	5.12	2.03	41.1	3.74	7.60	7.06	–	–	–	–	1910	37

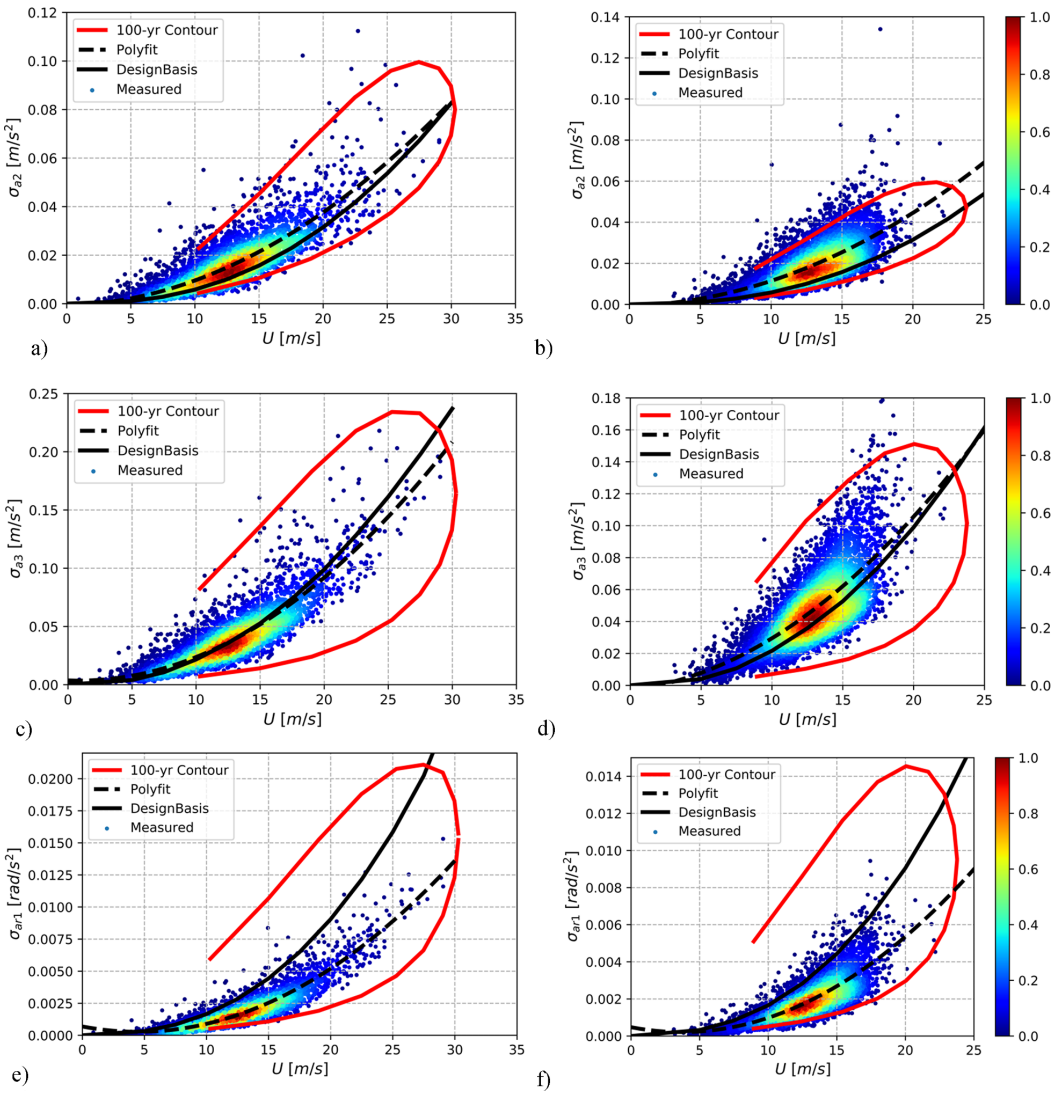

Fig. 17. Calculated and measured RMS girder acceleration response at the midspan with color bar indicating data density multiplied by U^2: (a) westerly winds lateral response, (b) easterly winds lateral response, (c) westerly winds vertical response, (d) easterly winds vertical response, (e) westerly winds torsional response and (f) easterly winds torsional response.

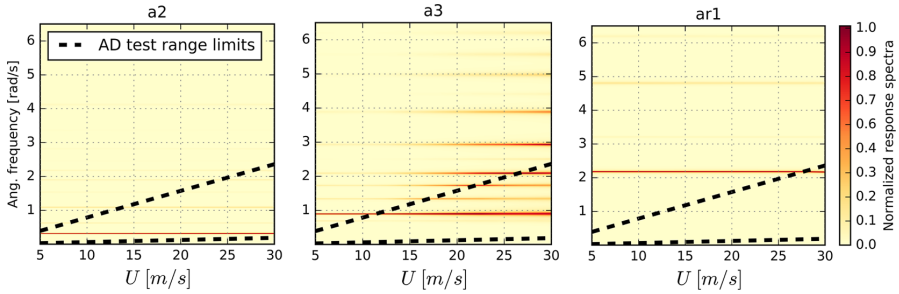

Fig. 18. Acceleration response spectral density, normalized on the maximum value for each wind speed, and AD test range indication.

as an advantage to focus the effort on fitting the PDF in the extreme tail region. Asymptotic extreme value theory was used in this work to transform the fitted extreme value distribution to the parent distribution form to achieve an enhanced marginal PDF estimate for the important range of mean wind velocities.

- Including the variability in the turbulence parameters by using the environmental contour method indicated significant effects on the important section moments for the Hardanger Bridge girder. Compared with the point on the contour with maximum mean wind velocity, an increased design response of up to ~60% was found.
- By estimating an upper and lower bound response using the environmental contour method, the scattered acceleration response measurements from the Hardanger Bridge were eclipsed, showing significant improvements to the traditional design methodology.
- The findings in this paper indicate that long-term response calculation methods, including the turbulence parameters as stochastic variables, should be considered for long-span bridges where the buffeting response is expected to significantly affect the structural reliability.

CRediT authorship contribution statement

Tor M. Lystad: Conceptualization, Methodology, Software, Formal analysis, Writing - original draft, Writing - review & editing, Visualization. **Aksel Fenerci:** Validation, Investigation, Data curation. **Ole Øiseth:** Conceptualization, Supervision, Project administration.

Declaration of Competing Interest

The authors declare that they have no known competing financial interests or personal relationships that could have appeared to influence the work reported in this paper.

Acknowledgments

Funding: The research presented in this paper has been financed by Norconsult AS, The Norwegian Public Roads Administration (NPRA) and The Research Council of Norway.

References

[1] Dunham KK. Coastal Highway Route E39 – Extreme Crossings. Transp Res Procedia 2016;14:494–8. https://doi.org/10.1016/J.TRPRO.2016.05.102.
[2] Fenerci A, Øiseth O, Rönnquist A. Long-term monitoring of wind field characteristics and dynamic response of a long-span suspension bridge in complex terrain. Eng Struct 2017;147:269–84. https://doi.org/10.1016/j.engstruct.2017.05.070.
[3] Fenerci A, Øiseth O. Measured buffeting response of a long-span suspension bridge compared with numerical predictions based on design wind spectra. J Struct Eng 2017;143. https://doi.org/10.1061/(ASCE)ST.1943-541X.0001873.
[4] Fenerci A, Øiseth O. Strong wind characteristics and dynamic response of a long-span suspension bridge during a storm. J Wind Eng Ind Aerodyn 2018;172:116–38. https://doi.org/10.1016/j.jweia.2017.10.030.
[5] Fenerci A, Øiseth O. Site-specific data-driven probabilistic wind field modeling for the wind-induced response prediction of cable-supported bridges. J Wind Eng Ind Aerodyn 2018;181:161–79. https://doi.org/10.1016/J.JWEIA.2018.09.002.
[6] Lystad TM, Fenerci A, Øiseth O. Evaluation of mast measurements and wind tunnel terrain models to describe spatially variable wind field characteristics for long-span bridge design. J Wind Eng Ind Aerodyn 2018;179:558–73. https://doi.org/10.1016/J.JWEIA.2018.06.021.
[7] Lystad TM, Fenerci A, Øiseth O. Aerodynamic effect of non-uniform wind profiles for long-span bridges. Proc. XV Conf. Ital. Assoc. Wind Eng. Springer; 2018. p. 427–39.
[8] Brownjohn JMW, Bocciolone M, Curami A, Falco M, Zasso A. Humber bridge full-scale measurement campaigns 1990–1991. J Wind Eng Ind Aerodyn 1994;52:185–218. https://doi.org/10.1016/0167-6105(94)90047-7.
[9] Miyata T, Yamada H, Katsuchi H, Kitagawa M. Full-scale measurement of Akashi-Kaikyo Bridge during typhoon. J Wind Eng Ind Aerodyn 2002;90:1517–27. https://doi.org/10.1016/S0167-6105(02)00267-2.
[10] Macdonald JHG. Evaluation of buffeting predictions of a cable-stayed bridge from full-scale measurements. J Wind Eng Ind Aerodyn 2003;91:1465–83. https://doi.org/10.1016/J.JWEIA.2003.09.009.
[11] Wang H, Li A, Guo T, Xie J. Field measurement on wind characteristic and buffeting response of the Runyang Suspension Bridge during typhoon Matsa. Sci China, Ser E Technol Sci 2009;52:1354–62. https://doi.org/10.1007/s11431-008-0238-y.
[12] Wang H, Asce M, Tao T, Asce SM, Gao Y, Xu F. Measurement of Wind Effects on a Kilometer-Level Cable-Stayed Bridge during Typhoon Haikui. J Struct Eng 2018;144:1–23. https://doi.org/10.1061/(ASCE)ST.1943-541X.0002138.
[13] Cheynet E, Bogunovic Jakobsen J, Snæbjörnsson J. Buffeting response of a suspension bridge in complex terrain. Eng Struct 2016;128:474–87. https://doi.org/10.1016/J.ENGSTRUCT.2016.09.060.
[14] Meng X, Nguyen DT, Xie Y, Owen JS, Psimoulis P, Ince S, et al. Design and implementation of a new system for large bridge monitoring—geoshm. Sensors 2018;18. http://doi.org/10.3390/s18030775.
[15] Stephen GA, Brownjohn JMW, Taylor CA. Measurements of static and dynamic displacement from visual monitoring of the Humber Bridge. Eng Struct 1993;15:197–208. https://doi.org/10.1016/0141-0296(93)90054-8.
[16] Mao J-X, Wang H, Feng D-M, Tao T-Y, Zheng W-Z. Investigation of dynamic properties of long - span cable - stayed bridges based on one - year monitoring data under normal operating condition. Struct Control Heal Monit 2018;25:1–19. https://doi.org/10.1002/stc.2146.
[17] Wang H, Hu R, Xie J, Tong T, Li A. Comparative study on buffeting performance of Sutong Bridge based on design and measured spectrum. J Bridg Eng 2013;18:587–600. https://doi.org/10.1061/(ASCE)BE.1943-5592.0000394.
[18] Naess A, Moan T. Stochastic Dynamics of Marine Structures. Cambridge University Press; 2013. http://doi.org/10.1017/CBO9781139021364.
[19] Winterstein SR, Haver S. Environmental Parameters For Extreme Response : Inverse FORM with Omission Factors. Proc 6th Int. Conf Struct. Saf. Reliab., Innsbruck, Austria: 1993.
[20] Haver S, Kleiven G. Environmental Contour Lines for Design Purposes: Why and When? 23rd Int. Conf. Offshore Mech. Arct. Eng. Vol. 1, Parts A B, 2004, p. 337–45. http://doi.org/10.1115/OMAE2004-51157.
[21] Bang Huseby A, Vanem E, Natvig B. A new approach to environmental contours for ocean engineering applications based on direct Monte Carlo simulations. Ocean Eng 2013;60:124–35. https://doi.org/10.1016/J.OCEANENG.2012.12.034.
[22] Vanem E. A comparison study on the estimation of extreme structural response from different environmental contour methods. Mar Struct 2017;56:137–62. https://doi.org/10.1016/j.marstruc.2017.07.002.
[23] Chai W, Leira BJ. Environmental contours based on inverse SORM. Mar Struct 2018;60:34–51. https://doi.org/10.1016/J.MARSTRUC.2018.03.007.
[24] Moriarty PJ, Holley WE, Butterfield S. Effect of trbulence variation on extreme loads prediction for wind turbines. J Sol Energy Eng 2002;124:387–95. https://doi.org/10.1115/1.1510137.
[25] Fitzwater LM, Cornell CA, Veers PS. Using environmental contours to predict extreme events on wind turbines. Proc Wind 2003 ASME Wind Energy Symp 2003. https://doi.org/10.1115/WIND2003-865.
[26] Saranyasoontorn K, Manuel L. Design loads for wind turbines using the environmental contour method. J Sol Energy Eng 2006;125:554–61. https://doi.org/10.1115/1.2346700.
[27] Hannesdóttir Á, Kelly M, Dimitrov N. Extreme wind fluctuations: joint statistics,

extreme turbulence, and impact on wind turbine loads. Wind Energy Sci 2019;4:325–42. https://doi.org/10.5194/wes-4-325-2019.
[28] Xu Y, Øiseth O, Naess A, Moan T. Prediction of long-term extreme load effects due to wind for cable-supported bridges using time-domain simulations. Eng Struct 2017;148:239–53. https://doi.org/10.1016/J.ENGSTRUCT.2017.06.051.
[29] Xu Y, Øiseth O, Moan T, Naess A. Prediction of long-term extreme load effects due to wave and wind actions for cable-supported bridges with floating pylons. Eng Struct 2018;172:321–33. https://doi.org/10.1016/J.ENGSTRUCT.2018.06.023.
[30] Davenport AG. The relationship of reliability to wind loading. J Wind Eng Ind Aerodyn 1983;13:3–27. https://doi.org/10.1016/0167-6105(83)90125-3.
[31] Kareem A. Aerodynamic response of structures with parametric uncertainties. Struct Saf 1988;5:205–25. https://doi.org/10.1016/0167-4730(88)90010-0.
[32] Solari G. Wind-excited response of structures with uncertain parameters. Probabilistic Eng Mech 1997;12:75–87. https://doi.org/10.1016/S0266-8920(96)00027-6.
[33] Zhang L, Li J, Peng Y. Dynamic response and reliability analysis of tall buildings subject to wind loading. J Wind Eng Ind Aerodyn 2008;96:25–40. https://doi.org/10.1016/J.JWEIA.2007.03.001.
[34] Pagnini LC, Solari G. Gust buffeting and turbulence uncertainties. J Wind Eng Ind Aerodyn 2002;90:441–59. https://doi.org/10.1016/S0167-6105(01)00202-1.
[35] Pagnini L. Reliability analysis of wind-excited structures. J Wind Eng Ind Aerodyn 2010;98:1–9. https://doi.org/10.1016/J.JWEIA.2009.08.010.
[36] Seo D, Caracoglia L. Statistical buffeting response of flexible bridges influenced by errors in aeroelastic loading estimation. J Wind Eng Ind Aerodyn Wind Eng Ind Aerodyn 2012;104–106:129–40. https://doi.org/10.1016/j.jweia.2012.03.036.
[37] Seo D, Caracoglia L. Estimating life-cycle monetary losses due to wind hazards: Fragility analysis of long-span bridges. Eng Struct 2013;56:1593–606. https://doi.org/10.1016/j.engstruct.2013.07.031.
[38] Solari G, Piccardo G. Probabilistic 3-D turbulence modeling for gust buffeting of structures. Probabilistic Eng Mech 2001;16:73–86. https://doi.org/10.1016/S0266-8920(00)00010-2.
[39] Moan T, Gao Z, Ayala-Uraga E. Uncertainty of wave-induced response of marine structures due to long-term variation of extratropical wave conditions. Mar Struct 2005;18:359–82. https://doi.org/10.1016/J.MARSTRUC.2005.11.001.
[40] Jonathan P, Flynn J, Ewans K. Joint modelling of wave spectral parameters for extreme sea states. Ocean Eng 2010;37:1070–80. https://doi.org/10.1016/J.OCEANENG.2010.04.004.
[41] Ewans K, Jonathan P. Evaluating environmental joint extremes for the offshore industry using the conditional extremes model. J Mar Syst 2014;130:124–30. https://doi.org/10.1016/J.JMARSYS.2013.03.007.
[42] Salvadori G, Tomasicchio GR, D'Alessandro F. Practical guidelines for multivariate analysis and design in coastal and off-shore engineering. Coast Eng 2014;88:1–14. https://doi.org/10.1016/J.COASTALENG.2014.01.011.
[43] Montes-Iturrizaga R, Heredia-Zavoni E. Environmental contours using copulas. Appl Ocean Res 2015;52:125–39. https://doi.org/10.1016/J.APOR.2015.05.007.
[44] Eckert-Gallup AC, Sallaberry CJ, Dallman AR, Neary VS. Application of principal component analysis (PCA) and improved joint probability distributions to the inverse first-order reliability method (I-FORM) for predicting extreme sea states. Ocean Eng 2016;112:307–19. https://doi.org/10.1016/J.OCEANENG.2015.12.018.
[45] Haver S. Wave climate off northern Norway. Appl Ocean Res 1985;7:85–92. https://doi.org/10.1016/0141-1187(85)90038-0.
[46] Gumbel EJ. Statistics of extremes. New York: Columbia University Press; 1958.
[47] Madsen HO, Krenk S, Lind NC. Methods of structural safety. New York: Dover Publications; 1986.
[48] Rosenblatt M. Remarks on a Multivariate Transformation. Ann Math Stat 1952;23:470–2.
[49] Kaimal J, Wyngaard J, Izumi Y, Coté OR. Spectral characteristics of surface-layer turbulence. Q J R Meteorol Soc 1972;98. https://doi.org/10.1002/qj.49709841707.
[50] Davenport AG. The spectrum of horizontal gustiness near the ground in high winds. Q J R Meteorol Soc 1961;87:194–211. https://doi.org/10.1002/qj.49708737208.
[51] Statens-Vegvesen. The Hardanger Bridge: Design basis - Wind characteristics. Norway: 2006.
[52] Lieblein J. Efficient methods of extreme-value methodology. Washington D.C.: 1974.
[53] Cook NJ. Towards better estimation of extreme winds. J Wind Eng Ind Aerodyn 1982;9:295–323.
[54] Harris RI. Improvements to the 'Method of Independent Storms'. J Wind Eng Ind Aerodyn 1999;80:1–30. https://doi.org/10.1016/S0167-6105(98)00123-8.
[55] Jain A, Jones NP, Scanlan RH. Coupled aeroelastic and aerodynamic response analysis of long-span bridges. J Wind Eng Ind Aerodyn 1996;60:69–80. https://doi.org/10.1016/0167-6105(96)00024-4.
[56] Jain A, Jones NP, Scanlan RH. Coupled flutter and buffeting analysis. J Struct Eng 1996;122:716–25. https://doi.org/10.1061/(ASCE)0733-9445(1996)122:7(716).
[57] Chen X, Kareem A, Matsumoto M. Multimode coupled flutter and buffeting analysis of long span bridges. J Wind Eng Ind Aerodyn 2001;89:649–64. https://doi.org/10.1016/S0167-6105(01)00064-2.
[58] Øiseth O, Rönnquist A, Sigbjörnsson R. Simplified prediction of wind-induced response and stability limit of slender long-span suspension bridges, based on modified quasi-steady theory: A case study. J Wind Eng Ind Aerodyn 2010;98:730–41. https://doi.org/10.1016/j.jweia.2010.06.009.
[59] Katsuchi H, Jones NP, Scanlan RH, Akiyama H. Multi-mode flutter and buffeting analysis of the Akashi-Kaikyo bridge 1998;77–78:431–41. http://doi.org/10.1016/S0167-6105(98)00162-7.
[60] Python Software Foundation. Python Language Reference; 2019.
[61] Dassault Systèmes W. ABAQUS;2018.
[62] Siedziako B, Øiseth O, Rønnquist A. An enhanced forced vibration rig for wind tunnel testing of bridge deck section models in arbitrary motion. J Wind Eng Ind Aerodyn 2017;164:152–63. https://doi.org/10.1016/J.JWEIA.2017.02.011.
[63] Larose GL. The dynamic action of gusty winds on long-span bridges: The dynamic action of gusty winds on long-span bridges; 1997.
[64] Standard Norge. Eurocode 1: Actions on structures - Part 1-4: General actions, Wind actions; 2009.
[65] Scanlan RH, Tomko JJ. Airfoil and bridge deck flutter derivatives. J Eng Mech Div 1971;97:1717–37.
[66] Zasso A. Flutter derivatives: Advantages of a new representation convention. J Wind Eng Ind Aerodyn 1996;60:35–47. https://doi.org/10.1016/0167-6105(96)00022-0.
[67] The SciPy Community. SciPy.org. May 17 2019. https://docs.scipy.org/doc/scipy/reference/generated/scipy.optimize.minimize.html [accessed August 22, 2019].

Paper IV

Tor Martin Lystad, Aksel Fenerci and Ole Øiseth

Long-term extreme buffeting response of cable-supported bridges with uncertain turbulence parameters

Engineering structures 2021:236, Copyright Elsevier

Engineering Structures 236 (2021) 112126

Contents lists available at ScienceDirect

Engineering Structures

journal homepage: www.elsevier.com/locate/engstruct

Long-term extreme buffeting response of cable-supported bridges with uncertain turbulence parameters

Tor M. Lystad [a,b,*], Aksel Fenerci [b], Ole Øiseth [b]

[a] Bridge Department, Norconsult AS, Sandvika, Norway
[b] Department of Structural Engineering, Norwegian University of Science and Technology, Trondheim, Norway

ARTICLE INFO

Keywords:
Long-span bridge
Extreme response
Long-term response
Turbulence variability

ABSTRACT

Although the full long-term method (FLM) is recognized as the appropriate way to identify the design stresses of marine structures subjected to stochastic environmental loading, the FLM has not yet been adopted for the design of wind excited long-span bridges. The results presented in this study show that the current design practice, through short-term extreme response analyses with deterministic turbulence parameters, may significantly underestimate the long-term design stresses of long-span bridges. Both the variability of the turbulence parameters and the uncertainty in the short-term extreme response are found to be important when estimating the design stresses. In addition, the long-term extreme acceleration responses have been compared with the acceleration responses measured in full scale at the Hardanger Bridge, showing considerable improvements to the current design practice.

1. Introduction

Several full-scale measurement campaigns around the world have identified large variability in the measured dynamic response of long-span bridges subjected to wind loading [1–7]. By accounting for the uncertainty in the turbulence field, it was found in [8,9] that the variability in the measured acceleration response of the Hardanger Bridge could be predicted. They also showed that the design guidelines strongly underpredicted the largest root-mean-square acceleration responses measured in full scale at the Hardanger Bridge. The observations from these studies indicate a need to revisit the design practice for long-span bridges, especially as bridges become increasingly longer and more sensitive to dynamic wind loading [10].

The characteristic load effect used in structural design calculations is defined by a yearly exceedance probability, p. This probability can be expressed through a statistical return period in years, $p = 1/R_{yr}$. A common simplification in design calculations for linear systems is to define the return period of the load effect equal to the return period of the load. This approach will, in general, not be correct for a cable-supported bridge subjected to turbulent wind loading since the load effect will be a stochastic process. However, in current bridge engineering practice, this simplification is widely used, and the characteristic load effect is calculated as the expected extreme response from a short-term storm defined by a mean wind velocity with a return period, R_{yr}, and its corresponding deterministic turbulence parameters. This approach introduces two important assumptions: 1) the variability of the turbulence parameters can be neglected or treated in a simplified manner, and 2) the uncertainty of the short-term extreme peak response can be treated deterministically by its expected value.

In recent years, some studies have investigated the effect of these assumptions. Lystad et al. [8] investigated the effect of uncertain turbulence parameters on the buffeting response of the Hardanger Bridge using the environmental contour method (ECM), identifying considerable effects on the prediction of the largest bridge response. Xu et al. [11] found that due to the uncertainty of the short-term response, the long-term extreme response would significantly exceed the expected value of the short-term extreme buffeting response of a long-span suspension bridge. This effect is well-known in the field of marine engineering [12,13], and standards for the design of offshore structures already recommend accounting for such effects [14]. These studies indicate that the abovementioned simplifications may introduce significant inaccuracies in the current design practice.

Long-term extreme value methodology is recognized as the most accurate way to estimate the extreme load effects from stochastic environmental excitation of marine structures [15]. In such calculations, the R_{yr} return period load effect is calculated directly, accounting for the

* Corresponding author at: Bridge Department, Norconsult AS, Sandvika, Norway.
E-mail address: tor.m.lystad@ntnu.no (T.M. Lystad).

https://doi.org/10.1016/j.engstruct.2021.112126
Received 23 November 2020; Received in revised form 18 February 2021; Accepted 23 February 2021

uncertainty of the structural response. The important parameters defining the load process are treated as stochastic variables and described by a joint probability distribution.

Several formulations of the full long-term method (FLM) exist [16], and they all need to integrate the short-term response statistics over all relevant environmental combinations, making them very computationally demanding. The long-term extreme value problem can also be solved by simplified reliability methods such as the inverse first-order reliability method (IFORM) [17,18] and the environmental contour method (ECM) [19]. These methods are attractive because they are relatively efficient from a computational perspective. The IFORM can be used to estimate the R_{yr} return period long-term extreme response directly, where the short-term extreme response is included as a random variable. The ECM is an inverse reliability method that can be used to identify R_{yr} return period short-term load situations based on the joint probability of several environmental variables. The environmental contour method separates the variability of the environmental parameters and the uncertainty of the short-term extreme response itself. Therefore, to estimate the long-term extreme load effect, the omission of this variability needs to be corrected.

Probabilistic frameworks in wind engineering have been investigated in the literature [20–29]. These frameworks focus mostly on uncertainties in the load and the structural properties with methods to estimate the reliability of the structure. With the FLM, the probability distribution of the extreme response of a system subjected to stochastic environmental loads is calculated. This process is valuable since the R_{yr} return period load effect can be drawn directly from this distribution to be used in ordinary design calculations, but it can also provide valuable information for possible structural reliability considerations.

In this paper, long-term extreme value methodology is used to investigate the extreme design stresses in the Hardanger Bridge girder due to turbulent wind loading. In Section 2, the theoretical basis is outlined, and in Section 3, the buffeting analyses are described. In Section 4, long-term extreme value predictions are presented for the design stresses of the Hardanger Bridge girder, showing significant effects from extreme value- and turbulence uncertainty on the extreme stresses. The FLM, IFORM and ECM are all used to estimate the long-term extreme response. Furthermore, in Section 5, long-term extreme acceleration response predictions are compared with full-scale measurements, showing considerable improvements to the current design practice.

2. Extreme response calculation methods

For the ultimate limit state design of structures subjected to stochastic wind loads, three approaches can be used to estimate the design load effects:

- The short-term design wind speed approach
- The short-term environmental contour method
- The long-term design approach.

In a short-term extreme value calculation, stationary and ergodic extreme storm conditions with a statistical return period R_{yr} are defined by a set of environmental variables given by the vector $\mathbf{w}$. In the short-term design wind speed approach, the environmental variables are defined by the event of a mean wind velocity with a return period R_{yr}, and the corresponding turbulence parameters are chosen deterministically. In the short-term environmental contour method, the extreme storm condition is defined by the environmental contour method, accounting for the variability in the turbulence parameters as well as the mean wind velocity.

When considering a short-term stochastic response time series from the extreme storm condition defined by $\mathbf{w}$, the largest response during that time window is the short-term extreme response, $\widetilde{R}|\boldsymbol{W}$. However, for another stochastic response realization of the same environmental load definition, $\mathbf{w}$, the extreme peak might be different. Thus, the short-term extreme peak response is uncertain. In current design practice for cable-supported bridges, the expected value of this uncertain peak is used to define the design load effects, $E[\widetilde{R}|\boldsymbol{W}]$, based on the short-term design wind speed approach.

In a long-term design approach, a long-term time window is defined by a sequence of short-term time series. Then, the cumulative probability density function of the long-term extreme response is established, $F_R(r,\ 0 \le t < T)$. This function is calculated based on the response statistics of each short-term condition, weighted by the probability of the environmental parameters, $f_{\boldsymbol{W}}(\boldsymbol{w})$. In this way, the extreme response with a statistical return period can be calculated directly from $F_R(r,\ 0 \le t < T) = 1\text{-}p = 1\text{–}1/R_{yr}$,

The methodology presented in this paper relies on the assumption of stationarity within each short-term event. Wind loads are often separated into synoptic and non-synoptic winds [30], and non-synoptic winds can dominate the extreme responses in some areas of the world. Non-synoptic effects can be an important aspect when considering extreme buffeting response [31], and proper investigations needs to be carried out where these events are important. The methodology presented herein focus on the extreme response due to synoptic winds, where the stationarity assumption is reasonable. The strong winds in Norway, and at the Hardanger Bridge site, is dominated by synoptic winds and extratropical cyclones [32] and is a suitable case for investigation of the proposed methodology.

2.1. Short-term extreme response

If the zero-mean response process can be assumed to be Gaussian, ergodic and stationary within a short-term period, $\widetilde{T}$, the short-term extreme peak distribution of that process can be completely defined by the mean upcrossing rate of a threshold, $\widetilde{r}$ [15]. The mean $\widetilde{r}$-upcrossing rate can be defined as:

$$v^{+}(\widetilde{r}|\boldsymbol{w}) = v^{+}(0)exp\left\{-\frac{\widetilde{r}^2}{2m_0(\boldsymbol{w})}\right\} \tag{1}$$

where

$$v^{+}(0) = \frac{1}{2\pi}\sqrt{\frac{m_2(\boldsymbol{w})}{m_0(\boldsymbol{w})}} \tag{2}$$

and $\mathbf{w}$ is the vector containing the environmental variables, $v^{+}(0)$ is the zero-upcrossing rate and m_i is the ith moment of the response spectrum, $\boldsymbol{S}_{\widetilde{R}|\boldsymbol{W}}(\omega|\boldsymbol{w})$:

$$m_i(\boldsymbol{w}) = \int_0^{\infty} \omega^i \boldsymbol{S}_{\widetilde{R}|\boldsymbol{W}}(\omega|\boldsymbol{w})d\omega \tag{3}$$

and ω is the angular frequency. Then, the short-term extreme value cumulative density function (CDF) can be defined as follows by introducing the assumption of independent peaks for reasonably large values of $\widetilde{r}$:

$$\begin{aligned} F_{\widetilde{R}|\boldsymbol{W}}(\widetilde{r}|\boldsymbol{w}) &= exp\left\{-v^{+}(\widetilde{r}|\boldsymbol{w})\widetilde{T}\right\} \\ &= exp\left\{-\frac{\widetilde{T}}{2\pi}\sqrt{\frac{m_2(\boldsymbol{w})}{m_0(\boldsymbol{w})}}exp\left\{-\frac{\widetilde{r}^2}{2m_0(\boldsymbol{w})}\right\}\right\} \end{aligned} \tag{4}$$

The expected value of the short-term extreme peak response can be estimated as follows, given that $ln(v^{+}(0)\widetilde{T})$ is sufficiently large:

$$E[\widetilde{R}] = k_p\sqrt{m_0(\boldsymbol{w})} \tag{5}$$

where

$$k_p \approx \left\{ \sqrt{2ln(v^+(0)\widetilde{T})} + \frac{\gamma}{\sqrt{2ln(v^+(0)\widetilde{T})}} \right\} \tag{6}$$

and $\Upsilon \approx 0.5772$ is the Euler constant, $E[\cdot]$ is the expectation operator and k_p is the short-term peak factor.

2.2. The full long-term method (FLM)

The FLM is relatively simple to use but very computationally demanding since, in principle, the short-term response statistics needs to be calculated and integrated over all possible combinations of the environmental variables, weighted by their probability of occurrence.

Different formulations of the full-long-term method can be found in the literature, but under the appropriate assumptions, they are mathematically equivalent [16].

2.2.1. Formulation based on the upcrossing rate of the short-term response

Naess [33] proposed a formulation that calculates the full long-term extreme value CDF based on the $\widetilde{r}$-upcrossing rate of each short-term process. In the long-term period, T, the response process can no longer be considered a stationary process, so Eq. (4) is generalized for a nonstationary process by replacing the short-term upcrossing rate with its mean value over the long-term period:

$$F_R(r) = exp\left\{ -T\frac{1}{T}\int_0^T v^+(r,t)dt \right\} \tag{7}$$

By describing the long-term period as a sequence of stationary short-term periods, the following formulation is reached:

$$F_R(r) = exp\left\{ -T\int_W v^+(\widetilde{r}|\boldsymbol{w})f_W(\boldsymbol{w})d\boldsymbol{w} \right\} \tag{8}$$

where $f_W(\mathbf{w})$ is the joint PDF of the environmental parameters defined in the vector $\mathbf{w}$, $T = N_{st}\widetilde{T}$is the long-term period, and N_{st} is the number of short-term conditions. This formulation is the full long-term formulation with the least limiting assumptions [16], relying only on the ergodicity assumption and that the high-level upcrossings follow a Poisson distribution and will be used in the full long-term calculations in this paper.

2.2.2. Formulations based on all short-term extreme values

In a full long-term calculation, the long-term extreme response CDF is calculated based on the response statistics of each short-term condition. Borgman [34] presented an expression for the long-term extreme value CDF based on the short-term extreme values:

$$F_R(r) = exp\left\{ \int_W ln\left\{ F_{\widetilde{R}|W}(\widetilde{r}|\boldsymbol{w}) \right\} f_W(\boldsymbol{w})d\boldsymbol{w} \right\} \tag{9}$$

This formulation is valid under the assumption of statistically independent short-term extreme values. The formulation proposed by Borgman [34] is based on ergodic averaging. This is often referred to as the exact formulation of the full long-term extreme value CDF, but it should be noted that it is exact only under the many assumptions previously listed. An approximate formulation of this problem exists as well. This formulation is based on the population mean and not the ergodic average, hence the approximation. The formulation reads:

$$\overline{F}_R(r) = \int_W F_{\widetilde{R}|W}(\widetilde{r}|\boldsymbol{w})f_W(\boldsymbol{w})d\boldsymbol{w} \tag{10}$$

This formulation is often a good approximation, although it is strictly unconservative as shown by Jensen's inequality theorem, stating that the expected value of a function is greater than or equal to the expected value of the function after a concave transformation. In Eq. (9), the natural logarithm is a concave function and the following will apply [35]:

$$F_R(r) \leqslant \overline{F}_R(r) \tag{11}$$

and in effect, the R_{yr} return period response quantity estimated by the approximate formulation will be less than or equal to the exact formulation.

2.3. Reliability theory-based calculation methods

2.3.1. Expressing the approximate full long-term formulation as a reliability problem

The approximate formulation for the full long-term extreme value CDF shown in Eq. (10) can be reformulated as a reliability problem. An interesting effect from this reformulation is that it can be solved in an approximate manner using known structural reliability theory such as the first-order reliability method (FORM).

The reliability problem can be written as [36]:

$$p_f = \int_{G(\boldsymbol{x})\leqslant 0} f_X(\boldsymbol{x})d\boldsymbol{x} \tag{12}$$

where p_f is the failure probability, $\mathbf{X}$ is a vector of random variables described by the joint probability density function (PDF) $f_X(\mathbf{x})$, and $G(\mathbf{x})$ is the limit state function in the real space. In the reliability problem, $\mathbf{X}$ contains random variables describing the uncertain load and the uncertain capacity, and then $G(\mathbf{x}) \leq 0$ defines failure. The approximate formulation of the long-term extreme value can be rewritten in a similar form:

$$\overline{F}_R(r) = \int_W F_{\widetilde{R}|W}(\widetilde{r}|\boldsymbol{w})f_W(\boldsymbol{w})d\boldsymbol{w} = \int_W \int_{\widetilde{r}\leqslant r} f_{\widetilde{R}|W}(\widetilde{r}|\boldsymbol{w})d\widetilde{r}f_W(\boldsymbol{w})d\boldsymbol{w} \tag{13}$$

Now, if we define a vector $\boldsymbol{X} = \left[\boldsymbol{W}, \widetilde{R}\right]$, we can construct a joint PDF of the environmental variables and the short-term extreme response as:

$$f_X(\boldsymbol{x}) = f_{\widetilde{R}|W}(\widetilde{r}|\boldsymbol{w})f_W(\boldsymbol{w}) \tag{14}$$

and then Eq. (13) is rewritten to the same format as Eq. (12):

$$\overline{F}_R(r) = \int_{\widetilde{r}\leqslant r} f_X(\boldsymbol{x})d\boldsymbol{x} = 1 - \int_{G(\boldsymbol{x})\leqslant 0} f_X(\boldsymbol{x})d\boldsymbol{x} = 1 - p_f \tag{15}$$

where $G(\boldsymbol{x}) = \boldsymbol{r} - \widetilde{\boldsymbol{r}}$.

2.3.2. Expressing the exact full long-term formulation as a reliability problem

Giske et al. [35] proposed a method to formulate the exact full long-term method shown in Eq. (9) as a reliability problem as well, avoiding the strictly unconservative simplification that the approximate formulation introduces. Since $ln\left\{F_{\widetilde{R}|W}(\widetilde{r}|\boldsymbol{w})\right\}$is not a CDF, they rewrote the expression:

$$F_R(r) = exp\left\{ \int_W \left(1 + ln\left\{F_{\widetilde{R}|W}(\widetilde{r}|\boldsymbol{w})\right\}\right) f_W(\boldsymbol{w})d\boldsymbol{w} - 1 \right\} \tag{16}$$

and then introduced a new random variable, Y, so a CDF-like function could be defined as:

$$F_{Y|W}(y|\boldsymbol{w}) = max\left(1 + ln\left\{F_{\widetilde{R}|W}(\widetilde{r}|\boldsymbol{w})\right\}, 0\right) \tag{17}$$

Thus, the formulation reads:

$$F_R(r) \approx exp\left\{ \int_W F_{Y|W}(y|\boldsymbol{w})f_W(\boldsymbol{w})d\boldsymbol{w} - 1 \right\} \tag{18}$$

Similar to the definition in Eq. (15), the reliability problem becomes:

$$F_R(r) \approx exp\left\{ -\int_{G(\boldsymbol{x})\leqslant 0} f_X(\boldsymbol{x})d\boldsymbol{x} \right\} = exp\{-p_f\} \tag{19}$$

where

$$f_X(\boldsymbol{x}) = F_{Y|W}(y|\boldsymbol{w})f_W(\boldsymbol{w}) \tag{20}$$

However, even though this method is based on the exact FLM formulation, the IFORM solution in itself is an approximation.

2.3.3. Solving the long-term extreme value problem using the inverse first-order reliability method (IFORM)

The FORM procedure can be used to calculate the probability of exceedance, p_f, by transforming the random variables in **X** into the standard normal space, **U**, and minimizing the distance to the limit state function:

$$\beta = \arg min|\boldsymbol{u}|; \text{ constrained to } g(\boldsymbol{u}) = 0 \tag{21}$$

where $g(\boldsymbol{u}) = \boldsymbol{r} - \widetilde{r}(\boldsymbol{u}) = 0$ is the limit state function in the standard normal space. β is the reliability index related to the return period as follows:

$$\beta = -\Phi^{-1}(1/[\frac{R_{yr} \times 365.25 \times 24 \times 60}{\widetilde{T}}]) \tag{22}$$

where Φ is the standard normal CDF, R_{yr} is the statistical return period in years, and $\widetilde{T}$ is the short-term duration in minutes.

In the FORM, the limit state function is approximated by a first-order Taylor expansion through the design point identified in the standard normal space [36].

The failure probability is related to the reliability index by the relationship:

$$p_f = \int_{g(\boldsymbol{u})\leqslant 0} f_U(\boldsymbol{u})d\boldsymbol{u} = \Phi(-\beta) \tag{23}$$

However, in the inverse FORM procedure, the reliability index is indirectly known through the given return period, and the response, $\boldsymbol{r}$, is sought. Thus, the solution to the long-term extreme value problem in Eq. is found by maximizing the response under the following constraint:

$$r = \arg max\widetilde{r}(\boldsymbol{u}); \text{ constrained to } |\boldsymbol{u}| = \beta \tag{24}$$

2.3.4. The environmental contour method (ECM)

Winterstein and Haver [19] presented a method based on the IFORM to establish environmental contours for combinations of environmental variables with a combined target statistical return period. The method is also referred to as the IFORM with omission factors since it decouples the variability of the environmental variables from the uncertainty of the structural response itself. In this method, combinations of environmental variables in a standard normal space with a given distance to the origin, namely, the reliability index β, are transformed into the real space based on a joint probability distribution of the environmental variables.

The extreme response is calculated by the short-term method, but it was shown in [19] that the omission factors could be used to inflate the contours to account for the neglected short-term extreme value uncertainty. However, Kleiven and Haver [12] found that the best way to correct for the neglected extreme response uncertainty was by multiplying the expected short-term extreme response by a correction factor or by choosing a higher percentile of the short-term extreme response CDF as the design value. The correction factor is defined as:

$$C_{corr} = \frac{r_{LT}}{\widetilde{r}_{ECM}} \tag{25}$$

where r_{LT} is the long-term extreme response and $\widetilde{r}_{ECM}$ is the expected value of the short-term extreme response found by the ECM. The percentile in the short-term extreme response distribution corresponding to the long-term extreme response is defined by:

$$p_{corr} = F_{\widetilde{R}|W}(r_{LT}) = exp\left\{ -\frac{\widetilde{T}}{2\pi}\sqrt{\frac{m_2(\boldsymbol{w})}{m_0(\boldsymbol{w})}}exp\left(-\frac{r_{LT}^2}{2m_0(\boldsymbol{w})}\right)\right\} \tag{26}$$

where $F_{\widetilde{R}|W}$ is the short-term extreme response CDF defined in Eq. (4).

2.3.5. Finding the design point by the ECM and the IFORM

The design point on the environmental contour can be found by manual iterations and engineering judgment, but it can also be found by numerical optimization [8]. The ECM problem is similar to the IFORM problem, but the number of random variables included is reduced by one in the ECM since the variability of the short-term response itself is excluded. For a system dominated by an environmental load described by two random variables, the environmental contour will be a plane circle in the standard normal space, but the random variables in the IFORM problem will define a sphere in this space. Since the design point solution of both methods needs to have the target distance to the origin, β, the IFORM solution will always fall within the environmental contour when plotted in the two-dimensional space, as illustrated in Fig. 1. Transformation between the real and standard normal space can be performed by different procedures such as the Rosenblatt transformation or by a simple linear transformation [8,37].

The difference in the solution algorithm between the IFORM and the ECM is that with the IFORM, the short-term extreme value $\widetilde{r}(\boldsymbol{u})$ is found directly by transformation of the **u**-vector, but in the ECM, $\widetilde{r}(\boldsymbol{u})$ is treated as a deterministic value given the environmental variables defined by the **u**-vector and is calculated as the short-term expected extreme value defined in Eq. (5).

The iteration algorithm to solve the IFORM problem shown in Eq. (15) and Eq. (19), as proposed by Li and Foschi [17] reads:

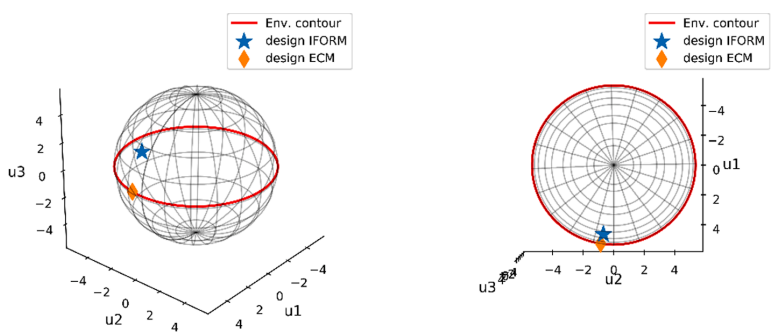

Fig. 1. Illustration of the difference between ECM and IFORM and the effect of the added dimension due to the inclusion of the short-term extreme response uncertainty shown in the standard normal space.

$$\boldsymbol{u}^{k+1} = \beta \frac{\nabla \widetilde{r}_{n+1}(\boldsymbol{u}^k)}{\left|\nabla \widetilde{r}_{n+1}(\boldsymbol{u}^k)\right|} \tag{27}$$

where n is the number of environmental variables and k indicates the iteration. Since the short-term extreme value uncertainty is not included as a variable in the ECM, the expression above reduces to:

$$\boldsymbol{u}^{k+1} = \beta \frac{\nabla \widetilde{r}_{n}(\boldsymbol{u}^k)}{\left|\nabla \widetilde{r}_{n}(\boldsymbol{u}^k)\right|} \tag{28}$$

This simple iteration scheme may fail to converge for some problems, so in the present study, the iteration algorithm defined by Giske et al. [35] was used. This is, in principle, the same algorithm as the one defined by Li and Foschi [17], but a backtracking approach is introduced to avoid diverging iterations. The convergence criterion was defined by the following:

$$\frac{|\boldsymbol{u}^{k+1} - \boldsymbol{u}^k|}{\boldsymbol{u}^{k+1}} < Tolerance \tag{29}$$

A *tolerance* = 10^{-3} was used in all IFORM and ECM solutions presented in this paper.

3. Buffeting analysis of the Hardanger Bridge

3.1. Probabilistic turbulence model

Fenerci and Øiseth [38] established a site-specific probabilistic model for the Hardanger Bridge (see Fig. 2) wind field representative of the bridge girder elevation based on full-scale measurement data. The model described 6 turbulence parameters as correlated lognormal stochastic variables, conditional on the mean wind velocity and the two dominating wind directions, East and West. The wind directions are channeled by the surrounding terrain, especially for the strong winds [39], so to assume the winds from East and West to be perpendicular to the bridge is a reasonable approximation.

The turbulence spectral model used to define the probabilistic turbulence parameters was a Kaimal-type spectra and a normalized cross-spectra as described in [40,41]:

$$\frac{S_{u,w}f}{\sigma^2_{u,w}} = \frac{A_{u,w}f_z}{(1+1.5A_{u,w}f_z)^{5/3}}\ ,\ f_z = \frac{fz}{U}$$
$$C_{u,w} = exp(-K_{u,w}\frac{f\Delta x}{U}) \tag{30}$$

where f is the frequency, z is the height above the ground, U is the mean wind velocity, $\sigma_{u,w}$ are the standard deviations of the along wind- (u) and the vertical (w) turbulence, $A_{u,w}$ are the nondimensional spectral parameters, $K_{u,w}$ are the decay coefficients and Δx is the separation distance along the bridge span. For a quantitative description of the model, the readers are referred to [38].

The mean wind velocity is described using Weibull distributions conditional on the main wind directions, east and west, established in [8,39]. The Weibull PDF model is described in Eq. (31), and the fitted parameters are shown in Table 1.

Table 1
Fitted Weibull distribution parameters [8].

	Weibull distribution	
	λ	k
East	5.1941	1.7946
West	1.4063	0.8616

$$f(u) = \frac{k}{\lambda}\left(\frac{u}{\lambda}\right)^{(k-1)} exp\left\{-\left(\frac{u}{\lambda}\right)^k\right\}\ ;\ u \geqslant 0 \tag{31}$$

where k is the shape parameter and λ is the scale parameter.

Based on this model, the vector describing the environmental variables in the long-term analyses will contain one or more of the variables $\boldsymbol{w} = \{U, \sigma_u, \sigma_w, A_u, A_w, K_u, K_w\}$.

3.2. Buffeting analysis

The buffeting analyses are performed in the frequency domain using multimode theory [42–46]. The structural properties are described by a detailed 3D finite element (FE) model in Abaqus [47] shown in Fig. 3, and a structural damping ratio of $\xi = 0.5\%$ was assigned to all vibration modes. The shape and frequency of the most important modes are shown in Table 2. All contributing modes below a cutoff frequency of 1 Hz were included in the analyses. This cutoff frequency is expected to be high enough to describe the stresses well. However, for the acceleration estimates, some contributions from higher frequencies may be excluded by this cutoff frequency. Although this exclusion will result in an underestimation of the acceleration predictions, this choice is made to be consistent with the filtering of the full-scale measurements for comparison reasons.

The girder is modelled with linear Timoshenko beam elements in the FE model. Stiffened steel box girders can be prone to stiffness reductions due to shear-lag effects in the areas of large shear forces, which will not be properly represented with the beam element model used. It is possible to account for this stiffness reduction by modelling the girder with shell elements or by adjusting the beam element formulation [48,49]. For the global buffeting response behavior considered in this paper, the shear forces are modest, and the bending moments are smooth. Therefore, the shear lag effects on the global stiffnesses is expected to be small in the considered application.

The steady-state static coefficients and the aerodynamic derivatives (ADs) for the bridge girder are based on wind tunnel experimental data as described in [50]. The static coefficients are presented in Table 3, and the aerodynamic admittance was neglected. Details on the fitted AD models can be found in [8].

Only the bridge girder and the main cable were subjected to wind loading in the calculations. The static coefficients for the main cables are based on recommendations in Eurocode 1–4 [51] for a painted circular cable and a Reynolds number of approximately 1.5e6, giving a drag coefficient of 1.0. The drag coefficient of the downstream main cable was reduced to 0.7 to account for possible shielding effects. The motion-induced forces on the main cables are described using quasi-steady theory [52].

3.3. Design stresses from stochastic section forces

Most modern suspension bridges today are constructed with a closed box steel girder. These cross-sections are composed of stiffened thin steel plates that can buckle when compressive stresses approach the capacity in the ultimate limit state. Eurocode 3 [53] proposes methods to account for this effect, where parts of the local steel plates under critical pressure are assumed to buckle and be ineffective. These plate parts are removed when the efficient cross-sectional properties are calculated. In addition to local plate buckling, the Eurocode describes methods to account for global buckling of stiffened plate fields. This global buckling is accounted for by reducing the effective thickness of the plates in the pressure zone when the efficient cross-sectional properties are calculated [54]. The Eurocode also states that the effect of plate buckling on the cross-sectional stiffness in an elastic global analysis can be neglected if the effective part of a plate is larger than half the total plate area. This applies for the Hardanger Bridge girder, and the cross-sectional stiffness is based on the full elastic cross section in the buffeting analyses.

Fig. 2. The Hardanger Bridge seen from the northeast (picture by the authors).

Table 2
Frequency and shape of the most important natural modes of the Hardanger Bridge.

Lateral			Vertical			Torsional		
Mode	Freq. [Hz]	Shape	Mode	Freq. [Hz]	Shape	Mode	Freq. [Hz]	Shape
1	0.050	Sym.	3	0.110	Asym.	15	0.359	Sym.
2	0.100	Asym.	4	0.141	Sym.	26	0.523	Asym.
5	0.173	Sym.	6	0.197	Sym.	49	0.783	Sym.
13	0.302	Asym.	7	0.211	Asym.	58	1.006	Asym.
21	0.443	Sym.	12	0.272	Sym.			
34	0.655	Asym.	14	0.329	Asym.			

Table 3
Geometry and steady-state static coefficients used in the buffeting analyses (0-degree angle of attack).

Bridge member	*Width* [m]	*Depth* [m]	C_D	C_L	C_L'	C_M	C_M'
Girder	18.3	3.33	1.050	−0.363	2.220	0.017	0.786
Main cables	0.6	0.6	1.0/ 0.7	0	0	0	0

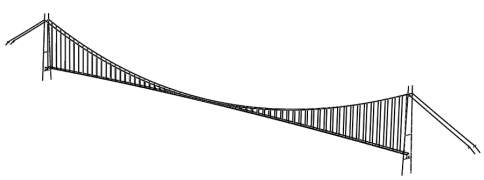

Fig. 3. FEM model of the Hardanger Bridge.

The Eurocode based methodology for the stress calculations are simplified, but suitable for practical applications.

The elastic design stresses for a steel cross-section considering plate buckling can be expressed in a simplified manner according to Eurocode 3 [53] as follows, provided that elastic flexural buckling of the beam is not present:

$$\sigma_{Ed} = \frac{N_x}{A_{eff}} + \frac{M_y + N_x e_z}{W_{eff,y}} + \frac{M_z + N_x e_y}{W_{eff,z}} \tag{32}$$

where A_{eff} is the effective area for pure compressive axial force (N_x), $W_{eff,y}$ is the effective section modulus for pure weak-axis bending (M_y) and $W_{eff,z}$ is the effective section modulus for pure strong-axis bending (M_z). The eccentricities e_y and e_z describe the shift of the neutral axes under pure compression of the cross-section. To estimate the stresses from a buffeting analysis, the contribution from each section force response process can be added according to Eq. (32). In a time-domain analysis, the stress process can be calculated directly based on the section force combination in each time step. In a frequency-domain analysis, the extreme response statistics can be performed directly on the stress process by utilizing the information available from the section force response cross-spectral density matrix.

Each section force process will contribute to the stresses at a considered point. To obtain the total stresses, the variance of a sum of correlated Gaussian processes is needed. From Eq. (32) we get:

$$\begin{aligned} m_{i,\sigma_{Ed}} &= m_{i,Z_1Z_1} + m_{i,Z_2Z_2} + m_{i,Z_3Z_3} + 2m_{i,Z_1Z_2} + 2m_{i,Z_1Z_3} + 2m_{i,Z_2Z_3} \\ m_{i,\sigma_{Ed}} &= a^2 m_{i,N_xN_x} + b^2 m_{i,M_yM_y} + c^2 m_{i,M_zM_z} + 2abm_{i,N_xM_y} + 2acm_{i,N_xM_z} + 2bcm_{i,M_yM_z} \end{aligned} \tag{33}$$

where

$$\begin{aligned} Z_1(t) &= \left(\frac{1}{A_{eff}} + \frac{e_z}{W_{eff,y}} + \frac{e_y}{W_{eff,z}}\right) N_x(t) = aN_x(t) \\ Z_2(t) &= \frac{1}{W_{eff,y}} M_y(t) = bM_y(t) \\ Z_3(t) &= \frac{1}{W_{eff,z}} M_z(t) = cM_z(t) \end{aligned} \tag{34}$$

From the frequency-domain buffeting analysis, the full response

spectral density matrix is established as:

$$\boldsymbol{S}_r(\omega) = \begin{bmatrix} S_{N_xN_x}(\omega) & S_{N_xM_y}(\omega) & S_{N_xM_z}(\omega) \\ S_{M_yN_x}(\omega) & S_{M_yM_y}(\omega) & S_{M_yM_z}(\omega) \\ S_{M_zN_x}(\omega) & S_{M_zM_y}(\omega) & S_{M_zM_z}(\omega) \end{bmatrix} \tag{35}$$

Then, the ith moment of the response cross spectral density can be calculated as:

$$m_{i,kl} = \int_0^\infty \omega^i S_{kl}(\omega) d\omega \tag{36}$$

where $i = 0$ defines the covariance of the response, and $i = 2$ defines response rate. In this way, the 0th and 2nd moments of the stress response spectrum needed to define Eq. (1) can be estimated.

The Hardanger Bridge girder cross-section is shown in Fig. 4. The top plate, including the top parts of the inclined webs, has a plate thickness of 12 mm, whereas the bottom plate and the bottom parts of the webs are 8 mm thick. All stiffeners are made from 6-mm-thick steel plates welded to the skin plates. The effective cross-sectional properties of the girder under different pure section force configurations are shown in Table 4, where a negative sign indicates compression, and the axis system is indicated in Fig. 5. The effective plate thickness reduction due to buckling of plate fields is calculated based on column-like behavior according to Eurocode 3 [53].

Three stress points, which are indicated in Fig. 4, are investigated in the following sections. The effective cross-sectional properties critical for all three points are shown in Table 4, and the effective cross-sections are shown in Fig. 5.

4. Long-term extreme stresses in the Hardanger Bridge girder

4.1. Quarter-span detailed investigations

Stress point 2 in the quarter span of the bridge girder was chosen for detailed investigations of the long-term extreme stresses. Fig. 6 shows that the quarter span is critical since all section forces considered are relatively large. Stress point 2 is chosen because it is affected by all three section force processes considered, although the strong-axis moment dominates the total stresses.

4.1.1. Sectorial extreme stress investigations

The extreme stresses given the two defined wind directions, East and West, are calculated using the five methods shown in Table 5. The table outlines the theoretical basis and limitations of all methods in brief, and further details are provided in Section 2.

In Figs. 7 and 8, the 100-year return period long-term extreme response is investigated by considering two environmental variables at a time, for easterly and westerly winds, respectively. Here, the mean wind velocity together with one turbulence parameter at a time are described as stochastic variables. The turbulence parameters that are treated deterministically are chosen according to the point on the contour with the case of maximum mean wind velocity, as shown in Table 6. For illustration purposes, the turbulence parameters used in the design calculations of the bridge are also shown in the table. The Design Basis

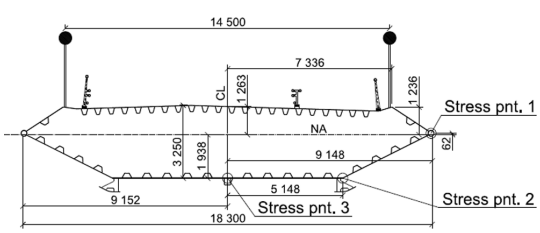

Fig. 4. The Hardanger Bridge girder cross-section.

mean wind velocity is significantly stronger than the full-scale measurements at the bridge midspan. Lystad et al. [39] concluded that the measuring mast used to establish the design basis for the Hardanger Bridge would likely overpredict the wind speed at the bridge midspan due to terrain wind speed-up effects at the mast position.

The 100-year return period environmental contour conditional on wind direction is shown together with the design point found by the IFORM and the ECM in Figs. 7 and 8. The design basis turbulence parameters are also indicated in the figures. In the background of the plots, the normalized contribution to the integral in Eq. (8) for the 100-year return period response is shown. The IFORM design point can be seen often to be located close to the maximum contribution to the FLM. Isoresponse lines for the expected value of the short-term extreme stresses at stress point 2, as defined by Eq. (5), are shown in the figures as solid gray lines. The inclinations of these lines are indications of the stress sensitivity to the turbulence parameters.

The design stresses calculated by all methods are shown for different combinations of stochastically described turbulence parameters in Fig. 9 and Tables 7 and 8 for easterly and westerly winds, respectively. The FLM calculations become very computationally demanding when the number of dimensions becomes large, so these calculations are performed only for up to three-dimensional combinations. The expected value of the short-term extreme response from the ECM along with the correction factor, C_{corr}, and percentiles needed to correct the short-term ECM solution, p_{corr}, corresponding to the different long-term extreme response estimates are shown in Figs. 10 and 11 and Tables 7 and 8.

The stresses at stress point 2 are greatly affected by the along-wind turbulence standard deviation σ_u, so by describing this parameter and the mean wind velocity as stochastic variables, the long-term extreme stresses at stress point 2 can be estimated quite well. By also including the vertical turbulence standard deviation, the accuracy of the predicted long-term extreme response will improve even further.

Relatively small differences between the long-term extreme value prediction methods can be found in Fig. 9 and Tables 7 and 8, although the methods based on the approximate formulation in Eq. (10) are slightly unconservative, as expected. However, larger deviations can be seen between the methods for the westerly winds, especially for combinations including the along-wind turbulence standard deviation.

Kleiven and Haver [12] concluded that the relative effect of short-term extreme response uncertainty was reduced when the number of influential environmental parameters was increased. For the easterly winds, a similar trend is seen for the Hardanger Bridge buffeting response as well. When influential environmental parameters such as the along-wind turbulence standard deviation are described as stochastic variables, the difference between the expected short-term extreme response predicted by the ECM and the long-term extreme responses is reduced, as reflected by the reduced correction factors and percentiles in Figs. 10 and 11 and Tables 7 and 8. This is also the case for westerly winds when using long-term methods based on the approximate formulation in Eq. (10). However, this effect is not clear for westerly winds when using long-term methods based on exact formulations. The westerly wind Weibull distribution used in the investigations herein, established in [8], has a low shape parameter, k, indicating a long-tailed distribution. The contributions to the FLM shown in the background of Fig. 8 are farther out in the tail of the joint PDF than for the easterly winds. In this case, the IFORM design point is farther away from the area contributing the most to the FLM extreme response. These observations indicate that the accuracy of the approximate methods is sensitive to the tail shape of the environmental parameter joint PDF.

The long-term stresses in all three stress points are calculated using the IFORM Eq. (15) and are shown in Fig. 12. Large effects on the long-term extreme stresses can be observed by describing different turbulence parameters as stochastic variables. Stress point 1 does not receive significant contributions from weak-axis bending, and as a result, only the along-wind turbulence parameters significantly affect the long-term

Table 4
Effective cross-sectional properties of the Hardanger Bridge under pure section force configurations (NA-i refers to the neutral axis of the full cross-section, and NA_{eff}-i refers to the neutral axis of the effective cross-section).

A [m^2]	A_{eff} [m^2]	I_y [m^4]	$I_{y,eff}$ [m^4]	I_z [m^4]	$I_{z,eff}$ [m^4]	NA-y [m]	NA-z [m]	NA_{eff}-y [m]	NA_{eff}-z [m]	N	M_y	M_z
0.565	0.372	0.969	0.629	15.193	9.016	0.000	0.000	−0.035	0.105	−1	0	0
0.565	0.489	0.969	0.722	15.193	13.413	0.000	0.000	0.005	0.249	0	−1	0
0.565	0.489	0.969	0.854	15.193	12.131	0.000	0.000	−0.821	0.011	0	0	−1

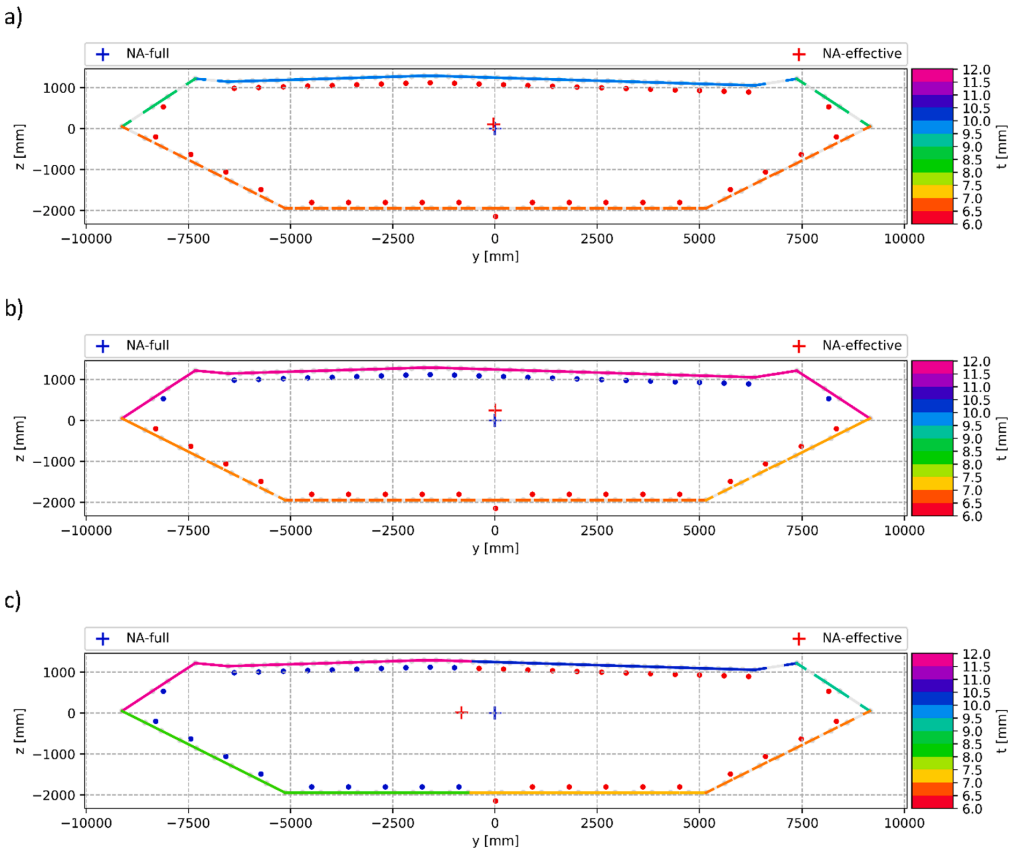

Fig. 5. Effective cross-sections for (a) pure axial compression (N = −1), (b) pure weak-axis bending with compression in the bottom plate ($M_y = -1$), and (c) pure strong-axis bending with compression on the right-hand side of the figure ($M_z = -1$). Effective thicknesses are indicated by the color bar, and the stiffener centroids are shown as red dots in compression and blue dots in tension. (For interpretation of the references to color in this figure legend, the reader is referred to the web version of this article.)

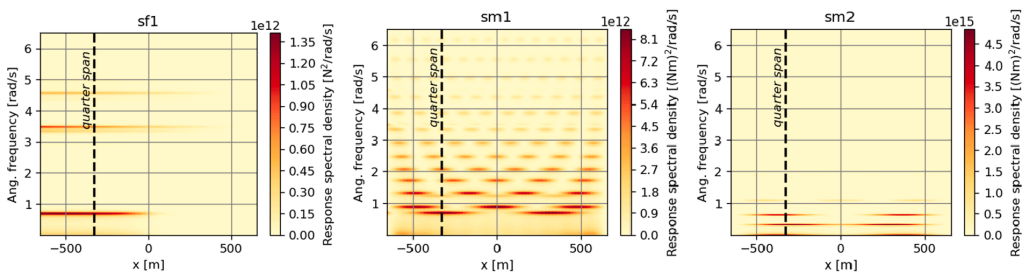

Fig. 6. Along-span response spectral density contour plots of the axial force (sf1), the weak-axis moment (sm1) and the strong-axis moment (sm2).

Table 5
Theoretical basis overview of considered extreme value methods.

	Full integration	Reliability method	Extreme response uncertainty	Exact formulation	Approx. formulation
FLM Eq. (8)	Yes	No	Yes	Yes	No
FLM Eq. (10)	Yes	No	Yes	No	Yes
IFORM Eq. (15)	No	Yes	Yes	No	Yes
IFORM Eq. (19)	No	Yes	Yes	Yes	No
ECM	No	Yes	No	No	No

Table 6
Deterministic turbulence parameters at girder height corresponding to the event of maximum mean wind velocity (contour tip and design basis values) [55].

Wind direction	U [m/s]	σ_u [m/s]	σ_w [m/s]	A_u	A_w	K_u	K_w
East	23.76	2.84	1.10	25.8	2.01	6.92	5.98
West	33.79	3.66	1.36	47.1	3.32	8.21	8.65
Design Basis	36.6	0.136U	0.068U	40.8	3.3	8.8	6.3

stresses. Stress point 3, however, is dominated by weak axis-bending, and the vertical turbulence parameters are more important to the estimated long-term stresses.

4.1.2. Omnidirectional extreme stresses by the FLM

The sectorial extreme response has been investigated thus far with a focus on methodology to estimate extreme stresses. However, the sectorial extreme response does not correspond directly to the omnidirectional extreme response.

The omnidirectional full long-term extreme response CDF can be calculated as a weighted sum of the CDFs conditional on wind direction [56]:

$$F_R(r) = \sum_i p_i F_{R|\theta}(r|\theta_i) \tag{37}$$

where p_i is the probability of the wind coming from sector θ_i. In general, the response CDF conditional on the wind direction needs to include the possible effects of skew winds. As mentioned in Section 3.1 and discussed in [8,39], the terrain surrounding the Hardanger Bridge channels the strong winds, so the two defined wind directions, East and West, can be considered to be perpendicular to the bridge.

In Table 9, the omnidirectional 100-year return period extreme stresses at stress point 2 are presented.

Estimating the omnidirectional extreme stresses using the environmental contour method and the IFORM, however, is not straightforward. Winterstein [56] suggested a simplified way to estimate a lower bound of the omnidirectional extreme response from sectorial subpopulations using the IFORM. Another method suggested by [56] was to fit a function to the tail of the long-term extreme response CDF based on IFORM extreme response estimates and use Eq. (37) to calculate the omnidirectional extreme response. Further, [57] and [58] estimated environmental contours by including the wind direction as a circular variable.

All these methods introduce some limitations and uncertainties, and the appropriate choice will be problem-specific. Such methods have not been investigated in the work presented here but to obtain omnidirectional design stresses, the directionality of the wind must be considered.

As seen in Table 9, with one wind direction dominating the response, the sectorial extreme response will be a conservative choice for the omnidirectional extreme response and could be a reasonable design value in some cases.

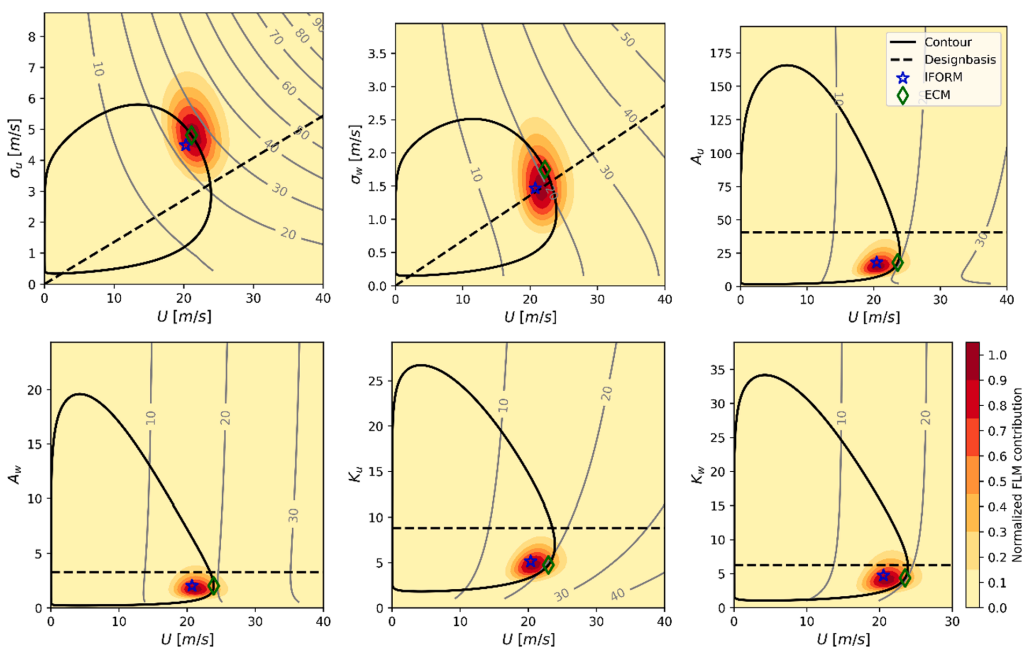

Fig. 7. Long-term extreme girder stresses at the quarter span in stress point 2 from easterly winds. The normalized contribution to the 100-year return period extreme value using the FLM is shown in the background, and the IFORM and the ECM design point are indicated.

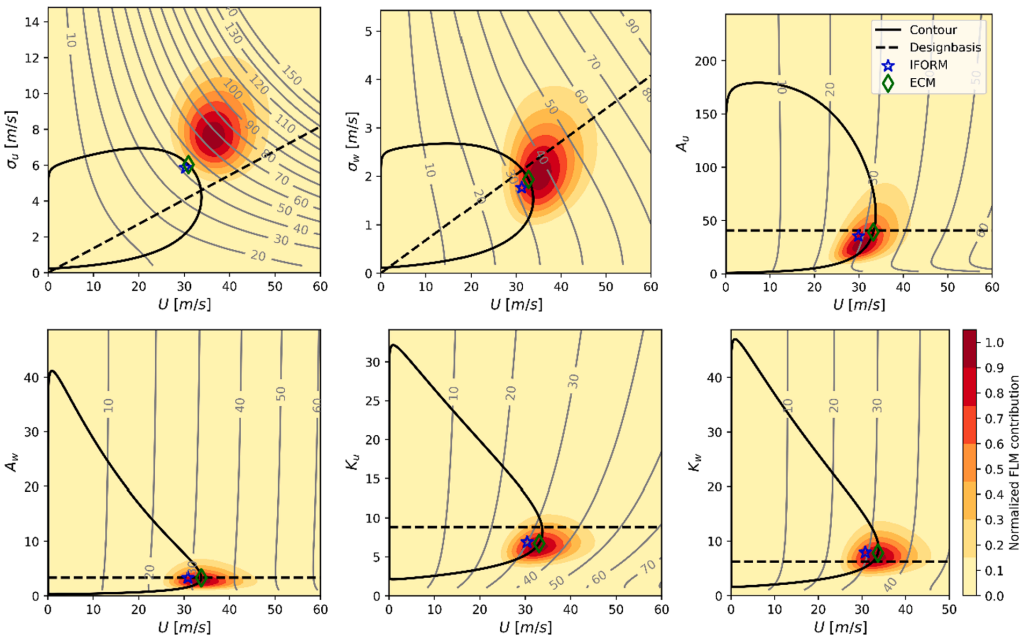

Fig. 8. Long-term extreme girder stresses at the quarter span in stress point 2 from westerly winds. The normalized contribution to the 100-year return period extreme value using the FLM is shown in the background, and the IFORM and the ECM design point are indicated.

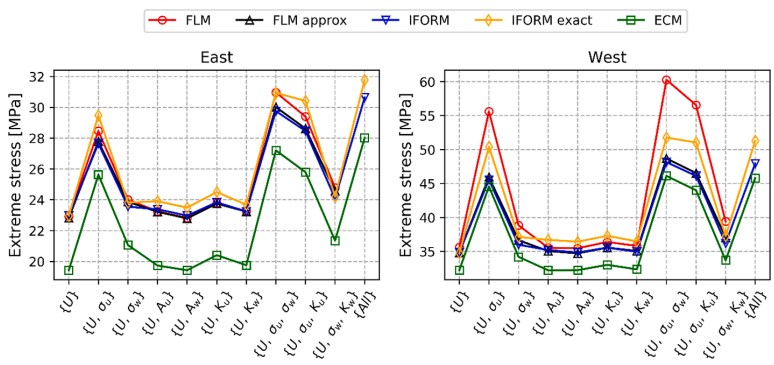

Fig. 9. Extreme girder stresses in stress point 2 at the quarter span, considering different combinations of turbulence parameters described as random variables.

4.2. Along-span investigations

In the previous sections, detailed investigations of the girder quarter span were presented. However, the bridge behavior can change along the span. In the following, the design point for the girder stresses conditional on the two wind directions is calculated along the span using the IFORM Eq. (15) and the ECM.

In Fig. 13, the stresses in the three stress points under consideration are plotted along the bridge span for easterly and westerly winds. In these calculations, all turbulence parameters are treated as stochastic variables. The 100-year return period long-term extreme stresses calculated by the IFORM are shown together with the expected short-term extreme response calculated by the ECM. The ECM correction factor and the short-term extreme response distribution percentile corresponding to the IFORM long-term stresses are shown in Fig. 13. Some variations in the correction factors and percentiles are seen along the span and between the different stress points, although the variations are relatively small.

In Figs. 14 and 15, the along-span variations in the turbulence parameters corresponding to the ECM design point are shown for the easterly and westerly winds, respectively. In general, small variations in the critical turbulence parameter combinations can be seen, below ± 6%. However, for the most influential turbulence parameters, even less variation is seen. Assuming that stress point 1 is affected only by the along-wind turbulence parameters such as σ_u, A_u and K_u, the variation in the critical turbulence parameter combinations is typically under ± 1%. This case is also pertinent when considering stress point 3, which is dominated by weak axis bending and thus sensitive to vertical turbulence, with a slight exception for the A_w parameter.

Based on these observations, a reasonable estimate for the long-term extreme response at all positions along the Hardanger Bridge girder could be achieved by the following simplified approach:

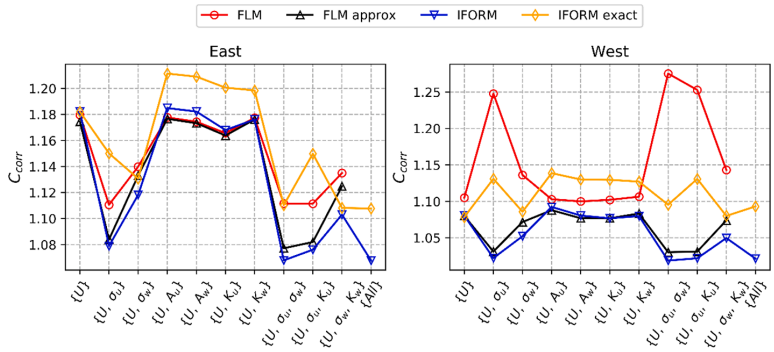

Fig. 10. Long-term correction factors (long-term/ECM) for the girder stresses in stress point 2 at quarter span, considering different combinations of turbulence parameters described as random variables.

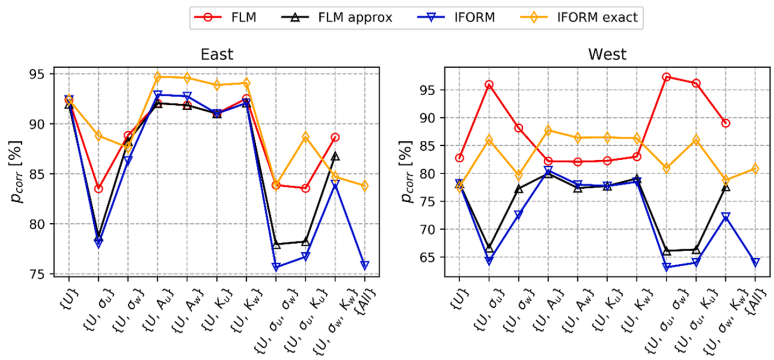

Fig. 11. ECM short-term extreme value CDF percentile corresponding to the long-term extreme girder stresses in stress point 2 at quarter span, considering different combinations of turbulence parameters described as random variables.

Table 7
Extreme stresses, correction factors and short-term percentiles for long-term correction of the ECM solution at quarter span in stress point 2 for easterly winds. Stresses from different long-term methods and combinations of turbulence parameters described as random variables are presented.

Included variables, **w**		*{U}*	*{U, σ_u}*	*{U, σ_w}*	*{U, A_u}*	*{U, A_w}*	*{U, K_u}*	*{U, K_w}*	*{U, σ_u, σ_w}*	*{U, σ_u, K_u}*	*{U, σ_w, K_w}*	*{All}*
Extreme response *[Mpa]*	FLM Eq. (8)	22.9	28.5	24.0	23.2	22.8	23.8	23.3	31.0	29.4	24.8	N/A
	FLM Eq. (10)	22.8	27.8	23.9	23.2	22.8	23.8	23.2	30.0	28.6	24.6	N/A
	IFORM Eq. (15)	23.0	27.7	23.6	23.4	23.0	23.8	23.2	29.8	28.5	24.1	30.6
	IFORM Eq. (19)	23.0	29.5	23.8	23.9	23.5	24.5	23.7	30.9	30.4	24.2	31.8
	ECM	19.4	25.6	21.1	19.7	19.4	20.4	19.8	27.2	25.8	21.4	28.0
C_{corr}	FLM Eq. (8)	1.18	1.11	1.14	1.18	1.17	1.17	1.18	1.11	1.11	1.13	N/A
p_{corr} *[%]*	FLM Eq. (8)	92	84	89	92	92	91	93	84	84	89	N/A

Table 8
Extreme stresses, correction factors and short-term percentiles for long-term correction of the ECM solution at quarter span in stress point 2 for westerly winds. Stresses from different long-term methods and combinations of turbulence parameters described as random variables are presented.

Included variables, **w**		*{U}*	*{U, σ_u}*	*{U, σ_w}*	*{U, A_u}*	*{U, A_w}*	*{U, K_u}*	*{U, K_w}*	*{U, σ_u, σ_w}*	*{U, σ_u, K_u}*	*{U, σ_w, K_w}*	*{All}*
Extreme response *[Mpa]*	FLM Eq. (8)	35.6	55.6	38.9	35.5	35.5	36.4	35.8	60.3	56.6	39.4	N/A
	FLM Eq. (10)	34.8	46.0	36.7	35.1	34.7	35.6	35.1	48.7	46.5	37.0	N/A
	IFORM Eq. (15)	34.8	45.6	36.0	35.2	34.8	35.6	35.0	48.2	46.1	36.2	47.9
	IFORM Eq. (19)	34.8	50.4	37.1	36.7	36.4	37.3	36.5	51.8	51.0	37.2	51.3
	ECM	32.3	44.6	34.2	32.2	32.3	33.0	32.4	46.1	44.0	33.7	45.8
C_{corr}	FLM Eq. (8)	1.11	1.25	1.14	1.10	1.10	1.10	1.11	1.28	1.25	1.14	N/A
p_{corr} *[%]*	FLM Eq. (8)	83	96	88	82	82	82	83	97	96	89	N/A

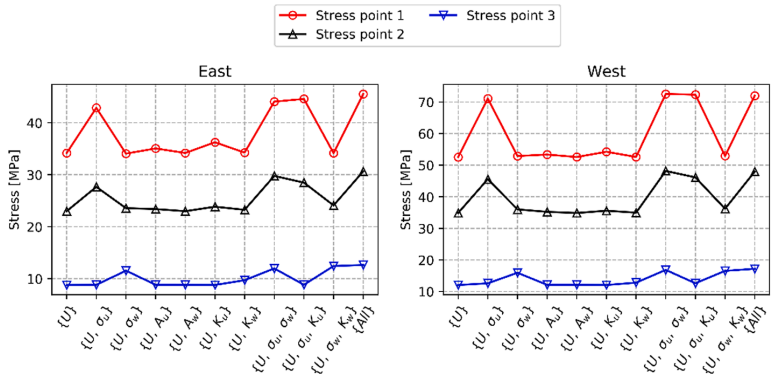

Fig. 12. Long-term extreme girder stresses at quarter span in all considered stress points, identified by the IFORM EQ.

Table 9
Omnidirectional 100-year return period extreme stresses at quarter span at stress point 2 for westerly winds. Combinations of stochastically described turbulence parameters are presented.

Included variables, **w**	*{U}*	*{U, σ_u}*	*{U, σ_w}*	*{U, A_u}*	*{U, A_w}*	*{U, K_u}*	*{U, K_w}*	*{U, σ_u, σ_w}*	*{U, σ_u, K_u}*	*{U, σ_w, K_w}*
FLM East	22.9	28.4	24.0	23.2	22.8	23.8	23.3	31.0	29.4	24.8
FLM West	35.6	55.8	38.9	35.5	35.4	36.4	35.8	60.3	56.6	39.4
FLM Omni	33.5	49.4	36.1	33.6	33.4	34.2	33.7	53.4	50.1	36.6

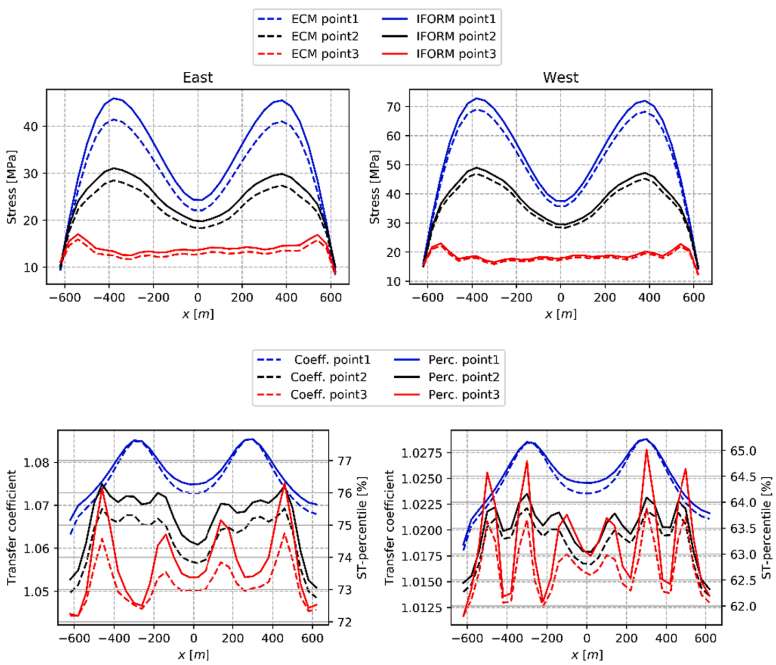

Fig. 13. Along-span stresses and correction factors and short-term extreme CDF percentiles from the ECM and the IFORM. Left; easterly winds, right; westerly winds.

1. Calculate the critical environmental parameter combinations in a representative section along the girder using the ECM.
2. Calculate the correction factor or the short-term extreme value distribution percentile corresponding to the long-term extreme value in the section considered.
3. Calculate the short-term response in all sections along the girder based on the critical turbulence parameter combination identified by the ECM in 1.
4. Correct the short-term response along the span with the correction identified in 2.

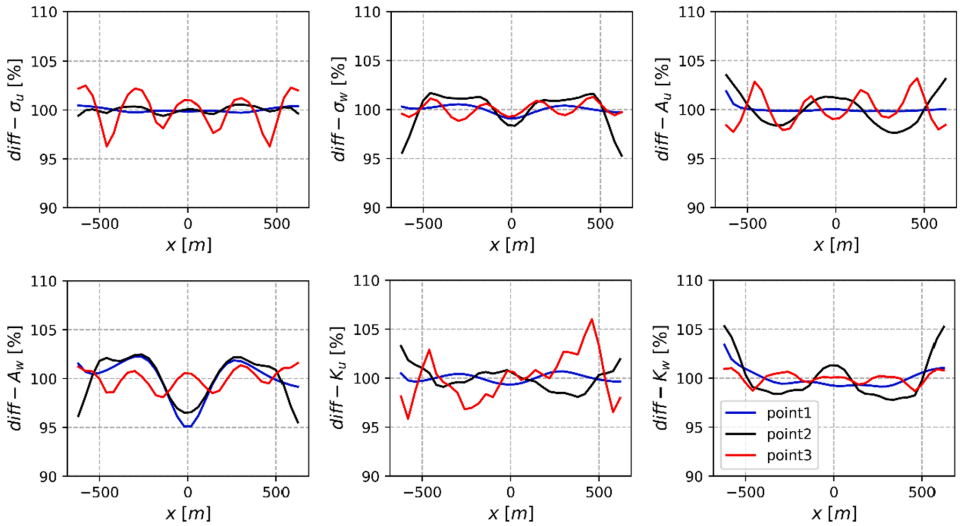

Fig. 14. Percentage of along-span mean critical turbulence variable identified by the ECM design point for easterly winds. diff-w_i = 100% * $w_i(x)$/mean(w_i).

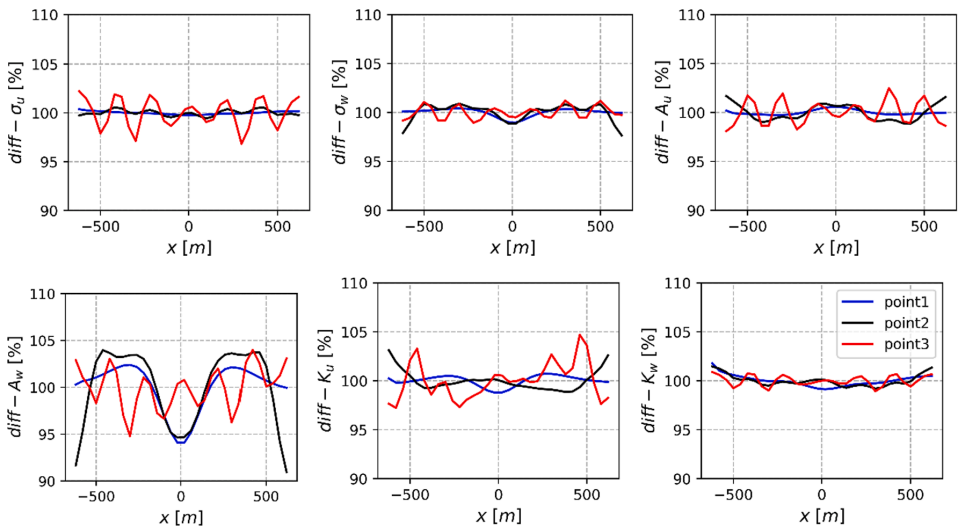

Fig. 15. Percentage of along-span mean critical turbulence variable identified by the ECM design point for westerly winds. diff-w_i = 100% * $w_i(x)$/mean(w_i).

5. Comparison with full-scale acceleration peak response measurements

Fenerci et al. [59] found that the buffeting acceleration response measured at full scale at the Hardanger Bridge was very scattered when plotted as function of the mean wind velocity. They concluded that most of the scattered data could be explained by the uncertainty in the turbulence field. In Fig. 16, the midspan peak acceleration measurements from the Hardanger Bridge are shown for lateral, vertical and torsional motions. The 10-minute maximum peaks are plotted, and the high-frequency content above 1 Hz is removed by low-pass filtering of the measurements. The measurement data are colored by the normalized scatter density multiplied by the mean wind velocity squared. The measurements are split into easterly and westerly wind directions, but the measurements for the opposite direction are shown as gray scatter in the background of the plot. The data from the full-scale measurement program at the Hardanger Bridge site is available with open access [60,61] and the measurement system is described in detail in [59].

To investigate the performance of the long-term extreme response analyses, the long-term acceleration response at the midspan of the Hardanger Bridge girder is calculated and compared with the full-scale measurements. The acceleration response has a different behavior than the design stresses which has been the focus in the previous parts of this paper, but the acceleration response comparison can provide an indication of the performance of the overall methodology.

The 100-year return period extreme accelerations estimated by the classical IFORM and the ECM, conditional on the mean wind velocity, are also shown in Fig. 16. A simple modification to the iteration algorithm shown in Eq. (27) is needed to solve the IFORM problem when the mean wind velocity is given. The modification reads:

$$\boldsymbol{u}^{k+1} = \sqrt{\beta^2 - u_1^2}\ \frac{\nabla \widetilde{r}_n(\boldsymbol{u}^k)}{\left|\nabla \widetilde{r}_n(\boldsymbol{u}^k)\right|} \tag{38}$$

where u_1 is the standard normal variable corresponding to the given mean wind velocity, n is the number of environmental variables and k indicates the iteration number. Since the short-term extreme value uncertainty is not included as a variable in the ECM, the expression above reduces to:

$$\boldsymbol{u}^{k+1} = \sqrt{\beta^2 - u_1^2}\ \frac{\nabla \widetilde{r}_{n-1}(\boldsymbol{u}^k)}{\left|\nabla \widetilde{r}_{n-1}(\boldsymbol{u}^k)\right|} \tag{39}$$

As Fig. 16 shows, the extreme accelerations predicted by the IFORM and the ECM correspond quite well with the upper bound of the full-scale measurement data. The extreme responses are calculated based on a 100-year return period, and the full-scale data are based on approximately 4 years of measurements, so theoretically, the measurements should all fall within the extreme response predicted with the IFORM. For illustration purposes, the expected value of the short-term extreme response calculated using the design basis turbulence parameters is also indicated in Fig. 16.

In general, uncertainties regarding static force coefficients for the different bridge members and limitations in the turbulence model can affect the comparison. For the lateral acceleration response, the calculations correspond quite well with the measurements, although some events fall well outside the extreme predictions. Some of the most profound uncertainties for the lateral response are the assumption of stationarity and the estimated static drag coefficients for the girder and the other bridge members.

When considering the vertical response, a kink in the predicted extreme response line can be observed at approximately 11 m/s. The vertical response is strongly influenced by the aerodynamic derivatives. The value of 11 m/s corresponds to the reduced velocity where the first vertical frequency falls within the experimental test range of the AD, as shown in [8]. Since the fitted model for the AD is not smooth in the transition between the experimental data range and the extrapolated area, this is reflected in the predicted extreme acceleration response.

When considering the torsional acceleration, the predicted extreme responses seem to be farther out in the tail of the measured scatter than

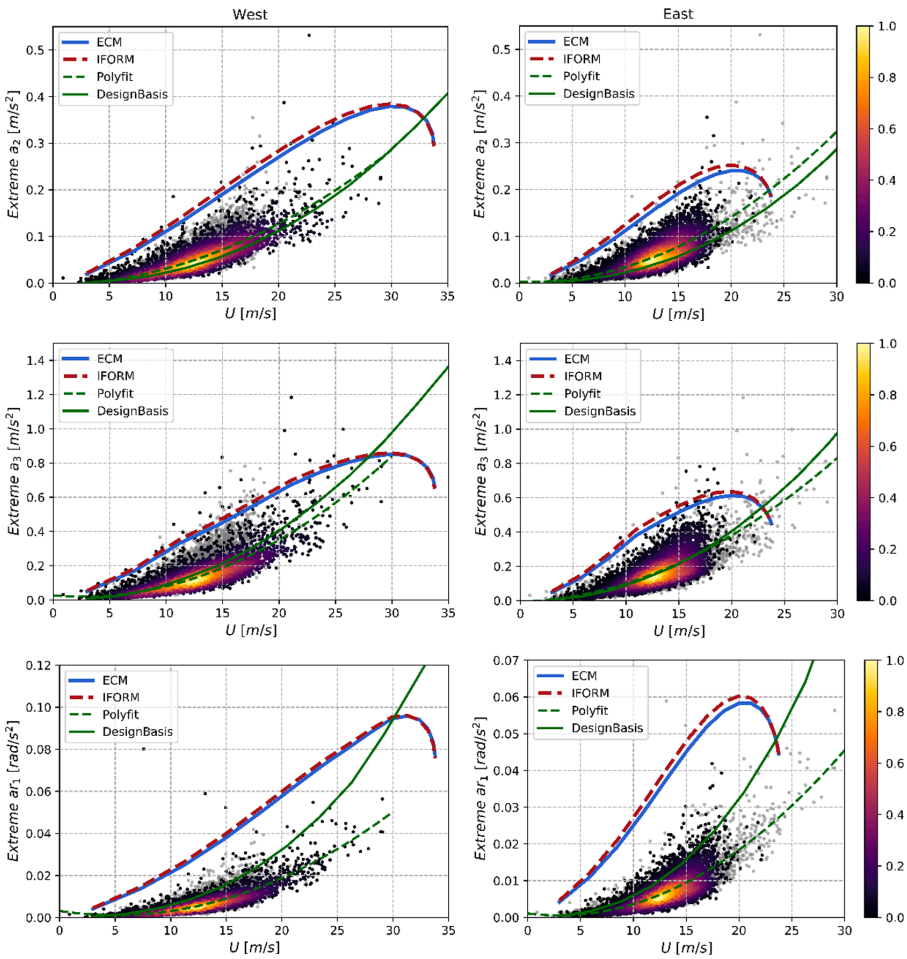

Fig. 16. Lateral- (a2), vertical- (a3) and torsional (ar1) peak acceleration responses of the Hardanger Bridge midspan, established by full-scale measurements (scattered data points colored by scatter density multiplied by the mean wind velocity squared, opposite wind direction indicated as gray data), the ECM and the IFORM conditional on mean wind velocity, the design basis turbulence parameters and a 2nd-order polynomial fit to the measured data.

the other acceleration components. The acceleration response is dominated by higher frequencies than the lateral and vertical responses, so neglecting aerodynamic admittance may significantly affect the torsional response. The first torsional mode is outside the reduced velocity experimental test range for all mean wind velocities below ~ 28 m/s, so almost all the predictions are based on aerodynamic damping and stiffness in the extrapolated range.

In Fig. 17, the short-term peak factor is shown for the measured data, plotted in the same way as in Fig. 16. The predicted peak factors from the design basis analyses are also indicated, corresponding very well with the polynomial fit to the full-scale data. However, the full-scale measured peak factors are very scattered, which is an illustration of the uncertainty in the short-term extreme peak response.

6. Conclusions

The long-term extreme response of the Hardanger Bridge considering uncertain turbulence parameters has been investigated. Considerable effects on the predicted extreme values relevant for design purposes were found, indicating a need to revisit the design methodology used for long-span bridges subjected to turbulent wind loading. In brief, the following conclusions are drawn:

- Extreme design stresses were predicted directly from the frequency-domain buffeting analyses.
- The turbulence uncertainty has large effects on the predicted extreme design stresses of the Hardanger Bridge. Treating the turbulence parameters as deterministic variables may introduce significant errors to the estimated extreme stresses.
- Uncertainty in the short-term extreme response should be considered when predicting extreme stresses for design purposes.
- Reliability-based methods such as the inverse first-order reliability method (IFORM) and the environmental contour method (ECM)

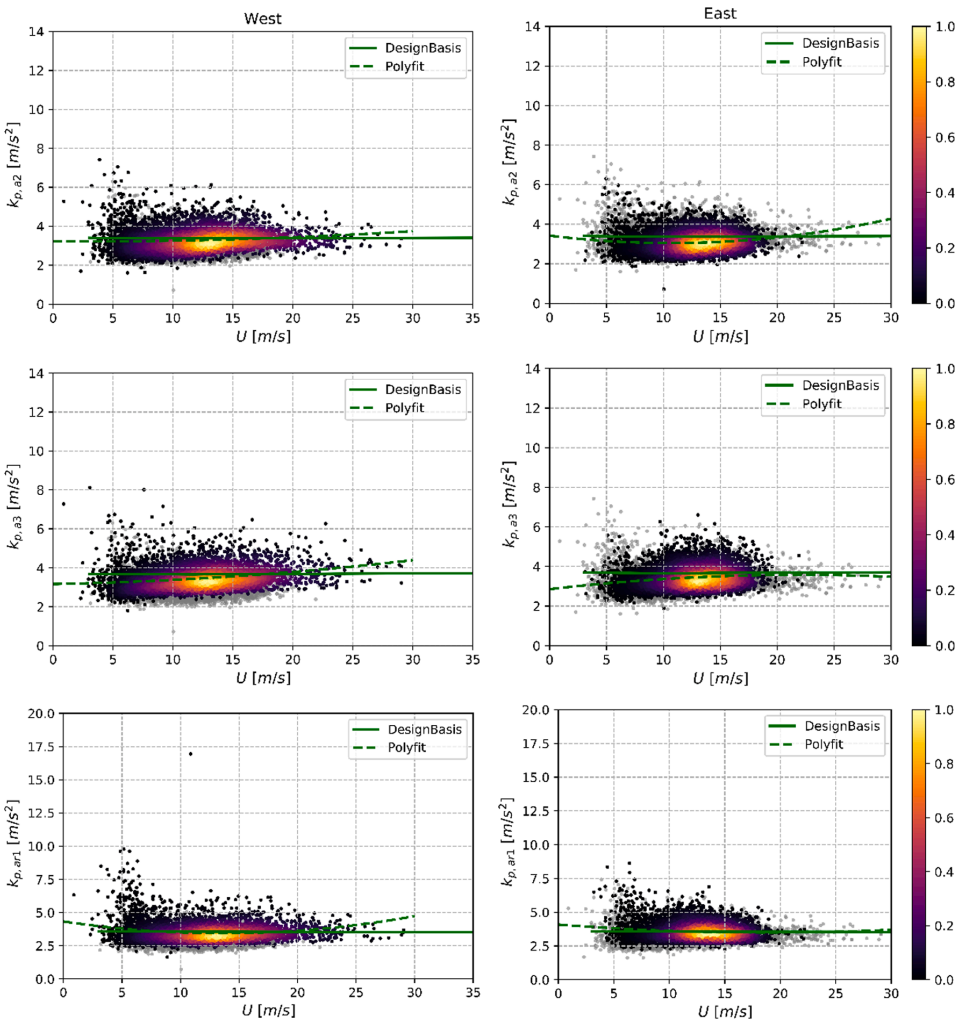

Fig. 17. Lateral- (a2), vertical- (a3) and torsional (ar1) short-term peak factors for the acceleration responses of the Hardanger Bridge midspan. The full-scale measurements are shown (scattered data points colored by scatter density multiplied by the mean wind velocity squared, opposite wind direction indicated as gray data) together with the peak factors estimated by the buffeting analyses using the design basis turbulence parameters. In addition, a 2nd-order polynomial fit to the measured data is shown.

become less effective than full long-term methods when many sections along a long-span bridge need to be assessed.
- With one wind direction dominating the response, the sectorial extreme response could be a reasonable conservative choice for the omnidirectional extreme response in some cases.
- Relatively small variations in the critical turbulence parameter combinations predicted by the ECM were found along the span of the Hardanger Bridge.
- The long-term methods IFORM and ECM were able to predict the variability in the scattered extreme peak acceleration response measured at full scale at the Hardanger Bridge, displaying significant improvement compared with the methodology used for the design of the bridge.

CRediT authorship contribution statement

Tor M. Lystad: Conceptualization, Methodology, Software, Formal analysis, Writing - original draft, Writing - review & editing, Visualization. **Aksel Fenerci:** Validation, Investigation, Data curation. **Ole Øiseth:** Conceptualization, Supervision, Project administration.

Declaration of Competing Interest

The authors declare that they have no known competing financial interests or personal relationships that could have appeared to influence the work reported in this paper.

Acknowledgements

Funding: The research presented in this paper has been financed by Norconsult AS, the Norwegian Public Roads Administration (NPRA) and the Research Council of Norway.

References

[1] Brownjohn JMW, Bocciolone M, Curami A, Falco M, Zasso A. Humber bridge full-scale measurement campaigns 1990–1991. J Wind Eng Ind Aerodyn 1994;52:185–218. https://doi.org/10.1016/0167-6105(94)90047-7.
[2] Miyata T, Yamada H, Katsuchi H, Kitagawa M. Full-scale measurement of Akashi-Kaikyo Bridge during typhoon. J Wind Eng Ind Aerodyn 2002;90:1517–27. https://doi.org/10.1016/S0167-6105(02)00267-2.
[3] Macdonald JHG. Evaluation of buffeting predictions of a cable-stayed bridge from full-scale measurements. J Wind Eng Ind Aerodyn 2003;91:1465–83. https://doi.org/10.1016/J.JWEIA.2003.09.009.
[4] Wang H, Asce M, Tao T, Asce SM, Gao Y, Xu F. Measurement of wind effects on a kilometer-level cable-stayed bridge during Typhoon Haikui. J Struct Eng 2018;144:1–23. https://doi.org/10.1061/(ASCE)ST.1943-541X.0002138.
[5] Wang H, Li A, Guo T, Xie J. Field measurement on wind characteristic and buffeting response of the Runyang Suspension Bridge during typhoon Matsa. Sci China, Ser E Technol Sci 2009;52:1354–62. https://doi.org/10.1007/s11431-008-0238-y.
[6] Cheynet E, Bogunovic Jakobsen J, Snæbjörnsson J. Buffeting response of a suspension bridge in complex terrain. Eng Struct 2016;128:474–87. https://doi.org/10.1016/J.ENGSTRUCT.2016.09.060.
[7] Meng X, Nguyen DT, Xie Y, Owen JS, Psimoulis P, Ince S, et al. Design and implementation of a new system for large bridge monitoring—geoshm. Sensors 2018:18. https://doi.org/10.3390/s18030775.
[8] Lystad TM, Fenerci A, Øiseth O. Buffeting response of long-span bridges considering uncertain turbulence parameters using the environmental contour method. Eng Struct 2020;213:110575. https://doi.org/10.1016/J.ENGSTRUCT.2020.110575.
[9] Fenerci A, Øiseth O. Measured buffeting response of a long-span suspension bridge compared with numerical predictions based on design wind spectra. J Struct Eng 2017;143.. https://doi.org/10.1061/(ASCE)ST.1943-541X.0001873.
[10] Dunham KK. Coastal highway route E39 – extreme crossings. Transp Res Procedia 2016;14:494–8. https://doi.org/10.1016/J.TRPRO.2016.05.102.
[11] Xu Y, Øiseth O, Moan T, Naess A. Prediction of long-term extreme load effects due to wave and wind actions for cable-supported bridges with floating pylons. Eng Struct 2018;172:321–33. https://doi.org/10.1016/J.ENGSTRUCT.2018.06.023.
[12] Kleiven G, Haver S. Met-ocean contour lines for design; correction for omitted variability in the response process. Proc. Fourteenth Int. Offshore Polar Eng. Conf., vol. 1, 2004, p. 202–10.
[13] Haver S, Kleiven G. Environmental contour lines for design purposes: why and when? 23rd Int. Conf. Offshore Mech. Arct. Eng. Vol. 1, Parts A B, 2004, p. 337–45. https://doi.org/10.1115/OMAE2004-51157.
[14] Norwegian Technology Standards Institution. NORSOK N-003 Actions and Action Effects. Oslo, Norway; 2007.
[15] Naess A, Moan T. Stochastic dynamics of marine structures. Cambridge University Press; 2013. https://doi.org/10.1017/CBO9781139021364.
[16] Sagrilo LVS, Naess A, Doria AS. On the long-term response of marine structures. Appl Ocean Res 2011;33:208–14. https://doi.org/10.1016/J.APOR.2011.02.005.
[17] Li H, Foschi RO. An inverse reliability method and its application. Struct Saf 1998;20:257–70. https://doi.org/10.1016/S0167-4730(98)00010-1.
[18] Der Kiureghian A, Zhang Y, Li C-C. Inverse reliability problem. J Eng Mech 1994;120:1154–9.
[19] Winterstein SR, Haver S. Environmental parameters for extreme response : inverse FORM with omission factors. Proc 6th Int. Conf Struct. Saf. Reliab., Innsbruck, Austria; 1993.
[20] Davenport AG. The relationship of reliability to wind loading. J Wind Eng Ind Aerodyn 1983;13:3–27. https://doi.org/10.1016/0167-6105(83)90125-3.
[21] Kareem A. Aerodynamic response of structures with parametric uncertainties. Struct Saf 1988;5:205–25. https://doi.org/10.1016/0167-4730(88)90010-0.
[22] Zhang L, Li J, Peng Y. Dynamic response and reliability analysis of tall buildings subject to wind loading. J Wind Eng Ind Aerodyn 2008;96:25–40. https://doi.org/10.1016/J.JWEIA.2007.03.001.
[23] Pagnini LC, Solari G. Gust buffeting and turbulence uncertainties. J Wind Eng Ind Aerodyn 2002;90:441–59. https://doi.org/10.1016/S0167-6105(01)00202-1.
[24] Pagnini L. Reliability analysis of wind-excited structures. J Wind Eng Ind Aerodyn 2010;98:1–9. https://doi.org/10.1016/J.JWEIA.2009.08.010.
[25] Seo D, Caracoglia L. Statistical buffeting response of flexible bridges influenced by errors in aeroelastic loading estimation. J Wind Eng Ind Aerodyn Wind Eng Ind Aerodyn 2012;104–106:129–40. https://doi.org/10.1016/j.jweia.2012.03.036.
[26] Seo D, Caracoglia L. Estimating life-cycle monetary losses due to wind hazards: Fragility analysis of long-span bridges. Eng Struct 2013;56:1593–606. https://doi.org/10.1016/j.engstruct.2013.07.031.
[27] Caracoglia L. Influence of uncertainty in selected aerodynamic and structural parameters on the buffeting response of long-span bridges. J Wind Eng Ind Aerodyn 2008;96:327–44. https://doi.org/10.1016/j.jweia.2007.08.001.
[28] Solari G, Piccardo G. Probabilistic 3-D turbulence modeling for gust buffeting of structures. Probabilistic Eng Mech 2001;16:73–86. https://doi.org/10.1016/S0266-8920(00)00010-2.
[29] Wu J, Chen SR. Probabilistic dynamic behavior of a long-span bridge under extreme events. Eng Struct 2011;33:1657–65. https://doi.org/10.1016/j.engstruct.2011.02.002.
[30] Vallis MB, Loredo-Souza AM, Ferreira V, Nascimento EL. Journal of Wind Engineering & Industrial Aerodynamics Classification and identification of synoptic and non-synoptic extreme wind events from surface observations in South America. R. J Wind Eng Ind Aerodyn 2019;193. https://doi.org/10.1016/j.jweia.2019.103963.
[31] Owen JS, Nguyen DT, Meng X, Psimoulis P, Xie Y. An observation of non-stationary response to non-synoptic wind on the Forth Road Bridge. J Wind Eng Ind Aerodyn 2020;206. https://doi.org/10.1016/j.jweia.2020.104389.
[32] Fenerci A, Øiseth O. Strong wind characteristics and dynamic response of a long-span suspension bridge during a storm. J Wind Eng Ind Aerodyn 2018;172:116–38. https://doi.org/10.1016/j.jweia.2017.10.030.
[33] Naess A. Technical note: On the long-term statistics of extremes. Appl Ocean Res 1984;6:227–8. https://doi.org/10.1016/0141-1187(84)90061-0.
[34] Borgman LE. Probabilities for heighest wave in hurricane. J Waterw Harb Coast Eng 1973;99:185–207.
[35] Giske F-IG, Leira BJ, Øiseth O. Full long-term extreme response analysis of marine structures using inverse FORM. Probabilistic Eng Mech 2017;50:1–8. https://doi.org/10.1016/J.PROBENGMECH.2017.10.007.
[36] Madsen HO, Krenk S, Lind NC. Methods of structural safety. New York: Dover Publications; 1986.
[37] Rosenblatt M. Remarks on a multivariate transformation. Ann Math Stat 1952;23:470–2.
[38] Fenerci A, Øiseth O. Site-specific data-driven probabilistic wind field modeling for the wind-induced response prediction of cable-supported bridges. J Wind Eng Ind Aerodyn 2018;181:161–79. https://doi.org/10.1016/J.JWEIA.2018.09.002.
[39] Lystad TM, Fenerci A, Øiseth O. Evaluation of mast measurements and wind tunnel terrain models to describe spatially variable wind field characteristics for long-span bridge design. J Wind Eng Ind Aerodyn 2018;179:558–73. https://doi.org/10.1016/J.JWEIA.2018.06.021.
[40] Kaimal J, Wyngaard J, Izumi Y, Coté OR. Spectral characteristics of surface-layer turbulence. Q J R Meteorol Soc 1972;98.
[41] Davenport AG. The spectrum of horizontal gustiness near the ground in high winds. Q J R Meteorol Soc 1961;87:194–211. https://doi.org/10.1002/qj.49708737208.
[42] Chen X, Kareem A, Matsumoto M. Multimode coupled flutter and buffeting analysis of long span bridges. J Wind Eng Ind Aerodyn 2001;89:649–64. https://doi.org/10.1016/S0167-6105(01)00064-2.
[43] Jain A, Jones NP, Scanlan RH. Coupled flutter and buffeting analysis. J Struct Eng 1996;122:716–25. https://doi.org/10.1061/(ASCE)0733-9445(1996)122:7(716).
[44] Jain A, Jones NP, Scanlan RH. Coupled aeroelastic and aerodynamic response analysis of long-span bridges. J Wind Eng Ind Aerodyn 1996;60:69–80. https://doi.org/10.1016/0167-6105(96)00024-4.
[45] Øiseth O, Rönnquist A, Sigbjörnsson R. Simplified prediction of wind-induced response and stability limit of slender long-span suspension bridges, based on modified quasi-steady theory: A case study. J Wind Eng Ind Aerodyn 2010;98:730–41. https://doi.org/10.1016/j.jweia.2010.06.009.

[46] Katsuchi H, Jones NP, Scanlan RH, Akiyama H. Multi-mode flutter and buffeting analysis of the Akashi-Kaikyo bridge. J Wind Eng Ind Aerodyn 1998;77–78: 431–41. https://doi.org/10.1016/S0167-6105(98)00162-7.
[47] Dassault Systèmes Simulia. ABAQUS 2018.
[48] Zhou S-J. Finite beam element considering shear-lag effect in box girder. J Eng Mech 2010;136:1115–22. https://doi.org/10.1061/(asce)em.1943-7889.0000156.
[49] Zhang Y-H, Lin L-X. Shear lag analysis of thin-walled box girders based on a new generalized displacement. Eng Struct 2014;61:73–83. https://doi.org/10.1016/j.engstruct.2013.12.031.
[50] Siedziako B, Øiseth O, Rønnquist A. An enhanced forced vibration rig for wind tunnel testing of bridge deck section models in arbitrary motion. J Wind Eng Ind Aerodyn 2017;164:152–63. https://doi.org/10.1016/J.JWEIA.2017.02.011.
[51] Standard Norge. Eurocode 1: Actions on structures - Part 1–4: General actions. Wind actions 2009.
[52] Strømmen E. Theory of bridge aerodynamics. Second edi. Springer; 2010.
[53] Standard Norge. Eurocode 3: Design of steel structures - Part 1-1: General rules for buildings; 2015.
[54] Beg D, Kuhlmann U, Davaine L, Braun B. Design of plated structures: eurocode 3: design of steel structures, part 1–5: design of plated structures. ECCS-European Convention for Constructional Steelwork 2012. https://doi.org/10.1002/9783433601143.fmatter.
[55] Statens-Vegvesen. The Hardanger Bridge: Design basis - Wind characteristics. Norway; 2006.
[56] Winterstein SR. Environmental contours : including the effects of directionality and other sub- probability-based engineering; 2018. https://doi.org/10.13140/RG.2.2.27196.69763.
[57] Haghayeghi ZS, Ketabdari MJ. A long-term joint probability model for metocean circular and linear characteristics. Appl Ocean Res 2018;75:143–52. https://doi.org/10.1016/j.apor.2018.03.009.
[58] Vanem E, Hafver A, Nalvarte G. Environmental contours for circular-linear variables based on the direct sampling method. Wind Energy 2020;23:563–74. https://doi.org/10.1002/we.2442.
[59] Fenerci A, Øiseth O, Rönnquist A. Long-term monitoring of wind field characteristics and dynamic response of a long-span suspension bridge in complex terrain. Eng Struct 2017;147:269–84. https://doi.org/10.1016/j.engstruct.2017.05.070.
[60] Fenerci A, Kvåle KA, Wiig Petersen Ø, Rønnquist A, Øiseth O. Wind and acceleration data from the Hardanger Bridge. Nor Univ Sci Technol 2020. https://doi.org/10.21400/5ng8980s.
[61] Fenerci A, Kvåle KA, Wiig Petersen Ø, Rønnquist A, Øiseth O. Dataset from long-term wind and acceleration monitoring of the Hardanger Bridge. J Struct Eng 2021;Forthcomin. https://doi.org/10.1061/(ASCE)ST.1943-541X.0002997.

Paper V

Tor Martin Lystad, Aksel Fenerci and Ole Øiseth

Full long-term extreme structural response with sequential Gaussian process surrogate modelling

Submitted for journal publication